KONA

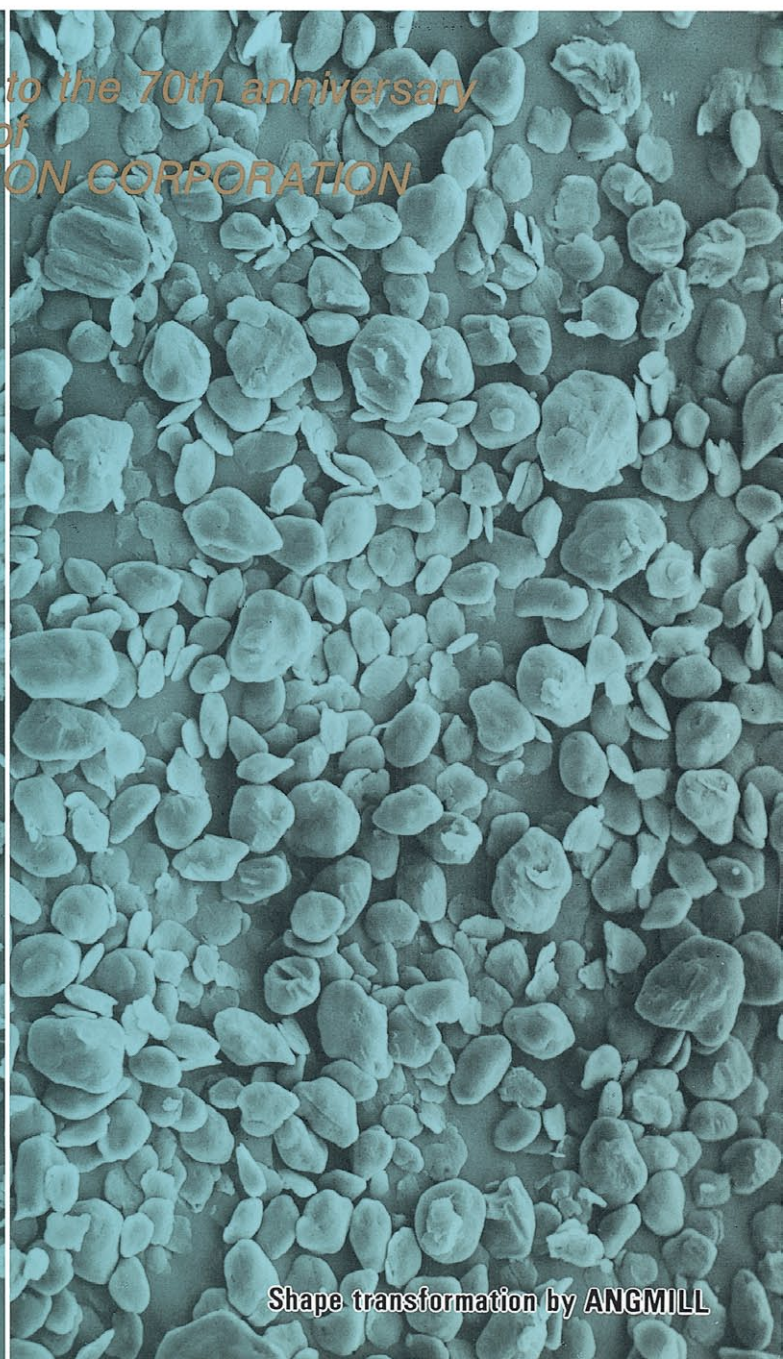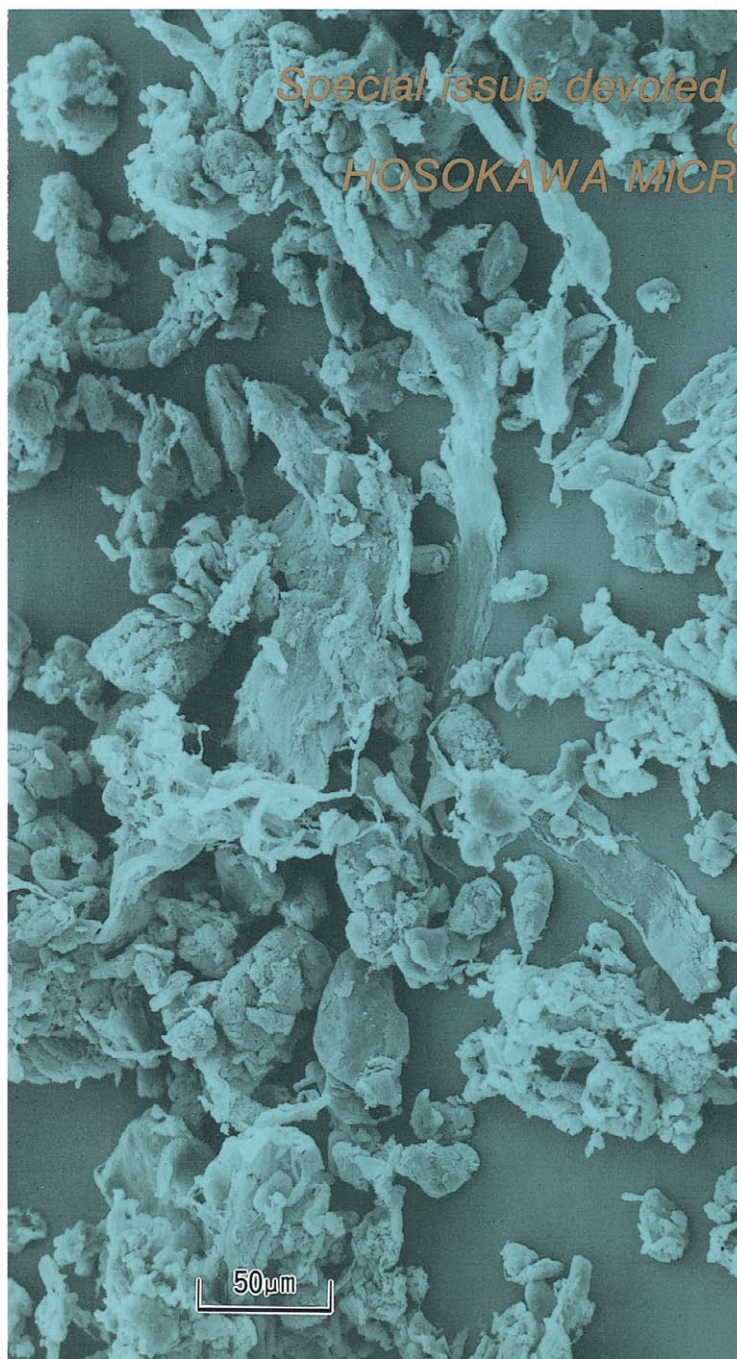## POWDER SCIENCE AND TECHNOLOGY IN JAPAN

No. 4 (1986)

Published by The Party of Powder Technology (JAPAN)

Special issue devoted to the 70th anniversary
of
HOSOKAWA MICRON CORPORATION

50μm

Shape transformation by ANGMILL

KONA is aimed, as its subtitle indicates, to introduce annually the recent works on powder science and technology in Japan to the interested parties in the world. It consists of the English version of reports and reviews carefully selected out of the latest papers which were originally written in Japanese.

KONA is distributed without charge to senior researchers, institutions and libraries in this field throughout the world under the sponsorship of Hosokawa Micron Corporation. Within these limits the editors are always glad to consider the addition of names to the mailing list.

Explanation of the Cover

" 粉 "; This Chinese character is pronounced as "KONA" in Japanese and means "Powder".
" 粉 " on the front page was written by the late Mr. Eiichi Hosokawa, founder of Hosokawa Micron Corporation.

Hosokawa Micron Corporation and its R&D Center

Contents

See page 34 for description of the cover photograph.

Message from the Editor

Three years have passed since the first issue of KONA was published in October, 1983. It is a great pleasure for us to publish the fourth issue which is in commemoration of the 70th anniversary of Hosokawa Micron Corp.

The past three issues of this journal have been, fortunately, welcome to many foreign readers who are not familiar with the Japanese language. Most letters received by our editors refer to the many significant papers concerning powder technology, and they hope that the high standard of quality presented in the first issue will be maintained in the future; KONA removed the language barrier.

Such friendly advices, encouragements, and responses from our readers, confirmed us that our intention and endeavor were useful, and they encouraged us to contiue our efforts. These comments from our readers are highly appreciated.
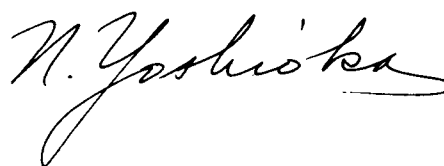
Our initial plan had been to publish 500 copies for each issue containing 50 to 60 pages. In the past three issues, however, the number of delivered copies and pages for each issue were 1500 and 90 to 100, respectively. This was because of the gradual increase in the number of papers to be introduced and additional demands to the mailing list. Increasing labors and expenses for publication have been entirely supported by Hosokawa Micron Corp.

Hosokawa Micron Corp. was founded by the late Mr. Eiichi Hosokawa, the former president, in April, 1916. Then this company gradually grew by the farseeing and positive management of Mr. Masuo Hosokawa, the present president, and it attained its 70th birthday this year. It has been developing original products for all the powder handling fields such as size reduction, classification, dust collection, drying, and trans-

portation, and actively introducing and exporting them to the world. On the other hand, it has been evaluating correctly the excellent technologies in foreign countries and absorbing them to strengthen its own technological competency through cross lisense contracts. Recently, it has incorporated about twenty distinguished companies in the world into its organization to construct the world-wide networks and aim at the international horizontal development.

The editorial board of KONA evaluates Hosokawa's contribution to "world-wide cooperation for advancement of powder technology", and agrees to publish KONA No. 4 as a special issue for commemorating the 70th anniversary of Hosokawa Micron Corp. We hope the steady growth of the company, and we will make efforts on circulating this "non-commercial base" journal to foreign readers under the sponsorship of the company.

Yours truly,

Naoya Yoshioka
Editor in chief

Void Fraction of Multi-Component
Randomly Packed Beds with Size Distributions[†]

Michitaka Suzuki and Toshio Oshima
Department of Chemical Engineering
Himeji Institute of Technology*

Hisaki Ichiba
Shin Nippon Kouki Co., Ltd.**

Isamu Hasegawa
Kokuyo Co., Ltd.***

Abstract

Experimental measurements and computer simulation are reported on the void fraction of multi-component randomly packed beds with log-normal, log-uniform, Rosin-Rammler or Andreasen (Gaudin-Schuhmann) size distributions. Packing experiments were done by two methods, i.e. prodding and tapping. Glass beads (spherical particles) and crushed glass (irregularly shaped particles) were used for these experiments.

The following results were obtained from the experiments and the simulations. A minimum void fraction of a packed bed with Andreasen distribution exists in the range of Fuller constant $q = 0.5 - 0.8$, and the void fractions of packed beds with the other three distributions decrease as the size distribution spreads.

The experimental and the simulated results for void fraction were compared with values calculated by our model and agreement between them was fairly good. This model is useful for estimating the void fraction in a multi-component randomly packed bed of spherical and irregularly shaped particles with size distribution.

1. Introduction

As well known, packing of particles is one of the fundamental characteristics of powder bed. In particular, packing of spheres with equal radii has been investigated by many workers because it is convenient to deal with for mathematical analysis. Real packing state, however, involves particles with a variety of particle-size distribution which has much effects on packing characteristics.

Void fraction of randomly packed particles of multi-components with particle-size distribution has been determined by Anderegg[1], Sohn and Moreland[8], Kawamura et al.[4], and Arakawa and Nishino[2]. Each of them has been obtained by using a few kinds of material with a single particle-size distribution through one packing method. Unfortunately, there appears to be no report presenting how void fraction depends on the kind of material and its particle-size distribution or on the packing method.

The aim of the present work is to study experimentally the influence of particle-size distribution, particle shape and packing method on void fraction of randomly packed beds of

* 2167 Shosha, Himeji, Hyogo, 671-22
TEL. 0792 (66) 1661

** 500, Hishigi, Sakai, Osaka, 593
TEL. 0722 (71) 1201

*** 1-1, Oh-imazato-minami 6-chome, Higashinari-ku, Osaka, 537
TEL. 06 (976) 6211

multi-component system. For the packing experiments, materials used are glass beads (spherical shape) and crushed glass particles (irregular shape) with several different particle-size distributions: log-normal, log-uniform, Rosin-Rammler, and Andreasen (Gaudin - Schuhmann) distributions. Each experiment employs both prodding and tapping for packing particles.

Experimentally obtained data are compared with the calculated results of a mathematical model for estimating void fraction in a multi-component system which was originally built for three-component (different in size) system[6], and also computer simulation.

2. Material, apparatus, and packing method

Material

Two kinds of material with different shape were used as samples: spherical glass beads and irregularly shaped crushed glass particles[☆] with a density of 2.5 x 10^3 kg·m^{-3}. After classified by sieve into 16 segments indicated in **Table 1**, each of the materials were mixed at a given ratio to prepare multi-component packed bed with an arbitrary particle-size distribution. The

mixed particles were dried at 120°C over 2 hours and then got cool naturally in desiccator, before being used for experiments which were made in the laboratory room conditioned at 20°C and a relative humidity of 50 percent.

Packing method

The sample particles were packed by prodding and tapping of which detail was stated in the previous paper[6]. In each case of the present work, the particles arranged to have a given particle-size distribution were put into a container after they were mixed sufficiently in a vinyl bag[☆☆]. After completion of packing, spare amount of particles were discarded and the mass of the whole sample was weighed to obtain the void fraction. Then, the particles were sieved for 12 minutes[☆☆☆] and the mass of particles remained on each sieve was weighed to check the particle-size distribution after operation.

The computer simulation program for random packing of two-component spherical particles[5] was revised to extend the simulation to 4-to-20-component spherical particles.

Table 1　Particle sizes and void fractions used for packing

Sieve range [μm]	Mean diameter Dp_j [μm]	Void fraction $\tilde{\varepsilon}_j$ [−]			
		Glass beads		Crushed glass	
		Tapping	Prodding	Tapping	Prodding
1410−1190	1242	0.394	0.389	0.451	0.475
1190−1000	1136	0.392	0.385	0.452	0.471
1000− 840	921	0.390	0.382	0.445	0.469
840− 710	794	0.389	0.381	0.453	0.478
710− 590	674	0.387	0.380	0.457	0.481
590− 500	542	0.387	0.386	0.456	0.484
500− 420	475	0.388	0.389	0.463	0.489
420− 350	388	0.384	0.388	0.470	0.490
350− 297	338	0.385	0.387	0.477	0.493
297− 250	287	0.380	0.387	0.483	0.500
250− 210	239	0.381	0.387	0.488	0.504
210− 177	199	0.380	0.388	0.494	0.508
177− 149	173	0.381	0.389	0.494	0.509
149− 125	141	0.381	0.390	0.495	0.510
125− 105	124	0.381	0.394	0.498	0.515
105− 88	102	0.381	0.388	0.504	0.520

☆☆ After the particles were ascertained by observation to be mixed almost homogeneously in a vinyl bag without segregation, they were put into a container gradually.

☆ The mean value of the shape factor defined as equivalent area diameter divided by the minimum diameter of circum-circle was 0.74.

☆☆☆ Sieve classification was carried out 9 minutes for three-component powder bed; whereas 12 minutes for multi-component powder bed to attain complete classification.

The total number of packed particles used for each simulation was 1000 to 2000.

Table 1 lists the measured result of void fraction of packed beds involving uniform-size particles classified into 16 segments and the corresponding sieve openings that were averaged arithmetically. The void fractions $\tilde{\epsilon}_j$ were obtained for glass beads (tapping and prodding), computer simulation, and crushed glass beads (prodding and tapping) in order of quantity. The value of $\tilde{\epsilon}_j$ crushed glass particles increased with decreasing particle size, while that of glass bead was kept almost constant, independently of particle size. The estimate of ϵ was carried out by using the values $\tilde{\epsilon}_j$ and the mathematical model mentioned later. Computer simulation was executed by assuming $\tilde{\epsilon}_j$ as a constant value of 0.423 that would be independent of particle size.

3. Mathematical model for predicting void fraction

Let us consider first a single particle in a packed bed consisting of m-component particles. When it contacts with surrounding particles, the number of combination is m^2, as schematically indicated in **Fig. 1**. In this case, the void fractions of each core particle surrounded by several particles are defined as $\epsilon_{(1,1)}, \epsilon_{(1,2)}, \cdots, \epsilon_{(m,m)}$ that can be calculated
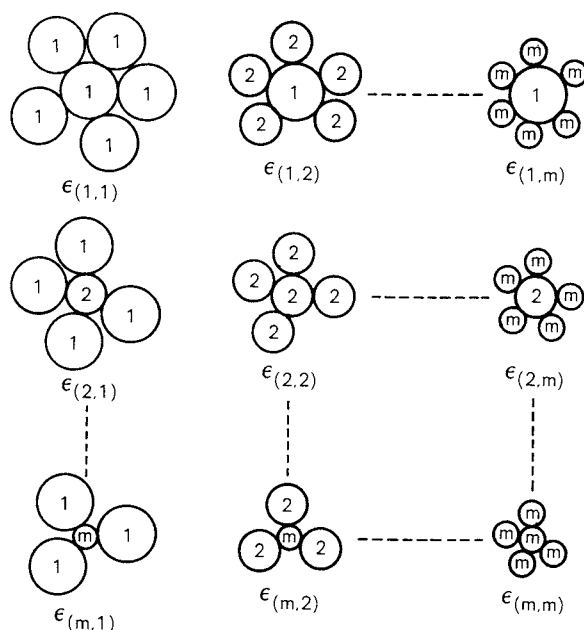

Fig. 1 Types of contact in a multi-component mixture

on the basis of the geometrical data, for example, particle-size ratio and so forth (refer to Appendix 1). The mathematical model employed in the present work, similar to the model for three-component systems, permits combination of m^2 particle void fractions to express the value of ϵ over the whole packed bed.

Let Sa_k be an fractional area of particle k and $\epsilon_{(j,k)}$ be a partial void fraction around a particle j in direct contact with particles k. The partial void fraction ϵ_j around a particle j in m-component packed bed can be written as follows if ϵ_j is assumed to be the sum of the product of Sa_k and $\epsilon_{(j,k)}$.

$$\epsilon_j = \beta_j \cdot \sum_{k=1}^{m} Sa_k \cdot \epsilon_{(j,k)} \tag{1}$$

where β_j is the proportionality constant, which is derived from $\tilde{\epsilon}_j$ measured in a packed bed that consists of only the assembly of particle j as follows.

$$\beta_j = \frac{\tilde{\epsilon}_j}{\epsilon_{(j,j)}} \tag{2}$$

The value of Sa_k, on the other hand, can be obtained by using a fractional volume of particle k, Sv_k:

$$Sa_k = \frac{Sv_k / Dp_k}{\sum_{i=1}^{m} Sv_i / Dp_i} \tag{3}$$

where Dp_k and Dp_i are the sizes of particle k and particle i, respectively. The values of Sv_k and Sv_i are calculated from cumulative undersize percentage, $D^{\star}$, of each size distribution.

The void fraction over the packed bed is finally obtained as follows, assuming that ϵ is composed of the total summation of ϵ_j multiplied by Sv_j:

$$\epsilon = \sum_{j=1}^{m} Sv_j \cdot \epsilon_j \tag{4}$$

The above expressions imply that ϵ is obtainable from particle-size distributions and void fractions in a packed bed consisting of uniformly sized particles $\tilde{\epsilon}_j$.

☆ In the present work, it is assumed that the fractional mass is equal to fractional volume since the density of sample particles used has been ascertained to be constant.

4. Comparison of measured results with computer simulation and model equation

The present work dealt with packed beds consisting of multi-component system having typical four particle-size distributions: the distribution of log-normal, log-uniform, Rosin-Rammler, and Andreasen. The void fraction obtained from above each case is discussed in this section, in comparison with the results of computer simulation and model calculation.

4. 1 Log-normal distribution

Log-normal distribution of particle size is defined as

$$D = \frac{100}{\ln \sigma_g \sqrt{2\pi}}$$

$$\times \int_0^{Dp} \exp\left\{-\frac{(\ln Dp - \ln Dp_{50})^2}{2(\ln \sigma_g)^2}\right\}$$

$$\times d(\ln Dp) \qquad (5)$$

where D, Dp, Dp_{50}, and $\ln \sigma_g$ denote the cumulative undersize mass percentage; the particle diameter, the mass-based cumulative 50 percent particle diameter, and the standard deviation of the distribution, respectively. A packed bed consisting of multi-component system was prepared to satisfy the above distribution. Typical particle-size data of glass beads obtained by sieve classification after the experiments are found to nearly fall on the straight line in **Fig. 2** that represents the calculated result of Eq. (5). This suggests the sufficient accordance of the experimental data with the log-normal distribution.

Based on this preparatory investigation, a lot of experiments and computer simulations were carried out in the wide range of the standard deviation $\ln \sigma_g$ to gain the relationship between $\ln \sigma_g$ and ϵ, and to compare with calculated result derived from the mathematical model. **Figure 3** shows the calculated results by curves and experimental or simulated ones by plotted circles (The same expressions are used in **Figs. 5, 7** and **9**). The void fraction ϵ decreased in order of crushed glass particles (prodding and tapping), computer simulation, and glass beads (prodding and tapping), similar to $\tilde{\epsilon}_j$ referred to in **Table 1**. This implies that the void fraction would decrease in any case with increasing

Fig. 2 Examples of log-normal size distribution for glass beads

Fig. 3 Comparison between calculated, simulated and experimental void fractions for spheres and irregularly shaped particles with log-normal size distribution

$\ln \sigma_g$, that is, broadly spreading particle-size distributions. Moreover, the calculated values derived from the model are found to be in suitable agreement with experimental and simulated data.

4. 2 Log-uniform distribution

This particle-size distribution is defined by

$$D = a \log Dp + b \qquad (6)$$

where a and b are the slope and the constant, respectively, in a semi-logarithmic graph paper where the horizontal axis denotes the particle

diameter D_p. Typical protted particle sizes of crushed glass particles used in the experiments are shown in **Fig. 4** and found to be sufficiently consistent with the straight lines that represent the calculated results of Eq. (6).

Figure 5 shows the relationships of a and ϵ obtained from experiments, computer simulations, and model calculations. The void fraction decreased with broadly spreading particle-size distribution, similar to the case of log-normal distribution. The effect of packing method was scarcely observed in the experiment for glass beads, whereas the effect of particle shape and packing method was similar to that of log-normal distribution. The calculated values derived from the model were in suitable agreement with experimental and simulated
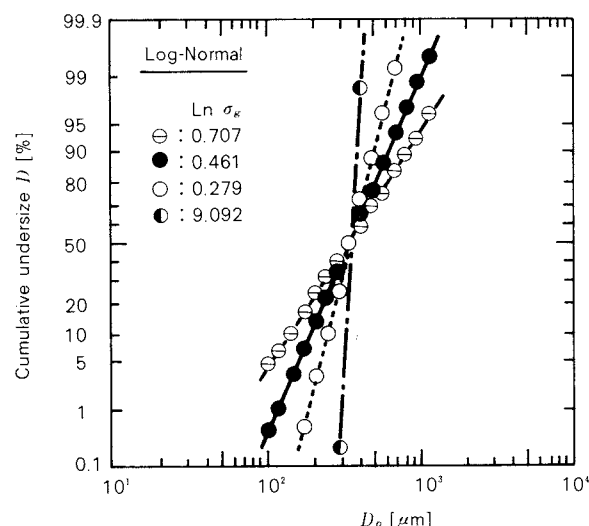

Fig. 4 Examples of log-uniform size distribution for crushed glass
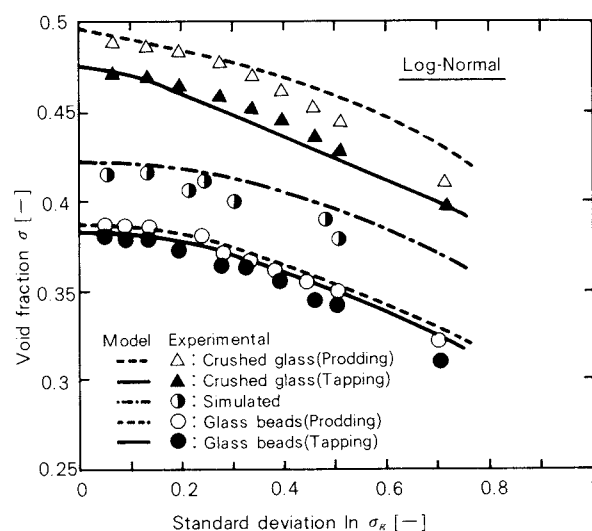

Fig. 5 Comparison between calculated, simulated and experimental void fractions for spheres and irregularly shaped particles with log-uniform size distribution

data.

4. 3 Rosin-Rammler distribution

This distribution is expressed as

$$D = 100 \left\{ 1 - \exp\left(- \frac{D_p}{D_e}\right)^n \right\} \qquad (7)$$

where n and D_e are the distribution constant and the absolute size constant, respectively. **Figure 6** shows an example of the measured results of glass beads. It is ascertained that these data would be fairly consistent with the straight lines representing the calculated result of Eq. (7). A large number of experiments and simulations were conducted by varying the n value to obtain the relationship between n and ϵ, and compare with the calculated result of the model. As shown in **Fig. 7**, ϵ decreased with decreasing n and the calculated result of the model was again in satisfactory agreement with the experimental and simulated data.

As for the three particle-size distributions mentioned above, every distribution permitted the void fraction to be reduced with broadly spreading size distributions. This is probably because the void fraction would decrease with broadly spreading distribution due to the enlarged ratio of the largest particle size to the smallest one and the presence of smaller particles in the unoccupied space among larger particles. The minimum void fraction was at-
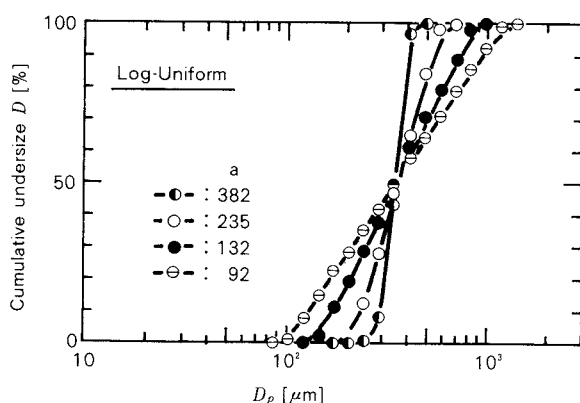

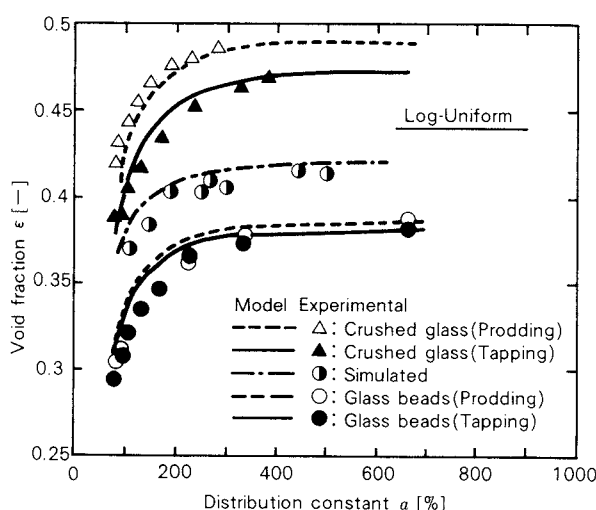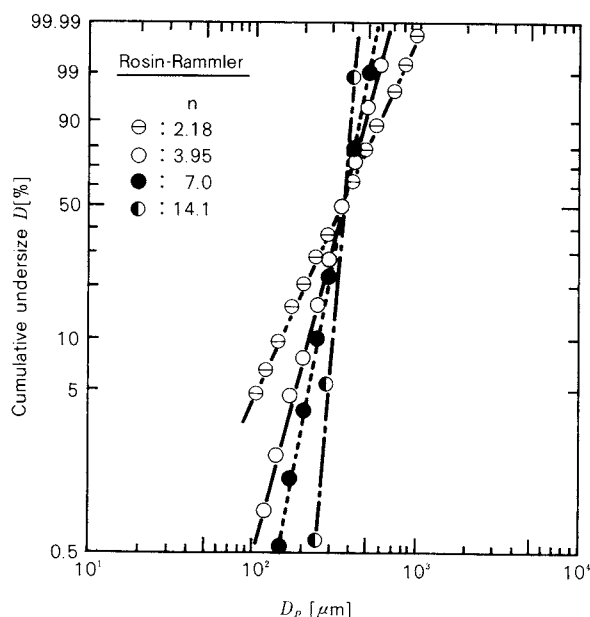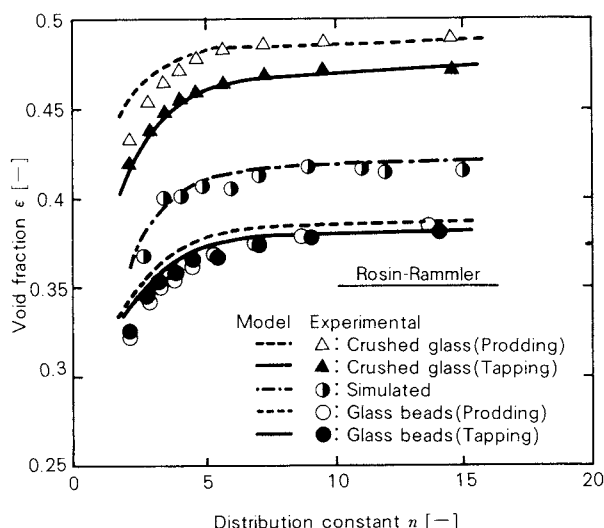Fig. 6 Examples of Rosin-Rammler size distribution for glass beads

Fig. 7 Comparison between calculated, simulated and experimental void fractions for spheres and irregularly shaped particles with Rosin-Rammler size distribution

Fig. 8 Examples of Andreasen (Gaudin-Schuhmann) size distribution for crushed glass

tained in the case of the log-uniform distribution; yet the difference of it among the three distributions was insignificant, i.e., in the range of 0.005 to 0.01, which was insufficient to clarify the effect of the distributions.

4. 4 Andreasen (Gaudin - Schuhmann) distribution

The maximum and the minimum particle sizes depend upon the shape of the particle-size distribution that was referred to in the previous sections. The following expression of particle-size distribution presented by Andreasen is based on the state where the maximum and the minimum particle sizes are fixed and the mixing ratio of particles varies.

$$D = 100 \left(\frac{Dp}{Dp_{\max}} \right)^q \tag{8}$$

where q is the Fuller constant, which has influence on the fractional volume of each size; the rise and drop of this value provide the increasing volume fraction of larger and smaller particles contained, respectively.

As examples of measured results of crushed glass particles is shown in **Fig. 8**. The measured data are found to be in good agreement with curves which represent the calculated result of Eq. (8). A lot of experiments and simulations were conducted by varying the Fuller constant, q, to obtain the relationship between q and ϵ,

and compare with the calculated result of the model. As shown in **Fig. 9**, the void fraction became minimum in any case within the Fuller constant range of 0.5 to 0.8. This is probably because unoccupied spaces among particles would decrease at q of 0.5 to 0.8 which means the furthest state from packing particles of equal size. It was also reported by Kawamura et al.[4] that the void fraction could become minimum at $q = 0.6$. The result of computer simulation is found to be less dependent on the Fuller constant, compared with the experimental data. This is due to the difference in the ratio of maximum particle size to minimum one, $Dp_{\max}/Dp_{\min}$; the ratio was 12.2 in the experiment and 4.75 in the simulation. The calculated result of the model was in good agreement with the results of the experiments using glass beads and computer simulation. The measured values of void fraction in the case of crushed glass particles, however, were larger than that of the calculation by 0.02 to 0.04. This is because of the occurence of segregation at charge and the inapplicability of the assumption of uniform packing in the model.

5. Conclusion

In order to determine the void fraction, randomly packed beds of multi-component system were prepared which have several different particle-size distributions, that is, log-normal, log-uniform, Rosin-Rammler, and Andreasen distribution. Also two kinds of
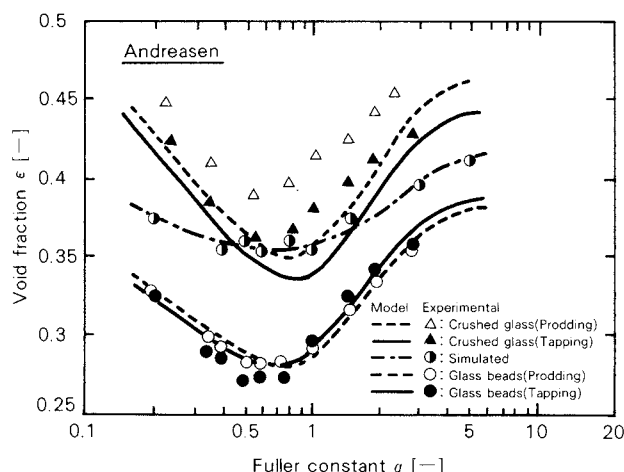
Fig. 9 Comparison between calculated, simulated and experimental void fractions for spheres and irregularly shaped particles with Andreasen (Gaudin-Schuhmann) size distribution

packing method were employed: prodding and tapping. In addition to such a packing experiment, computer simulation for randomly packed spheres was carried out. The results obtained in the present work are as follows.

First, the smallest value of void fraction was obtainable at the Fuller constant of 0.5 to 0.8 in the case of Andreasen distribution. Any distribution except Andreasen distribution allowed the void fraction to decrease with increasing broadly spreading distribution; yet, the dependance on the kind of distribution was not obvious.

Second, the void fractions were determined for crushed glass particles (prodding and tapping), computer simulation, and glass beads (nearly independent of packing method) in order of quantity.

Finally, the comparison of the experimental and simulated data was carried out with the three-component model already presented by the authors by extending it to multi-component systems. This model was ascertained to hold in applications since the calculated values of it were in good agreement in the experimental and simulated data.

Nomenclature

a	:	distribution constant in log-uniform size distribution function	[%]
B	:	Undeterminated constant in Eq. (A-7)	[m]
b	:	constant in log-uniform size distribution function	[%]

D	:	cumulative under size percent based on mass	[%]
D_e	:	absolute size constant in Rosin-Rammler size distribution function	[μm]
Dp_i, Dp_j	:	diameter of particle, i, j or k in	
Dp_k	:	a multi-component mixture	[μm]
Dp_{50}	:	mass median diameter	[μm]
Dp_{max}	:	maximum particle diameter	[μm]
Dp_{min}	:	minimum particle diameter	[μm]
m	:	number of component in a mixture	[—]
$N_{(j,k)}$	:	coordination number on particle j in direct contact with particle k	[—]
$\tilde{N}c_j$	:	cordination number in a uniform-sized particle bed	[—]
n	:	distribution constant in Rosin-Rammler size distribution function	[—]
q	:	Fuller constant in Andreasen size distribution function	[—]
Sa_k	:	fractional area of particle k in a multi-component mixture	[—]
Sv_k	:	fractional volume of particle k in a multi-component mixture	[—]
V	:	volume of a hypothetical sphere in Fig. A-1	[m^3]
V_1, V_2	:	volume of a cut sphere in Fig. A-1	[m^3]
α_j	:	proportionality constant in Eq.(A-5)	[—]
β_j	:	proportionality constant in Eq. (1)	[—]
ϵ	:	void fraction in a multi-component mixture	[—]
ϵ_j	:	partial void fraction around particle j	[—]
$\epsilon_{(j,k)}$	:	partial void fraction around particle j in direct contact with particle k	[—]
$\tilde{\epsilon}_j$	:	void fraction in a uniform-sized particle bed	[—]
σ_g	:	geometric standard deviation in log-normal distribution function	[—]

References

1) Andregg, F.O.: *Ind. Eng. Chem.*, **23**, 1058 (1931).
2) Arakawa, M. and M. Nishino: *J. Soc. Mat. Sci. Japan*, **22**, 658 (1973).
3) JIS A 1104 (1976).
4) Kawamura, J., E. Aoki and K. Okusawa: *Kagaku Kōgaku*, **35**, 777 (1971).
5) Suzuki, M. and T. Oshima: *Powder Technol.*, **35**, 159 (1983).
6) Suzuki, M., A. Yagi, T. Watanabe and T. Oshima: *Kagaku Kogaku Ronbun-shu*, **10**, 721 (1984); English translation in Intern. Chem. Eng., **26**, 491 (1986).
7) Suzuki, M., K. Makino, M. Yamada and K. Iinoya: *Kagaku Kogaku Ronbun-shu*, **6**, 59 (1980); English translation in Intern. Chem. Eng., **21**, 482 (1981).
8) Sohn, H. Y. and C. Moreland: *Can. J. Chem. Eng.*, **46**, 162 (1968).

Appendix 1. Derivation of $\epsilon_{(j,k)}$

The void fraction $\epsilon_{(j,k)}$ can be derived simply as follows. Consider a particle j with a diameter of Dp_j which is touched by $N_{(j,k)}$ particles with a diameter of k, as illustrated in **Fig. A-1** where O and D are the center of the particles j and the contact point between a pair of contacting particle k, respectively. If a hypothetical sphere with a radius of OD (which is indicated by one-dot-broken line in **Fig. A-1**), is assumed, $\epsilon_{(j,k)}$ in this hypothetical sphere is obtainable geometrically. When BED rotates around the BE axis, the volume of this solid, V_1, as

$$V_1 = \frac{\pi}{3} \, (\overline{BE})^2 \, (3\overline{OD} - \overline{BE}) \qquad (A\text{-}1)$$

Similarly, the volume V_2 is

$$V_2 = \frac{\pi}{3} \, (\overline{AB})^2 \, (3\overline{CD} - \overline{AB}) \qquad (A\text{-}2)$$

the volume of a hypothetical sphere with a radius of $\overline{OD}$ is

$$V = \frac{4}{3} \, \pi \, \overline{OD}^3 \qquad (A\text{-}3)$$

where $\overline{BE}$, $\overline{OD}$, $\overline{AB}$ and $\overline{CD}$ in Eqs. (A-1) to (A-3) are obtainable from Dp_j and Dp_k (Refer to Appendix 2).

Consider a hypothetical sphere which is formed by the particle j surrounded by $N_{(j,k)}$ particles k. The void fraction in this sphere $\epsilon_{(j,k)}$ is derived from Eqs. (A-1) to (A-3) as follows:
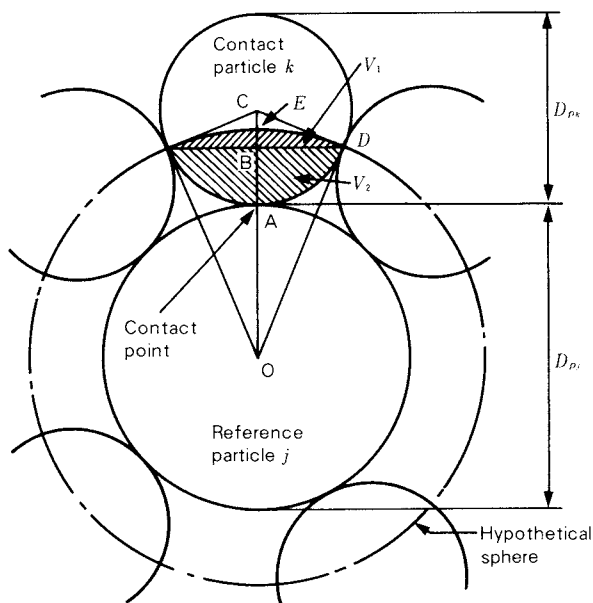

Fig. A-1 The model of a reference particle j in direct contact with particles k

$$\epsilon_{(j,k)} = 1 - \frac{\dfrac{\pi}{6} Dp_j^3 + N_{(j,k)} \cdot (V_1 + V_2)}{V} \qquad (A\text{-}4)$$

where $N_{(j,k)}$ is the co-ordination number and can be expressed as the following form through the model for predicting co-ordination number of randomly packed multi-component spheres[5]

$$N_{(j,k)} = \frac{2\,\alpha_j\left(\dfrac{Dp_j}{Dp_k} + 1\right)}{1 + \dfrac{Dp_j}{Dp_k} - \sqrt{\dfrac{Dp_j}{Dp_k}\left(\dfrac{Dp_j}{Dp_k} + 2\right)}} \qquad (A\text{-}5)$$

where α_j is the proportionality constant derived from $\widetilde{N}c_j$ that represents a measured value of co-ordination number of one-component packed bed consisting of the assembly of only particle j. The value α_j is written by

$$\alpha_j = \frac{\widetilde{N}c_j}{4} \, (2 - \sqrt{3}) = 0.067 \, \widetilde{N}c_j \qquad (A\text{-}6)$$

The above expression assumes that a packed bed can be formed geometrically, i.e., $N_{(j,k)}$ is larger than 2.

As well known, measurement of $\widetilde{N}c_j$ compels a worker to require much labor and time to spare. To overcome such a problem, the authors attempted to estimate $\widetilde{N}c_j$ from $\widetilde{\epsilon}_j$ which could be given in the packed bed was assumed to consist of the assembly of only particle j. This value can be derived from the following form[7]:

$$\widetilde{N}c_j = \frac{2.812\,(1 - \widetilde{\epsilon}_j)^{-\frac{1}{3}}}{\left(\dfrac{B}{Dp}\right)^2 \left\{1 + \left(\dfrac{B}{Dp}\right)^2\right\}} \qquad (A\text{-}7)$$

where B is an undeterminated constant, given by $\widetilde{\epsilon}_j$ in the following equation:

$$(1 - \widetilde{\epsilon}_j)^{-\frac{1}{3}} = \frac{1 + \left(\dfrac{B}{Dp}\right)^2}{1 + \left(\dfrac{B}{Dp}\right) \exp\left(\dfrac{Dp}{B}\right)^2 \cdot \text{Erfc}\left(\dfrac{Dp}{B}\right)} \qquad (A\text{-}8)$$

It seems difficult to obtain analytically the solution of B from the above equation. In practical viewpoint, the value of B can be approximately expressed by the following equation:

$$\frac{B}{Dp} = 7.318 \times 10^{-2} + 2.193 \, \tilde{\epsilon}_j$$

$$- 3.357 \, \tilde{\epsilon}_j{}^2 + 3.194 \, \tilde{\epsilon}_j{}^3 \qquad \text{(A-9)}$$

Other methods of obtaining $\tilde{N}_{c_j}$ have been proposed by Ridgway - Turback, Smith, etc.[7].

Appendix 2   Derivation of $\overline{BE}$, $\overline{OD}$, $\overline{AB}$ and $\overline{CD}$

Figure A-1 provides the following lengths:

$$\overline{OC} = \frac{Dp_j + Dp_k}{2} \qquad \text{(A-10)}$$

$$\overline{OA} = \frac{Dp_j}{2} \qquad \text{(A-11)}$$

$$\overline{CD} = \frac{Dp_k}{2} \qquad \text{(A-12)}$$

The triangle OCD has a right angle, thus

$$\overline{OD} = \sqrt{\overline{OC}^2 - \overline{CD}^2}$$

Substituting Eqs. (A-10) and (A-12) for $\overline{OC}$ and $\overline{CD}$ in the above form,

$$\overline{OD} = \frac{\sqrt{Dp_j (Dp_j + 2 Dp_k)}}{2} \qquad \text{(A-13)}$$

Similarly in the right-angled triangles OBD and BCD,

$$(\overline{OC} - \overline{BC})^2 + \overline{BD}^2 = \overline{OD}^2$$

$$\overline{BC}^2 + \overline{BD}^2 = \overline{CD}^2$$

From the above forms,

$$\overline{BC} = \frac{\overline{OC}^2 - \overline{OD}^2 + \overline{CD}^2}{2\overline{OC}}$$

Substituting Eqs. (A-10), (A-12) and (A-13) for the above form,

$$\overline{BC} = \frac{Dp_k{}^2}{2 (Dp_j + Dp_k)} \qquad \text{(A-14)}$$

Figure A-1 gives

$$\overline{BE} = \overline{BC} + \overline{OD} - \overline{OC}$$

Substituting Eqs. (A-10), (A-13) and (A-14) for the above form,

$$\overline{BE} = - \frac{Dp_j (Dp_j + 2Dp_k)}{2 (Dp_j + Dp_k)}$$

$$+ \frac{\sqrt{Dp_j (Dp_j + 2Dp_k)}}{2} \qquad \text{(A-15)}$$

Similarly,

$$\overline{AB} = \overline{OD} - \overline{BE} - \overline{OA}$$

Substituting Eqs. (A-11), (A-13) and (A-15) for the above form,

$$\overline{AB} = \frac{Dp_j(Dp_j + 2Dp_k)}{2 (Dp_j + Dp_k)} - \frac{Dp_j}{2} \qquad \text{(A-16)}$$

By substituting these values for Eqs. (A-1), (A-2) and (A-3), V_1, V_2, and V are obtainable.

Static Stress Conditions of a Cohesive Powder in Bins[†]

Kanji Matsumoto
Department of Chemical Engineering
*Yokohama National University**

Akira Suganuma
Department of Industrial and Engineering Chemistry
*Science University of Tokyo***

Ryuichi Aoki
Department of Food Technology and Engineering
*Tokyo University of Fisheries****

Abstract

The following results were experimentally obtained by analyzing the packing and stress conditions of $CaCO_3$ (P-30) powder filled through a sieve into a shallow and a deep bin of low and high powder-bed height to bin diameter ratio, respectively: 1) The ratio of horizontal stress to vertical stress in the powder at the bin wall increased linearly with decreasing porosity in both cases. 2) The relationship between the logarithm of mean consolidation stress and the void ratio was linear in both cases. 3) In the shallow bin the vertical stresses in the radial direction were observed to be almost uniform. Hence the stress condition in the powder was well expressed by Janssen's equation, evaluated using the coefficient of wall friction measured by a direct shear tester. 4) The Mohr circles which represented the stress conditions of the powder at the bin wall were not tangent to the effective yield locus, but approximately tangent to the wall yield locus. 5) The static state of the powder in the deep bin could be roughly estimated by using the results obtained in the shallow bin.

1. Introduction

The knowledge of the state of static stress in particulate materials stored in storage vessels is required to predict an extent of the powder pressure at the wall, a flow-pattern of the solids, a critical choking size at discharge, etc. Such a stress has been widely studied by Janssen[2], Jenike[1], Walker[8], and many other researchers. However, existing results obtained theoretically have not been always consistent with the actual observations at a bin wall because of the influences of charging method and height, and the variations in mechanical properties of materials[6].

An effective angle of internal friction and angle of friction at the wall have been regarded from the theoretical viewpoint as typical properties which represent stress conditions in storage vessels like a bin. Although these properties are measured by a shear tester, it is somewhat doubtful whether the data obtained can be applied to the prediction of the actual stress condition in a bin. For instance, with a cohesive fine power, one has much difficulty in obtaining suitable data using a shear tester, because the material filled in the shear tester cannot be so loose as that in an actual bin. It is

* 156, Johbandai, Hodogaya-ku, Yokohama, Kanagawa, 240
  TEL. 045 (335) 1451

** 2641, Yamazaki, Noda, Chiba, 272
   TEL. 0471 (24) 1501

*** 5-7, Kounan 4-chome, Minato-ku, Tokyo, 108
    TEL. 03 (471) 1251

† This report was originally printed in *Kagaku Kogaku Ronbun-shu*, **10**, 667-674 (1984) in Japanese, before being translated into English with the permission of the editorial committee of the Soc. Chemical Engineers, Japan.

also because the data obtained tend to be influenced by equipment factors like a type, a size, etc.

The present paper is concerned with analyzing a state of stress and packing of powder bed by employing both a shallow and a deep bin; when the ratio of depth to inside diameter of the bin, L/D, are small and large will be called a shallow bin and a deep bin, respectively in this paper. The data obtained in these bins will be related with the mechanical properties measured by a shear tester, and also compared with some of the existing theories.

2. Experiment

2. 1 Sample powder

As a test sample, $CaCO_3$ (P-30) was employed. This material is one of the standard powders manufactured by *Association of Powder Process Industries and Engineering, Japan*. It has the true density of 2.7×10^3 $kg \cdot m^{-3}$ and the mean diameter of about $5.7 \mu m$ determined by a sedimentation balance.

2. 2 Experimental equipment and method of powder charging

A bin used in the experiment consisted of a set of chrome plating iron rings with a inside diameter of 30 cm and outer diameter of 32 cm piled up with interlocking, as illustrated in **Fig. 1**. Each ring had the thickness of 10 cm except 5 cm of the bottom ring and had a hole of 3.0 cm in diameter at the center of its side face in which a pressure transducer for determining a horizontal stress was inserted. When the bin consists of less than two stages, it will be called a shallow bin at the ratio of depth to diameter of the powder bed, H/D, ≤ 0.25; while for more than three stages it will be called a deep bin at $H/D \leq 4.0$.

It is well known that the stress condition of materials in a bin are influenced by a charging method and height[4,7]. Thus the sample powder was charged into the bin as follows; the square-type sieve with a nominal opening size of 840 μm and each side of 40 cm was supported by the rollers about 5 cm high from the upper side of the bin. The sample powder contained in the sieve fell down like a film each time the sieve box was shifted horizontally to collide with each point of a or a' at the angle

① Sieve ② Bin ③ Pressure transducers
④ Rollers
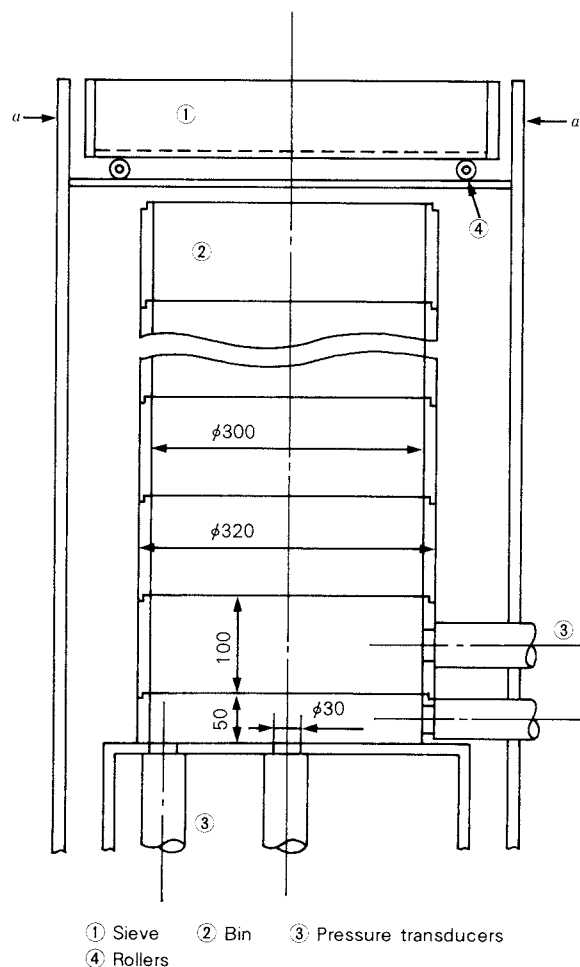
Fig. 1 Schematic view of experimental apparatus

rods illustrated in **Fig. 1**.

For the shallow bin, the sample was contained initially so that the upper level of the material in the bin might be kept 4 to 7 cm in consideration of the pressure sensor. Then the surface of the material was made uniform by brushing before loading. For the deep bin, on the other hand, the bin was made tall by piling up each three rings so as to prevent the impulse at falling from causing an excessive consolidation of the material in the bin. Little variation of stress at the bottom or the wall of the bin was observed during this experiment.

2. 3 Loading method and stress determination

For the shallow bin experiment, the condition after feeding was not changed artificially. For the deep bin experiment, on the other hand, the weight was placed in the following fashion. After the sample powder was charged,

initially an aluminum disk with 29.8 cm in diameter, 1.0 cm in thickness, and 1.84 kg in mass was placed on the upper surface of the material. Then a set of weights was placed in sequence on the disk with great care not to cause disturbance. This procedure resulted in the reduction of the depth of the powder bed because of the constant amount of the charged material. It may be pointed out that these weights would be supported partly by the powder which was penetrated in the shell-like gap between the inside wall of the bin and the outside of the aluminum disk. However such a influence was found to be negligible because the stress at the bin bottom was little changed in spite of the destruction of the powder bed in the gap with a fine wire.

The stress of the material in the bin was determined in the common mode to both the shallow bin and the deep bin. The vertical stress at the bin bottom or the horizontal stress at the wall was measured with a pressure transducer that had a sensing piece of 3.0 cm in diameter and the rated pressure of 9.8 kPa (PG-100 GD; manufactured by Kyowa Dengyo Co., Ltd.) and 49.8 kPa (PG-500 GD) as illustrated in **Fig. 2**. The pressure transducer was designed to be set at an arbitrary position of A to E in the bin bottom as shown in **Fig. 3**. Note that the vertical stress at the position A, for example, will be represented by Σ_{VA} (or Σ_{VA}) in this paper

The whole load exerted on the bin bottom was weighed by three compact load cells with each rated capacity of 98N. As illustrated in **Fig. 4**, these cells were placed to support a bot-
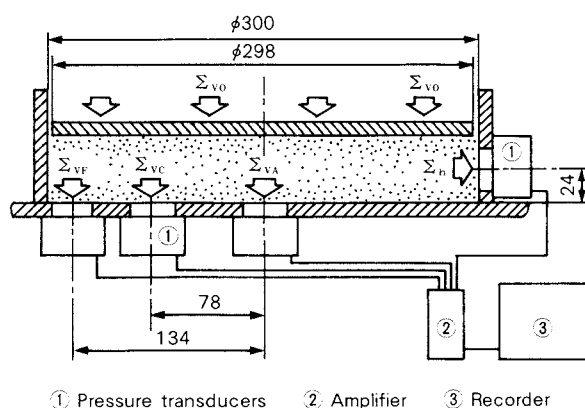

Fig. 3   Positions of the pressure transducers

① Pressure transducer   ④ Recorder
② Road cells   ⑤ Bin support
③ Amplifier
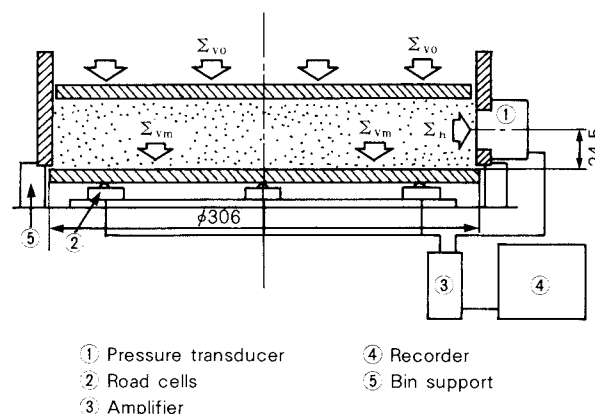
Fig. 4   Schematic diagram of the instrumentation used to measure the load acting on the bottom of the bin

① Pressure transducers   ② Amplifier   ③ Recorder

Fig. 2   Schematic diagram of the stress measurement instrumentation

tom brass disk in 30.6 cm diameter; this disc, which was a little larger than the bin diameter, was set to have the clearance of about 0.5 mm with the bin support. The whole load totaled by these three weights could provide a vertical stress averaged over the cross section area or a shear stress supporting the bin wall (a wall friction force). These stresses and their several relations will be discussed in detail in Section 4.3.

3.   Experimental   result   and   discussion   of shallow bin

3. 1   Relationship among consolidation stress, bottom stress, and porosity

Figure 5 shows the dependance of the consolidation stress, each weight devided by the bin cross section area, Σ_{VO}, on the radius ratio

Fig. 5 Example of the vertical stress distribution along
the radial direction in the shallow bin

Fig. 6 Relationship between the mean consolidation
stress and the porosity or the void ratio in
the shallow bin

fined by $\bar{e} = \bar{\epsilon}/(1 - \bar{\epsilon})$ is illustrated in **Fig. 6**.
This figure displays that the logarithmic plot
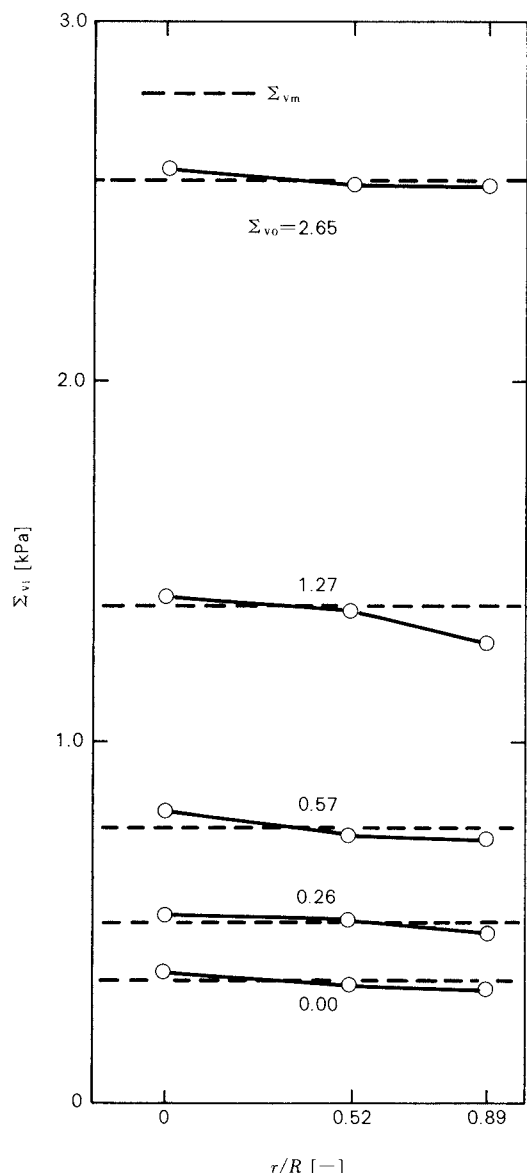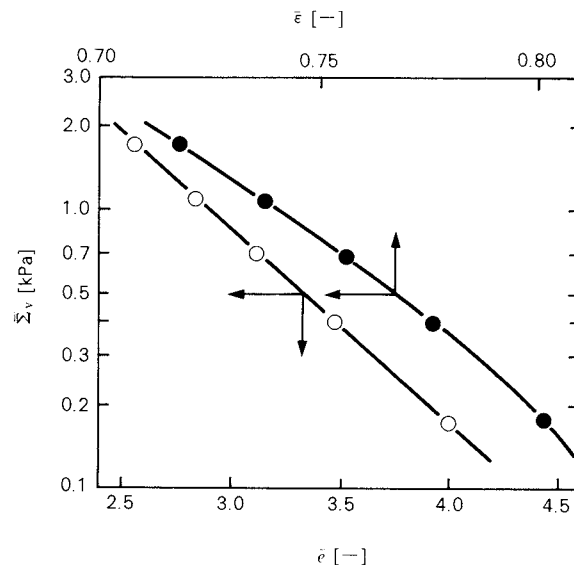of $\bar{\Sigma}_V$ would have almost linear relation with
$\bar{e}$; this tendency is consistent with the soil con-
solidation characteristics in the field of the soil
mechanics.

3. 2 The relationship between mean porosity
and stress ratio $\bar{K}$

The stress ratio, which is defined by the
ratio of the horizontal stress averaged over the
perimeter to the vertical stress over the cross-
sectional area, is one of the significant factors
that represent apparently the stress conditions
in bins. Although this ratio may be defined at
any position in the bin, the value near the bin
wall will be the most important for practical
use as indicated in Janssen's formulas. The
stress ratio (denoted by $\bar{K}$ for shallow bin) can
be obtained by measuring the horizontal stress
near the wall Σ_h with a pressure transducer,
while there is no means to determine the verti-
cal stress near the wall Σ_{Vw}. Therefore, as the
actual vertical stress around the center of the
pressure transducer Σ_{Vw}, the vertical stress
exerted on the same level as that of this sensor
$\hat{\Sigma}_V$ was taken, using the following expression
(refer to **Fig. 4**).

$$\Sigma_{VW} \approx \hat{\Sigma}_V = \Sigma_{Vm} - \frac{0.0245}{H}(\Sigma_{Vm} - \Sigma_{VO})$$

$$(1)$$

of r/R for each vertical stress at the bin bot-
tom, Σ_{Vi} (i = A, C and F). The value of Σ_{Vi} is
found from this figure to concord satisfactorily
with the mean vertical stress, which is denoted
as the whole weight exerted on the bin bottom
devided by the cross section area of the bin,
Σ_{Vm}, for a given value of Σ_{VO} measured in the
present experiment. This result suggests that
the pressure transducers used would be com-
monly applicable to determination of powder
stresses.

The relationship of the mean consolidation
stress defined by $(\Sigma_{VO} + \Sigma_{Vm})/2$, $\bar{\Sigma}_V$ and the
mean porosity, $\bar{\epsilon}$ or the mean void ratio de-

where the two assumptions are made:

(i) The vertical stress uniformly acts on the horizontal cross-sectional area including the vicinity of the wall (refer to 3.1).

(ii) The vertical stress increases linearly along the gravitational direction for small H/D (refer to Eq.(2)).

For a fine powder like $CaCO_3$ (P-30), $\overline{K}$, which in the measured Σ_h devided by $\widehat{\Sigma}_V$ obtained from Eq. (1), tends to increase with increasing $\overline{\epsilon}$, as shown in **Fig. 7**.

3. 3 Adaptability of Janssen's formula

Janssen's formula has been often used to predict the stresses exerted on the bottom and the wall of storage vessels. This formula requires basically the following four assumptions[2]:

(i) The vertical stress acts on uniformly a given horizontal cross-sectional area of the powder bed.

(ii) The pressure ratio $\overline{K}$ is constant without dependence on depth.

(iii) Bulk density ρ_B is also constant without dependence on depth.

(iv) The material near the wall is under the condition of critical stress.
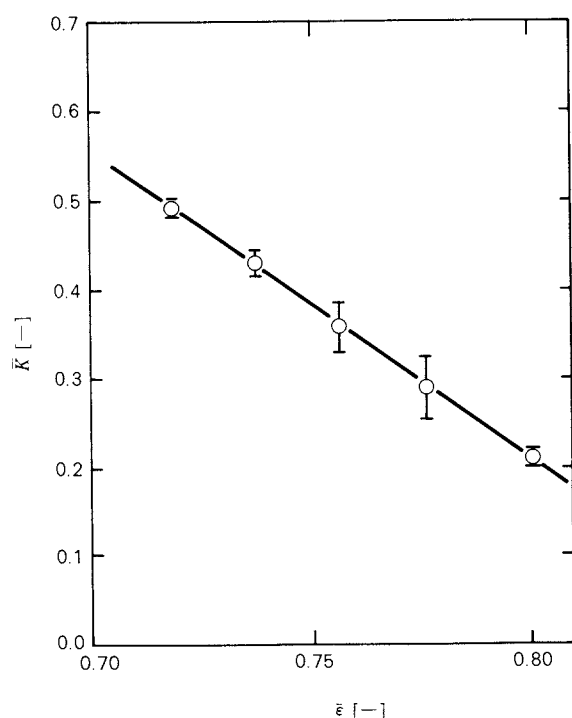

Fig. 7 Relationship between the ratio of horizontal stress to vertical stress and the porosity in the shallow bin

For shallow bin, the assumptions (i) and (iv) may be essentially satisfied; the assumptions (iii) and (iv), on the other hand, may be available if the averaged values of $\overline{K}$ and ρ_B are employed due to the thin bed of the powder materials. A generalized expression of Janssen's formula is written as

$$\Sigma_{Vm}^J = \frac{D\rho_B g}{4\mu_w \overline{K}}\left\{1 - \exp\left(-4\mu_w \overline{K}\frac{H}{D}\right)\right\} + \Sigma_{VO}\exp\left(-4\mu_w \overline{K}\frac{H}{D}\right) \qquad (2)$$

where μ_w is the coefficient of wall friction. If this coefficient is given, the vertical stress at the bin bottom Σ_{Vm}^J is obtainable from Eq. (2), since D, ρ_B, $\overline{K}$, and H are all known. As already reported[3], the value of μ_w was measured to be 0.57 (or 29.7° in wall friction coefficient) by using a material used in the present study and a chrome plating wall. Based on this data for calculation of Σ_{Vm}^J, **Table 1** lists the vertical stresses obtained by measurement Σ_{Vm} and by caculation Σ_{Vm}^J for several values of Σ_{VO} where $\overline{\epsilon}$ ranged from 0.602 to 0.664. It is found from this table that the calculated values were in agreement with the measured data within an error of a few percent. This result implies that Jassen's formula presents the state of the stress condition in shallow bins and the stress condition near the bin wall can be expressed by the Mohr circles in **Fig. 8**. Also the critical state line (CSL) and the effective yield locus (EYL) as well as the wall yield locus (WYL) are drawn in this figure in the variation of $\overline{\epsilon}$ between 0.544 and 0.640[10].

4. Experimental result and discussion of deep bin

4. 1 Distribution of stress and porosity along gravitational direction

Figure 9 shows that the variation of the

Table 1 Applicability of Janssen's equation to the powder stress in the shallow bin

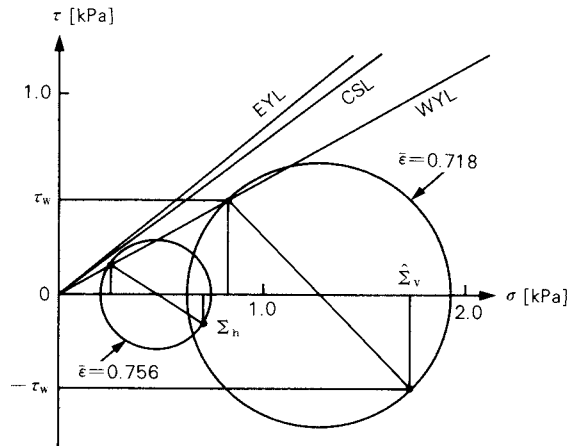| Σ_{VO} [kPa]	H [cm]	ρ_B [t/m^3]	K [−]	Σ_{Vm}^J [kPa]	Σ_{Vm} [kPa]
0.0	6.9	0.54	0.21	0.346	0.353
0.262	6.2	0.60	0.29	0.563	0.542
0.584	5.7	0.66	0.36	0.833	0.811
1.01	5.2	0.71	0.43	1.17	1.16
1.72	4.9	0.76	0.49	1.74	1.75

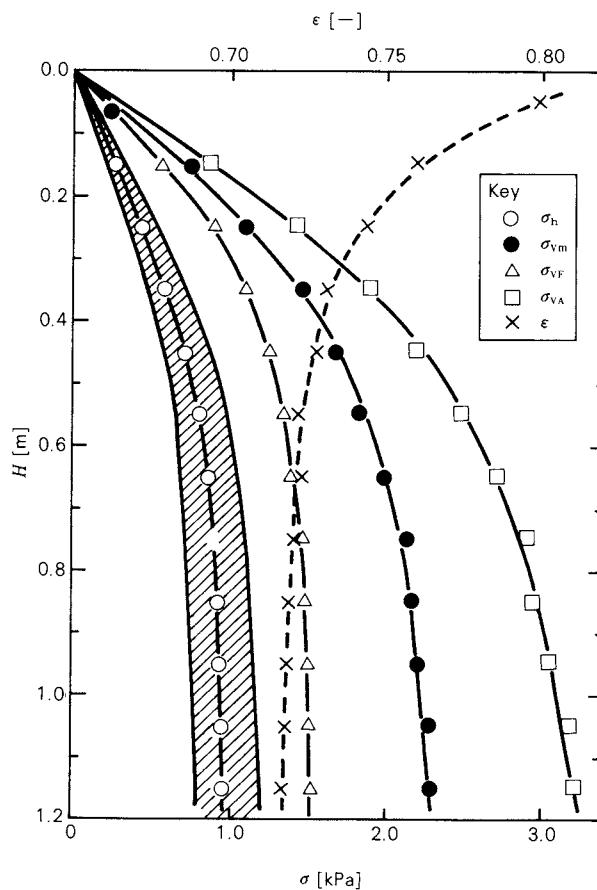Fig. 8 Mohr circles representing the powder stress conditions at the wall of the shallow bin

Fig. 9 Relationship among the stress, the porosity and the powder bed height in the deep bin

σ_{VA}, σ_{VF}, and σ_{Vm}, the average values of each three measurements were employed because of relatively acceptable reproducibility. The hatching region in this figure indicates the variation of the measured results of σ_h by six iterations for each depth, added by the averaged values represented by an open circle. It was confirmed that σ_h would depend only on the distance from the upper surface of the powder bed because the measurements at the different positions which were 2.4 cm and 12.4 cm high from the bottom provided a similar tendency. As known in this figure, all the stresses and the porosity could approach to each constant value with increasing the depth of the powder bed.

The effect of the depth on the vertical stresses σ_{VA}, σ_{VC}, and σ_{VF} are shown in **Fig.10**. It is found that σ_{VA} almost agreed with σ_{VC} while σ_{VA} much more deviated from σ_{VF} with increasing the depth.

The relationship between σ_{Vm} obtained from **Fig. 9** and ϵ or e are displayed in **Fig. 11**. The logarithmic value of σ_{Vm} almost linearly decreased with e like the case of the shallow bin indicated in **Fig. 6**; in comparison with these results, the vertical stress of the deep bin was a little larger than that of the shallow bin.

4. 2 Relationship between porosity and pressure ratio k

As already illustrated in **Fig. 7**, the stress ratio of the shallow bin, $\overline{K}$, was not constant but a function of the porosity $\overline{\epsilon}$. For the deep bin, the pressure ratio k would not be constant along the radial direction due to the dependence of the vertical stress on the radial position, as shown in **Fig. 10**.

Consider the ratios of k_A, k_F, and k_m which are represented by σ_h devided by σ_{VA}, σ_{VF}, and σ_{Vm}, respectively. As shown in **Fig. 12**, k_A was nearly constant ($k_A \approx 0.3$) without dependence on ϵ except the case of $\epsilon \approx 0.8$. The value of k_m was consistent with the result of the shallow bin represented by a solid line at $\epsilon \geq 0.75$, but it was constant ($k_m \approx 0.4$) at $\epsilon < 0.75$. For k_A and k_m, the result of the shallow bin was in sufficient agreement with that of the deep bin when ϵ was large, or namely, the powder bed depth was short. This may be because the vertical stresses would be similar at any measuring point for the short depth even in the deep bin (refer to **Fig. 10**). The

vertical stresses at the center σ_{VA} and near the wall σ_{VF}, the horizontal stress at the wall σ_h, the mean vertical stress measured by a compact load cell σ_{Vm}, and the porosity ϵ along the gravitational direction in the deep bin. For

18
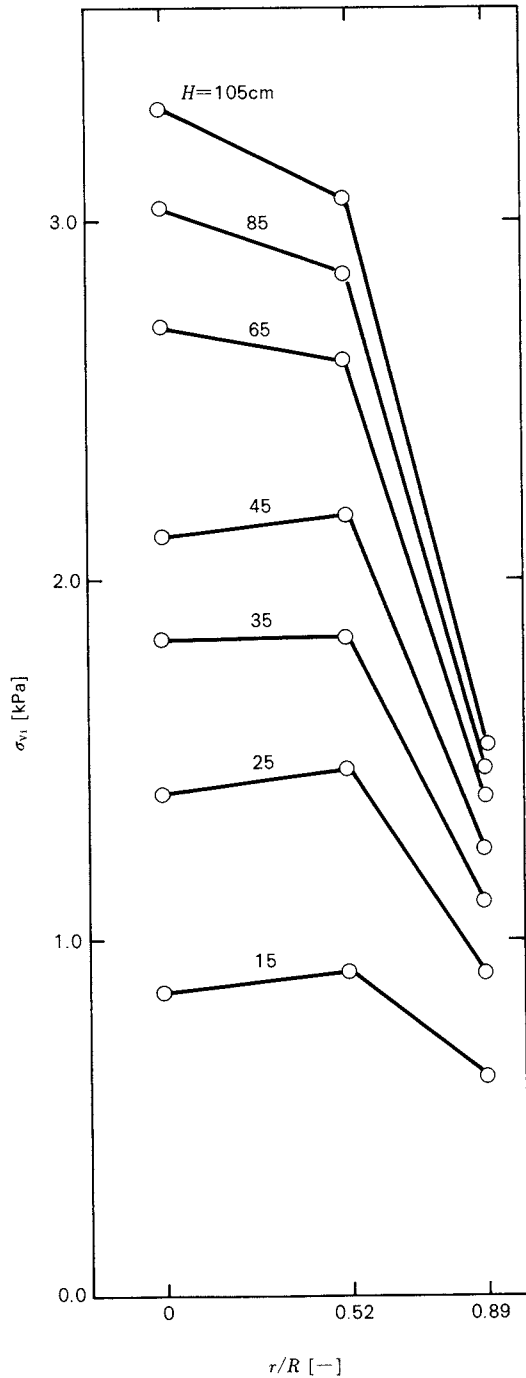
Fig. 10 Example of the vertical stress distribution along the radial direction in the deep bin

Fig. 11 Relationship between the mean vertical stress and the porosity or the void ratio in the deep bin
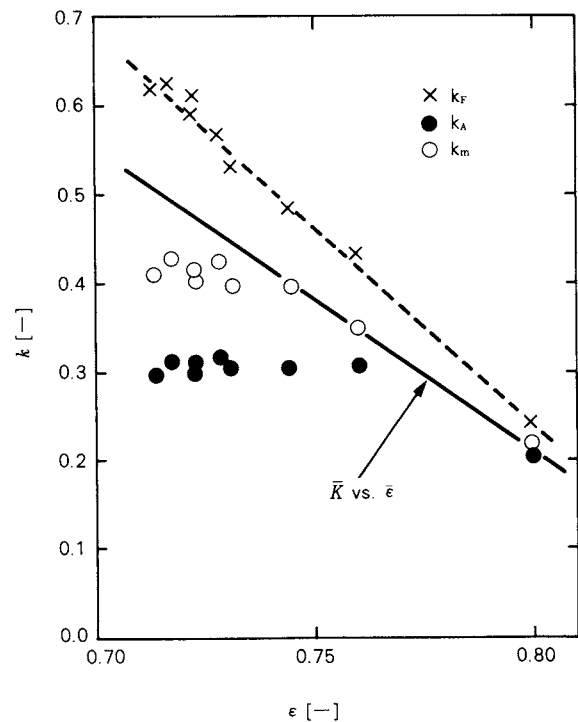
Fig. 12 Relationship between the ratio of horizontal stress to vertical stress and the porosity in the deep bin

value of k_A, on the other hand, increased linearly with decreasing ϵ, as denoted by the dotted line; these values were a little larger than $\overline{K}$ of the shallow bin.

Walters[9] assumed any Mohr circle to be tangent to EYL. If this assumption was satisfied, the pressure ratio at the wall, k', would

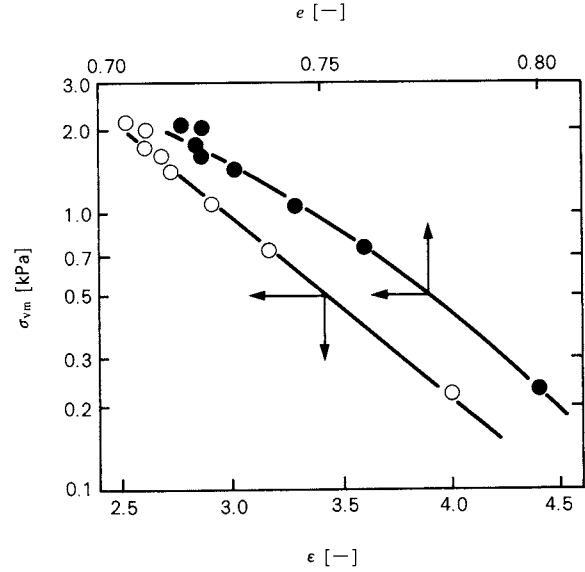be 0.24 by solving Eq. (23)[☆] in the literature[9] where the values of 0.57 and 0.82 were em-

$$\frac{\sigma_h}{\sigma_{Vm}} = k' = \frac{\cos^2 \delta}{\left\{1 + \sin^2 \delta + 2\sqrt{1 - (\tan\phi_W/\tan\delta)^2}\right\}^{\frac{1}{2}} \sin\delta}$$

ployed as $\tan\phi_W$ and $\tan\delta$, respectively. As shown in **Fig. 12**, k' was smaller than each k namely, k_F, k_A, and k_m except that $\epsilon \approx 0.8$. This result suggests that the practical stress conditions in bins would not be necessarily satisfied with Walters' assumption.

4. 3 Stress condition at bin wall

As described in Section 4.2, Walters[9] assumed that the stress condition at the bin wall would be expressed by the Mohr circles tangent to EYL and the coordinate (σ_h, τ_W) indicating the horizontal stress and the shear stress exerted on the wall would be on WYL. In general, the Morh circle that expresses the stress condition at the wall can be drawn by using the values of σ_h, σ_{VW}, and τ_W. These three values were obtained from the experimental result as follows.

(i) σ_h: This value is measured by a pressure transducer.

(ii) σ_{VW}: σ_{VF} obtained by the pressure sensor nearest to the wall ($r/R = 0.9$) is used as σ_{Vm} because the vertical stress at the wall is not obtainable in the present experiment.

(iii) τ_W: Based on the relation indicated in **Fig. 13**, the weight of powder bed with a depth of H, W_P, the force supporting partly the bed, or shear force, f_τ, and the load exerted on

the bottom f_B can be expressed as

$$f_\tau = W_P - f_B = \int_0^H 2\pi R \tau_W(h)\mathrm{d}h. \tag{3}$$

and

$$f_B = \pi R^2 \sigma_{Vm} \tag{4}$$

From Eq.(3), f_τ is obtainable by using the measured values of W_P and f_B. Thus τ_W is given by the shear force gradient $\mathrm{d}f_\tau/\mathrm{d}H$ derived from Eq. (3)

$$\tau_W = \frac{1}{2\pi R} \frac{\mathrm{d}f_\tau}{\mathrm{d}H} \tag{5}$$

Table 2 lists the calculated results of σ_h, σ_{VF}, τ_W at several positions in the powder bed. They are also shown as Mohr's stress circles in **Fig.14**, which implies that the coordinates of (σ_h, τ_W) are near WYL determined by the uniaxial shear tester without dependence on the powder depth like the result of the shallow bin. As clearly shown in this figure, the stress condi-

Table 2 Powder stress conditions at the wall of the deep bin

H [m]	σ_h [kPa]	σ_{VF} [kPa]	τ_W^+ [kPa]	τ_W^{++} [kPa]
0.15	0.26	0.61	0.151	0.147
0.35	0.58	1.10	0.329	0.319
0.55	0.79	1.34	0.453	0.417
0.75	0.89	1.45	0.509	0.490
0.95	0.94	1.49	0.533	0.527
1.05	0.95	1.51	0.539	0.539

$\tau_W^+ = \mu_W\sigma_h = 0.57\ \sigma_h$
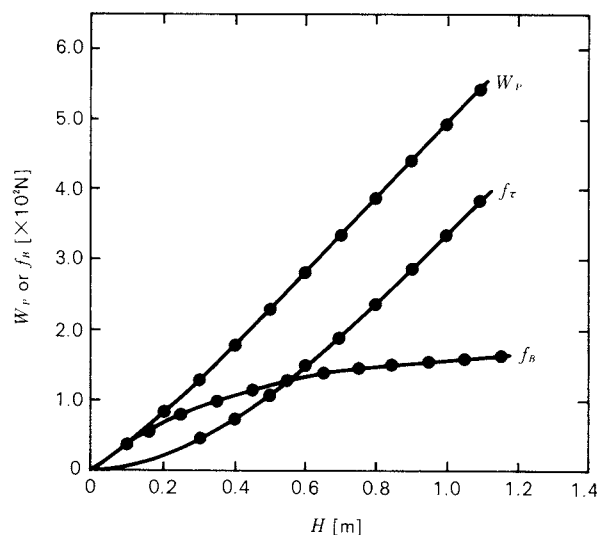τ_W^{++} : calculated value from Eq. (5)

Fig. 13 Relationship among the weight of powder, the friction force on the wall, the load acting on the bottom of bin and the depth in the deep bin.
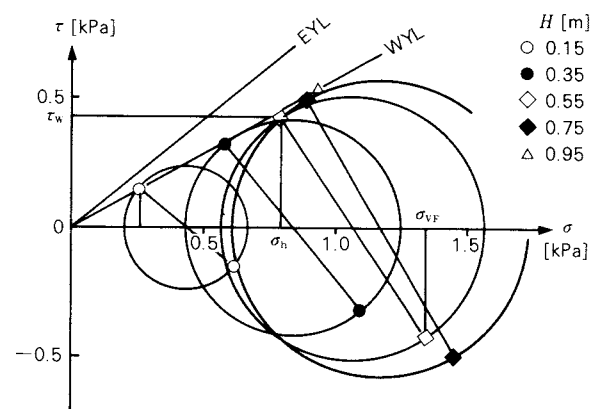

Fig. 14 Mohr circles representing the powder stress conditions at the wall of the deep bin

tion at the bin wall expressed by the coordinate of (σ_h, τ_w) tends to approach WYL rather than EYL. Here it may be pointed out that the Mohr circles are not tangent to EYL because of the assumption that $\sigma_{VW} \doteq \sigma_{VF}$, but in the actual case the Mohr circle will be farther from EYL as σ_{VW} is practically less than σ_{VF}.

4. 4 Prediction of powder bed in deep bins

In the present work, the apparent similarity of the conditions in the shallow bin and the deep bin was proved as shown in the figures, for example, **Figs. 6** and **7**. Therefore if the condition of the materials in the deep bin is to be predicted by the knowledge of that in the shallow bin, which is relatively easy to obtain by experiment, this prediction will be useful for practical cases like a scale-up design. It is known in general that the values of σ_h (related to the wall strength), σ_{Vm} (related to the base strength), and σ_{Vm} (related to contained amount of the material) are essential to practical design of the deep bin. From this viewpoint, the authors predicted σ_{Vm} and ϵ by using σ_h which was easiest to measure in the deep bin experiment.

The result of the shallow bin experiment is expressed as follows.

$$\widehat{\Sigma}_V = 1.9\,(\Sigma_h)^{0.72} \quad \text{(Refer to Fig. 15)} \quad (6)$$

$$\overline{K} = \frac{\Sigma_h}{\Sigma_V} = 3.0 - 3.5\,\epsilon \quad \text{(Refer to Fig. 7)} \quad (7)$$

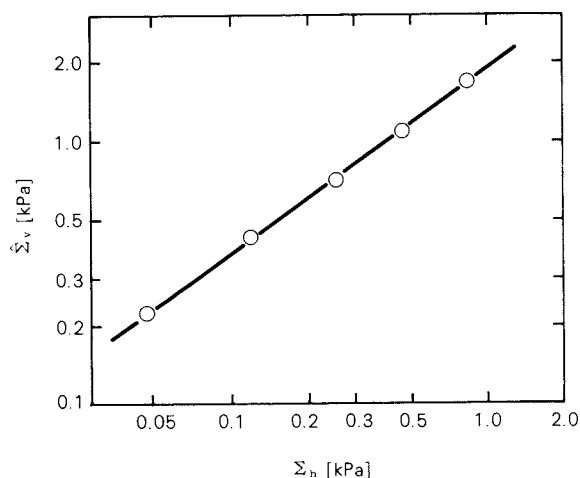$$\ln \overline{\Sigma}_{Vm} = \frac{4.47 - 6.02\,\epsilon}{1.00 - \epsilon} \quad \text{(Refer to Fig. 6)} \quad (8)$$

Fig. 15   Relationship between the vertical stress and the horizontal stress in the shallow bin

Note that the values of Σ_h, $\widehat{\Sigma}_V$, $\overline{K}$, and $\overline{\Sigma}_V$ correspond to σ_h, σ_{Vm}, k, and σ_{Vm}, respectively, in the deep bin. **Table 3** lists the values calculated from Eqs. (6) to (8) and the measured data of ϵ and σ_{Vm}. It is found from this table that the prediction would be relatively consistent with the measurement; in detail the calculated values of ϵ and σ_{Vm} were at most by 0.01 and 10% less than the measured ones, respectively.

This result suggests that, for CaCO$_3$ (P-30), there may partly be a possibility of prediction for the condition in the deep bin (σ_h, σ_{Vm}, and ϵ) by using the relations of the shallow bin.

5. Conclusion

The packing and stress condition of the powder bed of CaCO$_3$ (P-30) charged through a sieve were investigated for both the shallow bin ($H/D \leq 0.25$) and the deep bin ($H/D \leq 4.0$). The results obtained are:

(1) In case of the shallow bin, the stress ratio was not constant but increased linearly with decreasing the mean porosity. The mean void ratio had a linear relation with the mean consolidation stress expressed in a logarithmic form.

(2) The stress condition of the powder bed in the shallow bin could be precisely expressed Janssen's formula, by using the coefficient of wall friction obtained by the uniaxial shear tester. This result would imply that the vertical stresses over the same horizontal cross section were uniform.

(3) In case of the deep bin, the vertical stresses were dependent on the measuring points even in the same horizontal cross section. Thus the pressure ratio varied with the value used as the vertical stress. When the data of the vertical stress near the bin wall

Table 3   Comparison between the observed and estimated values of porosity and mean vertical stress in the deep bin

		observed values		estimated values	
H [m]	σ_h [kPa]	ϵ [-]	σ_{Vm} [kPa]	ϵ [-]	σ_{Vm} [kPa]
0.15	0.27	0.760	0.75	0.755	0.75
0.35	0.58	0.731	1.46	0.729	1.40
0.55	0.79	0.723	1.83	0.717	1.81
0.75	0.89	0.721	2.13	0.712	1.99
0.95	0.94	0.719	2.21	0.710	2.07
1.15	0.95	0.713	2.31	0.710	2.07

were employed, the stress ratio increased linearly with increasing the porosity; this tendency was similar to that of the shallow bin, but there was a slight difference between the values. When the data of the vertical stress at the center of the bin were employed, on the other hand, the stress ratio was held nearly constant at $0.71 < \epsilon < 0.75$. The porosity had the linear relation with the mean stress in the logarithmic form like the case of the shallow bin.

(4) For the both cases of the shallow bin and the deep bin, the coordinates expressing the stress condition at the wall (the horizontal stress and the shear stress) were found to be nearly placed on WYL. The Mohr circles were located far from EYL and rather tangent to WYL.

(5) The porosity and the mean vertical stress could be predicted from the equations expressing the conditions of the shallow bin by using the horizontal stress measured at the wall of the deep bin.

Nomenclature

D	:	diameter of bin	[m]
e	:	void ratio of powder in deep bin	[—]
$\bar{e}$	:	mean void ratio of powder in shallow bin	[—]
f_B	:	load acting on the bin bottom	[N]
f_τ	:	shear force acting on the bin wall	[N]
g	:	gravity acceleration	[m/sec²]
H	:	height of powder bed	[m]
$\bar{K}$	:	ratio of horizontal stress to vertical one used in shallow bin	[—]
k	:	ratio of horizontal stress to vertical one used in deep bin	[—]
L	:	height of bin	[m]
R	:	radius of bin	[m]
W_P	:	weight of powder in bin	[N]
δ	:	effective angle of yield locus	[degree]

ϵ	:	porosity of powder in deep bin	[—]
$\bar{\epsilon}$	:	mean porosity of powder in shallow bin	[—]
μ_W	:	coefficient of wall friction	[—]
ρ_B	:	bulk density of powder	[kg/m³]
Σ	:	stress used in shallow bin	[Pa]
Σ_{Vm}^J	:	stress calculated by Eq. (2)	[Pa]
$\hat{\Sigma}_V$	:	vertical stress defined by Eq. (1)	[Pa]
Σ_V	:	mean consolidation stress	[Pa]
Σ_{VO}	:	vertical stress by surcharge	[Pa]
σ	:	stress used in deep bin	[Pa]
τ_W	:	shear stress on the wall	[Pa]
ϕ_W	:	angle of wall friction	[degree]

<Subscripts>
h	:	horizontal (at the bin wall)
V_i	:	vertical (at the point i)
V_m	:	vertical (at the bin bottom)
VW	:	vertical (at the bin wall)

References

1) Arnold, P.C., A.G. McLean and A.W. Roberts: "Bulk Solids: Storage, Flow and Handling". Tunra Limited, New South Wales, Australia (1970).

2) Brown, R.L. and J.C. Richards: "Principles of Powder Mechanics", P.68, Pergaman Press, London (1970).

3) Matsumoto, K., M. Yoshida, A. Suganuma, R. Aoki and H. Murata: *J. Soc. Powder Tech., Japan,* **19**, 653 (1982).

4) Moriyama, R., N. Hayano and T. Jotaki: *ibid.,* **18**, 507 (1981).

5) Schofield, A. and P. Wroth: "Critical State Soil Mechanics". P.67, McGraw-Hill, London (1968).

6) Sundaram, V. and S.C. Cowin: *Powder Tech.,* **22**, 23 (1979).

7) Tsunakawa, H., Y. Asano and R. Aoki: *J. Soc. Powder Tech., Japan,* **14**, 497 (1977).

8) Walker, D.M.: *Chem. Eng. Sci.,* **21**, 975 (1966).

9) Walters, J.K.: *ibid.,* **28**, 13 (1973).

10) Yoshida, M., K. Matsumoto, A. Suganuma and R. Aoki: Preprints of The 16th Autumn Meeting of The Soc. of Chem. Engrs., Japan, Nagoya, P.467 (1982).

Discontinuous Flow and Frictional Property of Granular Materials[†]

Jusuke Hidaka, Yutaka Kirimoto and Shigeo Miwa
Department of Chemical Engineering, Doshisha University*

Kazutaka Makino
Department of Mining Engineering, University of Akita**

Abstract

The stress-strain relation in the deformation and flow of granular materials is generally discontinuous. The discontinuous behaviour is one of the fundamental properties of granular materials. The mechanism of discontinuous behaviour in the flow of granular materials is investigated by the penetration of a circular plate into a powder bed. The penetration characteristic curve (load-displacement curve) of a dense powder bed shows a step-wise curve. The load required to penetrate a circular plate into the powder bed is in satisfactory agreement with the values calculated from Meyerhof's equation. The plasticity pattern formed by the penetration of a plunger into the powder layer is observed by an X-ray radiograph. It is shown that discontinuous behaviour results in successive or periodical shear yields which occurred in the powder bed. The generating mechanism of intermittent or periodical shear yields is theoreticaly discussed, and the relationship between the periodity of intermittent shear yields and the frictional property of the powder bed is experimentally confirmed. The static and dynamic angles of the internal friction of powders can be measured by the penetration test.

1. Introduction

The stress-strain relation in the deformation and flow of the powder layer constructed by the particles contacting each other generally indicates discontinuous curve[1]. The discontinuous behaviour is one of the important fundamental properties of the powder layer in which the force is transmitted by the friction through the contact points of the particle. There are thus various phenomena caused by the discontinuity, such as the pulsation of the flow rate of the granular materials from the hopper and the wall pressure, the heterogeneity of the density within the compressed granular materials and the periodical fluctuation of the power required for powder mixing. Hence, the fundamental study on the discontinuous behaviour in the deformation and flow is of great importance for the powder handling.

For the purpose of elucidating the discontinuous flow property, the authors paid attention to the compressive flow caused by the penetration of a circular plate into a powder layer, of which the dynamic analysis could be conducted rather simply. Based on the experimental study on the relation between the penetration load and the displacement of the plate, the discontinuous behaviour has been investigated in relation to the frictional properties[1].

In this paper, the propagating condition of

the plasticity in the penetrating process within a relatively dense powder layer was observed by means of X-ray radiograph minutely. It verified that the load-displacement curve in the penetrating process showed a step-wise variation by the flow of granular materials which consisted of successive or periodical shear yields. Furthermore, the mechanism of generating the discontinuous behaviours was theoretically discussed on the basis of the observation of the forming process of the plasticity pattern. The measurement of the frictional angle property by the penetration method and its physical meaning will be also reported in the following.

2. Experimental apparatus and method

2. 1 Measurement of penetrating load and displacement

Figure 1 shows a schematic diagram of the measurement apparatus. The loading test apparatus (Model UMH-10 made by Shimadzu-seisakusho) was used to load the penetrating circular plate at a constant rate. The sample powder was fed through a sieve and uniformly packed in the cylindrical sample container, which was then set on the movable stage of the loading test apparatus. Raising the movable
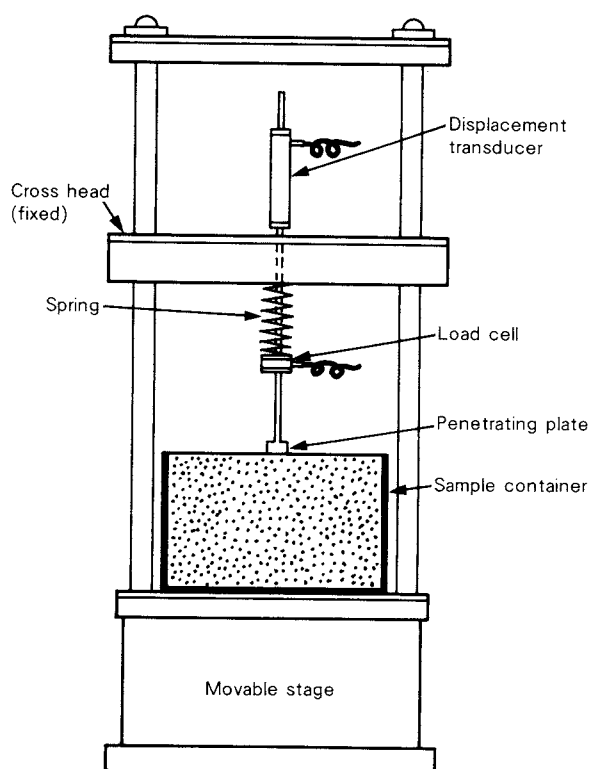
Fig. 1 Experimental apparatus

stage at a constant rate, the penetrating circular plate contacted with the surface of the powder layer and started to penetrate. The resistance force (load) acting on the penetrating plate from the powder layer and the depth of the penetrating plate (displacement) from the surface of the powder layer were measured by the load cell and the displacement transducer respectively. The cylindrical sample container ($\phi 298 \times H111$) was made of PVC resin. It was necessary to make the frictional force on the axis supporting the penetrating plate and its periphery negligibly small compared with the load acting on the bottom of the penetrating plate from the powder layer. The penetrating circular plates having a diameter 30[☆], 20 and 14.4 mm with the thickness of 5 mm were used and supported by the metal cylinder of a diameter of 4 mm. The measurements were conducted at constant penetrating velocities as well as at constant loading rate by setting a spring having a constant of 1.16 N/mm above the penetrating plate.

2. 2 X-ray observation of plasticity pattern within powder layer

In order to estimate the penetrating load into the powder layer and understand the deformation and flow mechanism, it is necessary to observe minutely the momentary plasticity pattern formed in the powder layer during the penetration of the plate. **Figure 2** shows a schematic diagram of the apparatus used for the observation. This consisted of the transparent box made of acrylic resin (430 x 470 x 50 in mm), the plunger (25 x 48 x 500 in mm) having the rectangular cross section, the motor for its penetrating into the powder layer at a constant speed and X-ray radiograph equipment. The way of filling the box with the sample was the same as mentioned above. Additionally, steel balls with a diameter of 3 mm were arranged in the lattice form having a side of 10 mm in the central plane vertically oriented to the X-ray radiation, to measure the displacement of the particles on the deformation and flow. Having the plunger penetrate at a constant velocity, the load and the displace-

---

☆ This size of penetrating disc was used only with the fine powder sample WA #3000.
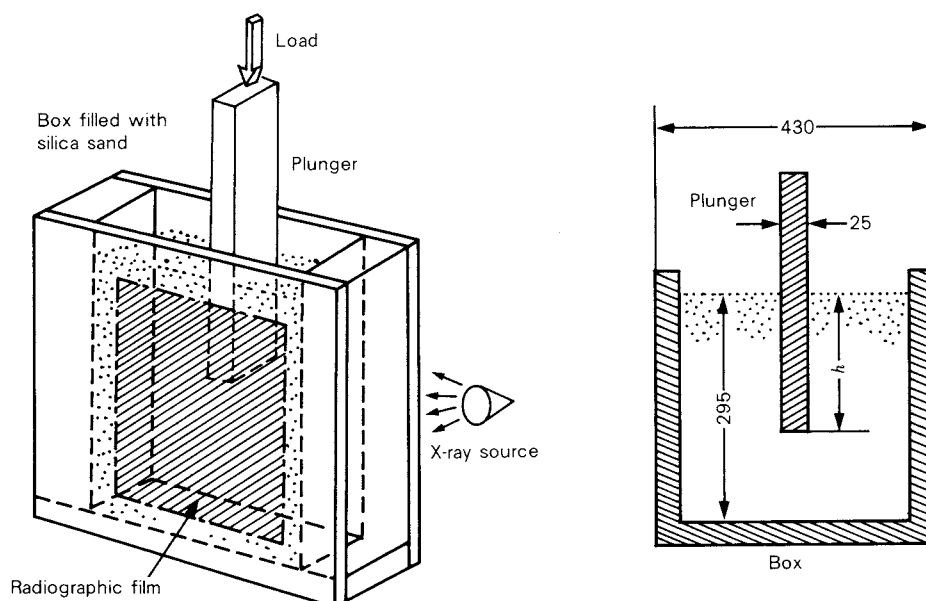
Fig. 2 Experimental apparatus for the observation
of plasticity pattern

ment were measured by the above-described method. At the same time, the X-ray radiographs of the plasticity pattern inside the powder layer were obtained using the intermittent pulses having a duration of 240 seconds from an X-ray source (ERESCO-300 operated at a tube voltage of 140 kV and a tube current of 5mA) and the X-ray film (Fuji Film IX-100 for industrial use, 300 x 250) attached to a side wall of the powder layer opposite to the one irradiated by the X-rays. Furthermore, the instantaneous change in the plasticity pattern was recorded and observed continuously with an X-ray video system (Rikagaku Denki).

2. 3 Sample

In this paper a silica sand was used as a sample to distinguish the discontinuous behaviour on the deformation and flow. The silica sand used for the X-ray observation of the plasticity pattern had an average particle size of 350 μm and the angle of internal friction of 35° measured by a direct shear test. On the other hand, an Ottawa sand classified into the range from 297 to 500 μm with JIS standard sieve (silica sand A) was used for the penetration test. In order to obtain a sample which was made of the same material as the silica sand A but differed in the internal friction, a silica sand B was prepared by washing sufficiently the particle surface of the silica sand A with pure water.

The angles of internal friction ϕ_i of the silica sands A and B by the direct shear test were ϕ_{ia} = 39° and ϕ_{ib} = 41° respectively, both of them having ρ_B = 1.700 g/cm^3. White corundum (WA #3000, D_p = 5 μm) was also used as a fine powder sample.

3. Results and discussions

3. 1 Penetration characteristic curve

The solid line in **Fig.** 3 shows an example of the penetration characteristic curve which represents the relationship between the load and
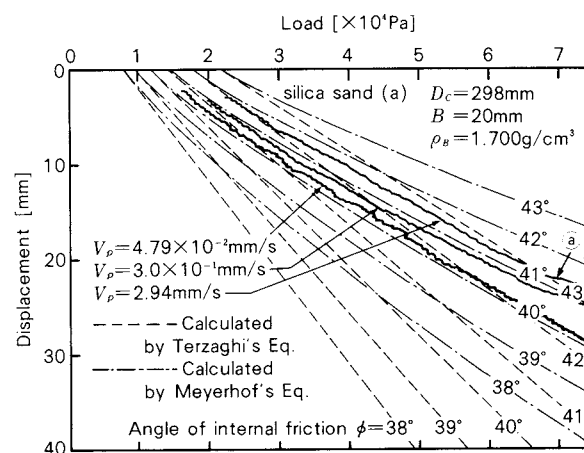

Fig. 3 Influence of penetrating speed on the penetration characteristic curve of silica sand (dispacement control test)

the displacement obtained from the penetration tests at a constant speed. It is apparent from **Fig.** 3 that the penetration characteristic curve is affected by the penetrating speed. Therefore decreasing the penetrating speed as far as less than 0.1 mm/s, the following experiments were conducted under the condition regarded as the quasi-static state. Consequently, the load required for the plate to penetrate the powder layer Q_u equaled so-called ultimate bearing capacity on the analogy of the bearing capacity problem in the soil mechanics.

It has been much debated about the ultimate bearing capacity of the circular foundation. Having applied here the semi-theoretical bearing capacity equations of Terzaghi and Meyerhof as expressed in the following equations, the calculated results for the penetrating plate (the circular foundation) are shown by broken lines and chain lines with the frictional angle ϕ as a parameter in **Fig.** 3[2,3].

Terzaghi's equation

$$Q_u = 1.3\, CN_c + \rho_B\, hN_q + 0.6\rho_B\,(B/2)\,Nr \tag{1}$$

Meyerhof's equation

$$Q_u = 1.3\, CN_c d_c + \rho_B\, hN_q d_q$$
$$+ 0.6\, \rho_B\,(B/2)\,N_r d_r \tag{2}$$

where C is the cohesive force, ρ is the bulk density, B is the diameter of the penetrating plate, h is the displacement and N_c, N_q, N_r are the coefficients of the bearing capacity given as a function of the angle of internal friction.

$$N_q = \frac{1}{(1-\sin\phi)}\, \exp\left[(\frac{3\pi}{2} - \phi)\tan\phi\right]$$
$$N_c = (N_q - 1)\cot\phi$$
$$N_r = (N_q - 1)\tan 1.4\phi \tag{3}$$

The coefficients d_c, d_q, and d_r considering the effect of the penetrated depth are represented by the following equations.

$$d_c = 1 + 0.4\,(h/B), d_q = 1 + 0.2\,(h/B)$$
$$d_r = 1 + 0.6\,(h/B) \tag{4}$$

Consequently if the compacting condition (the bulk density ρ_B) of the sample is decided, Eqs. (1) and (2) become the function of ϕ and h and are solved to give the broken and the chain lines in **Fig.** 3. On this experimental condition, the results from Eqs. (1) and (2) differ considerably as the displacement exceeds 5 mm.

As seen in **Fig.** 3, the measured value[☆] of the load changes according to the calculated value by Eq. (2), as far as the displacement reaches a certain value represented by the point a. Beyond the point, however, the measured load comes off from the curve obtained by the Meyerhof's equation considerably and suddenly increases[☆☆]. This is caused by the fact that Eq. (2) was developed for the shallow foundation ($h < B$) and that the actual load includes the passive resistance due to the sample container wall. Actually solving Kötter's equation for the axially symmetrical system[4] with the experimental condition give in **Fig.** 3 produces the slip line at the point a, the top of which reaches the wall of the container. However the trend of the change of the penetration curve up to the point a which is not affected by the wall is consistent with that of the bearing capacity obtained by Meyerhof's equation. Furthermore the shape of the penetration curve is not continuous but step-wise or serrated with alternated increase and decrease of the load as reported previously[1]. This feature becomes clearer if the constant load rate test is done as shown in **Fig.** 4. It is worthy of noticing that each curve enveloping the upper and the lower ends of the steps of the penetration curve obeys the tendency of Meyerhof's equation as shown by the broken line in **Fig.** 4.

3. 2 Plasticity pattern formed within the powder layer on the deformative flow process

The deformative flow process within powder layer has been analyzed previously by Bagnold's model[1], which included some problematical points. Therefore the momentary change of the plasticity pattern formed within a powder layer in the flow process was observed in detail by the visualization using the X-ray and the

---

☆ The load on the abscissa is given as a value per unit area of the penetrating plate i.e. the normal stress on the powder layer under the plate (Pa).

☆☆ The penetrating load on the surface of the powder layer represented with the solid line in **Fig.** 4 also does not agree with the bearing capacity obtained by Meyerhof's equation. This is attributed to various reasons, one of which seems to be the compaction of the powder layer near the surface caused by flattening it with a scraper after filling the container with the sample. Therefore, the data in the neighbourhood of the surface were neglected.
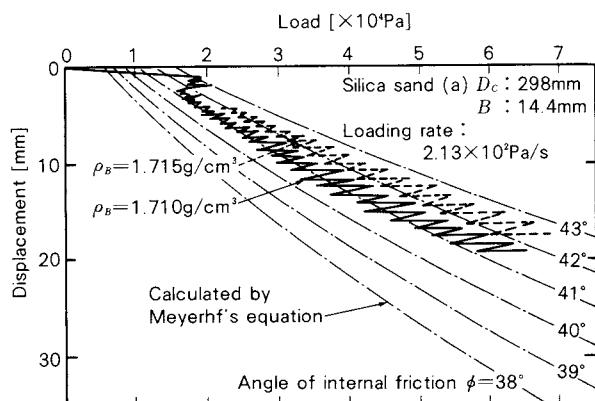
Fig. 4 Penetration characteristic curve for load control test

flow mechanism of the powder layer was attempted to make clear.

Figure 5 shows a typical example of the X-ray radiograph indicating the state of the plasticity within the powder layer generated by the penetration of the plunger. On the radiographs, the slip lines formed from the top of the plunger toward the circumference are remarked as the white strips. It can be confirmed that these white strips are the slip lines from the measurement of the displacement vectors of the steel balls (the black circles in the pictures) set to observe the displacement of the particles within the powder layer.

Figure 6 shows the displacement vector of the steel balls with arrows, after the plunger penetrated 60 mm from the surface of the powder layer (corresponding to **Fig. 5(c)**). The numerical figure represents the ratio of the initial area of the grid section formed by four adjacent steel balls to the area enveloped by the same balls after the penetration. Consequently the figure expresses the degree of local expansion or contraction of the powder layer. The broken lines in **Fig. 6** show the white strips in **Fig. 5(c)**. As the figures in the area enveloped by the broken lines represent the value more than 1.0, it is confirmed that they are the slip lines with the local expansion. Since this slip line has rather wide width, it is to call the slip belt. The specifically large dilatation in these parts is caused by the following factors. Noting the lowest slip lines formed just at the time when the X-ray radiograph was taken, quantity of the particle displacement over the slip line becomes maximum near the slip line and gradually decreases toward the surface of the powder
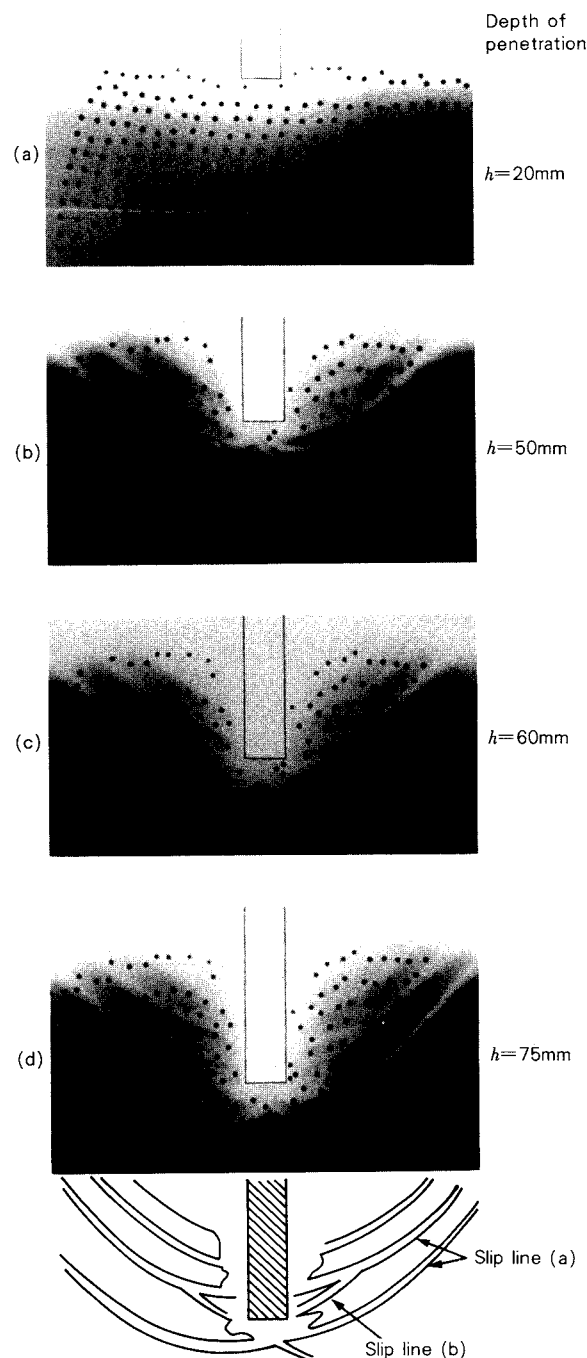

Fig. 5 X-ray radiographs of the plasticity pattern generated by the penetration of a plunger into powder bed

layer. Moreover, paying attention to the slip lines on the left side of the plunger, the displacement vectors of the particles over the slip line have the clock-wise rotational component to the slip line, while those under the slip line have the counterclock-wise rotational component, even if they are small. As a result, the local large dilatation takes place at the part of
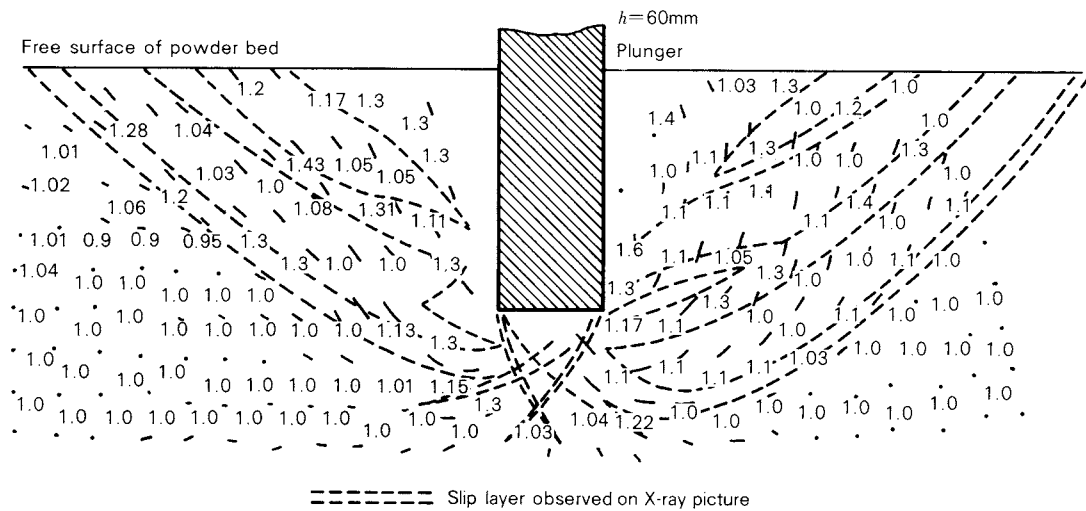
Fig. 6 Measured displacement of steel ball showing the evolution of dilatancy localization

(a) Under maximum loading
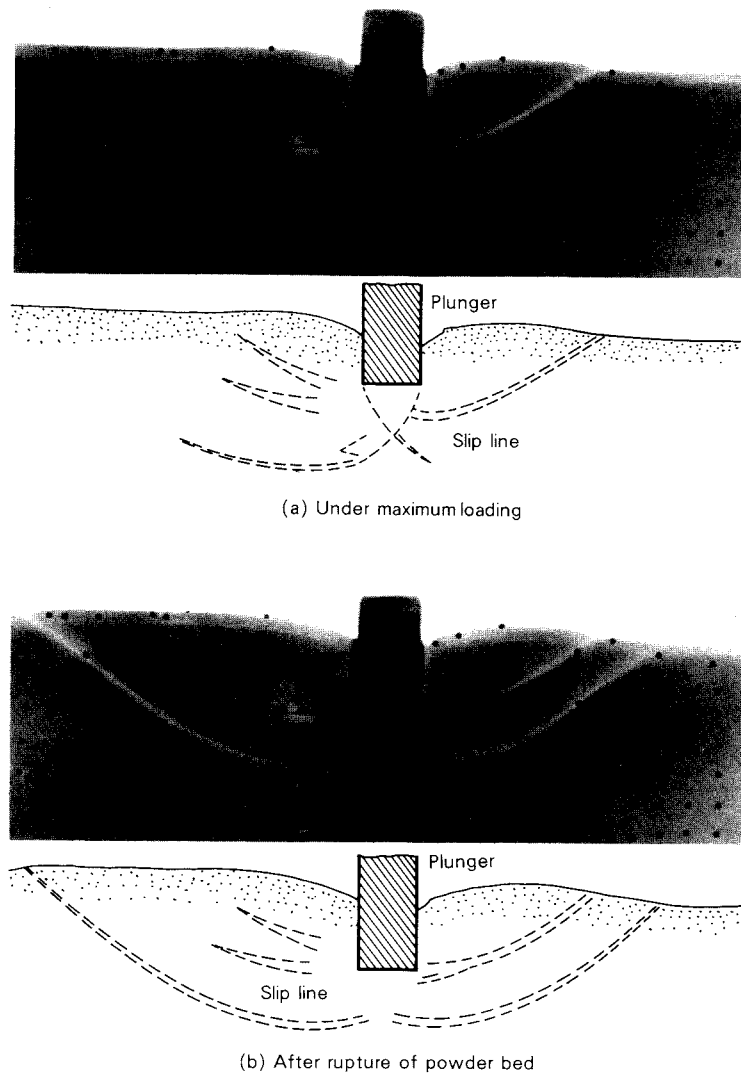

(b) After rupture of powder bed

Fig. 7 X-ray radiographs of rupture layer in powder bed

the slip line, which leads to the increase of the X-ray transmission and appears as the apparent white strip on the radiograph reversely developed.

A series of X-ray radiographs in **Fig. 5** distinctly shows how the slip lines appearing in the white strips were formed intermittently or periodically as the plunger penetrated.

Figure 7 shows the X-ray radiographs before and after a step-wise change in the penetration process curve formed by the increase and the following radical decrease of the load. That is to say, **Figs. 7(a)** and **(b)** indicate the X-ray radiographs as the load was close to the ultimate bearing capacity and as the load suddenly decreased respectively. A part of the slip line (a part of the transitional area) has been formed already right under the plunger in **Fig. 7(a)** and the top of the slip line reaches the surface of the powder layer with the large particle displacement in **Fig. 7(b)**. From this result, it is understood that each step of the penetration characteristic curve corresponds to each slip line in the powder layer.

3. 3 Shape of slip line

Terzagi's and Meyerhof's equations are obtained by the environing transition zone acted on the rigid zone under the plunger and the passive resistance from Rankine's passive zone as the plasticity on the ultimate state is assumed. The slip lines of the surface in the powder layer obtained by the numerical calculation of Meyerhof's and Kötter's equations are compared with that observed by X-ray in **Fig. 8**. Three slip lines appear to be consistent as a whole expect the difference of these top patterns.

As the load was added on the powder layer by the plunger, a transition zone was observed to take place in part under the condition of the ultimate bearing capacity. It is possibly considered that a slight difference of the top pattern of each slip line would hardly effect the bearing capacity and the tendency of the load against the displacement could be consistent with that of Meyerhof's hypothesis.

3. 4 Generation mechanism in discontinuous behaviour of powder layer

From the fact as mentioned above, the generation mechanism of the discontinuous flow within a powder layer can be described by the following Meyerhof's hypothesis. Consider, for simplification, that the penetration plate penetrates into the infinitely wide and dense powder layer at the fixed displacement rate as shown in **Fig. 9**. The resistance force, or the load $Q_u(\phi_s, h)$, depending on a static angle of internal friction and a displacement h acts the penetrating place, when it is placed at a given depth h within the powder layer. As the powder layer exhibits the ultimate bearing capacity, a part of the slip line represented by the solid line in **Fig. 9** is formed. Then, the slip line reaches the surface of the powder layer accompanied by the movement of the particles toward over the slip line. At this time, the dilatation of the particles over the slip line causes decrease of the static angle of internal friction ϕ_s and it becomes the dynamic angle of internal friction ϕ_d. Thus, the resistance force $Q_u(\phi_s, h)$ of the powder layer decreases $Q_u(\phi_d, h)$ at once. As ϕ_d decreases gradually with a dilatation of the powder layer, the penetrating plate penetrates by the displacement Δh until the
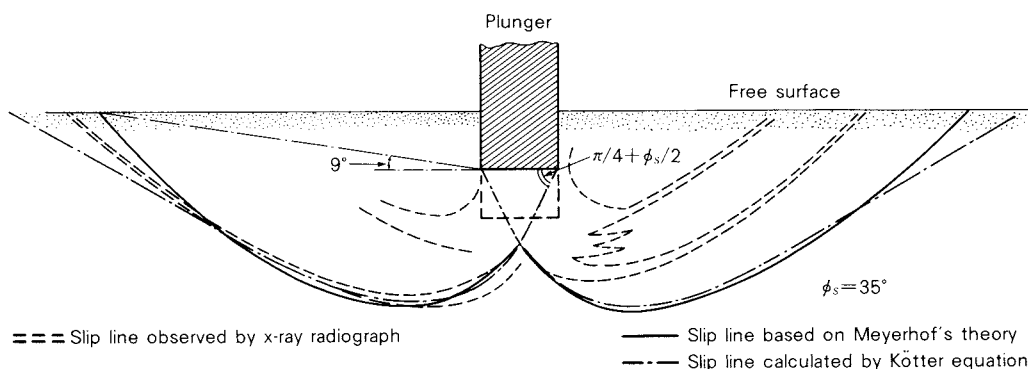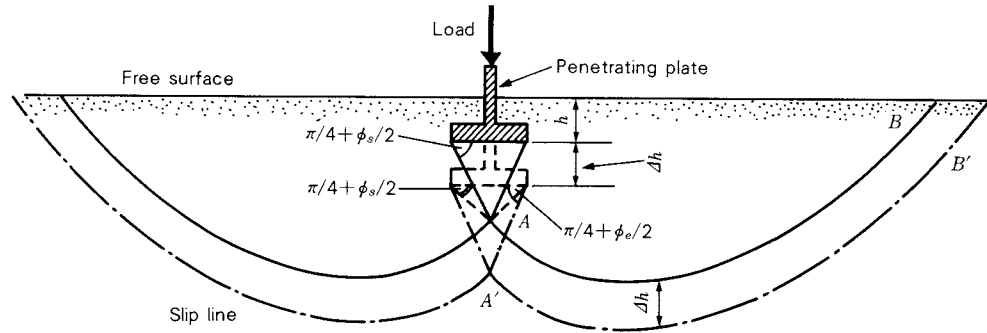

Fig. 8 Comparison of slip lines

Fig. 9 Schematic diagram of rupture model for
displacement control test

active zone (rigid zone) is formed. At this time, the bottom angle under the penetrating plate is $\pi/4 + \phi_s/2$ and the penetrating plate meets resistance of gradually decreasing $Q_u(\phi_d, h)$. The value, ϕ_e is related to the penetrating rate because ϕ_e is the dynamic angle of internal friction of the powder layer flowing over the slip surface at a constant penetrating rate V_p. The displacement Δh is given by ϕ_s and ϕ_e through the following equation.

$$\Delta h = \frac{B}{2} \tan\left(\frac{\pi}{4} + \frac{\phi_s}{2}\right) - \tan\left(\frac{\pi}{4} + \frac{\phi_s}{2}\right)$$
(5)

Where B is the diameter of the penetrating plate.

As the bottom angle of the active zone becomes $\dfrac{\pi}{4} + \phi_e/2$, the dilatancy motion of powder over the slip line stops and the ultimate bearing capacity $Q_u(\phi_s, h + \Delta h)$ at the depth $h + \Delta h$ of the powder layer acts on the penetrating plate. Then the new slip line A'B' is formed as shown by the chain line in **Fig. 9**. The penetrating plate penetrates into the powder layer with repeated this intermittent be-

haviour.

As the constantly increasing load through the spring is acted on the penetrating plate, the penetration at a constant rate can be observed as shown in **Fig. 10**. When the increasing load is equal to the ultimate bearing capacity at any depth h within the powder layer, the powder layer flows and the penetrating plate suddenly penetrates into the powder layer suffering from the decreasing resistant force $Q_u(\phi_d, h)$. The penetrating plate stops at the place where the equilibrium of the following equation is achieved.

$$Q_u(\phi_s, h) - f = Q_u(\phi_e, h + \Delta h)$$
(6)

where f is the decrease element of the load which is caused by the extension of the spring and Δh is given by the following equation.

$$\Delta h = \frac{1}{k} Q_u(\phi_e, h + \Delta h) - Q_u(\phi_s, h)$$
(7)

where k is a spring constant. Then, the penetrating plate is at the rest until the load of $Q_u(\phi_s, h + \Delta h)$ is acted, and the next flow was repeated.
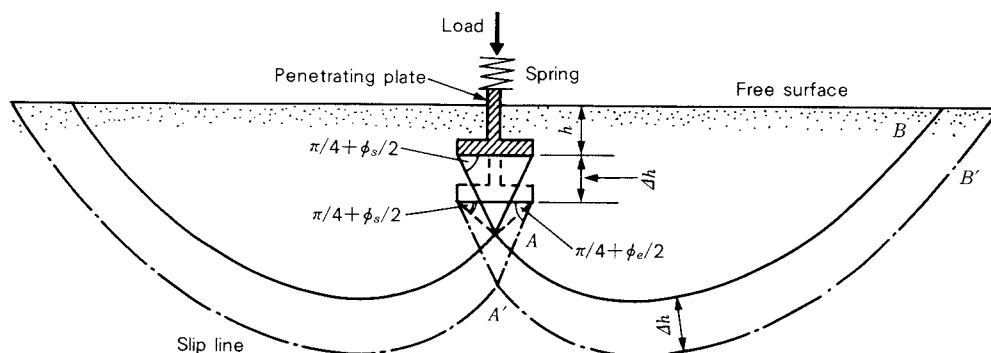

Fig. 10 Schematic diagram of rupture model for load
control test

Figure 11 illustrates the penetrating behaviour with the intermittent flow expressed as the penetration characteristic curve. The penetrating plate penetrates, suffering from the resistant force of $Q_u(\phi_s, h)$ and $Q_u(\phi_e, h)$ from the powder layer. When ϕ_s differed largely from ϕ_e, the powder layer under the penetrating plate dilates considerably. At this time, the structure of the powder layer is fluctuated and the passive zone based on the smaller angle of internal friction than ϕ_s is formed. Then the slip line (b) which the top of slip line intersects with the slip line (a) is formed as shown in **Fig. 6**. As a matter of course, the load is small at this time.

3. 5 Measurement of property of frictional angle by penetrating experiment

Discussion of the flow mechanism in the latest section implies that the static and dynamic angle of internal friction within the powder layer can be measured by the penetrating experiment. The top and the under load on each step of the penetration characteristic curve are expressed by $Q_u(\phi_s, h)$ and $Q_u(\phi_e, h)$ respectively, in **Fig. 11**. The values ϕ_e and ϕ_s can be obtained by the penetration characteristic curve enveloped at the top and the bottom of steps respectively, through the penetration characteristic curve corresponding to the angle of internal friction obtained by Eq. (2) and the measured penetration characteristic curve.

The measured result is shown in **Fig. 12**. For silica sand (a) ϕ_s and ϕ_e obtained under the constant displacement rate condition were 40.7° and 40.4° respectively and under the constant loading rate condition were 41.7° and 40.2°. For silica sand (b) ϕ_s = 42.3° and ϕ_e = 39.8° were obtained at the constant loading rate. Each ϕ_s was similar to the result of the direct shear test approximately. As previously reported[1], ϕ_s and ϕ_e of cohesionless powder were consistent with the angle of repose measured by the method of the inclined container of the powder with the same porosity.

For any powder ϕ_s obtained under the constant displacement rate condition was apt to become lower than that under the constant loading rate condition and conversely ϕ_e became higher. This is probably due to large deviation from the ideal whole shearing condition,
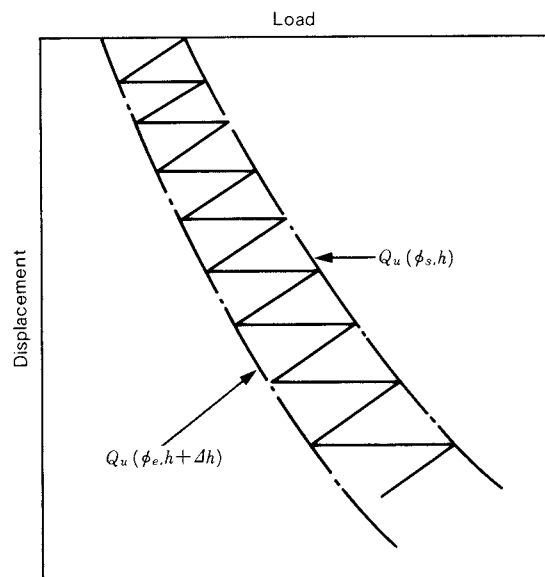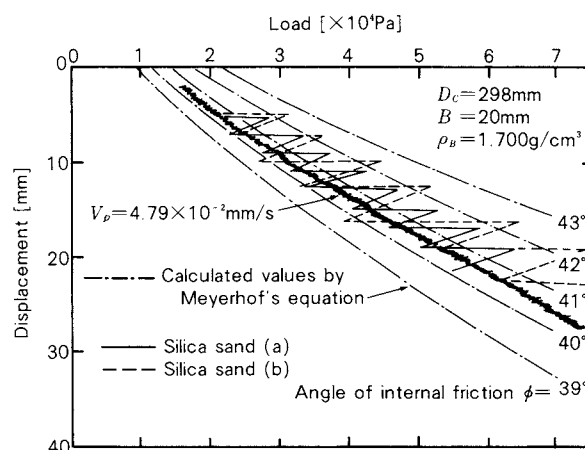

Fig. 11 Typical penetration characteristic curve

Fig. 12 Penetration characteristic curve of silica sand (a) and (b)

as ϕ_e became much smaller compared with the case of the constant loading rate test as mentioned below. The value ϕ_e, depending on the penetrating rate, took small value under the constant loading rate condition, because the penetrating rate of the flow had large value. Under the constant loading rate condition, Δh of the silica sand (a) and (b) were 2.2 and 3.1 mm respectively through the calculation of Eq. (7). These values were consistent with the measured result (average Δh were 1.96 and 3.20 mm, respectively). **Figure 13** shows the case of the smaller diameter of the penetrating plate (area ratio was 0.52). The result of the penetration test was very sensitive to the porosity ϵ (bulk density ρ) of the powder layer
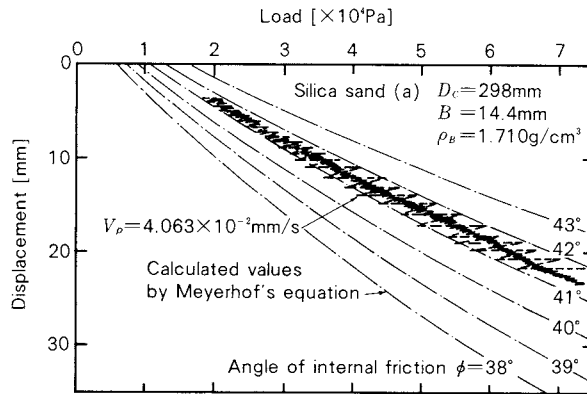
Load [×10⁴Pa]

Fig. 13 Penetration characteristic curve of silica sand (a)

Load [×10⁴Pa]
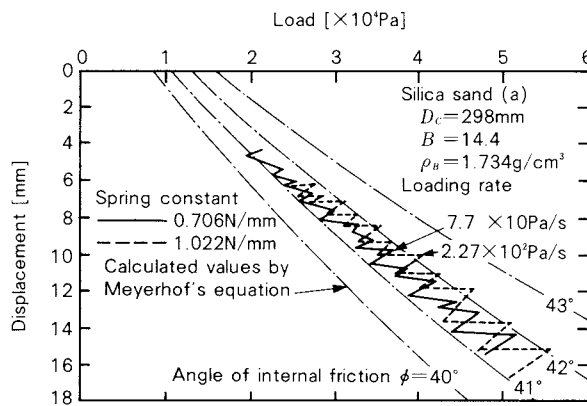
Fig. 14 Influence of the spring constant on penetration characteristic curve
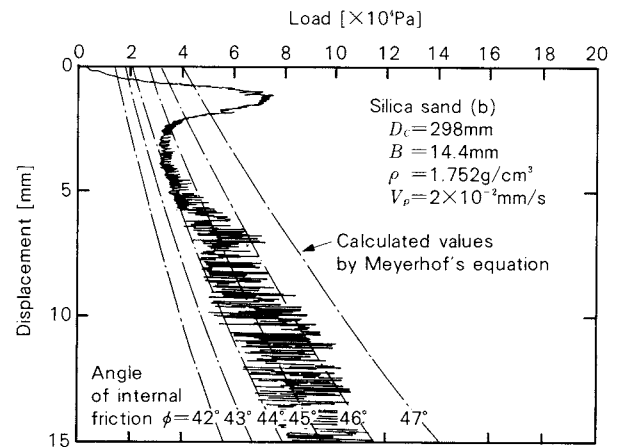
Load [×10⁴Pa]

Fig. 15 Penetration characteristic curve of silica sand (b) for displacement control test
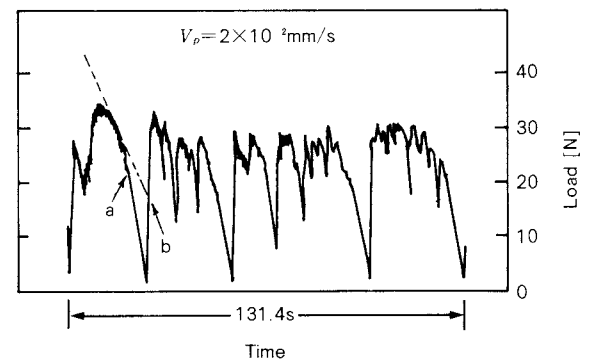
Fig. 16 Representative waveform of the load required to penetrate a circular plate into powder bed

and the value of ϕ_s and ϕ_e were a little different from the case of **Fig. 12**, and Δh took 0.84 mm which was about half of the silica sand (a) shown in **Fig. 12** as predicted from Eq. (7). **Figure 14** shows the influence of the spring constant. The calculated values corresponding to the spring constant 1.022 and 0.706 N/mm were 0.87 and 0.99 mm, respectively, and the average values of Δh of the measured result were 0.76 and 0.94 mm, respectively. Therefore Eq. (7) was found to be almost satisfied.

On the other hand, Δh obtained at the constant displacement rate was calculated from **Fig. 12** and Eq. (5) to be 0.20 mm. This value gives a question for the rupture model as mentioned above because Δh took a small value corresponding to a particle diameter of the sample powder. **Figure 15** shows the result of the constant displacement rate test of the silica (b) having the same particle diameter. Then ϕ_s and ϕ_e is 45.8° and 44.4° respectively and

0.61 mm was calculated from Eq. (5). This means that Δh would depend on ϕ_s and ϕ_e, independently of the particle diameter. **Figure 16** shows a part of the waveform which is indicative of the fluctuation of the load for the test in **Fig. 15**. Similar to the constant loading rate test, this test provided a periodical rapid decrease showing the failure at intervals nearly equal to the calculation (0.61 mm) as mentioned above[☆]. This implies that the model as described above would be available.

☆ When the load is applied under the displacement rate condition, it abruptly decreases, even to a non-loading state, at the powder layer deformation as shown in **Fig. 16**. As the load increases up to the point a, the particles near the slip line begins to flow and the succeeding collaspe takes place. In this work, the load was determined from the intersecting point b of the tangential line (dotted line) and the load curve at collaspe of the powder layer to obtain the penetrating load curve related to ϕ_s.
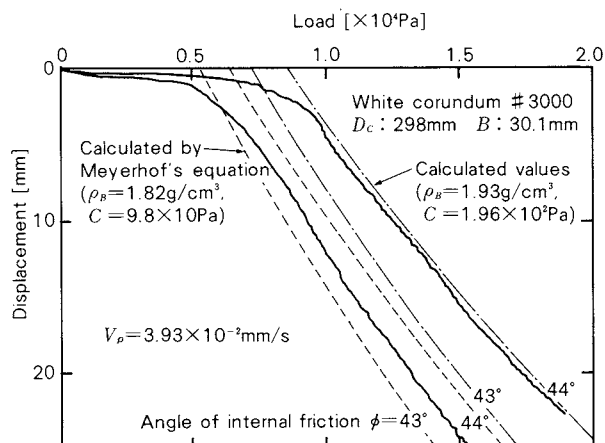
Fig. 17 Typical penetration characteristic curve of fine powder (white corundum #3000)

The above results indicate the measurement example on the property of the angle of internal friction and confirm suitability of the flow mechanism as mentioned in the former section. Although nothing is referred to in detail in this report, a fine powder was found to be packed loosely into a container due to its cohesiveness and to tend to cause, so called, propagating rupture at a surface of the powder layer as shown in **Fig. 17**. Therefore this test should be done after the dense packing was achieved in such a condition that the large deformation period disappears. The same slope of the penetration load curve calculated from Eq. (2) with the variation of the cohesive force C and the measured penetration characteristic curve can easily provides C and ϕ.

4. Conclusion

When a powder layer deforms or flows under the influence of an external force, its displacement varies discontinuously in general with the added stress. This discontinuous change causes various kinds of trouble in actual operations.

This report dealt with phenomena of plunger penetration into dense powder layer to elucidate the generation mechanism of such a discontinuous behaviour.

The results obtained are as follows:

— Penetrating load varied with penetrating displacement in a discontinuous step-wise manner. This means that the powder layer would deform discontinuously. The relation between penetrating displacement and penetrating load obtained by experiment was

consistent with the Meyerhof hypothesis.

— X-ray radiograph observation was carried out to obtain the plasticity patterns in the powder layer formed by penetration of the plunger. The result was that a set of slip lines could be formed in an intermittent, periodical manner; thus the penetration process was expressed as a discontinuous curves.

— The Meyerhof plasticity model was adopted to quantitatively elucidate how the extent of its discontinuity would be dependent upon powder characteristics, especially friction proerty.

— Further, based on such an experimental result, characteristics of friction angle were determined by use of the penetration test.

The authors intend to explore the dependence of penetration characteristic curve on penetrating rate and the relationship between the degree of discontinuity in the curve ($\Delta\phi$ or the difference of ϕ_s and ϕ_e) and the various powder behaviour.

Nomenclature

B	:	diameter of circular penetrating plate	[mm]
C	:	cohesive force of powder	[Pa]
D_c	:	diameter of sample container	[mm]
D_p	:	particle diameter	[μm]
N_c, N_q, N_r	:	coefficient for estimation of the load required to penetrate a circular plate into powder bed	[—]
Q_u	:	load required to penetrate a circular plate into powder bed (bearing capacity of powder bed)	[N]
V_p	:	penetrating speed of a circular penetrating plate	[cm/s]
d_c, d_q, d_r	:	coefficient on displacement of penetration	[—]
k	:	spring constant	[N/mm]
h	:	displacement of penetration plate from free surface of powder bed	[mm]
ϕ	:	angle of internal friction	[deg]
ϕ_i	:	angle of internal friction measured by direct shear test	[deg]
ϕ_d	:	transient dynamic angle of internal friction of powder bed in collapsing	[deg]
ϕ_e	:	dynamic angle of internal friction	[deg]
ϕ_s	:	static angle of internal friction	[deg]
ρ_B	:	bulk density	[g/cm^3]

References

1) Hidaka, J. and S. Miwa: *Kagaku-Kougaku Ronbunshu*, 7 [2] 184-190 (1981).

2) Akai, K.: "Tsuchi no Shijiryoku to Chinka", San-kaido (Tokyo) p. 37 (1964).

3) Meyerhof, G. G.: *Geotechnique,* 2, 301-332 (1951).

4) Mogami, T. (ed.): "Doshitsu Rikigaku", Gihoudo, (Tokyo) p. 865 (1969).

5) Yamaguchi, H.: "Doshitsu Rikigaku", Gihoudo, (Tokyo) p. 286 (1978).

6) Ishihara, K. and T. Kimura: "Doshitsu Rikigaku", Shoukokusha (Tokyo) p. 180 (1980).

Explanation of the cover photograph
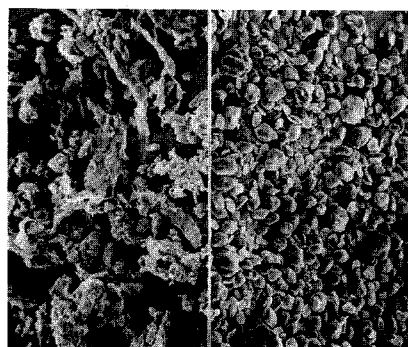
Hosokawa Micron Corp. has developed recently a fine-grinding equipment, called ANGMILL, which involves new grinding mechanisms. This equipment is designed to be available for mechanochemical applications such as homogenization (precise mixing), surface improvement (coating), and shape transformation, as well as fine grinding.

The left side of the cover photograph shows ground polymer particles which have very complicated shapes. The right side of it, on the other hand, indicates the same particles after treatment by ANGMILL; they look very spherical (about 20 μm in average particle diameter).

Flowability Assessment of Fine Coals Based on Dynamic Properties[†]

Keijiro Terashita and Kei Miyanami
Department of Chemical Engineering
University of Osaka Prefecture *

Takanobu Konishi
Hosokawa Micron Corp. **

Kazuo Furubayashi
Kawasaki Heavy Industry Co., Ltd. ***

Abstract

Flowability assessment of dry and wet fine coals has been attempted on the basis of their dynamic properties such as internal friction factor, shearing cohesiveness and tensile strength. The dynamic parameters have been determined by using a constant-load direct shearing tester and a hanging-type split-cell cohesiveness tester. Several kinds of coals with different water contents have been used.

The flowability of brown coal is highest with low values of the internal friction factor, shearing cohesiveness and tensile strength. The ranking of flowability is in order of bituminous coal and semi-bituminous coal. The flowability of anthracite is high. The flowability of fly ash is higher when compared to fine coals but it is easily influenced by a slight change in the water content.

The flowability of wet fine coals can be better evaluated by the tensile strength and shearing cohesiveness rather than by the internal friction factor. The tensile strength of wet fine coals shows a maximum when a comixture of funicular and capillary zones in formed. The flowability of wet fine coals is controlled by water adsorbed onto the surface of coal particles.

1. Introduction

Coal once replaced by oil is recognized anew as a substitute source of energy. The needs of the present time have stimulated extensive studies and developments of liquefaction, gasification and efficient combustion of coal.

Determination of physical characteristics such as internal friction factor, shearing cohesiveness and tensile strength of coal and fly ash as powder materials provides an exceedingly important key to rational design and smooth operation of combustion processes. Recent studies have described some aspects of the dynamic properties of coal. However, systematic approaches do not yet seem to have been adequately attempted. Despite obvious differences in the physicochemical characteristics of a variety of coals, existing studies seem to have dealt with only a limited range of various coals[1-11]. In addition, physicochemical characteristics have not been sufficiently compared between coal and fly ash. Adhesion and caking are problems that occur in fine coals rather than in coarse coals. The water content in coal usually increases due to rainfall or the water

---

sprinkled for prevention of dust spreading. Evaluation of the dynamic properties of fine coals in a wet state is, therefore, indispensable. Various shear tests have been performed on coals with different water contents. However, flowability studies of fine coals remain insufficient. The tensile strength of wet fine coals has been little reported.

We have earlier reported that the internal friction factors of coarse and fine powders, calculated from the relationship between the measured average vertical stress and stationary shearing stress in the vicinity of shearing plane, are almost free from the effects of experimental conditions[12] and that the flowability of powders can be estimated on the basis of the internal friction factor, shearing cohesiveness or pattern of vertical stress distribution in the vicinity of shearing plane[13]. We have also determined the internal friction factor and tensile strength of wet powders and discussed the problem of flowability[14].

In this study, direct shearing tests under a constant load condition and tensile breakup tests of fine powder beds have been carried out by using various kinds of fine coals with different water contents. Comprehensive evaluation of the flowability of fine coals and fly ash has been attempted by examining various parameters (internal friction factor, shearing cohesiveness and tensile strength) in relation to the fuel ratio in the coals. The flowability of wet fine coals has been discussed on the basis of the dynamic properties thus obtained. The results have been compared with those obtained with various other powder samples.

2. Materials and Methods

The vertical stress and its distribution in the vicinity of shearing plane were measured by a constant-load, monoplanar shearing tester. This tester is the same as used previously[13,14]. The shearing cell is an important part of the tester and is illustrated in detail in **Fig. 1**. The shearing stress $\bar{\tau}_x$ generated by shearing powder beds (coal or fly ash) was measured by a proving ring and dial gauges. The vertical stresses ($\sigma_{z,m}'$, $\sigma_{z,m}$) at six points were simultaneously measured by strain-gauge pressure transducers (sensing zone: 0.006 m in diameter, capacity: 196.2 kPa). $\bar{\tau}_x$ and vertical displacement δ_z were continuously recorded.
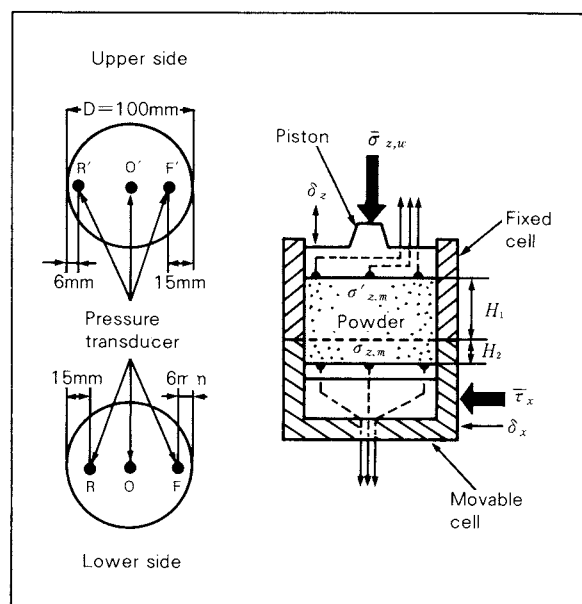

Fig. 1 Layout of pressure transducers in the vicinity of shearing plane

For the measurement of the tensile strength, a hanging-type cohesiveness tester[15] was utilized. This tester is a split-cell type that can provide vertical compression and horizontal tension. A movable cell is suspended by three phosphor bronze plates. The inside diameter of the cell measures 0.05 m. The tension velocity is 3.33 × 10^{-5} m/s. The tester is characterized by its advantage of permitting the determination of the relationship between tensile stress $\bar{\sigma}_x$ and horizontal displacement δ_x (this relationship is called tensile breakup process curve in what follows) of powder beds (coals).

The methods of direct shearing test and tensile breakup test have been reported elsewhere[13,15].

The fine coal samples used in this study have been obtained by sieving unpulverized coal into desired particle sizes ranging from 44 to 74 μm. **Table 1** lists the properties and fuel ratios of various coal samples used. The data in this table are based on JIS M8812. The fuel ratio indicates the ratio of fixed carbon to volatile matter. It is known to increase with coalification[16]. As coal can be classified by the fuel ratio, the kinds of coal used in this study are expressed in terms of the fuel ratio (*FR*). The fly ash samples used were fly ash A ($d_{w,50}$ = 13.6 μm, σ_g = 2.75), fly ash B ($d_{w,50}$ = 8.8 μm, σ_g = 2.35) and clinker ash. Fly ash A was obtained from Australian coal by combustion in

36

Table 1 Proximate analysis of coals

Coal	Moisture	Ash	Volatile matter	Fixed carbon	Fuel ratio
Japan A	5.5	16.4	44.1	34.0	0.77
Japan B	1.5	8.9	42.0	47.6	1.13
Australia	3.0	13.5	30.3	53.5	1.77
U.S.S.R. A	3.8	12.7	19.1	64.4	3.37
U.S.S.R. B	1.4	7.8	20.8	70.0	3.37
U.S.S.R. C	1.8	8.0	15.9	74.3	4.67
P.R.O.C. A	0.4	0.2	13.1	86.2	6.58
P.R.O.C. B	1.5	16.2	8.8	73.5	8.35
Vietnam	2.2	7.4	5.5	84.9	15.4

a boiler. Fly ash B and clinker ash were obtained likewise from fine Japanese coals A and B respectively. Clinker ash was used after sieving ($d_p = -44 \mu m$).

To adjust the water content in fine coals and powders, the samples were placed in a vertical cylindrical mixer[15] into which distilled water was added little by little and mixed homogeneously. The water content in the fly ash samples was adjusted by mixing regularly for 24 hours in a constant-temperature humidifier controlled at a specified humidity. The water content ϕ_v in these powders was calculated on the weight basis by drying the samples for an hour at 373-383K. The samples were collected from the cells after the tensile breakup and shearing tests. To avoid changes in the water content during the aging period after humidification, the wet fine powder samples adjusted at specified water contents were stored in a polyvinyl chloride vessel. The water content did not change during two weeks of aging period.

3. Results and Discussion

3. 1 Tensile strength, internal friction factor and shearing cohesiveness of powders

(1) Flowability of fine coal

Figure 2 shows an example of the relationship between the mean actual vertical stress $\bar\sigma_{z,m}$, the applied vertical stress $\bar\sigma_{z,w}$ and the stationary shearing stress $\bar\tau_{x,s}$. The actual vertical stress $\bar\sigma_{z,m}$ is the average of vertical stresses $\sigma_{z,m}$ (m = F, O, and R) measured at three points on the bottom of the powder bed (on the side of movable cell) (**Fig. 1**) after both the shearing stress $\bar\tau_x$ and vertical displacement

δ_z become stationary[12,13]. In the case of relatively small vertical load as used in this study, a flow surface of Roscoe's diagram is usually observed and powder yield locus is obtained[17,18].

As can be seen from **Fig. 2**, the $\bar\sigma_{z,w} - \bar\tau_{x,s}$ relation is convex and deviates from Coulomb's law. $\bar C_w$ in the figure is a shearing cohesiveness defined by Eq. (1)[19]:

$$(\bar\tau_{x,s}/\bar C_w)^n = 1 + \bar\sigma_{z,w}/\bar\sigma_{x,T} \qquad (1)$$

The values of $\bar\tau_{x,s}$ and $\bar\sigma_{x,T}$, respectively, should be read from the $\bar\tau_{x,s} - \bar\sigma_{z,w}$ and $\bar\sigma_{x,T} - \bar\epsilon_0$ relations for the same initial void fraction $\bar\epsilon_0$[20]. On the other hand, the $\bar\sigma_{z,m} - \bar\tau_{x,s}$ relation is linear, and Coulomb's law holds. Therefore, the internal friction factor $\mu_{m,s}$ and shearing cohesiveness $\bar C_m$ can be obtained from Eq. (2):

$$\bar\tau_{x,s} = \mu_{m,s} \cdot \bar\sigma_{z,m} + \bar C_m \qquad (2)$$

The value of $\bar\sigma_{x,E}$ in **Fig. 2**, which corresponds to a tensile strength, is obtained by extrapolating the line of Eq. (2) to $\bar\tau_{x,s} = 0$. It has been experimentally confirmed that the internal friction factor $\mu_{m,s}$, calculated by Eq. (2), is not influenced by the measurement condi-
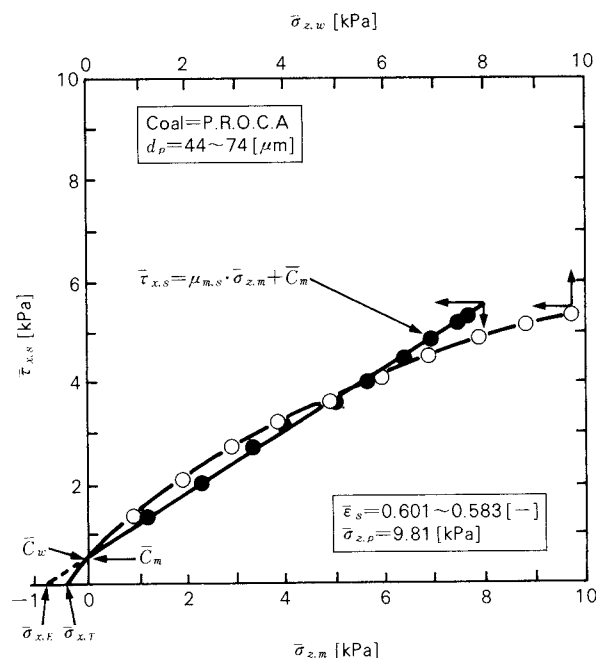

Fig. 2 Relationship between mean values of actual normal stress $\bar\sigma_{z,m}$ and stationary shearing stress $\bar\tau_{x,s}$, and between applied normal stress $\bar\sigma_{z,w}$ and $\bar\tau_{x,s}$

tions$^{12,13)}$. This implies that $\bar{C}_m$ as well as $\bar{\sigma}_{z,E}$ are also not influenced by the diameter of shearing cell and the height of powder bed in the cell. Furthermore, **Figure 2** also shows that the mean actual vertical stress $\bar{\sigma}_{z,m}$ is smaller than $\bar{\sigma}_{z,w}$, when the applied vertical stress $\bar{\sigma}_{z,w}$ $\geq$ 6 kPa. This indicates that the load applied onto the upper surface of the powder bed is not totally transmitted to the vicinity of shearing plane and a part of it is supported by the cell wall.

Figure 3 shows the ratio of the mean actual vertical stress $\bar{\sigma}_{z,m}$ to the applied vertical stress $\bar{\sigma}_{z,w}$ in relation to the fuel ratio FR of the coal under a specific measurement condition, for an example. It can be seen that the ratio, $\bar{\sigma}_{z,m}$ / $\bar{\sigma}_{z,w}$, decreases with an increase in FR and reaches a minimum at FR = 6.5 and then increases with an increase in FR ($>$ 6.5). This means that the applied vertical stress is well transmitted to the vicinity of the shearing plane of brown coal (Japan A) and anthracite (Vietnam) but only poorly transmitted for semibituminous coal (China A). Such a difference in the transmission of stress by the fuel ratio (the degree of coalification) suggests the importance of the kind of coal in designing and operation of a combustion installation.

Figure 4 shows the relations between the internal friction factor $\mu_{m,s}$, shearing cohesiveness $\bar{C}_m$ and the tensile strength $\bar{\sigma}_{x,E}$ for various fine coal samples as calculated by Eq. (2). The shearing cohesiveness and tensile strength are found to decrease with a decrease in the internal friction factor. Low values of these dynamic parameters mean a high flowability, as judged from actual experiences of handling fine coals. This is consistent with the evaluation based on the flow rate of fine coals through a cone hopper.

The internal friction factor $\mu_{m,s}$ and shearing cohesiveness $\bar{C}_m$ (shown in **Fig. 4**) are plotted against the fuel ratio in **Fig. 5**. It can be seen that the flowability of brown coal (Japan A) and anthracite (Vietnam) is highest, that of semibituminous coal (China A) lowest, and those of the others in between. Comparing the data in **Fig. 5** with those in **Fig. 3**, one can easily understand that a high flowability of fine coal corresponds to a high transmittancy of the applied vertical stress to the vicinity of shearing plane. This fact also applies to other fine

powders$^{13)}$. The increase in the internal friction factor $\mu_{m,s}$ with an increase in FR at $FR <$ 6.5 may be due to an increase in the content of fixed carbon. At $FR > 6.5$, $\mu_{m,s}$ decreases because of a decrease in the content of volatile matter. Phenomenologically, a maximum of
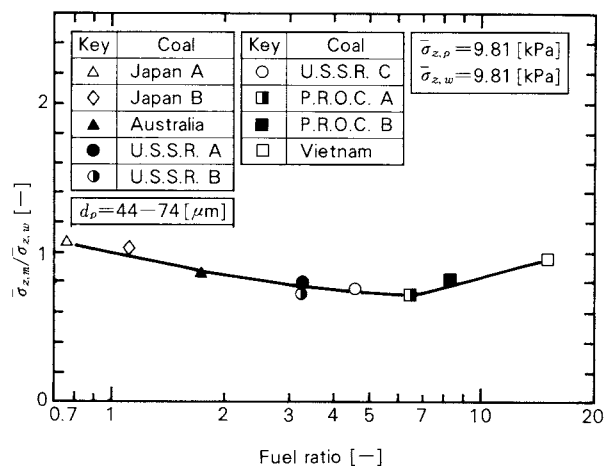

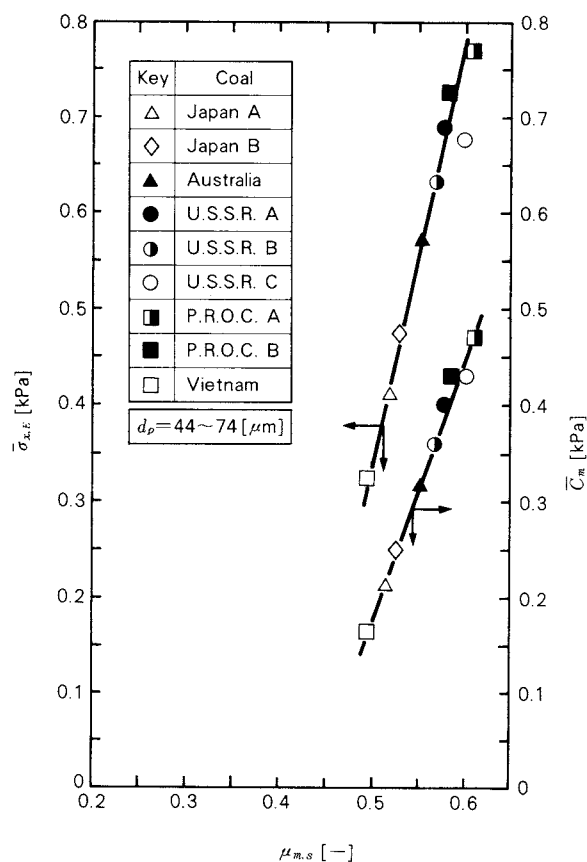Fig. 3 Relationship between transmission of the applied normal stress and fuel ratio

Fig. 4 Internal friction factor $\mu_{m,s}$, cohesion force $\bar{C}_m$ and tensile strength $\bar{\sigma}_{x,E}$ for several kinds of fine coals
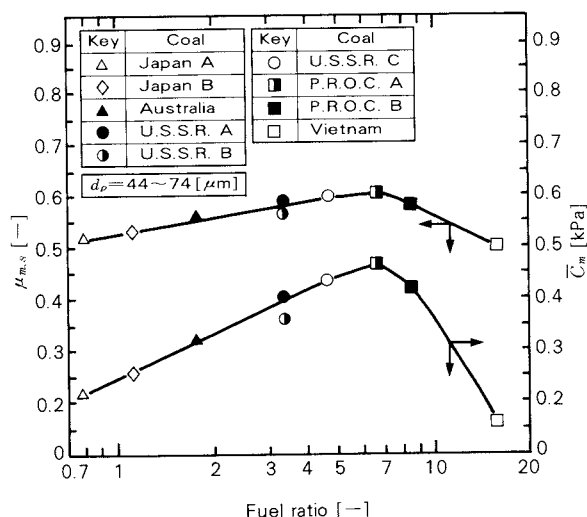
38

Fig. 5 Relationship among internal friction factor $\mu_{m,s}$, cohesion force $\overline{C}_m$ and fuel ratio of fine coals

internal friction factor at a certain fuel ratio (degree of coalification) may correspond to many physicochemical changes in coal particles such as porosity and surface area during coalification at the degree of which is 85 to 95[16]. It has been noted that the parameters n (shear index) and $\overline{C}_w$, derived from Eq. (1), cannot be well correlated with the fuel ratio.

Figure 6 shows an example of the tensile breakup test results of fine coals. The tensile strength $\overline{\sigma}_{x,T}$ is plotted against the fuel ratio in this figure. The tensile strength increases with an increase in FR at $FR \leq 6.5$, but decreases with $FR > 6.5$. The pattern of $\overline{\sigma}_{x,T} - FR$ relation, as shown in **Fig. 6**, has not changed even if the range of initial void fraction $\overline{\epsilon}_0$ is
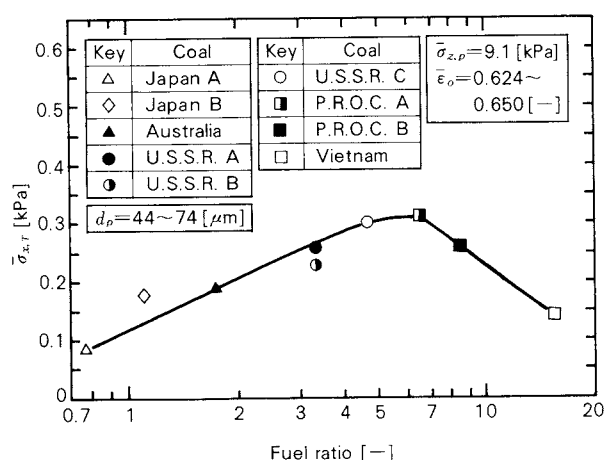

Fig. 6 Relationship between tensile strength $\overline{\sigma}_{x,T}$ and fuel ratio of fine coals

varied. The flowability evaluation of fine coals on the basis of their tensile strengths will give substantially the same results as the evaluation based on their internal friction factors and shearing cohesivenesses (**Fig. 5**).

When the internal friction factor $\mu_{m,s}$ and tensile strength $\overline{\sigma}_{x,T}$ were plotted against the carbon content or volatile matter, the data were rather scattered. This suggests an importance of taking not only the kind of coal but also the fuel ratio (degree of coalification) into considerations on transportation, storage, supply and handling of fine coals.

(2) Flowability of fly ash

Combustion of fine coal produces approximately 20% fly ash. It is, therefore, important to evaluate also the dynamic characteristics of fly ash in combustion processes of coal.

Figure 7 shows an example of the direct shearing test results of fly ash. Coulomb's law applies to both the $\overline{\sigma}_{z,m} - \overline{\tau}_{x,s}$ relation and the $\overline{\sigma}_{z,w} - \overline{\tau}_{x,s}$ relation. There is also no significant difference between them. The applied vertical stress $\overline{\sigma}_{z,w}$ is transmitted totally to the vicinity of shearing plane. The same results were also obtained for fly ash B and clinker. The vertical stress distribution in the vicinity of shearing plane was confirmed to be less uneven in fly ash than in any fine coal samples.

Table 2 summarizes the internal friction factor $\mu_{m,s}$, shearing cohesiveness $\overline{C}_m$ and tensile strength $\overline{\sigma}_{x,E}$ of fly ashes (A and B) and clinker. These parameters are all lower than those of fine coals. Therefore, fly ash is considered to be more flowable than fine coal. The lower values of internal friction factor and tensile strength for fly ashes than for fine coals may be attributed to the loss of fixed carbon and volatile matter, and the sphericity of fly ash particles resulting from high-temperature combustion.

Figure 8 compares $\mu_{m,s}$, $\overline{C}_m$, and $\overline{\sigma}_{x,E}$ of fly ashes together with those of various other powders[14]. The internal friction factor and shearing cohesiveness of fly ashes A and B are approximately intermediate between those of talc and magnesium stearate (both are lubricants). This fact implies a rather high flowability of fly ashes.
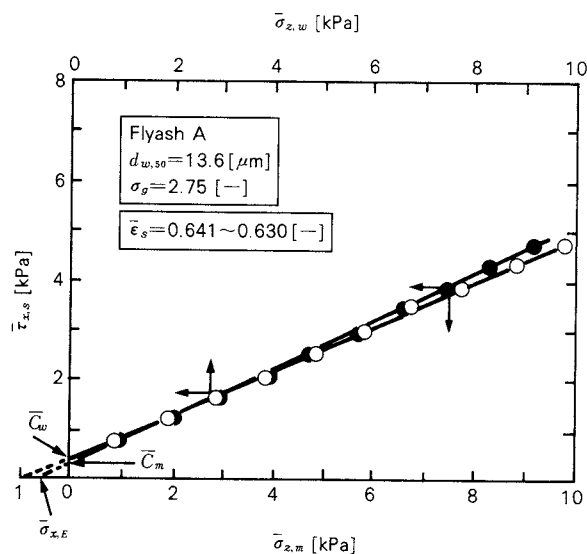
$\bar{\sigma}_{z,w}$ [kPa]

Flyash A
$d_{w,50}=13.6\,[\mu m]$
$\sigma_g=2.75\,[-]$
$\bar{\epsilon}_s=0.641\sim0.630\,[-]$

Fig. 7 Result of direct shear test for fly ash

Table 2 Comparison of $\mu_{m,s}$, $\bar{C}_m$ and $\bar{\sigma}_{x,E}$ of fly ash and those of fine coal

Coal, Ash	$\mu_{m,s}$ [-]	$\bar{C}_m$ [kPa]	$\bar{\sigma}_{x,E}$ [kPa]
Australia	0.56	0.32	0.57
Fly ash A	0.47	0.24	0.52
Japan A	0.58	0.33	0.57
Japan B	0.52	0.42	0.81
Clinker	0.45	$\doteqdot 0$	$\doteqdot 0$
Fly ash B	0.37	0.15	0.39

3. 2 Tensile strength, internal friction factor and shearing cohesiveness of wet fine coals

(1) Breakup process curve and packing characteristics of wet fine coals

Figure 9 shows an example of the tensile breakup process curves of wet fine coals with various water contents ϕ_v and initial void fraction $\bar{\epsilon}_0$. When the water content ϕ_v is low, a distinct disrupture of the coal bed occurs at a maximum tensile stress $\bar{\sigma}_{x,T}$. The tensile stress $\bar{\sigma}_x$ is then rapidly reduced. However, as the water content ϕ_v increases, $\bar{\sigma}_x$ gradually decreases without a distinct point of disrupture even after a maximum tensile stress. This is due to the effect of elongation of liquid bridges. Such a pattern of disrupture in relation to the water content was also observed in Japanese coal A and Toyoura sand[15]. Defining the maximum point of tensile stress $\bar{\sigma}_x$ as tensile strength $\bar{\sigma}_{x,T}$, the horizontal displacement at which $\bar{\sigma}_{x,T}$ be obtained is defined as breakup displacement $\delta_{x,T}$. As shown in **Fig. 9**, the tensile strength $\bar{\sigma}_{x,T}$ and the breakup displacement $\delta_{x,T}$ increase with an increase in the water content. Namely, the particle cohesiveness increases with an increase in the water content. However, when $\phi_v \geq 42\%$, the tensile strength decreases despite an increase in the
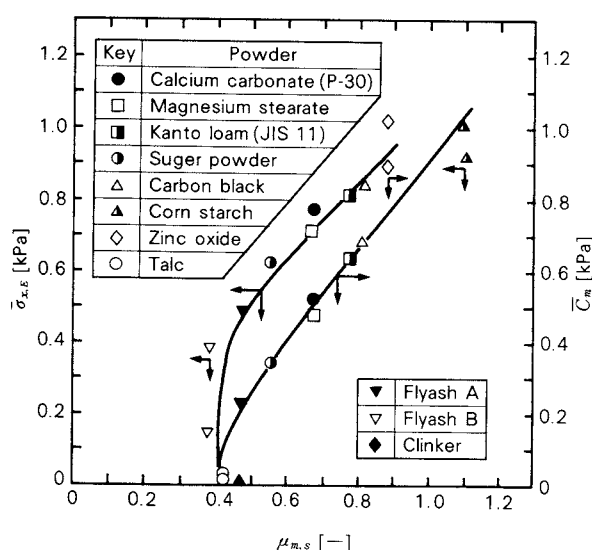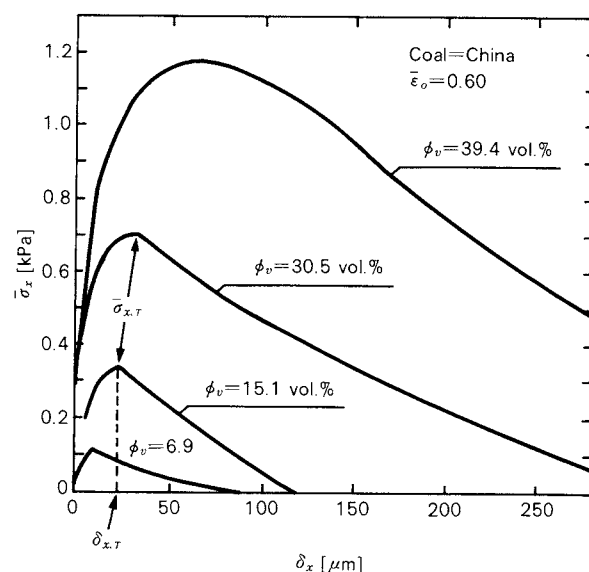

Fig. 8 Comparison of $\mu_{m,s}$, $\bar{C}_m$ and $\bar{\sigma}_{x,E}$ of fly ash and those of fine powders

Fig. 9 Tensile breakup process curves (the relation of tensile stress $\bar{\sigma}_x$ versus horizontal displacement δ_x)

breakup displacement (this point will be discussed later).

As the initial void fraction $\bar{\epsilon}_0$ was decreased with a constant water content, the point of disrupture of the coal bed became more sharp and the tensile strength increased. However, the breakup displacement $\delta_{x,T}$ was not affected by the void fraction.

Figure 10 shows the relation between the breakup displacement $\delta_{x,T}$ and water content ϕ_v. The data of Toyoura sand (d_p = 105 ~ 305 μm) and polyvinyl chloride (d_p = 63 ~ 177 μm) are also shown together for comparison[15]. The breakup displacement measured 15 to 20 times in the tensile breakup tests is expressed in terms of the mean value. From the relation between the breakup displacement and water content, the packing characteristics of powder-liquid system for wet Toyoura sand have been divided into a pendular zone ($\phi_v \leq$ 8%), in which the breakup displacement $\delta_{x,T}$ increases with an increase in ϕ_v, and a comixture of funicular and capillary zones in which the breakup displacement increases rapidly after passing through the funicular zone (8 < ϕ_v < 26%) where the breakup displacement

remains almost constant[15]. These zones have been clearly observed also for wet polyvinyl chloride powder. On the contrary, in case of wet fine coals, the funicular zone where the water phase forms a continuum within the coal bed is ambiguous. However, for the both coal samples, the pendular zone can be identified as ϕ_v < 10%. For Chinese coal A, the range of 10 < ϕ_v < 35% seems to correspond to the funicular zone. For Japanese coal, the range of 10 < ϕ_v < 20% may be identified as the funicular zone. Water contents exceeding these values may be regarded as a mixed region of the funicular and capillary zones. The difficulty in determining the packing characteristics of wet coal systems, as compared to other powders like Toyoura sand, is probably due to penetration of the added water into porous coal particles.

(2) Tensile strengths of fine coal and fly ash in a wet state

Figure 11 shows an example of the tensile strength of wet fine coals with various water contents ϕ_v and initial void fractions $\bar{\epsilon}_0$. The tensile strengths of wet fine coal beds with the water content $\phi_v \leq$ 6.5, are too small to be measured and shown in this figure, since almost all the water added penetrates into coal particles. At the water contents below 6.5%, the flowability of fine coals seems to be little affected by the water content. At ϕ_v = 6.5, adsorption of water on the particle surface induces formation of liquid bridge to result in a rapid increase in the tensile strength with an increase in the water content due to bridge-induced adhesion of particles (pendular zone, $\phi_v \leq$ 9.5). When 11.1 < ϕ_v < 21%, the tensile strength increases (funicular zone), because liquid bridge formation is further enhanced by an increased water content. With a further increase in the water content, the tensile strength is saturated (comixture of the funicular and capillary zones), because the water content exceeds the limit at which coal particles no longer can hold liquid. At any ϕ_v, the tensile strength is high when the initial void fraction is low. This may be due to increased contact points of particles and fusion of liquid films.

On the basis of the data shown in **Fig. 11**, the tensile strengths at the same void fractions are plotted against the water content ϕ_v in
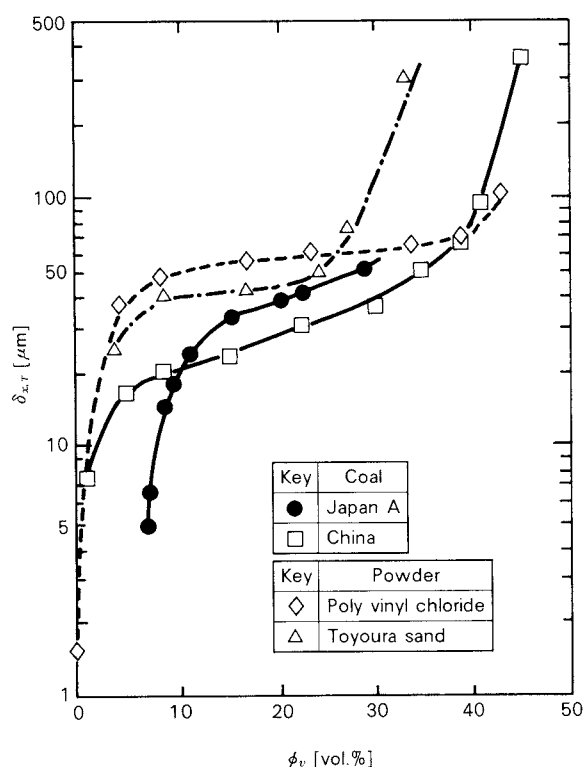

Key	Coal
●	Japan A
□	China

Key	Powder
◇	Poly vinyl chloride
△	Toyoura sand

Fig. 10 Relation of breakup displacement $\delta_{x,T}$ versus water content ϕ_v
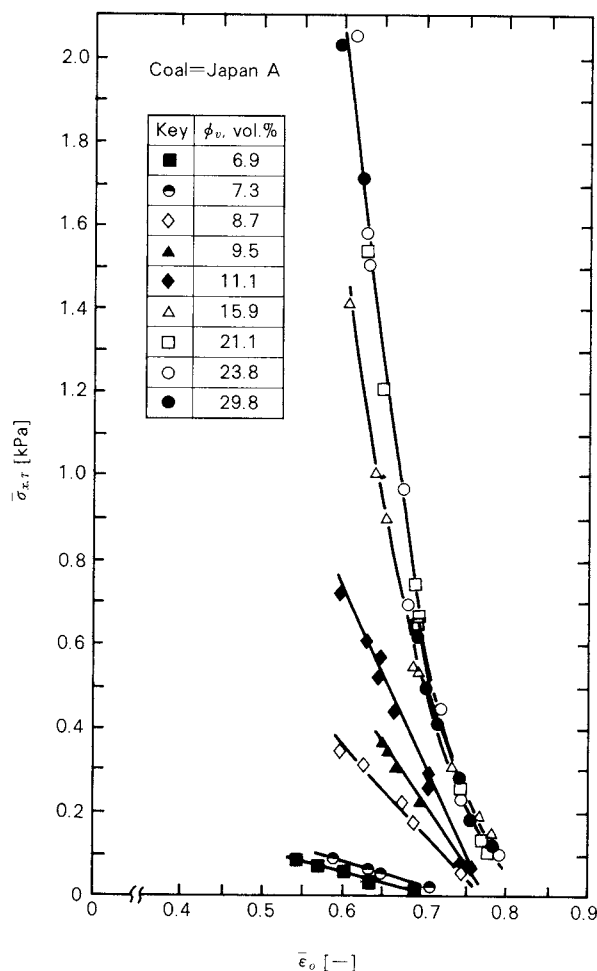
Fig. 11 Measured values of tensile strength $\bar{\sigma}_{x,T}$

Fig. 12 Relation of tensile strength $\bar{\sigma}_{x,T}$ versus water content ϕ_v

Fig. 12. The data of Toyoura sand and poly-vinyl chloride powder with different water contents are also shown together for comparison. As shown in **Fig. 12**, the tensile strength of Chinese coal A is found to get a larger increase at low ϕ_v (pendular zone). As ϕ_v increases, it continues to increase rather slowly and monotonically (funicular zone) and reaches a maximum at $\phi_v = 38\%$ (comixture of the funicular and capillary zones). A further increase in ϕ_v gives a decrease in the tensile strength, because the water content exceeds the limit at which coal particles can no longer hold the water added. The rate of increase in the tensile strength with ϕ_v is lower for Chinese coal A (semibituminous coal) than for Japanese coal A (brown coal). This may be attributable to a smaller inner surface area, smaller porosity (the ratio of capillaries and pores to total volume of particle)[16] and lower wettability of Chinese coal A. It can be noted that the flowability of
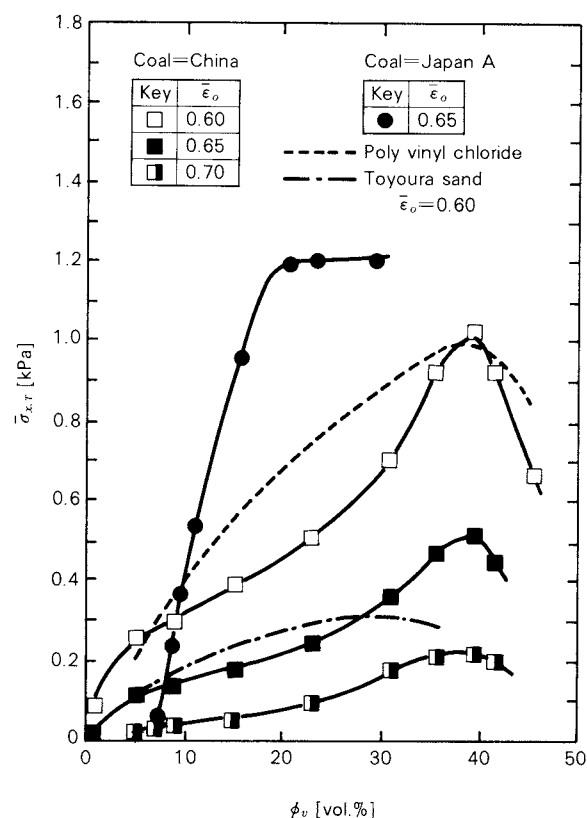
brown coals such as the sample used (Japan A) may be significantly influenced by a small change in water content. Therefore, in efficient handling of the coals with a low degree of coalification, a determination of the water content plays an important role.

Figure 13 gives an example of the effects of aging period (the elapsed time after addition of water) on the tensile strength—water content relations. When aged after addition of water, the tensile strength of wet fine coal in the pendular to funicular zones ($6.9 < \phi_v < 21\%$) is lowered. This may be due to the volume diminution of liquid bridge resulting from partial penetration of water into coal particles during the period of aging. Therefore, prolongation of aging period may improve the flowability of wet fine coals. This fact coincides with the phenomena that a higher flow rate in a cone hopper is obtained for the coals stored for a long time after addition of water[7]. This kind of improvement of the flowability has also been observed in green mold sands (silica-bentonite-water system)[21]. These findings
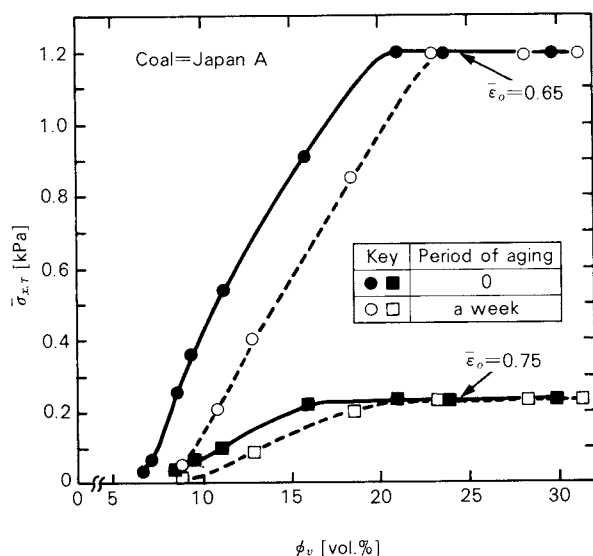
Fig. 13 Relation between tensile strength and water content after varying the period of aging (period after addition of water)

Fig. 14 Measured values of tensile strength of wet finel coal

verify that the flowability of fine coals is controlled by the water adsorbed onto the surface of coal particles.

Prolongation of the aging period of two weeks produced no difference in the results. The tensile strength of wet Chinese coal A was less affected by aging, because of its smaller inner surface area and porosity.

The measured values of tensile strength of wet fly ash and fine coal are shown in **Fig. 14**. Clinker ash gives the same value of tensile strength as its original material. On the other hand, the tensile strength of fly ash is less than that of fine coal at $\bar{\epsilon}_0 = 0.65$. The lower value of the tensile strength of wet fly ash compared to that of fine coal may be due to the disappearance of fixed carbon and volatile matter during high-temperature combustion and also to sphericity (surface smoothness) of ash particles, as previously described. From **Fig. 14**, the tensile strength of fly ash is found to increase with a very slight increase in the water content. This level of water content is within a range which is subject to be easily changed by the relative atmospheric humidity of 40 to 80%. This fact indicates that the flowability of fly ash is affected by climatic and seasonal humidity changes.

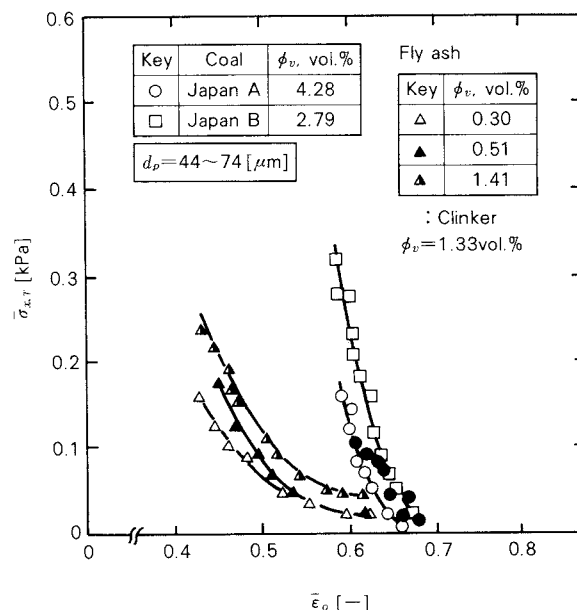(3) Internal friction factor and shearing cohesiveness of wet fine coals

Figure 15 shows the internal friction factor $\mu_{m,s}$ and shearing cohesiveness $\bar{C}_m$ in relation to the water content ϕ_v, as measured by the constant-load, direct shearing test. The internal friction factor of Japanese coal A remains constant when $\phi_v \leq 6.5$ and increases when $6.5 < \phi_v < 10\%$. At the water content exceeding this range, it again becomes constant after a slight decrease. On the other hand, the shearing cohesiveness is immeasurably small when $\phi_v \leq 6.5\%$, but increases with the water content over 6.5%. This indicates a reduction of the flowability by an increase in water content above 6.5%. This agrees with the flowability evaluation by actual experiences of handling wet fine coals. The same level of the internal friction factor and shearing cohesiveness of coals at ϕ_v of up to 6.5% as dry coals, coincides with the measurement results of dry coals described in subsection 3.2 (1). It has also been verified by the direct shear tests that Japanese coal A in a wet state has approximately the same flowability as dry coal when ϕ_v is 6.5% or below. **Figure 15** also shows that the internal friction factor of Chinese coal A increases monotonically with an increase in the water content, when the water content $0 < \phi_v < 15\%$. At $15 < \phi_v < 20\%$, the internal friction factor decreases. On the other hand, the shearing cohesiveness increases with an increase in the
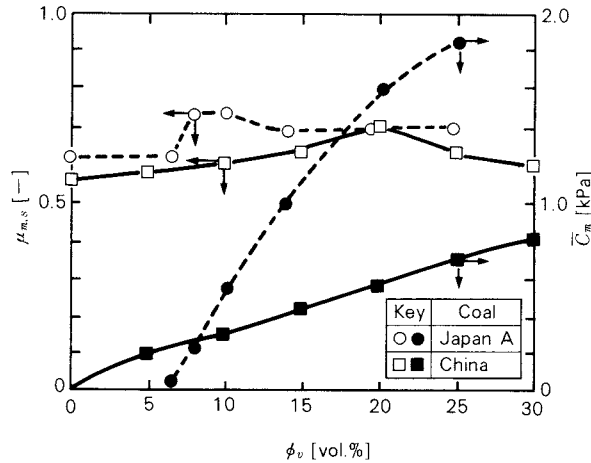
Fig. 15 Relations of internal friction factor $\mu_{m,s}$ and shearing force $\overline{C}_m$ versus water content

water content. This tendency is similar to the $\overline{\sigma}_{x,T} - \phi_v$ relation (**Fig. 12**). The ranking of the sample coals by their shearing cohesiveness does not conflict with that by their tensile strengths. No significant difference is also noted between $\overline{C}_m$ and $\overline{\sigma}_{x,T}$ themselves. These findings suggest that the flowability of fine coals in a wet state may be better evaluated by the shearing cohesiveness and tensile strength rather than by the internal friction factor.

4. Conclusion

Close correlations have been confirmed between the dynamic properties (internal friction factor, shearing cohesiveness and tensile strength) and fuel ratio of fine coals. The ranking of flowability of fine coals is in order of brown coal, bituminous coal and semibituminous coal. The flowability of semianthracite and anthracite is high. The flowability evaluation based on the dynamic parameters coincides with the empirical scoring of flowability based on the flow-rate from a hopper or on actual experiences of handling fine coals. Compared to fine coals, fly ash shows a higher flowability with lower values of both the internal friction factor and shearing cohesiveness.

The tensile strength of wet fine coals increases with an increase in the water content in the pendular to funicular zones, but becomes constant or shows a maximum in comixture of the funicular and capillary zones, and finally decreases with further increase in the water content. Brown coal, which has a

larger inner surface area and wettability shows a significantly larger increase of tensile strength with an increase in the water content, when compared to semibituminous coal. The flowability of wet fine coals can be better evaluated by the tensile strength and shearing cohesiveness rather than by the internal friction factor. Protraction of the aging period (time after addition of water) results in a higher flowability, because partial penetration of the added water into coal particles reduces the tensile strength. This indicates that the flowability is controlled by water adsorbed onto coal particles. The flowability of fly ash is easily affected by climatic and seasonal humidity changes.

Nomenclature

$\overline{C}_m$	: shearing cohesiveness, defined by Eq. (2) (**Fig. 2**)	[kPa]
$\overline{C}_w$	: shearing cohesiveness, defined by Eq. (1) (**Fig. 2**)	[kPa]
FR	: fuel ratio of coal	[—]
n	: shear index, defined by Eq. (1)	[—]
δ_x	: horizontal displacement of powder bed under tensile test	[μm]
$\delta_{x,T}$	: horizontal displacement at which tensile strength $\overline{\sigma}_{x,T}$ is obtained (**Fig. 9**)	[μm]
δ_z	: vertical displacement of powder bed under direct shear test	[μm]
$\overline{\epsilon}_0$	: initial void fraction of powder bed under tensile or shear test	[—]
ϕ_v	: volumetric water content in powder bed	[—]
$\mu_{m,s}$	: internal friction factor, defined by Eq. (2)	[—]
$\overline{\sigma}_x$	: horizontal or tensile stress in powder bed under tensile test	[kPa]
$\overline{\sigma}_{x,E}$	: tensile stress defined by Eq. (2) with $\overline{\tau}_{x,s} = 0$ (**Fig. 2**)	[kPa]
$\overline{\sigma}_{x,T}$	: tensile strength of powder bed (**Fig.9**)	[kPa]
$\sigma_{z,m}$	: vertical stress in the vicinity of shearing plane, measured at points, F, O, R (**Fig. 1**)	[kPa]
$\sigma_{z,m}'$	: vertical stress in the vicinity of shearing plane, measured at points F', O', R' (**Fig. 1**)	[kPa]
$\overline{\sigma}_{z,m}$	: mean vertical stress in the vicinity of shearing plane	[kPa]
$\overline{\sigma}_{z,w}$	: applied vertical stress to powder bed under direct shear test (**Fig. 1**)	[kPa]
$\overline{\tau}_x$	: shearing stress in powder bed under direct shear test	[kPa]
$\overline{\tau}_{x,s}$	: stationary shearing stress in powder bed under direct shear test	[kPa]

44

References

1) Tanaka, K., G. Hida and K. Imatani: *Sentan,* **12,** 366 (1962).
2) Honma, J., M. Yamamoto, H. Iwata and K. Masuda: *J. Fuel Soc., Japan,* **45,** 851 (1962).
3) Carr, J. F. and D. M. Walker: *Powder Technology,* **1,** 369 (1967/68).
4) Aoki, R. and H. Tsunakawa: *J. Soc. Materials Sci., Japan,* **18,** 497 (1967).
5) Jayasinghe, S. S. and N. Pilpel: *J. Inst. Fuels,* Feb., 51 (1970).
6) Shinohara, K. and T. Tanaka: *J. Chem. Eng., Japan,* **8,** 50 (1975).
7) Aoki, R. and S. Yasuda: *J. Soc. Powder Tech., Japan,* **14,** 390 (1977).
8) Arakawa, M.: *J. Soc. Materials Sci., Japan,* **30,** 878 (1981).
9) Aoki, R.: Preprint of the 48th Annual Meeting of Soc. Chem. Eng., Japan, p. 373 (1983).
10) Tsunakawa, H.: *J. Soc. Powder Tech., Japan,* **20,** 554 (1983).
11) Murata, H., M. Wakabayashi and T. Egusa: *ibid.,* **20,** 558 (1983).
12) Terashita, K., K. Miyanami, T. Yano and Y. Yamamoto: *ibid.,* **15,** 583 (1978).
13) Terashita, K., K. Miyanami, T. Yano and S. Iwasawa: *ibid.,* **17,** 373 (1980).
14) Terashita, K., K. Miyanami, M. Tanigawa and S. Iwasawa: *ibid.,* **18,** 896 (1981).
15) Terashita, K., K. Miyanami, T. Konishi and J. Yoshida: *J. Soc. Materials Sci., Japan,* **30,** 873 (1981).
16) Kimura, H. and S. Fujii: "Sekitan-Kagaku to Kogyo", p. 58, Kyoritsu Shuppan, Co. (1977).
17) Schwedes, J.: *Powder Technology,* **11,** 59 (1975).
18) Terashita, K., Y. Yamamoto, M. Tanigawa, K. Miyanami and T. Yano: *J. Soc. Materials Sci., Japan,* **29,** 876 (1980).
19) Ashton, D., C. Cheng, R. Farley and F.H. Valentin: *Rheological Acta,* **4,** 206 (1965).
20) Terashita, K., K. Miyanami, T. Konishi and K. Furubayashi: Preprint of the 14th Fall Meeting of Soc. Chem. Eng., Japan, p. 389 (1980).
21) Terashita, K., T. Kimura, E. Tsukaguchi and K. Miyanami: *J. Soc. Powder Tech., Japan,* **20,** 733 (1983).

Statistical Analysis of the Fatigue Failure Phenomenon of Powder Bed by Loading with Dynamic Repeated Tensile Stress[†]

Hidehiro Kamiya
*Department of Materials Science and Technology,
Nagoya Institute of Technology* *

Jun-ichiro Tsubaki and Genji Jimbo
*Department of Chemical Engineering,
Nagoya University* **

Abstract

To study more quantitatively the fatigue failure phenomenon of powder beds, which was earlier discovered and reported by a part of the authors, this study was an attempt to obtain the relation between repeated tensile stress and fatigue life, which is usually represented by S-N relation, in a wide range of the repeating number N. Experiments were carried out by using vibration to exert dynamic repeated tensile load on the powder bed, with a vertically vibrating cell and a horizontally splitting cell. The frequency of vibration used was in the region of 5–300 Hz, and Kanto loam powder (JIS-11), fused alumina powder and lactose powder were used as samples.

The results obtained are analyzed statistically and quantitatively concerning the distribution of fatigue failure life.

It is found that within the limited range of the number of repeated stress less than 10^6, the existence of a lower limit of tensile stress (endurance limit) where the powder bed fails is confirmed at a stress ratio of the order of 0.7. The distribution of fatigue life is expressed by a Weibull distribution, and then it is shown quantitatively that the distribution of fatigue life of the powder bed is wide compared with other kinds of material, and it is suggested that the S-N relation of the powder bed obtained previously can be divided into two ranges, a sloping part and a horizontal part.

1. Introduction

Mechanical properties of fine-powder bed have been investigated primarily by means of static failure tests for tensile and shear. In practical operations, however, there are specific phenomena which are difficult to be verified by use of such knowledge.

Consider, for instance, repeated application of impact stress perpendicularly to a dust layer deposited on a fabric filter. A part of the authors observed that the dust layer was allowed to be dislodged by the repeated application of relatively small impact stress that was insufficient enough to cause the dislodgement by only one trial. This fact could not be explained by an existing static model only based on a cohesion and separation force[7].

To solve the above problem, the authors introduced a concept of "fatigue failure" as a fundamental mechanical property of powder bed into a study on the dislodgement caused by a shear-directional repeated stress[2]. This study provided the fact that the shape of *S-N* relation curves, which were used to express fatigue failure phenomenon, would be depend-

ent on stress direction: vertical or shear direction.

Based on such a observation, a part of the authors started a preliminary study on the application of quasi-static repeated tensile stress to powder bed[5]. It was ascertained from this study using a simplified test apparatus that a fatigue failure could take place in powder bed.

The object of the present report, continued from the last report[6], is to relate the stress with the repeat number of applied stress required to cause split of powder bed so as to analyze more quantitatively fatigue failure phenomenon. In the present work, vibration techniques were used to obtain larger repeated number of stress application during a unit time. Such a test implies the extention to the treatment of fatigue failure under dynamic conditions. The obtained result will be discussed in such a way as that of material science and also a statistical analysis of fatigue life distribution, and this phenomenon will be considered quantitatively.

2. Experimental apparatus and methods

Two kinds of vibration (high and low frequency) were adopted to apply repeated tensile stress to powder bed. High frequency vibration was used for the case where the split of powder bed needed many repeated times of stress application; while low frequency vibration was done for few repeated times.

2. 1 Repeated application of high frequency vibration (Experiment I)

This experiment was carried out to break off an exposed part of sample material in a cell by applying repeatedly tensile stress caused by a vertical vibration. The apparatus and the cell used in this experiment are schematically illustrated in **Fig. 1 (a)**. The cell, made of stainless steel with diameters of 25.2 mm (inside) and 30 mm (outside), and a depth of 32 mm, was mounted on an electromagnetic vibrator (Node, VT-10) with the continuously controlled range of 5 to 50000 Hz.

The test cell ① and a split-type frame ② were fixed by using a ring ③ as shown in **Fig. 1 (b)**. A sample powder was fed into this test cell with a spatular and was consolidated with a weight as shown in **Fig. 1 (c)**. In this case, each
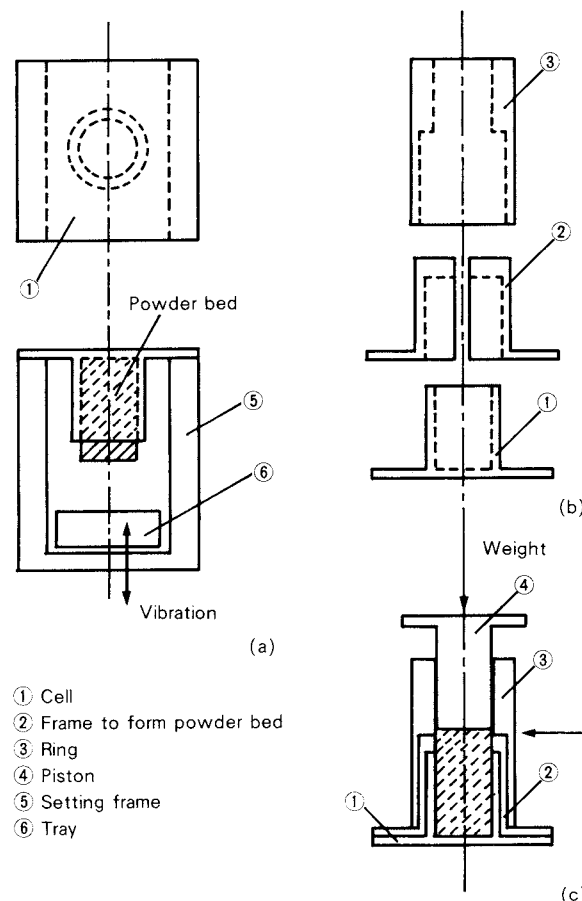

Fig. 1 (a) Schema of apparatus with vertically vibrating cell to load repeated stress on powder bed

(b) Schema of sections to form powder bed

(c) Assemblage of sections to form powder bed

height of a powder bed was adjusted to be by 1 mm higher than the frame depth after preconsolidation. After this consolidation was made for 10 minutes, the weight, the piston ④, and the ring ③ were removed. Then the powder bed was cut off at the top of the frame ②, and finally the frame ② was removed to complete forming of the test sample.

The experiment was carried out in the following procedure. First, the high-frequency vibration was applied increasingly until the set value of acceleration was achieved. Then this vibration was applied continuously in a constant magnitude until the exposing part of the powder bed was fallen on the tray ⑥. At that time, the period from the start of the constant vibration to fall of the powder bed was counted as an effectively operated time, and its mass in the tray ⑥ was weighed. The vibratory acceleration was measured by a pick-up (EMIC

Piezoelectric type, Model 541-AT) mounted perpendicularly on the cell.

In this experiment, pre-consolidation stress and vibration frequency were varied. The former was limited within 11.4 and 41.3 kPa because too little pre-consolidation stress could not keep the powder bed from dropping off out of the cell. For the latter, 70, 100, and 300 Hz were adopted because the acceleration ratio of vertical direction to horizontal one was less than 5 percent that was measured by the pick-up mounted on the upper part of the cell side. The time required to reach the set value was a few seconds by adjusting the rise-up time to be constant. Since this method made use of high-frequency vibration, the time required was very short when the failure took place in a few repeated times. This does not tend to give exact time which would be required to cause failure. Therefore the iterative loading by low-frequency vibration is required. As this method, however, acceleration large enough to cause failure was not able to be obtained due to the limited amplitude of vibrator, the authors used the following low-frequency vibratory tester to achieve an expected object.

2. 2 Application of iterative loading by low-frequency vibration (Experiment II)

A hunger-type cohesion tester was used as a test equipment for this experiment. As shown in **Fig. 2**, the movable cell of this tester was connected with a vibrator to exert iterative stress on a powder bed in the cell by a low-frequency vibration.

The sample powder was packed by a spatura into the split cell with a inside diameter of 50 mm an a depth of 20 mm. The powder bed was formed by cutting off the over-flowing material after 10 minutes pre-consolidation. The experiment was made in the following procedure. First, the vibration was started to apply on the movable cell which was kept fixed by a clamp. Then, when the magnitude of vibration was increased gradually and reached the set value, the fix was released. After the stress was applied repeatedly, failure of the powder bed was observed to take place. At that time, the period from release of the hook to failure of the powder bed was measured.

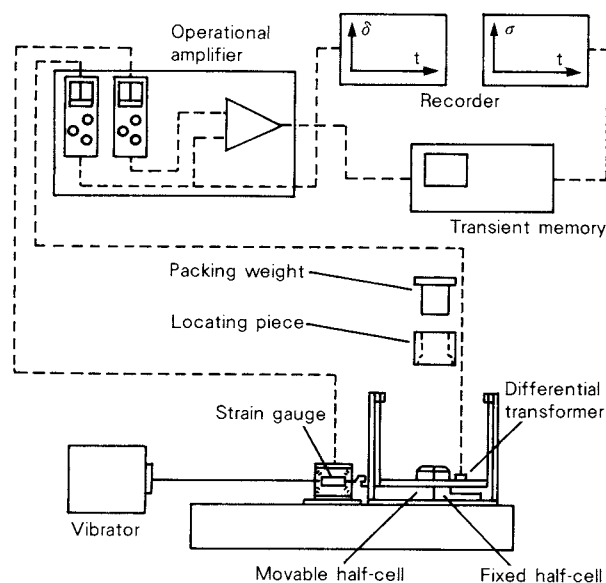**Table 1** shows the average particle diameter, true density, and porosity of the fracture sur-

Fig. 2 Schema of apparatus with horizontally splitting cell to load repeated tensile stress of powder bed by using vibration

Table 1 Sample

Sample	d_p [μm]	$\rho_p \times 10^{-3}$ [kg/m^3]	ϵ [−]
Kanto loam (JIS-11)	2.0	3.0	0.720~0.770
Fused alumina	1.7	3.9	0.675~0.710
Lactose	46.9	1.53	0.510, 0.545

face of the three kinds of sample materials used. In this experiment, the pre-consolidation pressure varied from 4.0 to 21.5 kPa and the vibration frequency was 5 and 20 Hz. Although displacement of the powder bed could not be obtained in the experiment I. This value was obtainable in this experiment, by using a differential transducer.

3. Experimental result

As is well known in the field of material science, fatigue failure phenomenon of solid materials have been investigated by using S-N relations; S and N represent an applied stress and its application frequency (hereinafter referred to as "life"), respectively.

In the present work, this S-N relation was introduced by taking the maximum value of stress σ_s as a representative one in the experiment I and II. The value of σ_s in the experiment I is given by

$$\sigma_s = \frac{m_f(\alpha_0 \omega^2 + g)}{A} \qquad (1)$$

where m_f is the mass of a sample material falling on the tray, α_0 the amplitude of vibration, ω the angular frequency, and A the cross-sectional area of fracture surface. Also, N_b is the repeat time of applied vibration.

Figure 3 shows a typical result of the *S-N* relations of Kanto Loam (JIS No. 11) of which data were abundantly obtainable. The values at $N = 10°$ denote average ones of static tensile strength at various porosities determined by a hunger-type cohesion tester. As indicated clearly in this figure, the fatigue strength increased as the porosity decreased, that is, the static strength increased. The effects due to the difference in the type of apparatus, the cell shape, and the vibration frequency in the experiment I and II could not been observed obviously. These tendencies were similar in other sample materials used. Thus, the following discussion will take into no account of these factors.

In **Fig. 4**, all the results obtained in the present experiments are indicated in the term of dimensionless value that represents the ratio of actual stress to average static tensile strength $\bar{\sigma}_z$. The use of this stress ratio, independent of the magnitude of static strength, would permit the *S-N* relation to be more distinguished. In

this figure, the data where no failure was observed (represented by the symbol —O—) are found to exist at N_b of more than 3×10^4. Also, when the stress ratio was less than 0.7, there was no failure at N_b of less than 10^6. This implies that there would be a minimum stress, so-called endurance limit, below which there is no possibility to cause a fatigue failure. When the stress ratio was more than a unit, on the other hand, a fatigue failure took place. This phenomenon should be noticed as one of the dynamic characteristics because it could not be seen in a static test.

4. Statistical analysis on phenomenon of fatigue failure

Wide variation of data shown in **Fig. 4** implies that there could be fatigue failure life distribution according to certain stress ratios. To bring out more distinct relations, the authors tried to analyze statistically the stress ratio distribution of **Fig. 4**, as follows.

4. 1 Procedure of statistical analysis

The statistical analysis was carried out, based on the following method: Standard Method of Statistical Fatigue Testing (JSME-S-002-1981)[4]:
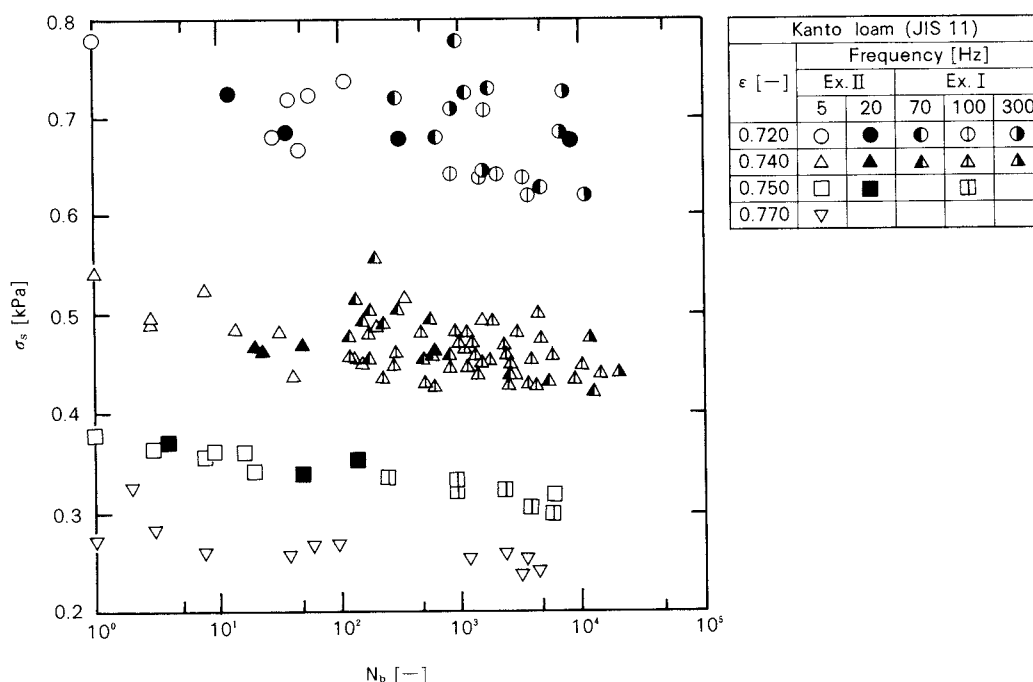

Kanto loam (JIS 11)				
ε [−]	Frequency [Hz]			
	Ex. II		Ex. I	
	5	20	70	100	300
0.720	○	●	◑	⬤	◕
0.740	△	▲	▲	△	▲
0.750	□	■		⊞	
0.770	▽				

Fig. 3 An example of *S-N* relation

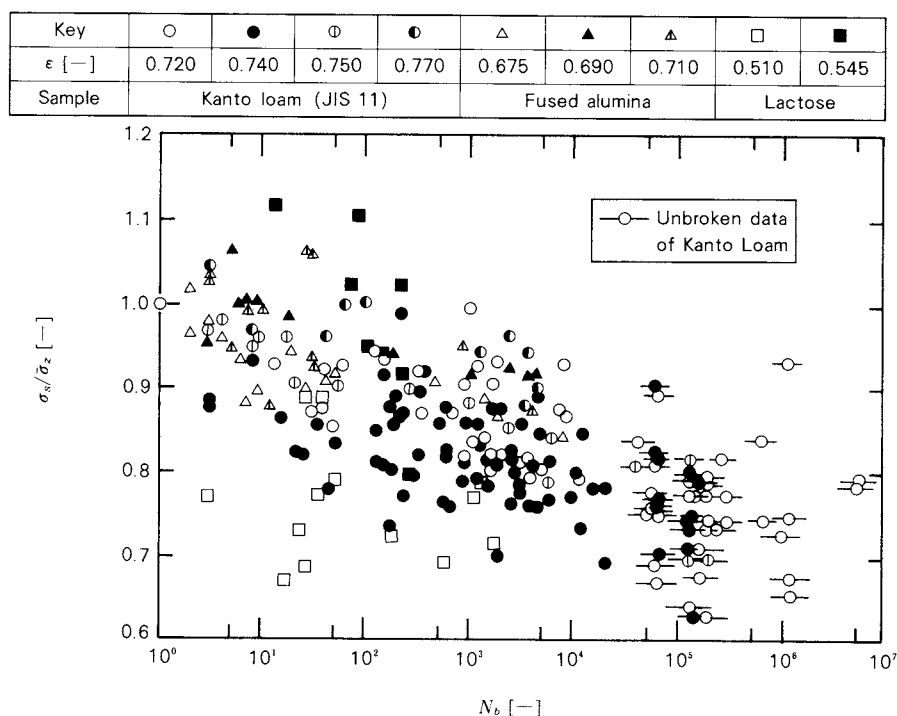| Key	○	●	⊕	◐	△	▲	▲	□	■
ε [−]	0.720	0.740	0.750	0.770	0.675	0.690	0.710	0.510	0.545
Sample	Kanto loam (JIS 11)				Fused alumina			Lactose	

Fig. 4 Relation between stress ratio and fatigue life (S-N relation)

1) Data of the stress ratio were classified into 2 to 7 segments containing same numbers of data in each experimental condition.

2) Order of small to large number was adjusted for each segment to arrange as a serial statistical value.

3) Median rank was used to obtain a mortal probability corresponding to each serial number, that is, the portion of powder bed broken under its own life, because the distribution shape of population was unknown.

In the present work, analysis was carried out by including data on survivalship.

Fatigue life distributions obtained by the above method could be the most successfully arranged by the cumulative Weibull-distribution function of two population parameters expressed as

$$P(N) = 1 - \exp\left\{-\left(\frac{N}{N_c}\right)^m\right\} \qquad (2)$$

or written by the probability-density function:

$$p(N) = \left(\frac{1}{N_c}\right)^m m\, N^{m-1} \exp\left\{-\left(\frac{N}{N_c}\right)^m\right\} \qquad (3)$$

where N_c is the characteristic fatigue life in Weibull-distribution function at the failure probability of 63.2 percent. The value of m, so-called sharp parameter, characterizes the variation of fatigue lives and is expressed as the slope on the Weibull-probability graph.

4. 2 Result of statistical analysis

The data on Kanto Loam (JIS No. 11) with a porosity of 0.740 were most abundantly obtainable in the present work. The result of analyzing statistical fatigue failure life distribution of these data is expressed by Weibull distribution in **Fig. 5**, where the range of the stress ratio is also attached. The solid line represents a least square approximation of mortal probability obtained from a failure life and a median rank, while the one-point-dashed and broken lines denotes the limits of 90 percent in confidence.

Figure 6 shows the measured result of fused almina (W.A. #8000) with a porosity of 0.675 whose data were also much obtained. As seen in this figure, the characteristic fatigue life in Weibull-distribution function, N_c, would be much dependent on the region of the stress ratio and also the shape parameter in Weibull-
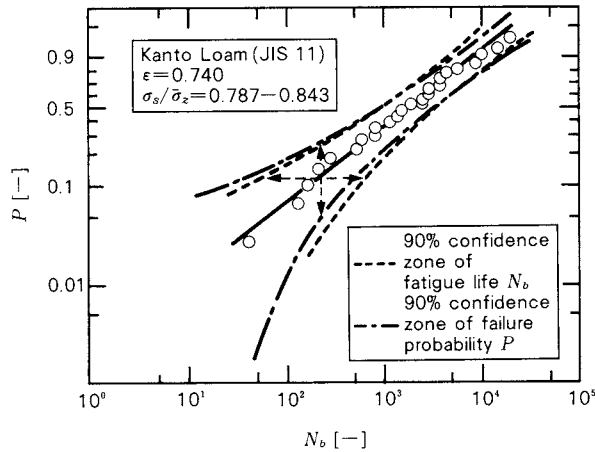
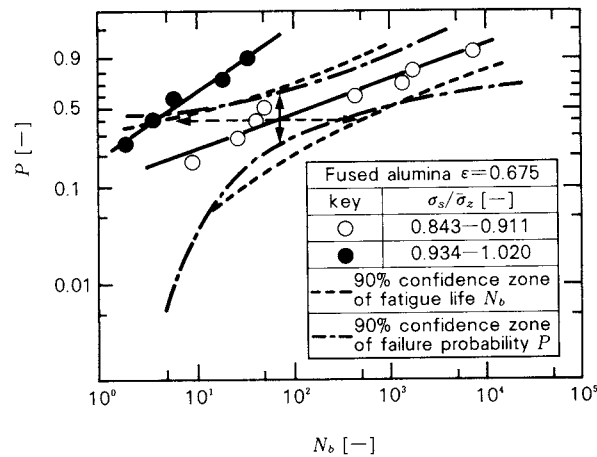Fig. 5 Fatigue life distribution of Kanto Loam powder (JIS-11) expressed by Weibull distribution

Fig. 6 Fatigue life distribution of fused alumina powder expressed by Weibull distribution

Fig. 7 Estimates of the characteristic fatigue lives in Weibull distribution

Key	O	●	◐	◑	△	▲	◮	□	■
ε [—]	0.720	0.740	0.750	0.770	0.675	0.690	0.710	0.510	0.545
Sample	Kanto Loam (JIS 11)				Fused alumina			Lactose	
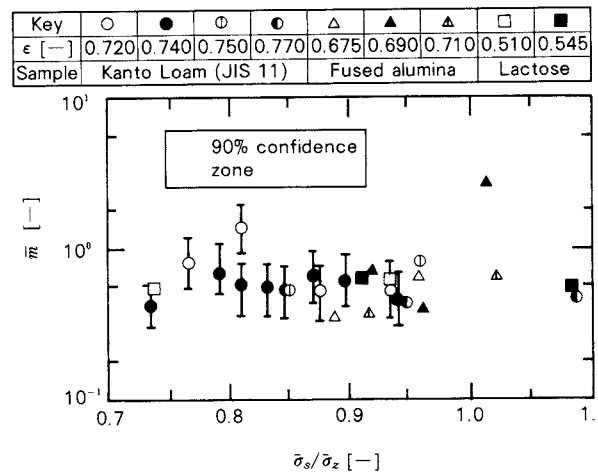
Fig. 8 Estimates of the shape parameters in Weibull distribution

distribution function, m, which characterizes the spread of the distributions. Similar results were obtainable on lactose powder, through they are not indicated in the present paper.

In **Figs. 7** and **8**, the mean values of the characteristic life N_c and the shape parameter m are indicated as a function of the mean value of stress ratio $\bar{\sigma}_s / \bar{\sigma}_z$. These data are all that were gained in the present work within the confidence zone of 90 percent. The value of $\overline{N}_c$ is found to decrease with increasing the stress ratio in **Fig. 7**. In particular, the data of Kanto Loam (JIS No. 11) with a porosity of 0.72 and 0.74, which were abundantly obtainable in the present work, can be devided into two regions: one has a steep slope within the stress ratio of 0.7 to 0.85 and the other has a gentle slope at the ratio of larger than 0.85. Such a tendency

is supported by the 90 percent confidence zone. Thus, this implies that the present analysis used the number of data enough to estimate qualitative variations in N_c.

It is also considered that the position and

sharpness of S-N curves depend on experimental conditions, because estimates of other data which were scantily obtainable distant from the hard line in **Fig. 7**.

On the other hand, the shape parameter m was almost constant, independently of the stress ratio, as shown in **Fig. 8**. Therefore, the shape of fatigue-life distribution would be almost unchangeable within the conditions adopted in the present work.

The above statistical analysis could lead to a significant result: two slopes representing different tendencies of decreasing N_c. This suggests that fatigue failure phenomenon could be classified into two regions.

5. Discussion

As illustrated in **Fig. 7**, it is shown that the characteristic life N_c decreased rapidly below a certain value as the stress ratio was reduced. This is probably because of not only increase of the failure life but also increase of the survival possibility without failure of powder bed, accompanied by a decrease of the stress under the present test condition.

To demonstrate the relationship between such a survivalship phenomenon and the difference of the slopes indicated in **Fig. 7**, consider **Fig. 9** that shows a mortal probability obtained from the present work. The value of $P_{3 \times 10^4}$ was defined here as a mortal probability where failures of powder bed took place at the repeated times of less than 3×10^4; for there were no data of failure obtained at N of more than 3×10^4.

The failure probability at $N \leq 3 \times 10^4$ was obtained as follows: After the stress ratio was classified into some segments containing the same numbers of data, that probability was represented by the ratio of the failure data to the total data containing unbroken data in each segment.

In **Fig. 9** the mortal probability $P_{3 \times 10^4}$ approached to almost a unit at the stress ratio of 0.85 where the slope of the line changed abruptly in **Fig. 8**. When $\bar{\sigma}_s/\bar{\sigma}_z < 0.85$, there would exist a limiting region including survivalship under the finite repetition of stress loading. The characteristic life N_c would increase infinitely, when $P_{3 \times 10^4} = 0$ or $\bar{\sigma}_s/\bar{\sigma}_z \approx 0.68$. This implies that the S-N relationship could be expressed as a horizontal line parallel to the N_b
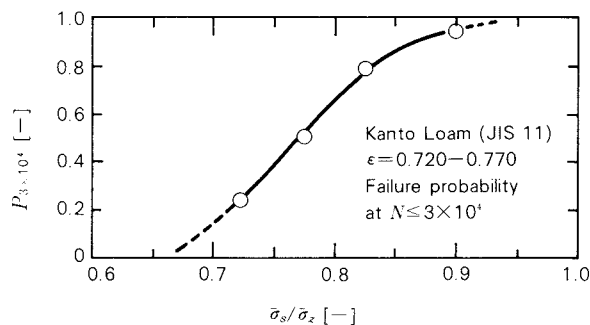

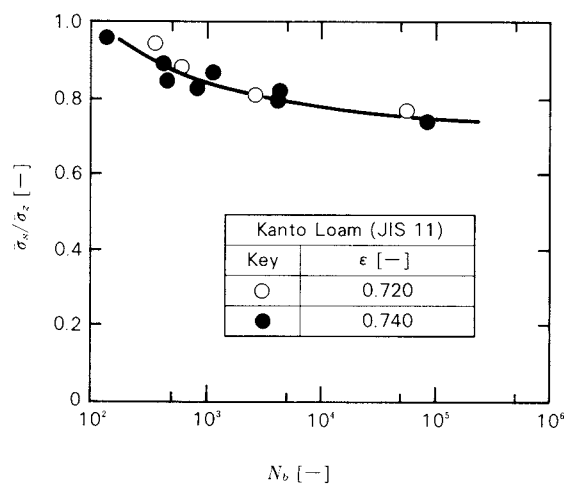Fig. 9 Fatigue failure probability at $N \leq 3 \times 10^4$

Fig. 10 S-N curve estimated by statistical analysis

axis.

When $\bar{\sigma}_s/\bar{\sigma}_z > 0.85$, on the other hand, failure of powder bed never failed to take place at N_b of less than 3×10^4. **Fig. 7** shows that the S-N relation in this mortal region was declined against the N_b axis, compared with the horizontal region.

Figure 10 shows S-N curve based on assuming the presence of inclined and horizontal part for date on the half survivalship in number of Kanto Laom (JIS No.11) indicated in **Fig. 7**. It is found from this figure that the line would become horizontal at N_b of more than about 10^3. However, whether the S-N curve is parallel to the N_b axis seems to be dependent on the data which can be given at N of more than 10^6. The stress ratio at $N = 10°$ was over a unit. This is probably because the tensile stress $\bar{\sigma}_z$ would vary at the extent of 5 percent and also dynamic, but very short loading, repetition could provide larger stress required to cause failure by each loading than static action. In practice, it has been ascertained in the field

52

of soil mechanics that a tri-axial compression test permits a failure strength to increase when the loading time is limited within a second[1]. Thus, the S-N curve obtained in the present work is considered to include an effect of increasing strength resulting from the dynamic characteristics of powder bed.

The shape parameter m can be estimated to be constant at both inclined and horizontal part of S-N relation, judging from the result of **Fig. 8**. Other materials, like iron steel, allow m to increase in the inclined part due to relatively narrow distribution and to decrease in the horizontal part due to broad distribution. Therefore, the S-N curve for these materials can be classified easily into inclined and horizontal parts. As for powder bed, on the other hand, there are wide distributions of fatigue life even in a inclined part. This implies that data of powder bed tend to vary considerably in the view of fatigue failure phenomenon as well as other specific characteristics. It should be also noticed that the probability-density distribution function $p(N)$ decreased monotonously with an increase of N because the values of m were almost below a unit.

6. Conclusion

In the present work, experiments were conducted by using vibratory motions to load repeatedly powder bed with tensile stress less than static strength. The conclusions obtained are:

1) There existed a lower limit stress (endurance limit) in fatigue failure of powder bed suffering from dynamic tensile stress load under the repetition of 10^6 times.

2) Application of the tensile stress repeated over the lower limit permitted the mortal life due to fatigue failure to be expressed as a Weibull distribution.

3) The S-N relation of tensile fatigue failure was shifted from inclined part to horizontal one as the stress ratio decreased.

4) The shape parameter was kept constant ($m \simeq 0.5$), in both the inclined and the horizontal part. The fatigue failure test of

powder bed was found to provide the wide range of data.

Nomenclature

A	: sectional area of vertical cell	[cm^2]
d_p	: mean particle diameter	[μm]
f	: frequency of vibration	[Hz]
g	: gravitational acceleration	[m/s^2]
m	: shape parameter in Weibull distribution function	[$-$]
$\overline{m}$	: estimate of shape parameter in Weibull distribution function	[$-$]
m_f	: mass of separated powder bed	[kg]
N	: number of repeated stress	[$-$]
N_b	: number of repeated stress to failure, fatigue life	[$-$]
N_c	: characteristic fatigue life in Weibull distribution function	[$-$]
$\overline{N}c$	: estimate of characteristic fatigue life in Weibull distribution function	[$-$]
N_{50}	: fatigue life that failure probability is 50 percent	[$-$]
$P_{3\times10^4}$	: failure probability at $N \leq 3 \times 10^4$	[$-$]
P	: cumulative distribution of fatigue life	[$-$]
p	: probability density of fatigue life	[$-$]
α_0	: amplitude of vibration	[m]
ϵ	: porosity rate	[$-$]
ρ_p	: particle density	[kg/m^3]
σ_s	: repeated tensile stress	[kPa]
$\overline{\sigma}_s$	: mean repeated tensile stress	[kPa]
$\overline{\sigma}_z$	: mean static tensile strength of powder bed	[kPa]
ω	: angular frequency	[l/s]

References

1) Ishihara, K.: "Doshitsu Dōrikigaku no Kiso", p.125, Kashima Syuppankai, Tokyo (1975).

2) Naito, M., J. Tsubaki and G. Jumbo: *Kagaku Kogaku Ronbun-shu,* **10**, 744 (1984).

3) Shiomi, H.: "Shinraiseikōgakunyūmon", p. 60, Maruzen, Tokyo (1972).

4) The Japan Society of Mechanical Engineers (ed.), "Standard Method of Statistical Fatigue Testing JSME-S-002-1981", p. 13 (1981).

5) Tsubaki, J., K. Kato, G. Jimbo: *Journal of the Society of Powder Technology, Japan,* **20**, 63 (1983).

6) Tsubaki, J., K. Kato, T. Takeyama and G. Jimbo: *Kagaku Kogaku Ronbun-shu,* **10**, 402 (1984).

7) Tsubaki, J., M. Naito, H. Tagami, F. Kousaka and G. Jimbo: *ibid.,* **8**, 481 (1982).

Grinding Rate of a Ball Mill Operated under Centrifugal Force[†]

Torajiro Honma, Masafumi Kuriyama
and Yoshiteru Kanda
*Department of Chemical Engineering
Yamagata University**

Masahiro Hasegawa
*Department of Chemical Engineering
Tohoku University***

Abstract

Measurements of specific surface area of product were made on a new type of ball mill operated under centrifugal force. The results indicated that this type of mill was superior in grinding performance to the conventional ball mill operated under gravitational force and that the use of centrifugal force was effective in reducing the grinding time.

An empirical equation was proposed for expressing the increase of specific surface area of product by the introduction of a non-dimensional parameter to evaluate the effect of centrifugal force. This equation was found to express well the grinding process under gravitational force as well as that under centrifugal force.

1. Introduction

A ball mill is one of the most commonly used devices for fine grinding on an industrial scale. Its grinding ability is based on gravitational force alone, and requires lengthy grinding time in a batchwise operation to produce fine particulate materials which have been more necessary to industrial use. It is expected that this operation time is reduced from the viewpoint of practical energy saving effort.[2] One of the effective methods of shortening this operation time is to employ an enhanced centrifugal force instead of a gravitational force.

It has been reported that this type of mill has much higher grinding capacity than conventional tumbling ball mills which are operated only under gravitational forces[1,3,5,9]. Unfortunately, however, there are few papers describing the grinding rate quantitatively and in detail; in particular, there has been little knowledge of relation between a grinding rate and an added centrifugal force which is the most important to estimate the mill performance.

In the present work, a planetary-type ball mill was used to investigate experimentally the effects of an added centrifugal force, fractional ball filling, and fractional material filling on a grinding rate in the mill.

2. Experimental equipment and method

2. 1 Experimental equipment

Fritsch planetary-type ball mill was used as an experimental equipment. The geometrical outline and dimensions are shown in **Fig.1**. This mill had a pair of stainless steel grinding bowls with an internal volume of 280 cm^3, filled with steel bearing balls of 7.2 mm in diameter, as shown in **Fig. 2**. These bowls mounted on the horizontal base disc rotated on their own vertical axis at the rate of N_M. The base disc, on the other hand, revolved inversely at the rate of N_S and the centrifugal force caused by the

---
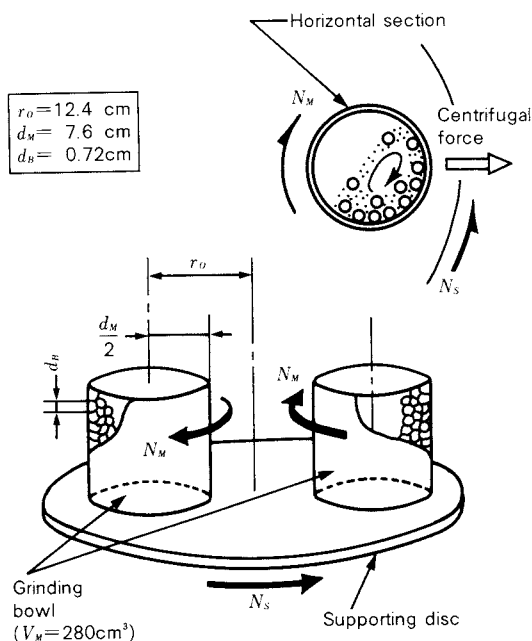
Fig. 1 Schematic diagram of a planetary-type ball mill

r_0=12.4 cm
d_M= 7.6 cm
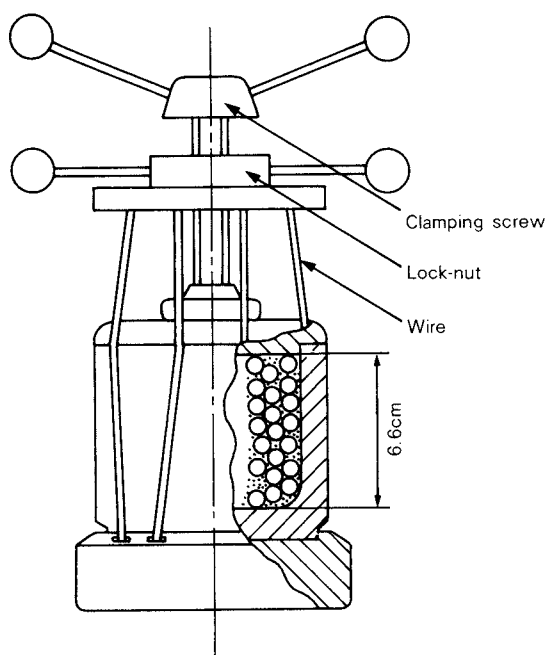d_B= 0.72cm

Fig. 2 Detail of grinding bowl

revolution acted on the media as an acceleration force. The rotation speed was set to be 2.2 times as large as the revolution speed which could vary from 70 to 300 r.p.m.

2. 2 Sample material

The sample material used in the present work was a feldspar powder with a specific gravity of 2.55 and a specific surface area of

26.5 m² · kg⁻¹. This powder was obtained by crushing a material produced in Niigata and sieving it to the particle size range from 74 to 149 μm.

2. 3 Experimental method

Experiments on size reduction were carried out batchwise in a dry state. Change of specific surface area of the sample powder according to time was obtained by *Surface area analyzer* (Shimadzu Seisakusho Co., Ltd., Type SS100) to assess a grinding process. The experimental procedure employed was:
— Given amounts of sample material and grinding media were put into the grinding bowls.
— After grinding operation was conducted during a given period, the ground material of 3 g was sampled by the cone and quartering sampling method to be used for the specific surface area measurement.
— Then, the material taken out for such a measurement was entirely returned into the grinding bowls.
— The above procedure was repeated.
In addition to this measurement, experiments on a conventional-type ball mill operated under a gravitational force[☆] were made to compare these two results.

These experiments were conducted with some variations of a fractional ball filling, J, and a fractional powder filling, U, defined by the following expressions.

$$J = \frac{\text{Packing volume of balls}}{\text{Internal volume of grinding bowl}} \quad (1)$$

$$U = \frac{\text{Net volume of test material}}{\text{Net volume of balls}} \quad (2)$$

3. Critical rotation speed of planetary-type ball mill

It is well known that there is a critical state for a conventional ball mill where the balls would rotate at the same speed as that of the bowl. By using a conventional method[4], the authors attempted to derive the critical condition of a planeatary-type ball mill.

We consider the rotating coordinate system

☆ The experiment under gravitational force was entirely conducted at the rotation speed of 112 r.p.m. This corresponds to 69 percent of the critical rotation speed.
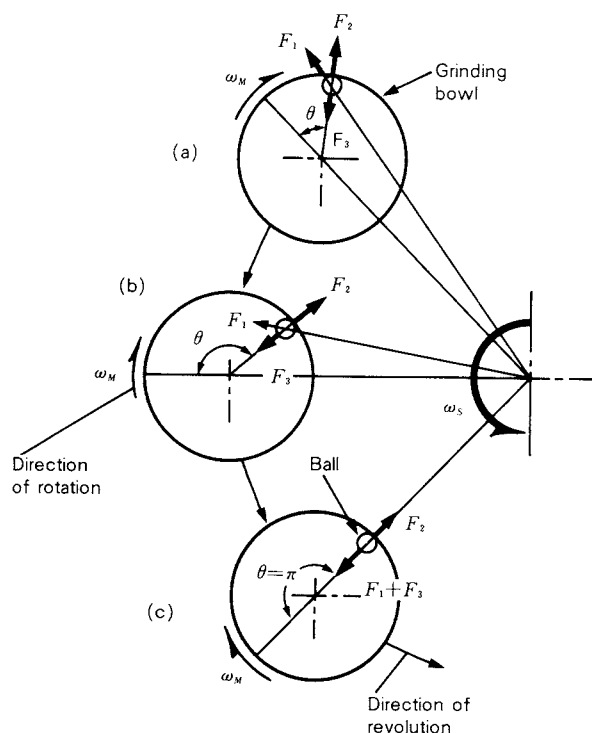
Fig. 3 Description of forces acting on a ball

fixed on the base disc indicated in **Fig. 3**. A ball is balanced in the bowl by the three forces: the centrifugal force caused by revolution and rotation, F_1 and F_2, and Coriori's force F_3 expressed respectively as

$$F_1 = m_B r \omega_S^2 \qquad (3)$$

$$F_2 = \frac{1}{2} m_B (d_M - d_B) \omega_M^2 \qquad (4)$$

$$F_3 = m_B (d_M - d_B) \omega_S \omega_M \qquad (5)$$

where m_B is the mass of a ball and r is the distance between the revolution center and the ball center given by

$$r = \sqrt{r_0^2 + (\frac{d_M - d_B}{2})^2 + r_0(d_M - d_B)\cos\theta} \qquad (6)$$

When the critical state is achieved as shown in **Fig. 3 (C)**, the three forces can be balanced at $\theta = \pi$ as follows:

$$F_2 = F_1 + F_3 \qquad (7)$$

Substituting Eqs. (3), (4), (5) and (6) into Eq. (7), the critical condition can be obtained by using the revolution-to-rotation speed ratio:

$$\varphi = \frac{N_M}{N_S} \qquad (8)$$

$$\varphi_C = 1 + \sqrt{\frac{2r_0}{d_M - d_B}} \qquad (9)$$

The above form demonstrates that the critical condition of a planetary-type ball mill can be expressed by the revolution-to-rotation speed ratio.

The value of φ_C obtained by substituting practical equipment dimensions for Eq. (9) was 2.9, and the present experimental condition ($\varphi = 2.2$) is found to correspond to 76 percent of the critical value. The experimental condition employed in the present work proves to have been adopted adequately, because it is recognized in general that a conventional ball mill runs effectively at 60 to 80 percent of its own critical rotation speed[7].

4. Experimental result and discussion

4. 1 Increasing process of specific surface area

As the size reduction proceeded, the specific surface area S increased, as indicated in **Fig. 4** where N_t of the horizontal axis denotes a summation of the rotation numbers of the grinding bowl. This figure shows clearly that the size reduction under a centrifugal force would permit a specific surface area to increase more rapidly and shorten the operation time, compared with that only under a gravitational force which is expressed as a plot of closed circle symbols. During each initial period of the size reductions, S appears to increase linearly with N_t, and this means the applicability of Rittinger's law[7]. On the other hand, after a certain period of operation was conducted,
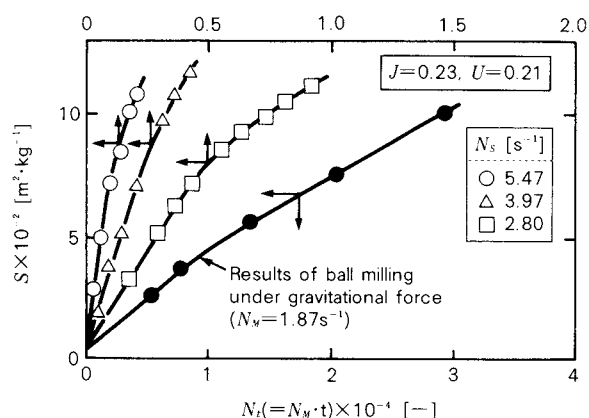

Fig. 4 Relationship between specific surface area of product and number of bowl rotations in the beginning of grinding

the grinding rate would decrease due to the production of fine fragments. On the basis of such an experimental result, the following grinding rate equation was introduced under the assumption of the general relation between particle size and grinding energy:

$$\frac{dS}{dN_t} = KS^{-m} \tag{10}$$

Integration of Eq. (10) under the assumption that the initial surface area would be negligible in comparison with the value in the state after the grinding operation leads to

$$S = kN_t^m$$

where (11)

$$K = nk^{\frac{1}{n}} \quad \text{and} \quad m = \frac{1-n}{n}$$

The log-log plots of S against N_t obtained through Eq. (11) from the experimental result are illustrated in **Fig. 5** and **Fig. 6** for the cases under centrifugal and gravitational force, respectively. Each result is found to be consistent with the relation given by the Eq. (11) except the initial and the final period of size reduction.
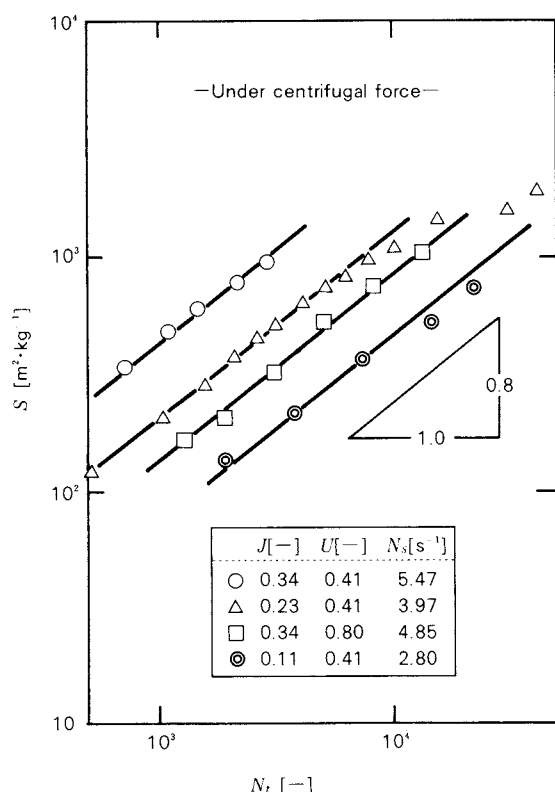
Fig. 5 Relationship between specific surface area of product and number of bowl rotations
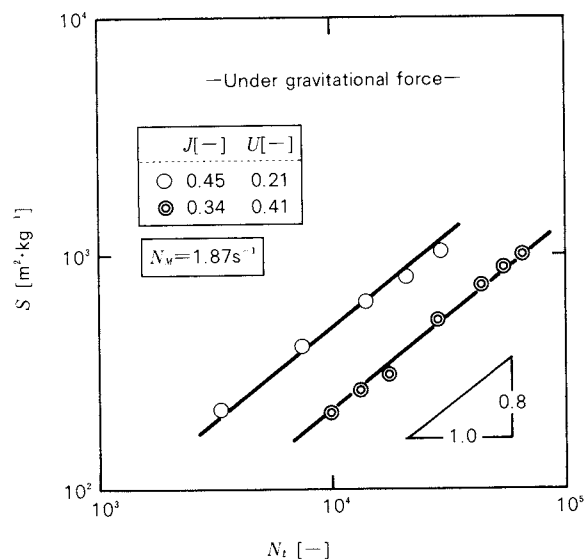
Fig. 6 Relationship between specific surface area of product and number of bowl rotations

The slope of any straight line, n, in the both figures is close to the constant value of 0.8 (or 0.25 for m), independently of the experimental conditions. This suggests probably that n in Eq. (11) or m in Eq. (10) tends to be dependent solely on the type of material used.

As mentioned above, Eq. (11) expresses adequately the increasing processes on specific surface area. Thus, the effect of operating factors on grinding rate can be assessed by the coefficient of k used in Eq. (11).

4. 2 The relationship between grinding rate and fractional ball and powder fillings

As indicated in **Fig. 7**, k reached a maximum of $J = 0.34$ for the both cases under centrifugal and gravitational force. This value is substantially consistent with the optimum value obtained in a practical ball mill operated under a gravitational force. With an increase in U, which is not shown in the present paper, k was found to tend to decrease monotonously. This is probably because an increase in the material-to-ball mass ratio would result in reducing grinding energy applied to a material of a unit mass.

It may be considered that there is an optimum value of fractional powder filling at which the power input into the grinding system can be consumed most effectively. In this case, it will be convenient to use the product of k and the feed material weight, W_F to obtain an opti-
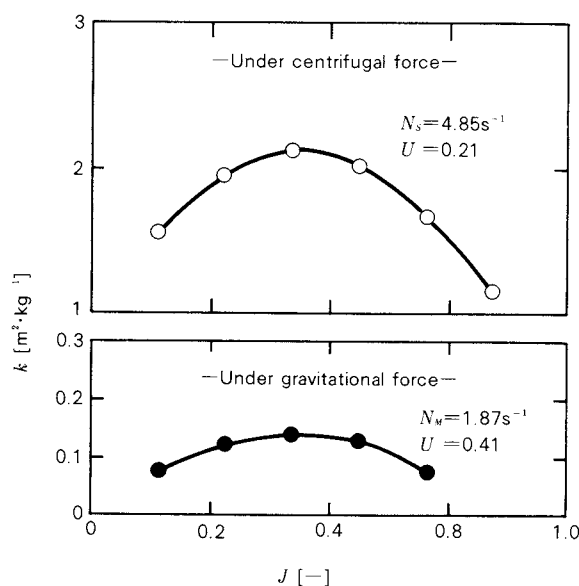
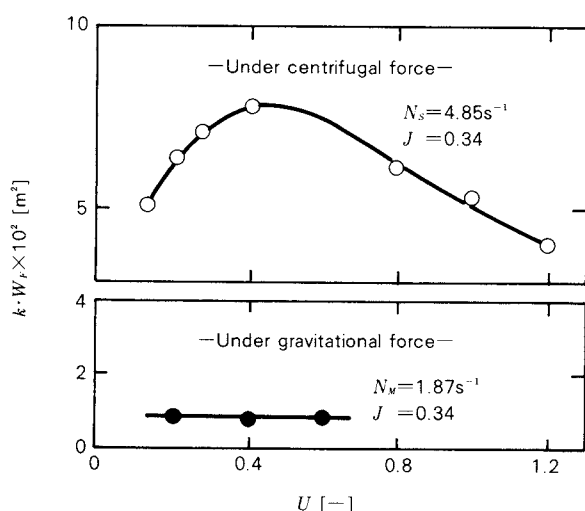Fig. 7 Effect of fractional ball filling on grinding rate

Fig. 8 Effect of fractional powder filling on grinding rate

mum value of U; this product means the rate of increase in the whole surface area of all the particles. **Figure 8** shows a typical relationship between kW_F and U in the case an optimum fractional ball filling J, of 0.34. In this figure, kW_F reached the maximum nearly at $U = 0.4$ when the operation was conducted under a centrifugal force, while the maximum value was not found clearly under a gravitational force. If we obey Rose's concept[6] that a ball mill can be operated most effectively when the clearance among the grinding balls are filled with a powder, U defined by Eq. (2) will

become 0.4^{*}, and this corresponds to the optimum value operated under centrifugal force.

Although the rotating direction of the centrifugal ball milling was different from that of the gravitational ball milling, the moving behavior of balls and bowl appeared to be similar in these two different operations.

Thus it is estimated that there might be no radical difference between their grinding mechanisms. However, relatively slow revolution under a centrifugal ball mill operation might cause dissimilar behavior to that mentioned above. This is because balls and a powder are accumulated at the bowl bottom due to innegligible gravitational influence. Therefore the effect of added centrifugal force on grinding rate is required to be examined.

4. 3 The relationship between grinding rate and added centrifugal force

When grinding bowls are not so far from their revolution center, like the present experimental case, the centrifugal forces will not act uniformly on balls in the bowl. Thus there arises a problem on whichever characteristic quantity should be employed to estimate the influence of centrifugal force. The authors attempted to use, as a characteristic quantity, the following centrifugal effect Z_m defined as the centrifugal force arising at the

---

☆ If one takes ρ_S, ϵ_S, and ϵ_B as the particle density, the porosity of powder bed, and the porosity of packed balls, he can get

$$V_{S,ap.} = \frac{W_F}{\rho_S(1 - \epsilon_S)}$$

$$V_g = V_M J \epsilon_B$$

where $V_{S,ap.}$ is the apparent volume of the material and V_g is the gap volume among the balls. Thus, the optimum feed amount is given by the following form under the assumption of the optimum condition proposed by Rose: $V_{S,ap.} = V_g$.

$$W_{F,opt.} = V_M \rho_S J \epsilon_B (1 - \epsilon_S)$$

Since U, on the other hand, is expressed from Eq. (2) as:

$$U = \frac{W_F/\rho_S}{V_M J(1 - \epsilon_B)}$$

It can be optimized by substituting $W_{F,opt.}$ into W_F; that is,

$$U_{opt.} = \frac{\epsilon_B (1 - \epsilon_S)}{1 - \epsilon_B}$$

In general, the porosity is 0.4 when spheres of equal size are packed at random. Therefore if one takes ϵ_S as ϵ_B, he can obtain $U_{opt.}$ of about 0.4.

58

bowl rotation center devided by the gravitational force:

$$Z_m = \frac{r_0\,\omega_S^{\,2}}{g} = \frac{r_0\,(2\pi N_S)^2}{g} \qquad (12)$$

For a conventional ball mill, Z_m becomes unity, because gravitational force is the only force acting on the balls when centrifugal force is not applied.

The authors investigated whether or not Z_m might be suitable as a characteristic quantity. In **Fig. 9**, the specific surface area S, which is indicated in **Fig. 4**, is plotted against the product of Z_m and N_t, that is, the quantity corresponding to the energy added by a centrifugal force. This figure shows that all the experimental values might be expressed by a single straight line. In the Rittinger region, or the initial grinding region, where grinding energy is proportional to the increase of specific surface area, all the measurements including the result of gravitational grinding could be expressed as a single straight line. In the Rittinger region, the relationship between the increment of specific surface area ΔS and the increment of grinding energy ΔE is written by

$$(\Delta S/\Delta N_t) = (\Delta S/\Delta E) \cdot (\Delta E/\Delta N_t) \qquad (13)$$

The Rittinger number $(\Delta S/\Delta E)$ can be considered to be independent of Z_m. Thus the result of **Fig. 9** shows

$$\Delta E/\Delta N_t \varpropto Z_m \qquad (14)$$

This suggests that Z_m could correspond to the grinding energy per one rotation of the bowl.

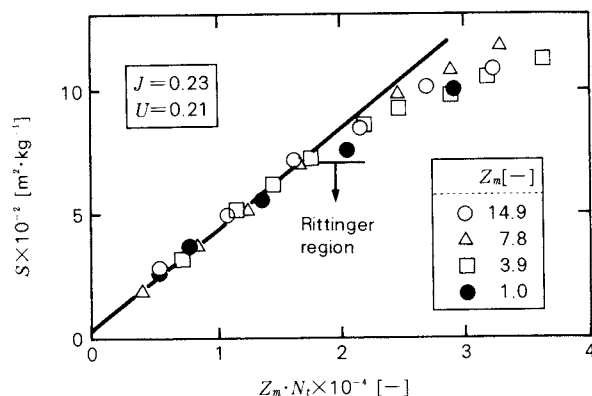The relationship between K and Z_m is

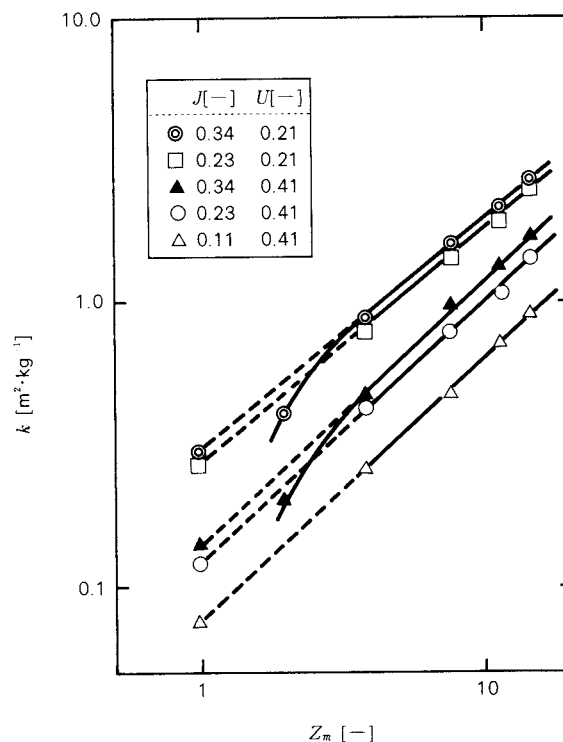Fig. 9   Correlation of specific surface area of product with $Z_m \cdot N_t$

Fig. 10   Effect of centrifugal force on grinding rate

shown by log-log expression in **Fig. 10**, where the values at $Z_m = 1$ represent measured results obtained by the experiments under only gravitational force. It is found from this figure that K could be related linearly to Z_m in a log-log graph at the region of $Z_m > 4$ where the effect of gravity would be negligible, compared with that of centrifugal force. That is,

$$K = K_1 Z_m^{n_1} \qquad (15)$$

It is also found that the extrapolation of this relation would reach the individual value at $Z_m = 1$. This implies that the use of Z_m could connect the rate of gravitational grinding with that of centrifugal grinding. When $Z_m < 4$, on the other hand, the poor effect of centrifugal force could produce small grinding rate. This suggests that efficient operation might be given in the region of larger centrifugal force.

Substituting Eq. (15) for Eq. (11), the following equation of grinding rate is obtainable.

$$S = K_1 Z_m^{n_1} N_t^{n} \qquad (16)$$

or

$$\frac{\mathrm{d}S}{\mathrm{d}N_t} = K_1 Z_m^{m_1} S^{-m} \qquad (16)'$$

The above equation can be rewritten by using differential form with respect to time.

$$\frac{dS}{dt} = K_1 N_M Z_m{}^{m_1} S^{-m} \qquad (17)$$

Where K_1, n_1, K_1, and m_1 depend on kinds or fractional fillings of materials. These values used in the present work were K_1 of 0.14 $m^2 kg^{-1}$, n_1 of 0.92, K_1 of $6.9 \times 10^{-2} m^{\frac{1}{n}}$, $kg^{-\frac{1}{n}}$, and m_1 of 1.15 under the optimum condition ($J = 0.34$, $U = 0.41$) which was referred to in Section 3.2.

With regard to a ball mill under centrifugal force, the rotation speed of a bowl-N_M varies proportionally with the revolution speed N_S. Thus, N_M is related to Z_m as

$$N_M = \frac{\varphi}{2\pi} \sqrt{\frac{g}{r_0} \cdot Z_m} \qquad (18)$$

The above equation states that more added centrifugal force never fails to provide larger value of N_M. Consequently, the duplicated effect caused by them tends to increase the grinding rate. For instance, if a feldspar is ground at $Z_m = 15$ and under optimum fractional fillings of J and U, dS/dt will be 57 times as large as that under gravitational force ($N_M = 130$ r.p.m.)

5. Conclusion

Size reduction by a ball mill under centrifugal force was investigated experimentally. The result shows that the addition of centrifugal force could reduce effectively operation time. The overall grinding rate equation was presented to describe the variation of specific surface area under both centrifugal and gravitational force, by the introduction of a typical descriptor to assess an extent of added centrifugal force.

Nomenclature

d_B	: diameter of ball	[m]
d_M	: diameter of grinding bowl	[m]
ΔE	: grinding energy	[W]
F_1, F_2, F_3	: forces acting on a ball, shown in Fig. 3	[N]
g	: gravitational acceleration	[m/s^2]
J	: fractional ball filling defined by Eq. (1)	[-]
K, k_1	: coefficients in Eqs. (10) and (15), respectively	[m$^{\frac{1}{n}}$·kg$^{-\frac{1}{n}}$]
k	: coefficient in Eq. (11)	[m^2/kg]
m, m_1	: exponents in Eqs. (10) and (16)	[-]
N_M	: rotation speed of grinding bowl	[s^{-1}]
N_S	: revolution speed of grinding bowl	[s^{-1}]
N_t	: number of rotations ($N_M \cdot t$)	[-]
n, n_1	: exponents in Eqa. (11) and (15), respectively	[-]
r	: distance from revolution center to ball center	[m]
r_0	: distance from revolution center to rotation center	[m]
S	: specific surface area	[m^2/kg]
t	: grinding time	[s]
U	: fractional powder filling defined by Eq. (2)	[-]
V_M	: internal volume of grinding bowl	[m^3]
W_F	: weight of feed material	[kg]
Z_m	: centrifugal effect defined by Eq. (12)	[-]
θ	: angle shown in Fig. 3	[-]
φ	: ratio of rotation speed to revolution speed, expressed by Eq. (9)	[-]
φ_C	: critical value of φ	[-]
ω_M	: angular velocity of rotation ($= 2\pi N_M$)	[s^{-1}]
ω_S	: angular velocity of revolution ($= 2\pi N_S$)	[s^{-1}]

References

1) Cronan, C.S.: "Process Equipment News", *Chem. Eng.*, **61**, 266 (1954).
2) Jimbo, G.: *Kagaku Kōgaku*, **47**, 99 (1983).
3) Matsumoto, H. and S. Yamauchi: *Reports of the Government Industrial Research Institute, Nagoya*, **7**, 291 (1958).
4) Miwa, S.: "Funtai Kogaku Tsuron", Nikkan Kogyo Shinbunsha (1981).
5) Fritsch, P.W. and M. Mehmel: *Keramische Zeitschrift*, **15**, 467 (1957).
6) Rose, H.E.: *Trans. Inst. Chem. Engrs.*, **35**, 87 (1957).
7) Kagaku Kogaku Kyokai (ed.): "Kagaku Kogaku Binran", 4th Ed., Maruzen, Tokyo (1978).
8) Walker, W.H., W.K. Lewis, W.H. McAdams and E.R. Gilliland: "Principles of Chemical Engineering" (1937).
9) Yamauchi, S. and H. Matsumoto: *Reports of the Government Industrial Research Institute, Nagoya*, **7**, 612 (1958).

Coating of Seed Particles in Tumbling Fluidized Bed by Atomizing the Suspensions of Clayey Particles[†]

Eiichi Abe and Hideharu Hirosue
*Government Industrial Research Institute, Kyushu**

Hiroshi Kikuchi
*Kunimine Kogyo Co., Ltd.***

Abstract

Coating seed particles of 53 to 210 μm with clayey particles was carried out by means of a tumbling fluidized bed in order to enlarge and reuse the clayey particles wasted in producing a carrier for driftless dust formulation. The influence of operating factors on the coating efficiency η and on the growth rate of seed particles was investigated. η varied depending upon thermal operating factors but was not influenced much by mechanical ones. It was found that η was related roughly to R_W defined as the ratio of the feed rate of water fed as slurry droplets to the maximum theoretical evaporation rate of water in a coating chamber. η increased with R_W. The relationship between η and R_W varied with the additive ratio of binder PVA to clayey particles, C_b, and η became high with increasing C_b. The growth rate of seed particles was explained well by an equation derived on the basis of the mass balance of clayey particles in a coating chamber.

1. Introduction

Recently, the particle size of the dust among the various agricultural chemicals tends to be enlarged to reduce the public nuisances caused by the drift of fine particles generated on the spraying.

This agricultural chemicals called DL dust (particles size; 10 ~ 46 μm) contains few fine particles smaller than 10 μm. Therefore the fine particles smaller than 10 μm are generated as by-products in large quantities, when they produce carrier of DL dust, which leads to a possibility of causing problems in the disposition.

As one of the means of solving the problem, the authors have investigated the coating of the seed particles (about 100 μm) with the above-mentioned by-product particles using a tumbling fluidized bed coater[1] to develop a new type carrier for the agricultural chemicals, F micro-granules (particle size 63 ~ 210 μm).

The tumbling fluidized bed coater has been devised as an apparatus that makes possible to coat particles less than 300 or 500 μm, which is a critical size for conventional fluidized bed coater. With regard to this apparatus, however, few studies have been reported so far and the instructions for optimum operating conditions to get desirable results have not been made clear yet at all.

This work elucidates the effect of the operating factors of the tumbling fluidized bed coater on the coating efficiency, indicates the instructions for the optimum operating conditions. The growth rate of seed particles is also discussed in this work.

2. Samples

As coating particles, Roseki (density; 2710

kg/m³, particle size; < 10 μm, mass median Stokes diameter; 3.6 μm) or Kunimine clay (density; 2710 kg/m³, particle size; < 20 μm, mass median Stokes diameter; 7 μm) and as seed particles, ground Toyoura sands (density; 2630 kg/m³, particle size; 53 ~ 210 μm) or calcite (density; 2700 kg/m³, particle size; 250 ~ 590 μm) were used in the experiments.

Roseki was a product from Kawatana factory of Goto Mining in Nagasaki pref. consisting mainly of quartz and agalmotalite. Kunimine clay was a product by Kunimine Kogyo Co., Ltd., which consisted mainly of quartz and feldspar and contained some clay minerals such as chlorite, sericite and talc.

3. Experimental apparatus and procedures

3. 1 Tumbling fluidized bed coater

A schematic diagram of a tumbling fluidized bed coater (Okada Seiko Co., Ltd., type SP-25) is shown in **Fig. 1**.

The air from a blower through a heater and damper is introduced into the coating chamber (250 mmϕ) through the gap (10 mm) between a rotating disk and the chamber wall. By the disc rotation, the tumbling seed particles in the chamber are forced to exist in the vicinity of the chamber wall, where they are fluidized by the hot air. The coating particles dispersed in water are sprayed to such violently moving seed particles from a nozzle (Fuso Seiki, Co., Ltd., type Rumina ST-5, external mixing type pneumatic nozzle, liquid outlet diameter; 1.0 mmϕ) set above in the center of the disc. The spray of the slurry is directed to the point 9 cm away from the center on the disc face. The slurry droplets which adhered to the sur-

face of the seed particle are dried by the hot air, so that the particles in the droplets coat the surface of the seed particle. A part of the coating particles which failed to adhere to the seed particles as a result of peeling etc. are discharged from the coating chamber and collected in a cyclone on the way to the air exhaust of this system.

The experimental procedures were as follows. The disc rotation speed and the flow rate of inlet air were adjusted after charging the coating chamber with a required amount of seed particles. When the temperature of the air reached a fixed value, the slurry was fed to the nozzle at a constant rate by a gear pump and began to spray under the constant air pressure (0.294 MPa). During the experiment, the air temperature after passing through the fluidized bed was measured with a thermocouple set near the nozzle. After a fixed coating time, the coated particles were taken out from the outlet, as soon as the feed of the slurry was stopped. The representative sample of 0.04 ~ 0.06 kg out of the product taken out from the chamber was sifted through the standard sieve (37 μm) after stirring in hot water (343 ~ 353 K, 400 cm³) for 4 hours. Having had confirmed that the particles of Roseki and the Kunimine clay passed the standard sieve (37 μm) entirely, the undersize was regarded as the coating particles. The mass of the undersize per total mass of the seed particles supplied to the coating chamber was adopted as the total mass of the coating particles adhering to the seed particles.

In this article, the coating efficiency η is defined as the ratio of the total mass of the coating particle adhering to the seed particles to the total mass of the coating particles fed into the coating chamber during the coating operation.

As for the operating factors, there are the mechanical operating factors such as the disc rotation speed N [s^{-1}] and the mass of seed particles M_s [kg] etc., and the thermal operating factors such as the feed rate of the coating particles F_c [kg/h], the slurry concentration (mass ratio of coating particles to slurry) s [kg/ kg], the flow rate of inlet air Q [m³/h], the humidity of inlet air H [kg H$_2$O/kg dry air] and the temperature t_i [K] etc. The experiments were carried out under the wide range of conditions shown in **Table 1** to make clear the
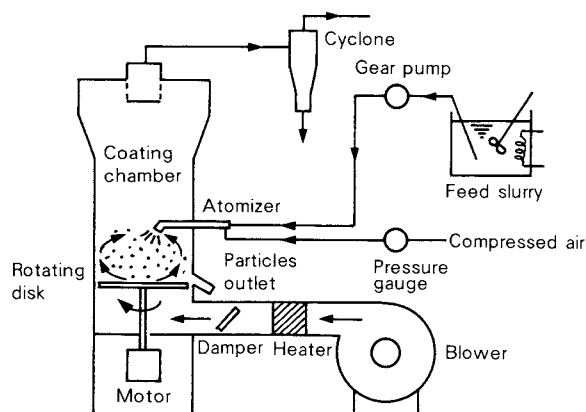

Fig. 1 Schematic diagram of coating apparatus

Table 1 Operating conditions

Thermal operating factors	
Humidity of inlet air	$H = 0.006 \sim 0.02$ kg H_2O/kg dry air
Flow rate of inlet air	$Q = 48 \sim 75$ m³/h
Temperature of inlet air	$t_i = 313 \sim 338$ K
Slurry concentration	$s = 0.2 \sim 0.37$ kg solid/kg slurry
Feed rate of coating particle	$F_c = 0.23 \sim 0.67$ kg/h
Mechanical operating factors	
Disk rotation speed	$N = 1.5 \sim 3.3$ s⁻¹
Mass of seed particle	$M_s = 0.6 \sim 2.52$ kg
Additive ratio of binder	$C_b = 0 \sim 0.04$ kg PVA/kg solid

relationship between those operating factors and the coating efficiency. In the experiments, ground Toyoura sands and Roseki were used as the seed particles and as the coating particles respectively.

Additionally, PVA (Nippon Gosei Kagaku Kogyo Co., Ltd., Gohsenol GL-05S) was used as a binder to improve the coating efficiency. The influence of the additive ratio of binder C_b on the coating efficiency was also examined.

The concentration of PVA in the water solution is $0.5 \sim 1.2$ wt% under the condition of $C_b = 0.02$, $s = 0.2 \sim 0.37$, and $0.2 \sim 1.7$ wt% in the case of $s = 0.3$, $C_b = 0.005 \sim 0.04$.

According to Yamada et al., Roseki slurry with PVA indicates the flow characteristic of thixotropy, newtonian or dilatancy depending upon the additive ratio of PVA[2] and the viscosity increases with increasing slurry concentration[3].

Roseki slurry in this work showed dilatancy when $s = 0.3$, $C_b = 0.02$, and the apparent viscosity was $2.8 \times 10^{-1} \sim 4 \times 10^{-3}$ Pa·s at the shear rate of $81 \sim 401$ s⁻¹ and the temperature of 307 K.

In addition to the above-mentioned coating experiments, the coating experiments (using Kunimine clay as coating particles and calcite as seed particles) were carried out and compared with the case of coating ground Toyoura sands with Roseki, in order to examine whether the relation between the operating factors and coating efficiencies depends on the physical properties of the seed and coating particles or not. The coating time was 0.5 hr in all the experiments except the one conducted to ex-

amine the growth rate of the seed particles.

The nozzle height is another mechanical operating factor in addition to the disc rotation speed and the mass of the seed particles. Harada et al.[4] have made clear already that the coating efficiency of a conventional fluidized bed coater is decreased as the nozzle height increases. Therefore, it becomes a problem how near the distance between the nozzle and the disc face can be fixed for the troubleless operation.

In preliminary experiments under the condition of $M_s = 0.6$ kg and $N = 1.5$ s⁻¹ when the nozzle height varied from 22, 16, 13 down to 10 cm, the seed particles on the disc face were eliminated by the air flow from the nozzle and the coating particles adhered to the disc face directly in case of the nozzle height less than 13 cm. On the other hand, no difference in the coating efficiency between the nozzle heights 16 and 22 cm was noticed. Therefore, all the following experiments were conducted with the nozzle height of 16 cm or 22 cm.

3. 2 Measurement of the porosity of the coating layer

To consider the growth rate of the seed particles, the value of the porosity of the coating layer on the surface of particles must be known. The porosity was measured with two methods, a method of measuring the packed volume of the seed particle before and after the coating individually and the mercury porosimetry.[5]

Assuming that the particles have the same shape before and after the coating and that the porosity ϵ_s in case of packing non-coated particles equals the one of interstices of particles in the case of packing coated particles, the porosity of the coating layer ϵ is given by,

$$\epsilon = 1 - \frac{m_c/\rho_c}{V(1 - \epsilon_s) - m_s/\rho_s} \tag{1}$$

where m_s [kg] is the mass of the seed particles packed in a vessel, m_c [kg] is the mass of the particles coating the seed particles having the mass of m_s, V [m³] is the packed volume of the particles having the mass of $m_s + m_c$, ρ_c, ρ_s [kg/m³] is the density of the coating particles and the seed particles respectively. V was measured by tapping a vessel of 28 mm diameter under the condition of the stroke 1 cm

and counts of tapping 200.

On the other hand, POROSIMETO SERIES 1500 (CALRO ERBA STRUMENTAZIONE) was used as the instrument of the mercury porosimetry.

3. 3 Measurement of volume shape factor of the seed particles before and after coating

To consider the growth rate of the seed particles, the value of volume shape factor is required in Eq. (11) that will be described later in this article.

On the basis of Eq. (2), the volume shape factor ϕ_v was obtained by counting the number n_p of the particles having the size D and the mass M_p enlarged with a projector.

$$\phi_v = \frac{M_p}{n_p D^3 \rho_p} \qquad (2)$$

where D is the arithmetic mean of sieve aperture, ρ_p is the average particle density calculated from Eq. (3) using the porosity ϵ of the coating layer.

$$\rho_p = \frac{m_s + m_c}{m_s/\rho_s + m_c/(1 - \epsilon)\rho_c} \qquad (3)$$

4. Experimental results and Discussions

4. 1 Droplets size

The results of the photographical size analysis of more than 1000 droplets collected by the immersion liquid method[6] are shown in **Fig. 2**.

It's seen that the droplets having the mass median diameter of 17 ~ 28 μm are formed under the following conditions; the additive
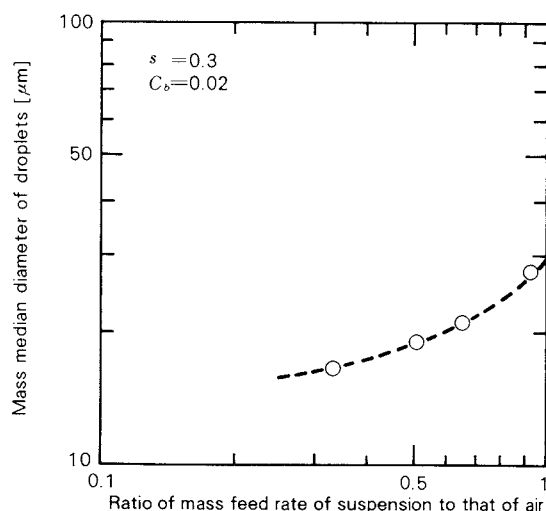
Fig. 2 Measured values of slurry droplet size

ratio of binder C_b = 0.02, the slurry concentration s = 0.3, the ratio of mass feed rate of slurry to that of air from the nozzle 0.35 ~ 1.0.

The droplet size distributions obeyed lognormal distributions as reported by Yamada et al.[2], and the geometrical standard deviations were about 1.5. Under the operating conditions shown in **Table 1**, the ratio of mass feed rate of slurry to that of air from the nozzle was within the range of 0.33 to 0.69.

4. 2 Influence of thermal operating factors on the coating efficiency

(1) Evaporation of water in fluidized bed

Some examples of the relationship between the thermal operating factors and the coating efficiencies are shown in **Fig. 3**.

As seen from the figure, the coating efficiency η increases as the feed rate of water W_E increases when other conditions are kept constant. Conversely, η decreases with increasing the difference between the adiabatic saturation humidity and the humidity $H_s - H$, the temperature t_i, or the volume flow rate of the inlet air Q. These experimental results lead to the following consideration.

In **Fig. 3 (a)**, the evaporation rate of water in the fluidized bed must have a maximum value because the operating factors except W_E are kept constant. If only W_E increases under the condition, a certain amount of water exceeding the evaporation rate is accumulated in the fluidized bed.

Similarly in **Figs. 3 (b)**, **(c)** and **(d)** the decrease of $H_s - H$, t_i or Q makes the accumulation rate of water increase, if the other factors are constant. Above-mentioned considerations suggest that the coating efficiency η might be determined by the accumulation rate of water in the fluidized bed and η becomes higher as this rate increases. The evaporation of water in the tumbling fluidized bed will be discussed in the following.

If the tumbling fluidized bed coater is regarded as an adiabatic humidifier in terms of the inlet air, the variation of air temperature and humidity through the apparatus ought to be illustrated as **Fig. 4**.

The air of temperature t_r and humidity H from the blower is heated by the heater until the temperature reaches t_i. This heated air
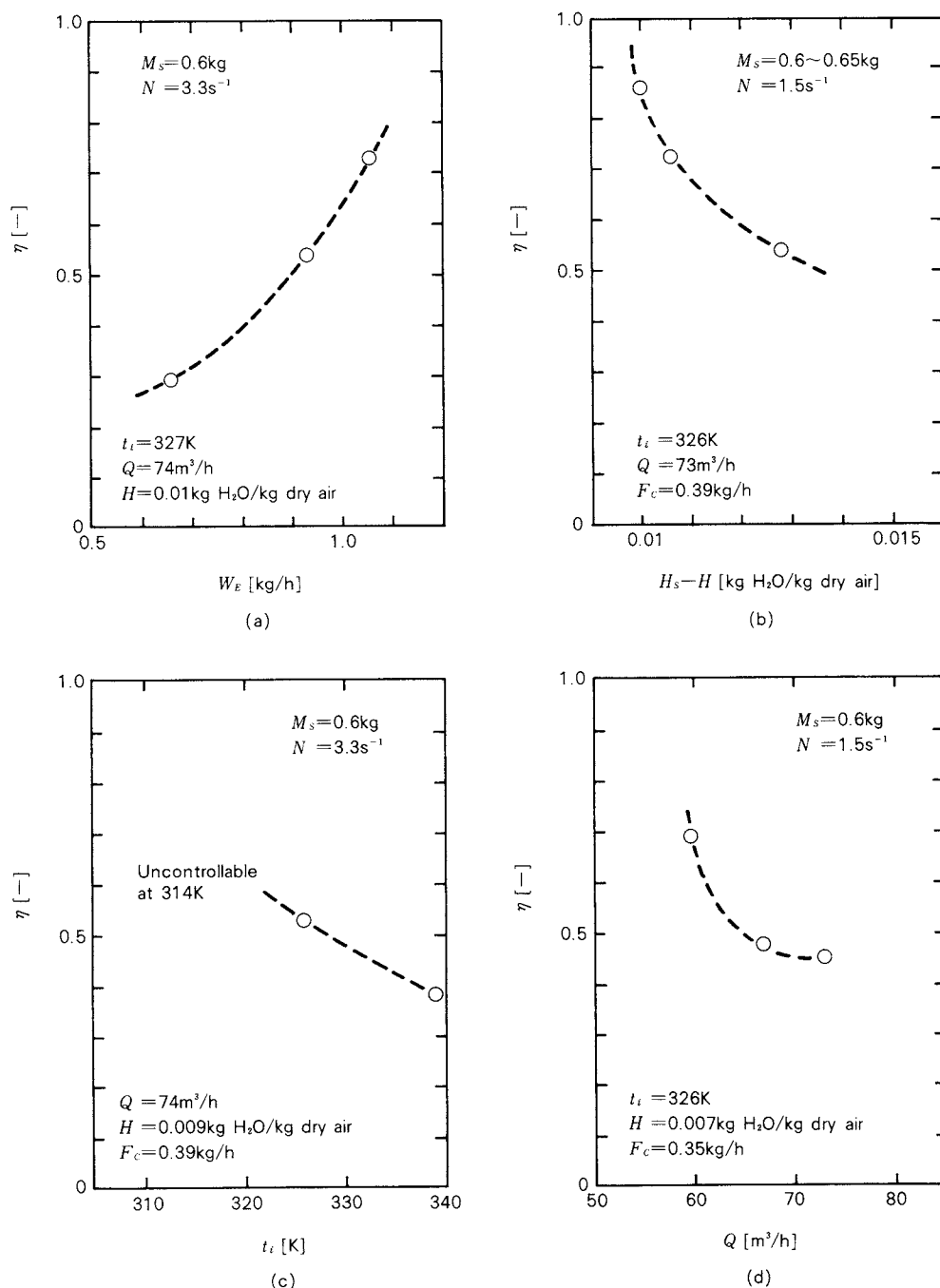
Fig. 3 Relationship between coating efficiency and operating factors

gives the latent heat of vaporization to the slurry droplets in the fluidized bed. As a result, the temperature of the air decreases along the adiabatic cooling line through the point (t_i, H) and the humidity increases.

If the contact time between the air and the seed particles is assured long enough, the maximum theoretical evaporation rate of water in the coating chamber W_T [kg H_2O/h] is ex-

pressed by

$$W_T = W_G (H_s - H) = (\frac{Q}{v}) \times (H_s - H)$$

(4)

where

W_G [kg dry air/h] ;
mass flow rate of inlet air

H [kg H_2O/kg dry air] ;
humidity of inlet air
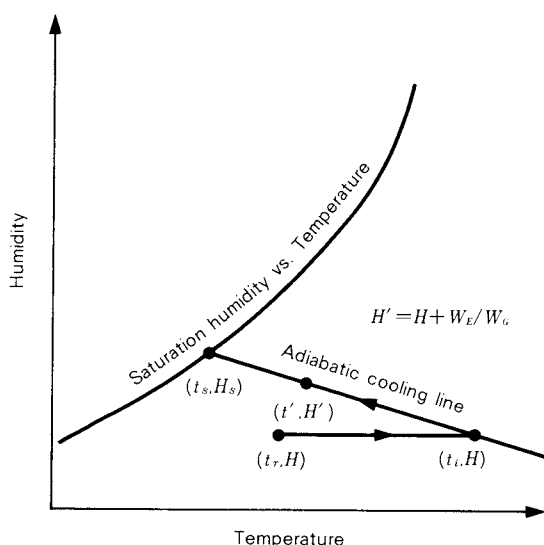
Fig. 4 Temperature and humidity variation of air
through a coating apparatus

Fig. 5 Comparison of theoretical values of temperature
in a fluidized bed with experimental ones

H_s [kg H_2O/kg dry air] ;
adiabatic saturation humidity of inlet air

v [m^3/kg dry air] ;
humid volume of the inlet air.

On the other hand, the feed rate of water W_E
[kg H_2O/h] is given by

$$W_E = F_c \left(\frac{1-s}{s} - C_b \right) \qquad (5)$$

where

F_c [kg/h] ; feed rate of coating particles

s [kg/kg] ; slurry concentration

C_b [kg PVA/kg solid] ; additive ratio of
PVA

It is presumable that the air temperature
becomes the adiabatic saturation temperature
t_s in case of $W_E > W_T$, while it reaches the
temperature t' in case of $W_E < W_T$, where t'
is the temperature at the humidity of $H + W_E /$
W_G on the adiabatic cooling line of the inlet air.

Figure 5 shows the comparison of the meas-
ured values of the air temperature in the fluid-
ized bed obtained from all the coating experi-
ments in this work with the theoretical values
from a humidity chart on the basis of the
above-mentioned procedure. The difference
between the measured values and the theoreti-
cal ones is at most within ±2 K as seen from the
figure so that it is considered that adiabatic
humidification takes place actually in the
tumbling fluidized bed coater.

(2) Effects of moisture on the coating effi-
ciency

As is already mentioned, adiabatic humidifi-
cation takes place practically in the tumbling
fluidized bed coater and the coating efficiency
tends to become higher as the accumulation
rate of water in the fluidized bed increases.

Since the accumulation rate of water in the
fluidized bed is determined by the synthetic
effect of the thermal operating factors, we use
R_W defined by Eq. (6) as an index to evaluate
the synthetic effect of the thermal operating
factors and examine whether the coating effi-
ciency can be definitely related to R_W.

$$R_W = \frac{W_E}{W_T} \qquad (6)$$

Figure 6 shows the relation between the
coating efficiency η and R_W under the condi-
tion of $C_b = 0.02$, $N = 1.5$ s^{-1}, and $M_s = 0.6 \sim$
0.69 kg.

The figure indicates that as far as the ther-
mal operating factors vary in the range shown
in **Table 1**, η is strongly correlated with the
index R_W.

The relationship between η and R_W at slurry
concentration of $s = 0.5$, however, shifted to
high efficiency in the figure. The reason has
not been clear and is the subject to be investi-
gated in the future. Therefore, it is not to af-
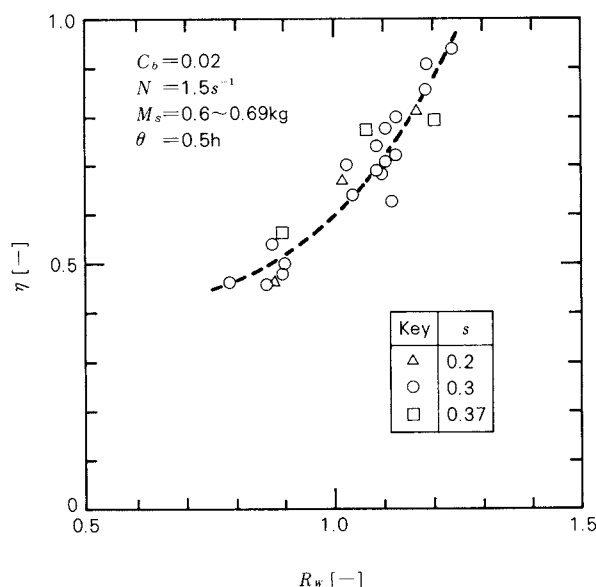firm that η should be determined by R_W de-

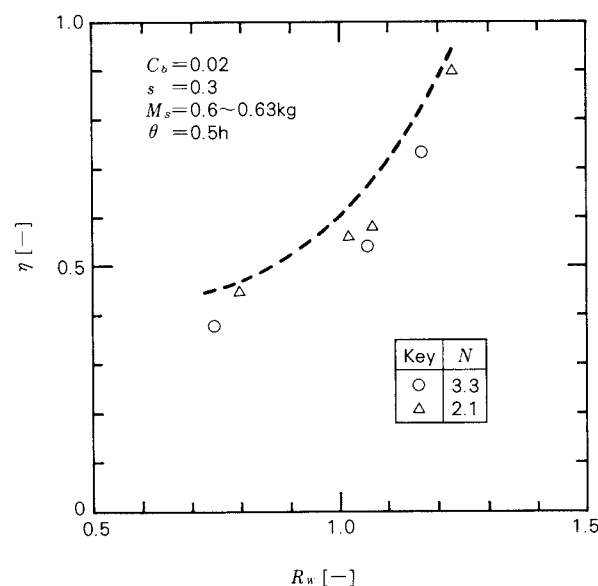Fig. 6 Relationship between coating efficiency and R_W

Fig. 7 Relationship between coating efficiency and R_W

finitely without any restriction. Nevertheless, the relationship between η and R_W is considered to be valuable since more synthetic instructions to find the optimum operating conditions can be obtained from the relations than from those between the individual operating factor and the coating efficiency shown in **Fig. 3**.

4. 3 Influence of mechanical operating factors on the coating efficiency

Figure 7 shows the relationship between η and R_W in the case of the disc rotation speed $N = 2.1$ s^{-1} and 3.3 s^{-1} under the condition of the slurry concentration $s = 0.3$, the additive ratio of PVA $C_b = 0.02$, the mass of the seed particles $M_s = 0.6 \sim 0.63$ kg.

The broken line in the figure indicates the relationship between η and R_W in case of $N = 1.5$s^{-1} shown in **Fig. 6**. Though a slight difference is noticed between the experimental results in case of $N = 2.1$ s^{-1}, 3.3 s^{-1} and $N = 1.5$ s^{-1} in the figure, the coating efficiency is hardly influenced by the disc rotation speed as far as it varies from 1.5 s^{-1} to 3.3 s^{-1}.

The relation between the mass of the seed particles M_s and coating efficiency η is shown in **Fig. 8**. The figure makes clear that η scarcely varies with M_s. Therefore, the mass of the coating particles per unit mass of the seed particles M_c/M_s naturally decreases in inverse proportion to the mass of the seed particles as seen in
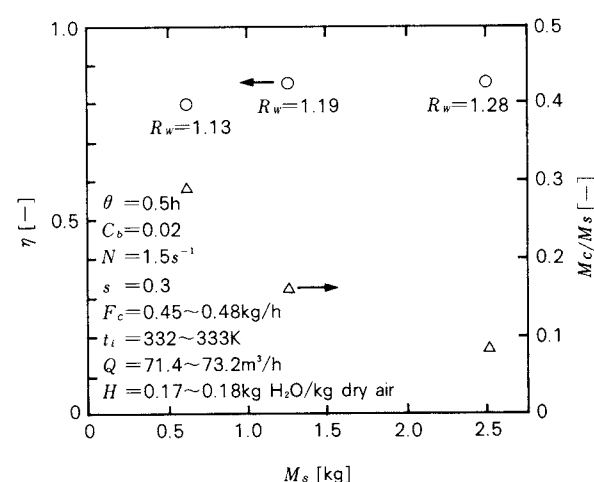
Fig. 8 Coating efficiency or coating ratios vs. mass of seed particles in a coating chamber

the figure, when the feed rate of the coating particles is kept constant.

4. 4 Influence of the additive ratio of binder on the coating efficiency

Figure 9 shows the relation between η and R_W obtained under the condition of the additive ratio of binder C_b ranging from 0 to 0.04. The operating conditions of other factors are shown in **Table 1**. In the figure, the data under the condition $C_b = 0.02$ are the ones already shown in **Figs. 6, 7** and **8**.

As clearly seen from the figure, the coating efficiency η is correlated well with R_W by in-

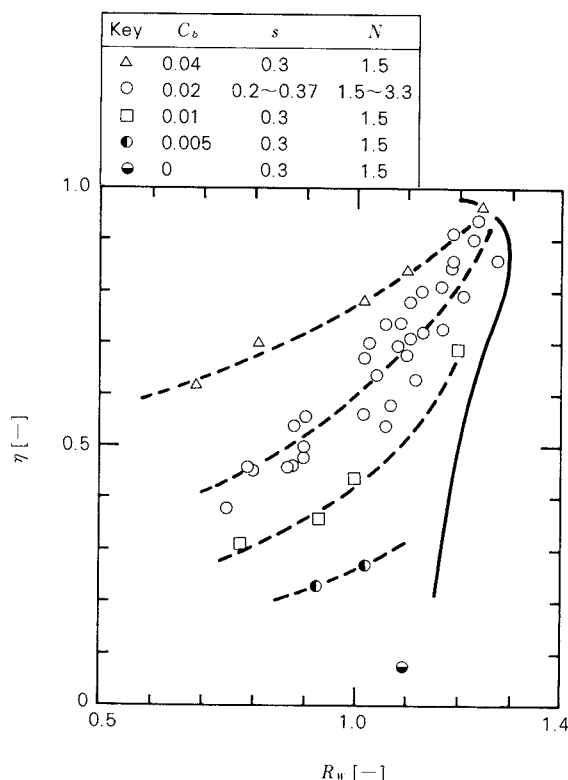| Key	C_b	s	N
△	0.04	0.3	1.5
○	0.02	0.2~0.37	1.5~3.3
□	0.01	0.3	1.5
◐	0.005	0.3	1.5
◒	0	0.3	1.5

Fig. 9 Relationship between coating efficiency and R_W

troducing C_b as a parameter and η increases with increasing C_b at the same value of R_W. η without addition of binder is so low that the addition of binder like PVA etc. is indispensable to carry out the coating with fine particles.

Although η increases with increasing R_W, there exist critical values of R_W depending upon C_b beyond which particles are inclined to agglomerate and it is no longer possible to continue coating operation.

The solid line in **Fig. 9** indicates the critical values determined roughly by the observation. The critical value of R_W varies slightly with C_b, and it gets larger a little with increasing C_b in the range $C_b < 0.02$. In the case of $C_b = 0.04$, however, 30 per cent of the whole particles become agglomerates having the size of about 3.0 mm at $R_W = 1.25$ so that the critical value of R_W is rather smaller than that in the case of $C_b = 0.02$.

As is clear from the figure, the coating efficiency of 90 per cent is able to be achieved in the case of coating Toyoura sands with Roseki under the operating conditions of $C_b = 0.02$ and $R_W \doteqdot 1.2$.

The reason why the coating efficiency η be-

comes high with increasing R_W and a parameter C_b will be discussed in the following.

The coating operation in the tumbling fluidized bed coater may be regarded as a process where the sprayed slurry droplets being dried by the hot air collide with and adhere to the seed particles being tumbled or fluidized and the coating particles in the droplets coat the surface of the seed particles by further drying.

Regarding the slurry droplets as water droplets to simplify the phenomena, the water droplets need longer time with increasing R_W for disappearance by the evaporation in the range of $R_W < 1$. On the other hand, when $R_W > 1$, only a fraction of W_T in the fed water is evaporated and the water droplets equivalent to $W_E - W_T$ still remain. Moreover the higher R_W is, the larger are the diameters of the remained droplets. Therefore the probability of the collision between the droplets and the seed particles which would dominate the coating efficiency becomes higher with increasing R_W, whether R_W is smaller than 1 or not. Consequently, the coating efficiency will become higher with increasing R_W.

According to the above-mentioned considerations, the increase of C_b is surmised to cause more droplets to collide with and to adhere to the seed particles and to give rise to the higher coating efficiency in consequence, because the drying rate of the droplets of PVA solution is small in comparison with that of the water alone[7].

4. 5 Variation of the coating efficiency with the difference in physical properties of the seed particles or the coating particles

Figure 10 shows the experimental results in the case of coating calcite having the size of 297 ~ 590 μm or ground Toyoura sands as the seed particle with Roseki and the case of coating calcite with Roseki or Kunimine clay. The experimental conditions were $s = 0.5$ and $C_b = 0.02$ in the both cases.

The coating efficiency η is correlated with R_W as well as in the case of **Fig. 9**.

If the seed particles differ in material such as calcite or Toyoura sands as well as in particle size, the relation η vs R_W is unvaried as far as the coating particles are the same. Conversely, the relation η vs R_W is different obviously depending upon the physical properties of
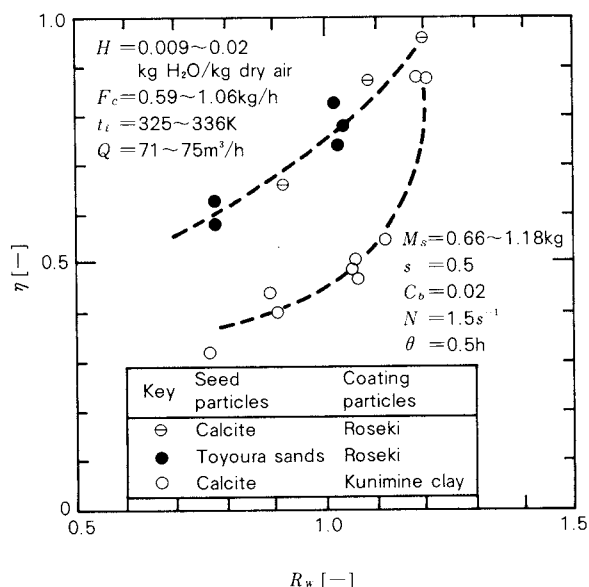
Fig. 10 panel text:

$H = 0.009 \sim 0.02$ kg H₂O/kg dry air
$F_c = 0.59 \sim 1.06$ kg/h
$t_i = 325 \sim 336$ K
$Q = 71 \sim 75$ m³/h

$M_s = 0.66 \sim 1.18$ kg
$s = 0.5$
$C_b = 0.02$
$N = 1.5s^{-1}$
$\theta = 0.5$ h

Key	Seed particles	Coating particles
⊖	Calcite	Roseki
●	Toyoura sands	Roseki
○	Calcite	Kunimine clay

η [−] R_w [−]

Fig. 10 Relationship between coating efficiency and R_W

Fig. 11 panel text:

Key	θ	R_w	η	M_c/M_s
○	0	—	—	—
△	0.5	1.13	0.80	0.29
□	1	1.14	0.89	0.64
●	2	1.22	0.97	1.46

$C_b = 0.02$
$s = 0.3$

Cumulative weight percent finer

Particle size [μm]

Fig. 11 Time change of size distribution of seed particles

coating particles if the same seed particles are used. For example, the coating efficiency of Kunimine clay is lower than that of Roseki at the same value of R_W.

This seems to be due to the fact the tensile strength of the wet powder bed reduces as the particle size increases[8]. It would be also attributed to the trend that the sprayed droplets of larger solid particles contain less fraction of liquid as confirmed by Yamada et al.[2]. In this way, the particles of Kunimine clay are less adhesive to the seed particles than Roseki and are more likely to come off from them even having adhered, since the median diameter of the former is twice as large as that of the latter.

To examine the coating efficiency more minutely and quantitatively, hereafter it is necessary to analyze the drying process of the slurry droplets in the tumbling fluidized bed and that in the coating layer of fine particles on the surface of the seed particles, particularly the case with addition of high molecular binder such as PVA.

4. 6 Growth rate of the seed particles

Figure 11 shows an example of the variation of the size distribution of the seed particles with time. The reason for the slight differences in the values of η and R_W at each coating time noticed in the figure is attributed to the fact

that the experiments were carried out individually in case of $\theta = 0.5$, 1.0 and 2.0. The figure clearly shows the steady growth of the seed particles with coating time.

As the relationships between η and R_W at each coating time agree well with the result obtained under the condition of $s = 0.3$ and $C_b = 0.02$ in **Fig. 9**, it is obvious that the coating efficiency is not affected by the coating time.

Harada et al.[4] derived the growth rate equation of uniform sized spherical seed particles in the case of coating with a eductional solution (sucrose) in a conventional fluidized bed.

In the present work, the authors deal with the coating of the seed particles having size distribution with fine particles. Then the variation of the mean diameter of the seed particles with time in the coating with fine particles is discussed below.

From the material balance of the coating particles, the following equation is obtained

$$\frac{\int_0^\infty n f(D,\theta)\phi_v D^3 \, dD - \int_0^\infty n f_0(D,\theta)\phi_{v0} D^3 \, dD}{\int_0^\infty n f_0(D,\theta)\phi_{v0} D^3 \, dD}$$

$$= \frac{M_c/(1-\epsilon)\rho_c}{M_s/\rho_s} \qquad (7)$$

where

n ; total number of seed particles
$f_0(D, \theta)$; frequency number size distribution of seed particles at $\theta = 0$

$f(D, \theta)$; frequency number size distribution of seed particles at $\theta = \theta$

ϕ_v ; volume shape factor of particles of size D at $\theta = \theta$

ϕ_{vo} ; volume shape factor of particles of size D at $\theta = 0$

Substituting $M_c = \eta F_c \theta$ into Eq. (7) yields,

$$\frac{\int_0^\infty f(D, \theta)\phi_v D^3 \,dD}{\int_0^\infty f_0(D, \theta)\phi_{vo} D^3 \,dD} - 1 = \frac{\eta F_c \theta \rho_s}{M_s(1 - \epsilon)\rho_c} \quad (8)$$

When the volume mean diameters of the seed particles at $\theta = \theta$, $\theta = 0$ and the average volume shape factors at $\theta = \theta$, $\theta = 0$ are denoted by $\overline{D}$, $\overline{D}_0$ and $\overline{\phi}_v$, $\overline{\phi}_{vo}$ respectively, the numerator and denominator of the left side of Eq. (8) are rewritten based on the definition of the volume mean diameter as follows.

$$\int_0^\infty f(D, \theta)\phi_v D^3 \,dD = \overline{\phi}_v \overline{D}^3 \quad (9)$$

$$\int_0^\infty f_0(D, \theta)\phi_{vo} D^3 \,dD = \overline{\phi}_{vo} \overline{D}_0^3 \quad (10)$$

Substituting Eqs. (9), (10) into Eq. (8), yields the growth rate equation of the seed particles in the coating process with fine particles.

$$(\frac{\overline{D}}{\overline{D}_0})^3 = \left\{ \frac{\eta F_c \theta \rho_s}{M_s(1 - \epsilon)\rho_c} + 1 \right\} \frac{\overline{\phi}_{vo}}{\overline{\phi}_v} \quad (11)$$

In Eq. (11), ϵ equals 0 for the coating with eductional solutions, and $\overline{\phi}_v/\overline{\phi}_{vo}$ equals 1.0, unless the shape of the particles varies during the coating. In this case, Eq. (11) is reduced to the equation proposed by Harada et al.

Experimental values of the volume mean diameter at each coating time are compared with the calculated ones from Eq. (11) in the following. To make use of the equation, the volume shape factor and porosity of the coating layer must be known.

Table 2 shows the measured values of the volume shape factor of the particles sifted in the ranges of $125 \sim 149 \,\mu$m and $177 \sim 210 \,\mu$m. It is clear from the table that though there exists a difference in the volume shape factors between the two groups, they increase with increasing θ, which means the particles get spherical gradually with time. This tendency was also confirmed visually on a projector.

Table 3 shows the measured values of the porosity of coating layer ϵ by the packing method. The value of the porosity of the non-coated seed particles ϵ_s was 0.37. The measured values of ϵ were 0.55 regardless of the coating ratio m_c/m_s.

The relation between the pore radius and the specific pore volume measured by the mercury porosimetry is shown in **Fig. 12**.

The pore volume consists of both the volume of interstices of coated particles and the pore volume of coating layer, as generally seen on the penetration of mercury into a layer of fine granules[5,9]. The median of the pore radius of coating layer is about 0.4 μm. The specific pore volume of the coating layer gives the porosity of 0.54, which is nearly equal to the value obtained by the packing method.

The assumption at the time when Eq. (1) was derived is not valid in the strict sense because the particle shape varies with coating time as shown in **Table 2**. However, the values of the coating ratio demonstrated in **Table 3** are not so large that the difference of the volume shape factor before and after the coating is small. Hence, it appears that the values of porosity obtained by both methods were almost the same.

Table 4 shows the experimental values of

Table 2 Measured values of volume shape factor

size range \ θ	0	0.5	1	2
$125 \sim 149 \,\mu$m	0.68	0.70	0.81	0.92
$177 \sim 210 \,\mu$m	0.63	0.68	0.72	0.76

Table 3 Measured values of porosity of coating layer

$m_s \times 10^3$	$m_c \times 10^3$	m_c/m_s	$V \times 10^6$	ϵ
49.8	0	0	30.2	0.37 (= ϵ_s)
40.1	5.63	0.14	31.5	0.55
35.9	6.84	0.19	30.5	0.55
32.4	8.03	0.25	30.0	0.55

Table 4 Comparison of experimental values of volume mean diameter of coated particles with calculated ones

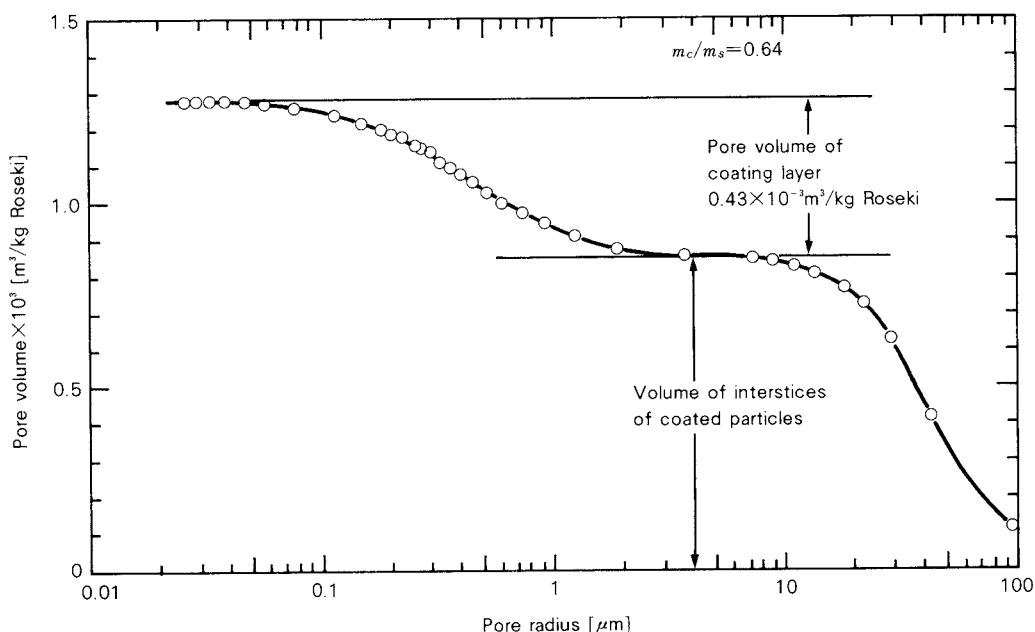| θ	0	0.5	1	2
m_c/m_s	0	0.29	0.64	1.46
$\overline{D} \times 10^6$	103	118	126	146
$\overline{D}_{cal} \times 10^6$	–	119	130	152
$\overline{D}_{cal}' \times 10^6$	–	121	137	165

Fig. 12 Pore radius distribution of coating layer
measured by mercury porosimetry

the volume mean diameter $\bar{D}$ at each coating time and the calculated values $\bar{D}_{cal}$, $\bar{D}_{cal}'$ obtained from Eq. (11) regarding as $\epsilon = 0.54$, the variation of the particle shape being taken into account and not respectively.

$\bar{D}$ was calculated from Eq. (12) on the basis of the particle size distribution shown in **Fig. 11**, assuming the volume shape factor was independent of particle size.

$$\bar{D} = \left\{ \frac{\Sigma w}{\Sigma (w/D^3)} \right\}^{\frac{1}{3}} \qquad (12)$$

In calculation of Eq. (11), the arithmetic mean values of volume shape factor of two groups shown in **Table 2** were used for $\bar{\phi}_v$, $\bar{\phi}_{v0}$.

As seen from the table $\bar{D}_{cal}$ calculated taking the variation of shape factor with time into account agrees better with the measured values than $\bar{D}_{cal}'$ obtained assuming $\bar{\phi}_{v0}/\bar{\phi}_v = 1$.

5. Conclusions

Coating of seed particles in the tumbling fluidized bed was carried out by atomizing the suspensions of clayey particles. Investigating the influence of operating factors on the coating efficiency and the growth of seed particles, the following conclusions have been obtained.

(1) The coating efficiency hardly depends on the mechanical operating factors such as the mass of the seed particles, the disk rotation speed and the coating time.

(2) Introducing the additive ratio of binder, C_b, as a parameter, the coating efficiency η is roughly related to and increased with R_W, which is an index to evaluate the synthetic effect of the thermal operating factors and the ratio of the feed rate of water as slurry droplets to the maximum theoretical evaporation rate of water in the tumbling fluidized bed coater.

η becomes high with increasing C_b under the same value of R_W. There exist critical values of R_W depending upon C_b beyond which it is no longer possible to continue the coating operation.

The instructions for the optimum operating condition of the tumbling fluidized bed coater can be obtained according to the relationship between η and R_W.

(3) The growth of the seed particles can be known as the variation of the volume mean diameter with coating time calculated from the growth rate equation proposed in this article on the basis of the material balance of the coating particles.

Nomenclature

C_b : additive ratio of binder to coating particle [kg/kg]

D : particle size [m]

$\bar{D}$: volume mean diameter of seed particle at $\theta = \theta$ [m]

$\bar{D}_0$: volume mean diameter of seed particle at $\theta = 0$ [m]

$\bar{D}_{cal}$: $\bar{D}$ calculated from Eq. (11) taking account of volume shape factor [m]

$\bar{D}_{cal}'$: $\bar{D}$ calculated from Eq. (11) regarding as $\bar{\phi}_{v0}/\bar{\phi}_v = 1$ [m]

F_c : feed rate of coating particle [kg/h]

$f(D, \theta)$: frequency number size distribution of seed particle at $\theta = \theta$ [−]

$f_0(D, \theta)$: frequency number size distribution of seed particle at $\theta = 0$ [−]

H : humidity of inlet air [kg H$_2$O/kg dry air]

H_s : adiabatic saturation humidity of inlet air [kg H$_2$O/kg dry air]

H' : humidity of outlet air [kg H$_2$O/kg dry air]

M_c : total mass of coating particle adhering to seed particle of mass M_s [kg]

M_s : total mass of seed particle in coating chamber [kg]

M_p : mass of coated particle of size D and number n_p [kg]

m_c : mass of coating particle adhering to seed particle of mass m_s [kg]

m_s : mass of seed particle [kg]

N : rotation speed of disk [s^{-1}]

n : total number of seed particle in coating chamber [−]

n_p : number of particle of size D and mass M_p [−]

Q : volume flow rate of inlet air [m^3/h]

R_W : index defined by W_E/W_T [−]

s : slurry concentration [kg/kg]

t_i : temperature of inlet air [K]

t_r : room temperature [K]

t_s : adiabatic saturation temperature [K]

t : temperature at H' on adiabatic cooling line [K]

V : packing volume of particle [m^3]

v : humid volume of inlet air [m^3/kg dry air]

W_E : feed rate of water as slurry droplet [kg/h]

W_G : mass flow rate of inlet air [kg/h]

W_T : maximum theoretical evaporation rate of water in coating chamber [kg/h]

w : mass fraction of particle of size D [−]

ϵ : porosity of coating layer [−]

ϵ_s : porosity of packed bed of seed particle [−]

η : coating efficiency $(= M_c/F_c\theta)$ [−]

θ : coating time [h]

ρ_c : density of coating particle [kg/m^3]

ρ_s : density of seed particle [kg/m^3]

ρ_p : density of coated particle [kg/m^3]

ϕ_v : volume shape factor of particle of size D at $\theta = \theta$ [−]

ϕ_{v0} : volume shape factor of particle of size D at $\theta = 0$ [−]

$\bar{\phi}_v$: average volume shape factor at $\theta = \theta$ [−]

$\bar{\phi}_{v0}$: average volume shape factor at $\theta = 0$ [−]

References

1) Kobayashi, N. and J. Imai: *Kagaku Kojo*, 17, No.5, 87 (1973).

2) Yamada, N., H. Hirosue, A. Ihara and T. Murayama: *J. Soc. Powder Technol., Japan,* 20, 211 (1983).

3) Yamada, N.: *ibid.,* 20, 218 (1983).

4) Harada, K. and J. Fujita: *Kagaku Kogaku,* 31, 790 (1967).

5) Mukaida, K.: *Powder Technology,* 29, 99 (1981).

6) Ushiki, K. and K. Iinoya: *J. Res. Ass. of Powder Technol., Japan,* 13, 315 (1976).

7) Sano, Y. and S. Nishikawa: *Kagaku Kogaku,* 29, 294 (1965).

8) Williams, J. C. and T. Allen: "Hand book of Powder Technology", Vol. 1, p.32, Elsevier (1980).

9) Yamada, N. and H. Hirosue: *J. Soc. Powder Technol., Japan,* 21, 482 (1984).

Enrichment Behavior of Sulfur on Ash Particles and Collection Characteristics of Electrostatic Precipitator in Pulverized Coal Combustion System[†]

Ken Okazaki, Takashi Nishikawa and Kazutomo Ohtake
Department of Energy Engineering
Toyohashi University of Technology *

Abstract

Physicochemical properties of ash particles and their effects on the collection characteristics of electrostatic precipitator in the pulverized coal combustion system were investigated, focussing on enrichment processes of sulfur on the particle surface. An experimental system composed of one-dimensional laminar flow furnace, cyclone, bag-filter and electrostatic precipitator was used to derive the mutual relations among coal properties, combustion conditions and characteristics of ash particles collected in each device. The following conclusions were obtained.

1) Chemical properties on the particle surface are affected not only by the shape and surface structure of particles but also by particle size, temperature history and coal properties.

2) Soot particulates attached to the small ash particles enhances the enrichment of sulfur on them, and this effect depends on coal properties and combustion conditions.

3) Collection characteristics of ash particles in the electrostatic precipitator largely depend on the enrichment behavior of sulfur in it for the case of high sulfur coal.

1. Introduction

Pulverized coal combustion is now likely to become increasingly important for electrical power generation. Among various pollutants from pulverized coal combustion system, fly ash particles formed from the mineral matter in the coal are one of the most important emissions of environmental concern. In a practical system, almost all fly ash particles are collected mainly in the electrostatic precipitator equipped in the down stream, and the collection performance is largely affected by the electrical properties such as electrical resistivity and dielectric constant of particles, which will de-

pend on the chemical compositions of particle surface[1]. Further, some of hazardous elements such as As, Se, Pb etc. would evaporate in the high temperature zone of the furnace, condense and enrich especially on the small ash particles[2] in the down stream and could be exhausted into atmosphere from the system, because of the relatively low collection efficiency for the very small submicron particles in an electrostatic precipitator[3]. So, it is very important for the development of a system of low pollutant emissions to make clear the physicochemical characteristics of ash particles and its correlations with the combustion conditions, coal properties and collection performance of electrostatic precipitator.

Recently, there have been reported the investigations on the ash formation processes[4] and enrichment of trace elements on the particle surface[2,5,6]. However, there are few reports which discuss the performance of electrostatic precipitator with considering

physicochemical processes of particle formation in the furnace and its down-stream.

From the point of view above, this study is intended to investigate the physicochemical properties of various types of ash particles, especially enrichment behavior of sulfur, and their effects on the collection characteristics of ash particles in an electrostatic precipitator by use of an experimental system composed of one-dimensional pulverized coal combustion furnace, cyclone, bag-filter and cylindrical electrostatic precipitator. This type of combustion furnace has a large advantage of giving the pure effects of coal properties and experimental conditions on the ash particle formation.

2. Experimental system and procedure

A schematic of the experimental system used in this study is shown in **Fig. 1**. The method of one-dimensional combustion[7] was adopted to eliminate the effect of turbulent mixing on the properties of exhaust gas and particles, and so the pure effects of coal properties on the particle formation could be derived in this system. The mixture of coal dust and air enters into the combustion furnace through a radiation shielding grid and burns one-dimensionally. Experiments were performed under the condition of excess air ratio of 1.2 and maximum temperature of 1500°C, which corresponds to that of practical boilers, and the coal feeding rate was about 3 kg/h. As a fuel, eight different kinds of pulverized coals shown in **Table 1** were used.

Almost of the exhaust gas flows through a cyclone and bag-filter and is exhausted into atmosphere, and a part of it (about 15% by volume) is branched after the ash reservoir

① Filter ② Dust collecting electrode
③ Discharge electrode ④ Heater
⑤ Insulator
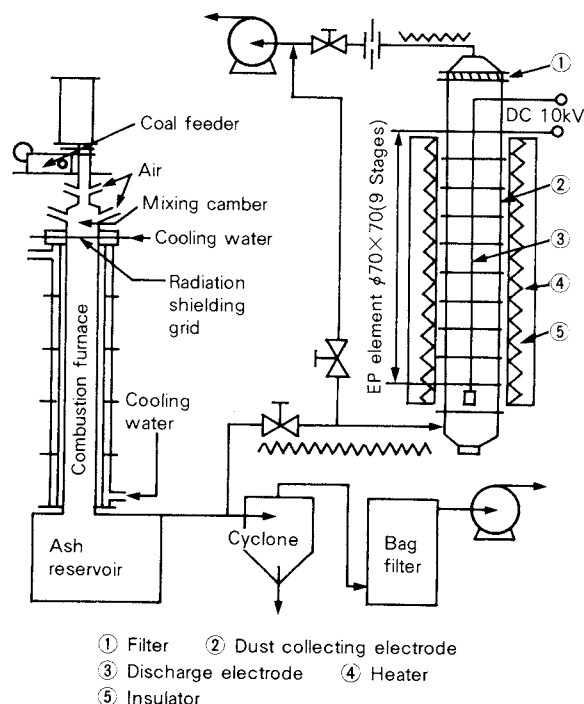
Fig. 1 Experimental apparatus

and introduced into the cylindrical electrostatic precipitator. The temperatures of cyclone and bag-filter are maintained to be 450°C and 100°C, respectively. The electrostatic precipitator consists of a discharge electrode wire of 0.4 mm in diameter set at the center line of the cylinder and a cylindrical collecting electrode which is 70 mm in inner diameter and 630 mm in length piled of nine cylindrical stages. At the exit of the electrostatic precipitator, a back-up filter is set to collect the submicron fine particles passed through the stages of electrostatic precipitator. The whole part of the electrostatic precipitator is heated up to be 150°C. Combustion products flows from the bottom to top and the gas flow velocity was

Table 1 Coal properties

| | Coal | Proximate analysis (%) | | | | Ultimate analysis (%, dry) | | | | | HHV (MJ/kg) |
		M	Ash	VM	FC	C	H	O	N	S	
Japan	A	5.5	14.9	42.0	37.6	65.4	5.47	12.5	0.79	0.21	26.5
	B	3.2	19.6	40.0	37.2	62.8	5.16	10.6	0.92	0.30	26.1
	C	1.4	17.7	38.5	42.4	67.0	5.00	7.4	0.66	2.70	28.9
China	D	5.8	7.8	27.8	58.6	77.3	3.98	9.0	0.79	0.70	29.7
Australia	E	4.4	10.1	26.1	59.4	73.6	4.08	9.8	1.60	0.35	28.8
	F	3.0	10.8	32.5	53.7	73.3	4.53	9.0	1.59	0.51	29.5
	G	3.7	8.8	34.3	53.2	75.2	5.04	8.8	1.48	0.38	30.5
South Africa	H	2.4	14.8	25.5	57.3	70.5	3.64	8.3	1.64	0.99	28.1

M: Moisture, VM: Volatile matter, FC: Mixed carbon, HHV: High heat value

set to be 1.0 m/s in this experiment.

After the experiment, ash particles collected in the electrostatic precipitator were recovered and the weight fraction of them in each stage was measured. Particles collected in the cyclone, bag-filter and each stage of the electrostatic precipitator were quantitatively analyzed by X-ray microanalyzer (XMA) and physicochemical features of them were systematically investigated. In the quantitative analyses by XMA, NBS 1633a was used as a standard sample, and elimination of back-ground, separation of the overlap of peaks and many other important corrections (ZAF correction) were performed by use of a microcomputer in order to obtain the individual characteristics of X-ray intensity. Weight fraction of unburned carbon in the collected ashes were also measured by the method defined by JIS standard.

3. Characteristics of ash particles

The physical and chemical analyses of ash particles could give us a lot of informations about their formation processes. In this chapter, the characteristics of ash particles relating to the combustion and ash formation processes are discussed, and the attention is especially focussed on the surface concentrations of elements on the ash particles of various shapes and structures.

Among the ash particles collected in the down-stream devices, two typical shapes of spherical and non-spherical particles are observed. The surfaces of spherical particles almost look like smooth, while non-spherical particles are classified into two types of surface structures of smooth and porous. The typical SEM photographs of these types of particles obtained by use of coal A are shown in **Fig. 2**. The **Photo (a)** shows a spherical smooth particle sampled in the cyclone, **(b)** a non-spherical porous particle in the same stage and **(c)** both spherical and non-spherical particles with smooth surface in the bag-filter. The **Photo (d)** was taken after oxidizing the bag-filter ash particles in an electric furnace and powdery materials observed on the particles in **Photo (c)** have disappeared. So, these powdery materials on the bag-filter ash particles could be considered as soot substances. Every photo has the cross marks and numbers. The marks represent the analyzed points by XMA and, for

(a) Cyclone ash (spherical)

(b) Cyclone ash (non-spherical, porus)

(c) Bagfilter ash (spherical and non-spherical)

(d) Bagfilter ash (spherical, burned)
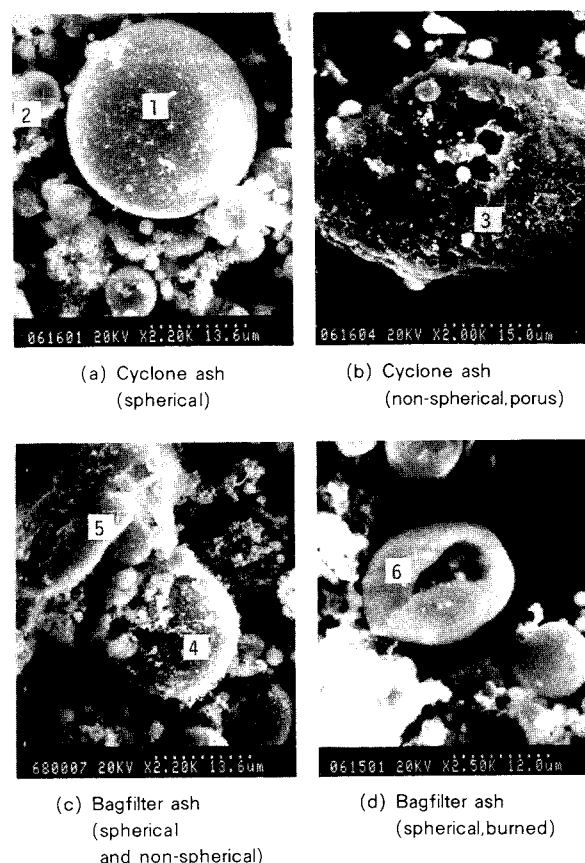
Fig. 2 SEM photographs of various kinds of ash particles (cross marks indicate the points analyzed by XMA)

examples, energy dispersive XMA spectra obtained for the points 1, 3 and 5 are shown in **Figs. 3 (a)**, **(b)** and **(c)**, which give the informations of the surface concentrations of elements indicated.

By the comparisons of the results obtained for the points 1 − 6, the following well-defined characteristics of selective existence of elements depending on the shapes and surface structures are noticed. The result at point 1 on the smooth spherical particle in the spectrum (a) shows that the most part of surface elements are occupied by Si and Al, and Ca, Fe, Mg and P follow those two elements in order. The points 2, 4 and 6 also give almost the same tendencies. The elements and their concentrations mentioned above could be considered to be typical for the smooth spherical particles. On the contrary, at the point 3 on the porous surface of non-spherical particles as shown in the spectrum (b), the concentrations of the elements other than Si and Al, especially sulfur, become higher than those at the point 1. Further, at the point 5 on the smooth surface of

VS : 66k
HS : 20keV
(10eV/CH)
PREC : 500sec
ELAP : 500sec

(a) Spherical particle

VS : 2K
HS : 20keV
(10eV/CH)
PREC : 500SEC
ELAP : 500SEC
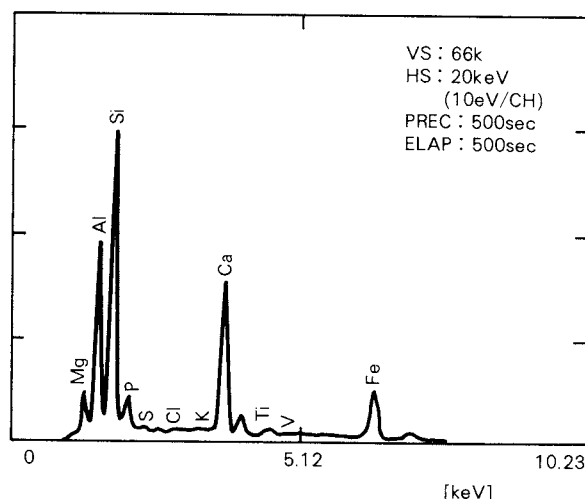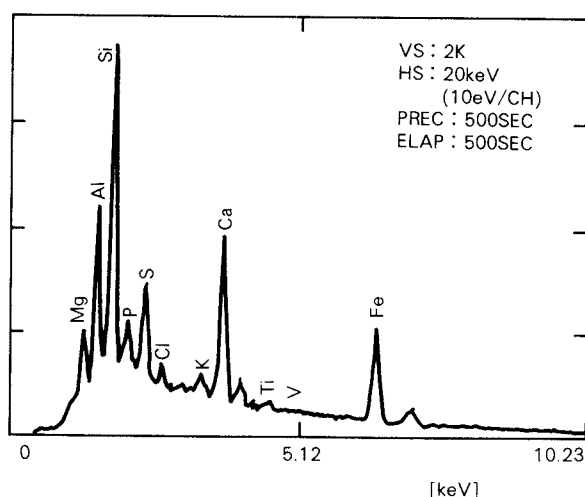
(b) Non-spherical particle
(Porous surface)

VS : 66k
HS : 20keV
(10eV/CH)
PREC : 500SEC
ELAP : 500SEC
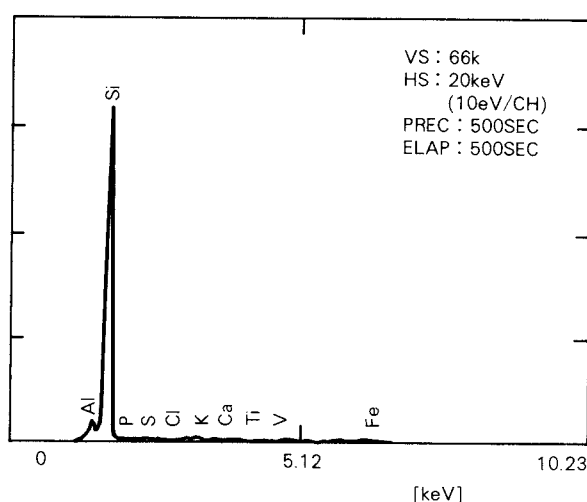
(c) Non-spherical particle
(Smooth surface)

Fig. 3 Energy dispersive XMA spectra (a)-point 1,
(b)-point 3, (c)-point 5

non-spherical particles, Si predominates over other elements as shown in the spectrum (c).

These elements analyzed above are considered to exist on the particle surface in the form of oxides, such as SiO_2, Al_2O_3, Fe_2O_3, CaO and so on. $Ca(OH)_2$ and $CaSO_4$ formed under the conditions with H_2O and SO_2 would largely contribute to the electrical conductivity and dielectric constant of particles, which affect the collection efficiency of ash particles in an electrostatic precipitator. From the results mentioned above, we can conclude that the materials which could have much influence on the performances of electrostatic precipitator might be not all over but locally condensed on the particles depending on the shape and surface structure of ash particles.

4. Enrichment of sulfur on ash particles

Various important elements on the surface of ash particles were quantitatively analyzed by XMA. Among them the authors are especially interested in the concentration of sulfur, which largely affects the performance of electrostatic precipitator. Though sodium is considered to be important from the same stand point of view, the discussion on it has been eliminated in this study because of the uncertainty of its quantitative data.

Here, the enrichment factor is introduced defined as

$$EF_x = \frac{(C_x/C_{ref})_{ash}}{(C_x/C_{ref})_{coal}} \tag{1}$$

where, C_x denotes the concentration of element x, and C_{ref} is that of the reference element in the sample. Si was selected as the reference element because of the stability of its concentration which is not affected by diameter and temperature history of ash particles.

Enrichment factors of sulfur on the various types of ash particles obtained for coal A are shown in **Fig. 4**. There are little effects of diameter and surface structure on the enrichment factor of sulfur for the cyclone ash. On the contrary, for the bag-filter ash, very large enrichment factors up to 5 appear on the porous surface of non-spherical particles, and enrichment factors for spherical particles increase with the decreasing diameter.

Figure 5 shows the effect of particle size on the enrichment of sulfur on the spherical parti-
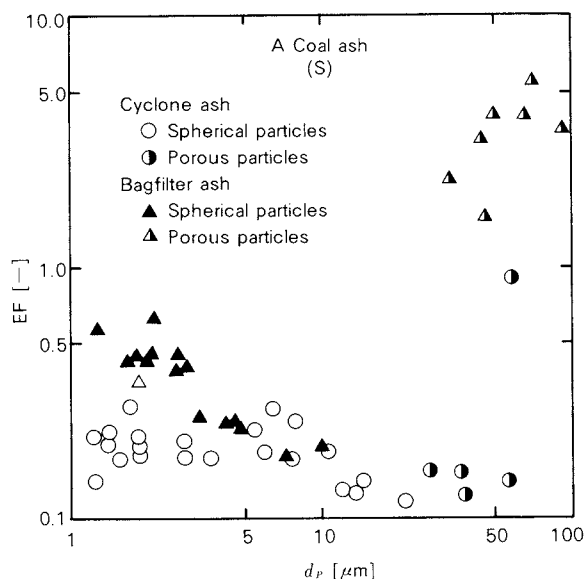
Fig. 4 Enrichment factors of sulfur on various kinds of ash particles

(a) A Coal ash

(b) H Coal ash
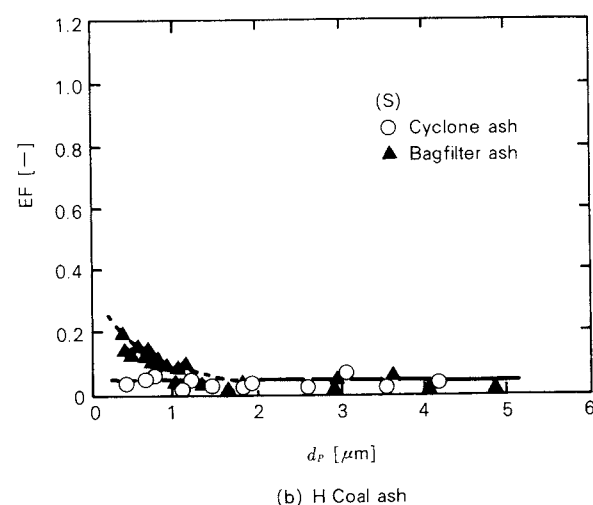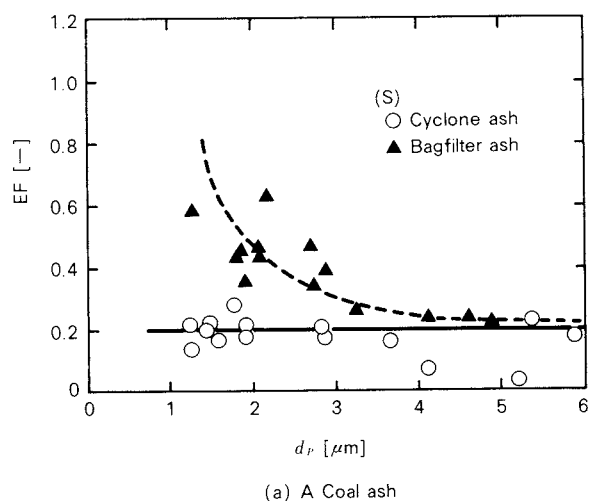
Fig. 5 Effect of particle size of enrichment factor of sulfur (spherical particles from cyclone and bag-filter)

cles. **Figs. 5. (a)** and **(b)** are the results for coal A and H, respectively. In both cases of **(a)** and **(b)**, it is clearly shown that enrichment has occurred selectively on the small particles of bag-filter ash, while little effect of particle size appears for cyclone ash. The deferences between the two enrichment behaviors for cyclone and bag-filter ashes could be explained by that the condensation and enrichment process of sulfur must have proceeded through the path from cyclone (450°C) to bag-filter (100°C) and that, in this process, the effect of diffusion of gas-phase sulfur compounds to the particle surface is larger for the smaller particles. Sulfur condensed on the particle surface is considered to exist mainly as the form of H_2SO_4 formed in the presence of H_2O and SO_3.

The effect of the enrichment of sulfur on the small particles of bag-filter ash is stronger for high volatile coal A than for low volatile coal H as distinctly shown in **Fig. 5**. The reason of this result could be due to that the soot particulates formed and attached on the ash particle surface must have a strong effect on the condensation process of sulfur on the particles, because less soot materials were observed on the bag-filter ash of coal H than on that of coal A.

In order to confirm the validity of this assumption above, unburned carbon contents in the cyclone and bag-filter ashes were measured as a function of volatile matter content in the raw coal for eight kinds of coals shown in **Table 1**. The result obtained is shown in **Fig. 6**. Cyclone ashes have lower unburned carbon content for higher volatile coals because high volatile coal has higher combustibility. On the other hand, the bag-filter ashes have higher unburned carbon content for higher volatile coals. The discrepancy of the unburned carbon content clearly corresponds to the gas-phase induced soot formed from hydrocarbons in the evolved volatile matter. This means that much more soot would have attached on the ash particles of high volatile coal A than low volatile coal H. The importance of the effect of soot particulates on the enrichment of sulfur could be also proved by the additional experiments in an electric furnace as described in the next section.

Ash particles with soot on it and those with-
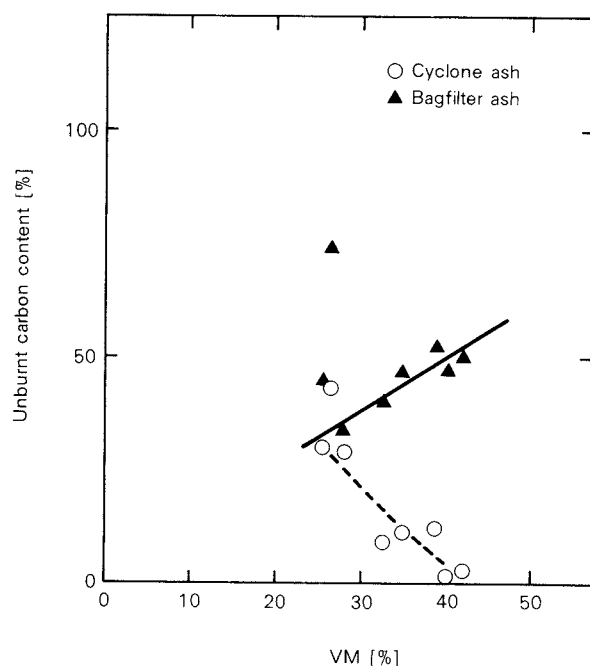
Fig. 6 Effect of volatile matter content in
the raw coal on the unburned carbon
content in the ashes

Fig. 7 Effect of soot particulates on the
enrichment behavior of sulfur

out soot artificially obtained by burning them at 815°C were dropped in a vertical electric furnace of 130°C, in which artificial gas having the similar concentrations of H_2O and SO_2 to the exhaust gas of coal combustion were flowed. The enrichment factors of those ashes collected at the bottom of the electric furnace are shown in **Fig. 7**. There appears the strong enrichment of sulfur for the smaller particles of ash with soot, while there is no such effect for burned ash without soot. Then it has been remarkably verified that gas-phase induced soot attached on the ash particles largely enhances the enrichment of sulfur on them. In fact, many soot particulates on the small ash particles were observed in the TEM photographs. In the practical furnace of coal combustion, such effect would not appear so much because of rather low amount of soot or unburned carbon in the exhaust gas.

From the investigation above, it has been made clear that chemical characteristics of ash particles and enrichment behaviors of volatile element such as sulfur are largely affected not only by the shapes and surface structures of ash particles but also by the particle size, temperature history of ash formation, raw coal properties and combustion conditions.
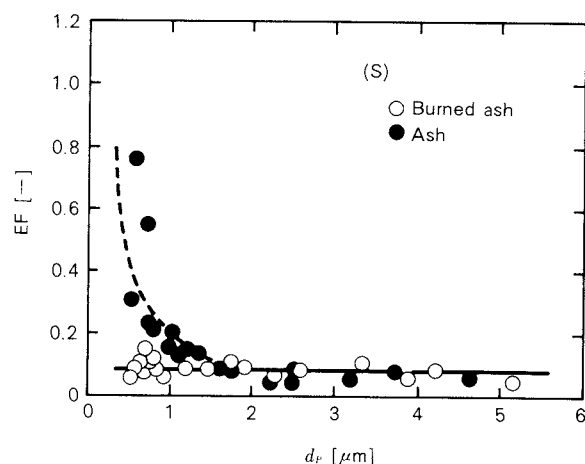
5. Collection characteristics of electrostatic precipitator

In this chapter, collection characteristics of ash particles in an electrostatic precipitator are investigated taking into consideration the physicochemical characteristics of ash particles, especially the enrichment behavior of sulfur described above. The ash particles obtained in the electrostatic precipitator were observed by SEM and analyzed by XMA, and the weight fraction of collected ash particles in each stage (from first to ninth) of electrostatic precipitator was measured.

For spherical particles, the drift velocity of a particle in an electrostatic precipitator is given as[8]

$$v = \frac{\epsilon_o E_o E_p}{3\mu} k_o d_p \qquad (2)$$

and the collection efficiency comes to be higher for the larger drift velocity. Here, dielectric coefficient k_o is given as

$$k_o = 3\epsilon_s / (\epsilon_s + 2) \qquad (3)$$

and is a weak increasing function of ϵ_s, which is larger for higher concentration of sulfur on the particle surface. From Eqs. (2) and (3), it can be seen that the drift velocity is larger and then the collection efficiency is higher for larger particles and larger enrichment of sulfur. For this reason, by the results of SEM observation, almost all relatively large non-spherical and porous particles were collected at the first stage of electrostatic precipitator and particles
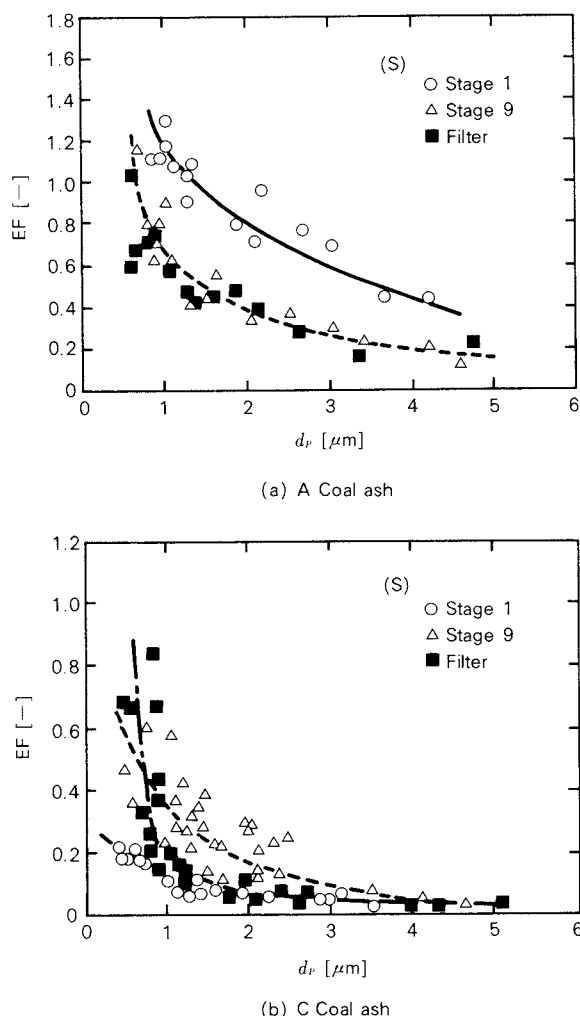
78

(a) A Coal ash

(b) C Coal ash

Fig. 8 Enrichment behaviors of sulfur on the ash particles collected in the electrostatic precipitator

Fig. 9 Collection characteristics of ash particles in the stages of electrostatic precipitator

collected in the following stages (second to ninth) are mostly spherical, the diameter of which rapidly becomes smaller along the latter stages.

The dependence on the particle size of the enrichment factors of sulfur on the surface of spherical particles collected in the first and ninth stages and back-up filter are shown in **Fig. 8** for low sulfur coal A and high sulfur coal C. The tendency of sulfur enrichment on the smaller particles appears in each ashes, though the enrichment behavior is very much different by the coal type. For low sulfur coal A, the enrichment process have finished before the entrance of electrostatic precipitator, and so the particles collected in the earlier stage have larger enrichment factors of sulfur. And, for the particles with the same enrichment factors of sulfur, the larger particles have col-

lected in the earlier stages. These results agree very well with the description of Eq. (2) for the drift velocity.

On the contrary, for high sulfur coal C, there must still have been the enrichment processes even in the electrostatic precipitator and enrichment behavior is very much complicated. The small submicron particles have a low collection efficiency as indicated by Eq. (2) and so those particles have higher enrichment factors of sulfur for the particles collected in the latter stages. For the particles from 1 μm to 3 μm, particles of the ninth stage have a larger enrichment than those of back-up filter and this result could be due to that sulfur enriched particles have been selectively collected in the earlier stages because of higher dielectric constant. The particles larger than 3 μm have low and almost constant enrichment factors.

For the ashes of coal C which have a very complicated but interesting behaviors of sulfur enrichment, the weight fractions of ashes collected in each stage of electrostatic precipitator are shown in **Fig. 9** by a bar graph. The weight fraction of ashes collected at the back-

up filter was very small and almost all ashes have been collected in the collecting electrodes. From this result, we can see the well-known tendency that the weight fraction decreases expotentially from bottom to top.

The solid line in **Fig. 9** is the calculated result with the assumption that every particles have the same chemical and electrical properties and that the drift velocity of Eq. (2) depends only on the particle size. As for the initial condition for the particle size distribution at the entrance of electrostatic precipitator, the measured data by the image analyzer were used. However, there exists a large discrepancy between the solid line and the measured results.

On the other hand, the dashed line in **Fig. 9** was obtained by introducing the effect of sulfur enrichment process in the electrostatic precipitator as shown in **Fig. 8(b)**. In this case, sulfur enrichment behaviors in the electrostatic precipitator which affect dielectric constant of particles and then drift velocity of them have been taken into consideration according to Eqs. (2) and (3). This result of dashed line agrees much better with the measured results than the solid line.

From the results above, we can emphasize that it is very important to consider the detailed enrichment processes of elements such as sulfur, which have a strong effect on the electrical properties of ash particles, in order to predict the correct collection performance of electrostatic precipitator in a pulverized coal combustion system.

6. Conclusions

The correlations between physicochemical properties of ash particles and collection characteristics of particles in an electrostatic precipitator have been investigated with focussing on the enrichment behavior of sulfur and considering the effect of coal properties and combustion conditions on it. The following important conclusions have been obtained.

1) Chemical properties of ash particles largely depends on their shapes and surface structures. Spherical particles mainly consist of Al and Si, non-spherical particles with smooth surface are exclusively made of Si, and on the surface of porous particles there exist rather high concentrations of volatile elements such as S and Cl.

2) The enrichment and recondensation processes of sulfur which have evaporated in the combustion process would proceed with decreasing temperature in the down stream and largely depend on the temperature history of the particles. The enrichment factors become higher for smaller particles, if they are spherical, and for the particles with porous surface.

3) The tendency of sulfur enrichment on the smaller spherical particles are much stronger for high volatile coals than for low volatile ones. This is due to the fact that gas-phase induced soot formed from volatile matter and attached on the ash particles largely enhances the enrichment of sulfur on them.

4) The enrichment behaviors of sulfur on the ash particles have a strong effect on their collection characteristics in an electrostatic precipitator. Especially for the case where the enrichment process still proceeds in an electrostatic precipitator, it is essential to consider their effects on the changes of electrical properties of particles in the electrostatic precipitator in order to grasp its detailed performances.

Acknowledgement

Nomenclature

C_x	: mass fraction of element x	[−]
d_p	: diameter of ash particle	[m]
E_o	: electric field of particle charging	[V/m]
E_p	: electric field near collecting electrode	[V/m]
EF	: enrichment factor	[−]
k_o	: dielectric coefficient defined by Eq. (3)	[−]
VM	: volatile matter content in coal	[%]
v	: drift velocity of ash particles	[m/s]
ϵ_o	: dielectric constant of free space	[F/m]
ϵ_s	: relative dielectric constant of ash particles	[−]
μ	: viscosity of exhaust gas	[kg/m·s]

References

1) Masuda, S.: "Handbook of Electrostatics", Chap. 16 (1981).

2) Coles, D.G., R.C. Ragaini, J.M. Ondov, G.L. Fisher, D. Silberman and B.A. Prentice: *Environ. Sci. and Techn.,* **13**, 4, 455 (1979).

3) Markowski, G.R., D. S. Ensor and R. G. Hopper: *Environ. Sci. and Techn.,* **14**, 11, 1400 (1980).

4) Flagan, R.C.: Spring Meeting of the Western States Section, The Combustion Institute, No. 77-4 (1977).

5) Neville, M. and A. F. Sarofim: 19th Symp. (Int.) on Combustion, The Combustion Institute, 1441

6) Smith, R.D.: *Prog. Energy Combust, Sci.,* **6**, 53 (1980).

7) Okazaki, K., K. Ohtake and T. Nishikawa: *ASME-JSME Thermal Engineering Conf.,* **4**, 143 (1983).

8) Iinoya, K.: "Shujin Souchi". p.233, Nikkan Kogyo Shinbunsha (1963).

9) Masuda, S.: Preprints of the 47th Annual Meeting of The Soc. of Chem. Engrs., Japan, p. 200 (1982).

Particle Size Measurement Based on Detection
of Unbalance by Centrifugal Sedimentation†

Noriyoshi Kaya and Tohei Yokoyama
*Hosokawa Micromeritics Laboratory**

Msafumi Arakawa
Department of Inorganic Materials
*Kyoto Institute of Technology***

Naohiko Yazawa
*Akashi Seisakusho Ltd.****

Abstract

For the purpose of determination of particle size distribution in the submicron range, a new apparatus has been developed on a basis of the principle of the balancing machine.

The change of balancing moment caused by the centrifugal sedimentation of the particles is detected with the sensors attached onto the rotor shaft and analyzed with personal computer, which gives particle size distributions according to the calculation proposed by one of the authors previously.

One of the advantages of this method is that the measurement by this method do not depend on the physical properties such as optical extinction coefficient, electric conductivity and so forth. It is also possible to determine the size distribution of the particles in a suspension of much higher concentration by this method than other ones. Furthermore, it is not necessary for the settling time of the particle to reach the detecting zone because the analysis by this method monitores the unbalance caused from the settling particles positioned in the whole suspension.

1. Introduction

The sedimentation method is one of the most popular ways to measure the particle size distribution of fine powders in the liquid phase. In order to determine the particle size in the submicron range, the sedimentation method is to be conducted in the field of the centrifugal force. Because of the simplicity in the measurement, photosedimentmeter in which the particle concentration is determined from the transmission of the light through the suspension has been often used as one of the sedimentation methods. This method, however, requires the different coefficient for each material depending on the physical properties and the particle size of the sample powder.

One of our authors has previously proposed a sedimentation method based on detecting the magnitude of unbalance of a rotor caused by the centrifugal settling of the particles in a cell set in the rotor to obtain the particle size distribution[1]. Resting on the basis of this principle, a new apparatus for size analysis has been constructed recently equipped with a microcomputer to process the data of unbalance swiftly. In order to shorten the time required for the measurement, it was attempted to increase the rotation speed linearly to a constant

value during the measurement and to determine the size distribution from the data during the period of the linear acceleration and the constant rotation[2,3].

The measurement using this analyzer was carried out in the size range down to 0.03 μm with a sample having a good dispersibility to examine the reliability of the results and to find the lower limit of the size measurable by this method.

Some results of the size distribution obtained with this analyser were compared with those by other methods using the same sample.

2. Principle

The equation of motion of a single particle having a radius r in the field of the centrifugal force with an angular velocity ω is expressed as follows,

$$\frac{dx}{dt} = \frac{2}{9} \left(\frac{\rho_P - \rho_L}{\mu_L} \right) r^2 \omega^2 x \tag{1}$$

where ρ_P [kg/m^3] is the particle density,
       ρ_L [kg/m^3] is the liquid density,
       μ_L [Pa·s] is the liquid viscosity,
       x [m] is the distance from the center in the radial direction.

Equation (1) is integrated under the condition of $x = x_i$ at $t = 0$, producing

$$\ln\left(\frac{x}{x_i}\right) = Kr^2 \omega^2 t \tag{2}$$

where

$$K = \left(\frac{2}{9}\right)\left(\frac{\rho_P - \rho_L}{\mu_L}\right) \tag{3}$$

When $Kr^2\omega^2 t$ is replaced by T, Eq. (2) becomes

$$x = x_i e^\tau \tag{4}$$

The displacement of the center of gravity caused by the sedimentation of the particles in the cell is divided into the one due to the particles which have settled onto the bottom of the cell and the one due to the particles settling in the suspension as shown in **Fig. 1**.

Asumming that the particles located between x_i and x_m at $t = 0$ settle out of the suspension completely by $t = t$, the displacement of the center of gravity caused by these particles ϵ_a is given in the following equation.[2]

$$\epsilon_a = \frac{m}{M} \frac{(1 - e^{-\tau})^2 x_m^2}{2(x_m - x_o)} \left(\frac{\rho_P - \rho_L}{\rho_P}\right) \tag{5}$$
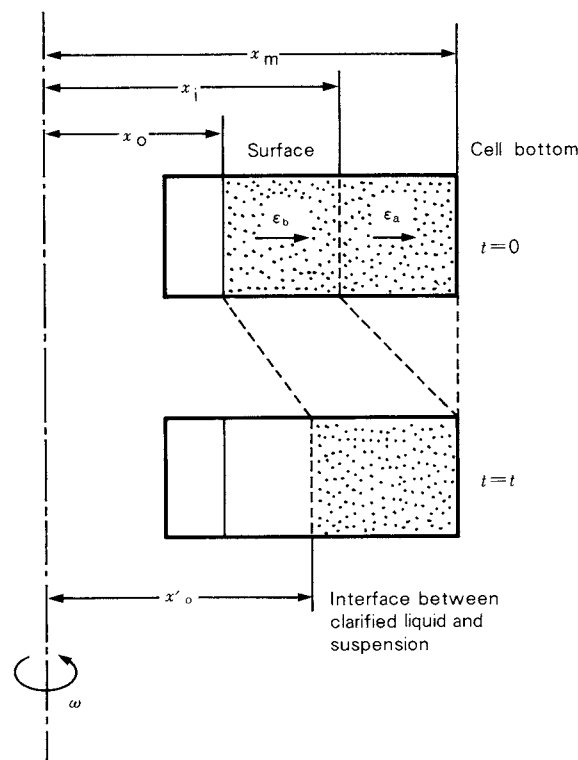
Fig. 1   Schematic diagram of unbalance caused by centrifugal sedimentation

where
     m [kg] is the weight of the particles in the cell,
     M [kg] is the weight of the rotating system.

In the similar way, assuming that the particles located between x_o and x_i at $t = 0$ do not reach the bottom of the cell by $t = t$, the displacement of the center of gravity caused by these particles is given in the following equation.

$$\epsilon_b = \frac{m}{M} \frac{(e^\tau - 1)(x_m^2 e^{-2\tau} - x_o^2)}{2(x_m - x_o)} \left(\frac{\rho_P - \rho_L}{\rho_P}\right) \tag{6}$$

The total displacement of the center of gravity ϵ is obtained as the sum of ϵ_a and ϵ_b from Eqs. (5) and (6).

$$\epsilon = \epsilon_a + \epsilon_b = \frac{m}{M}\left(\frac{\rho_P - \rho_L}{\rho_P}\right) \frac{(e^\tau - 1)(x_m^2 e^{-\tau} - x_o^2)}{2(x_m - x_o)} \tag{7}$$

Therefore the magnitude of unbalance $U = \epsilon M$ is

$$U(T) = m\left(\frac{\rho_P - \rho_L}{\rho_P}\right) \frac{(e^\tau - 1)(x_m^2 e^{-\tau} - x_o^2)}{2(x_m - x_o)} \tag{8}$$

From Eq. (8), the magnitude of unbalance caused by the monodispersed particles with a radius R and a total weight m is expressed in the following form.

$$U(t) = A(r, t)m \qquad (9)$$

On the linear acceleration of the rotor speed, the coefficient A is calculated as follows.

$$A(r, t) = (\frac{\rho_P - \rho_L}{\rho_P}) \frac{(e^\tau - 1)(x_m^2 e^{-\tau} - x_o^2)}{2(x_m - x_o)} \qquad (10)$$

In case that the sample contains the particles of different sizes, Eq. (9) will change to a series of equations.

$$U(t) = \sum_{i=1}^{n} m_i \cdot A(r_i, t) \qquad (11)$$

Equation (11) is expressed in the following matrix equation for the measuring time from t_1 to t_m.

$$\begin{pmatrix} A(r_1,t_1) & A(r_2,t_1) \ldots\ldots A(r_n,t_1) \\ A(r_1,t_2) & A(r_2,t_2) \ldots\ldots A(r_n,t_2) \\ \vdots & \vdots \\ A(r_1,t_m) & A(r_2,t_m) \ldots A(r_n,t_m) \end{pmatrix} \begin{pmatrix} m_1 \\ m_2 \\ \vdots \\ m_n \end{pmatrix} = \begin{pmatrix} U(t_1) \\ U(t_2) \\ \vdots \\ U(t_m) \end{pmatrix} \qquad (12)$$

In this way, when the magnitude of unbalance at each measuring time $t = t_1, t_2, \ldots, t_m$ and each corresponding element of the coefficient matrix are known, the masses $m_1, m_2, \ldots, m_n$ of the particles having each size are calculated, which gives the size distribution on the mass basis.

The calculation of the inverse matrix of Eq. (12) was carried out by the method of conjugate grandients which is suitable for the rapid computation with small capacity of memories.

This method has the following three advantages.

1) The measurement does not require the full time for the particles concerned to reach the detecting zone because the analysis of this measurement is carried out by monitoring the unbalance caused from the settling particles as well as completely settled ones in the whole suspension.

This analysis makes the time to obtain the

size distribution shorter than other centrifugal methods. However, to assure the precision of the calculation, there is a limitation in the shortening of the measuring time.

2) In many cases, size measurements such as the electric resistance, light scattering and photosedimentmeter give unreasonable results to evaluate the performance of the classifier or milling machines.

For instance, the size distribution of the raw material calculated from those of the classified coarse powder and the fine product does not always agree with that of direct measurement.

But the measurements such as a pipette method and sedimentation balance produce comparatively less difference between the direct measurement of the mixture and the calculation from the components.

Since this method detects the changes in the local concentration of the particles converted to the unbalance related to the weight, it tends to give the data coincident with those by the gravitational sedimentation methods mentioned above.

So, this method is well suited to evaluate the process handling the fine powders, especially submicron powders.

3) The photosedimentmeter is affected by the concentration of the powders even using dilute suspension and cannot be applied on the concentrated conditions.

The measurement of this method can be carried out at the higher concentration, which increases the S/N ratio.

We usually use the 3 wt% suspension for the measurements.

Even if the concentration is over 50 wt% as an extreme condition, the unbalance is still measurable but reliable size distribution cannot be obtained because of the interactions of particles in the suspension.

3. Apparatus

Photograph 1 shows the appearance of this apparatus. The rotor is made of aluminum casting with 300 mm diameter and equipped with two cells set symmetrically to the axis. The one is filled with the sample suspension and the other with the liquid of the same weight as the sample for balancing of the rotor. Each cell has 36 mm inner diameter with 50 mm depth and a maxi-
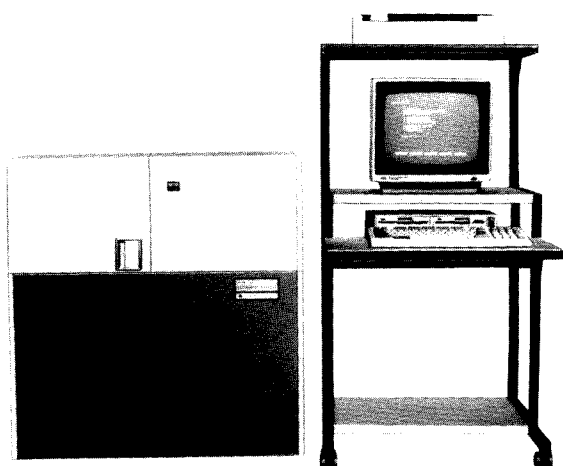
Photo. 1 Sedimenputer SPT-C

mum volume of 50 mℓ. A mechanical counter-balance with a screw to adjust its center of gravity is applicable in place of the cell filled with the liquid.

The measuring time required varies 5 to 45 minutes depending upon the particle diameter to be measured.

The apparatus is weighted with the rigid frames to avoid the resonance of the apparatus in the operation.

Figure 2 shows the schematic diagram of the measurement system. The details of the detecting part of the unbalance is shown in **Fig. 3**. The dynamic unbalance of the rotor produced by the centrifugal sedimentation of the particles exerts the centrifugal force F on the rotating shaft. The centrifugal force is converted to the amplitude χ of the vibration through the leaf springs with a spring constant k supporting the pillow block. The slight vibration of the

ω : Angular velocity
χ : Amplitude

e : Eccentric distance
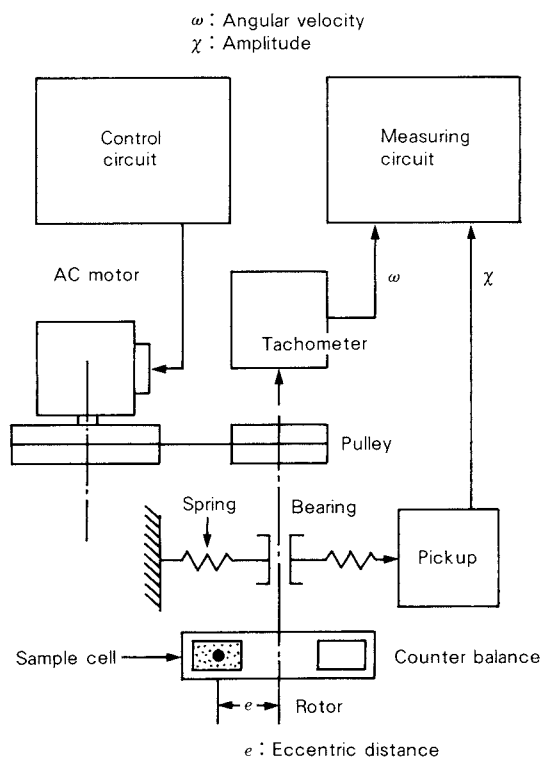
Fig. 3 Block diagram of the measuring unit

pillow block is detected with a pickup sensor of condenser type suitable to measure the minute amplitude and converted to the analog signals.

The rotor speed is counted with a non-contact magnetic proximity switch and converted to both the digital and the analog signals corresponding to the angular velocity ω in the measuring circuit.

In the measuring circuit, the magnitude of unbalance U is obtained from the relation de-
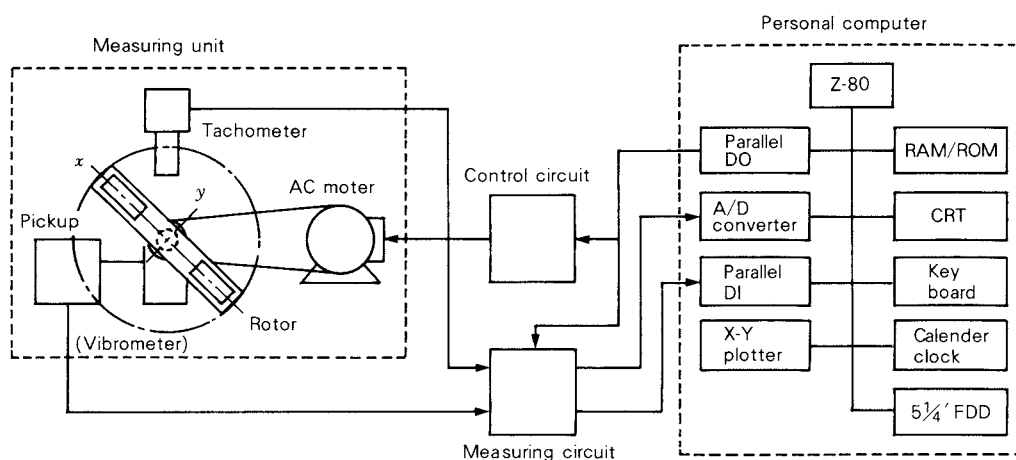
Fig. 2 Measurement system

scribed in the following equation with the data of the amplitude χ and the angular velocity ω and transferred to the micro computer.

$$U = (\frac{k}{\cos \omega t}) (\frac{\chi}{\omega^2}) \qquad (13)$$

This apparatus which works at the rotor speed far below the natural frequency corresponds to the balancing machine of so-called "hard type" from the functional viewpoint.

The microcomputer connected with the measuring part stores the transferred data of unbalance and the measuring time counted with a built-in timer and works out the size distribution from the stored data after the measurement. It also sends the signals to the driving circuit to start and stop the rotor and to regulate the rotation.

The computer applied for the size analysis was an 8-bit microcomputer made by NEC. PASCAL compiler was used to increase the computing speed.

The driving circuit has the function to control the rotation speed of the AC motor so that the rotor acquires the preset rotation speed in a certain time.

The measuring range of the applied tachometer was 400 to 8000 r.p.m. and the vibration pickup had the minimum reading 0.5 μm. The data of the magnitude of unbalance was processed with the computer through 12 bit A/D converter.

4. Results

Figure 4 shows the result of the measurement by this method at a constant speed of 2500 r.p.m. compared with those by other principles. Among the sedimentation methods applied for the liquid phase, the sedimentation balance, the X-ray extinction, the pipette and this unbalance method gave the similar results, while the photosedimentmeter presented the coarser size distribution. The results by the electric resistance method and the ultramicroscope were located between the former group of the sedimentation methods and the latter one.

This tendency of the size data obtained by various methods is not only for talc (**Fig.** 4) but also for CaCO₃ (**Fig.** 5). Therefore, it is supposed that the tendency was attributed to
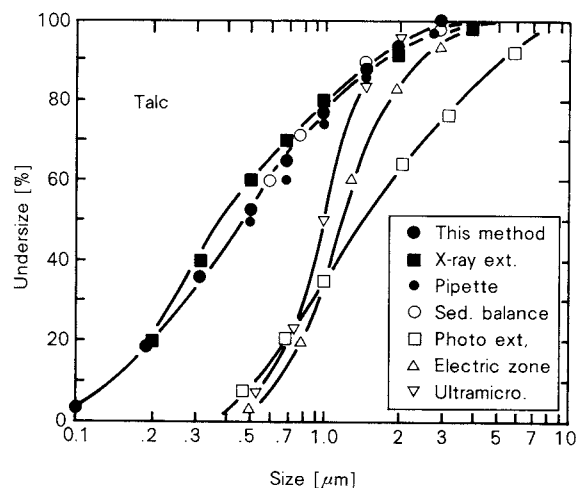
Fig. 4 Size distributions measured by different methods
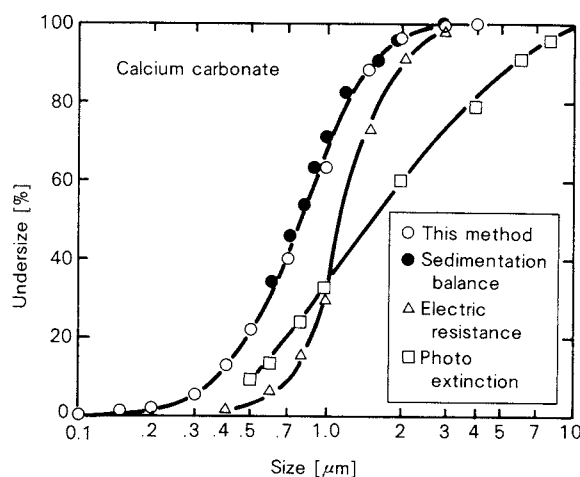
Fig. 5 Comparison with other measurements

the features of each method.

Figure 6 shows the size distributions of a finer and a coarser ground powder and a mixture of the same amount of them determined with the new apparatus. The dashed line was obtained by the calculation from the data of both ground powders.

If the measurement has no errors, the size of the mixed powder should be in complete agreement with the calculated result using the data of the raw materials before mixing.

However the actual measurement showed a slight difference in the finer range below 0.2 μm and the coarser part above 1 μm of the mixed powders.

This result implies some errors occur in the both sides, of the range. The cause of the errors has not been studied yet.
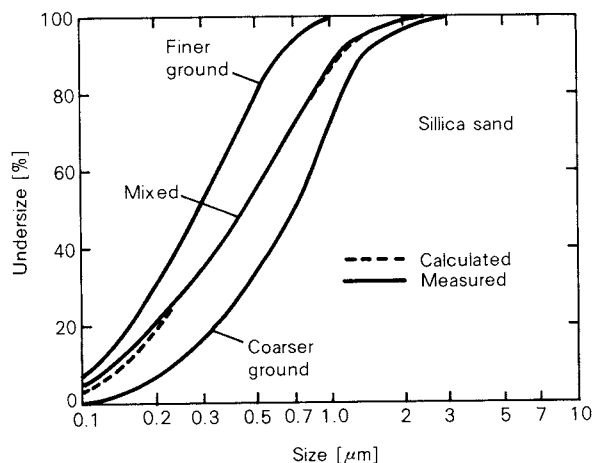
Fig. 6 Measured and calculated size distribution of a mixture of ground powders

Fig. 7 Variation of rotor revolution and unbalance with time

An example of the variation of the rotor speed and the magnitude of unbalance in the case of the linear acceleration followed by the constant speed is shown in **Fig. 7**. Since the resolution of the sensor is critical during the initial period of low rotation speed as seen from the figure, the size analysis was conducted based on the data of unbalance above 1000 r.p.m. to minimize the disturbance resulted from the noises. In **Fig. 7** the unbalances of the rotor in the axial and vertical directions of the cell shown in the x- and y-direction respectively. The constant unbalance in the y-direction except the initial period of rotation implies that the rotation of the rotor is very stable. The variation of the unbalance in the x-direction with time corresponds to the sedimentation curve to be obtained with the sedimentation balance and is used as the data for the calculation of the size distribution.

The comparison of the results obtained by this method of the linear acceleration followed by a constant rotation speed with those at a constant speed only is shown in **Fig. 8**. Both results agree well each other taking account of the experimental errors.

Figure 9 shows the results of the measurement with two samples including the particles finer than 0.1 μm which was carried out for the purpose of investigation of the lower limit size for this method. From the electron microscopic picture of $BaSO_4$ in **Photo. 2** used as the sample, it is recognized that this new apparatus applying the unbalance method is capable of determining the particle size under 0.1 μm.

Fig. 8 Comparison of the measurement at a constant rotation with that of the linear acceleration
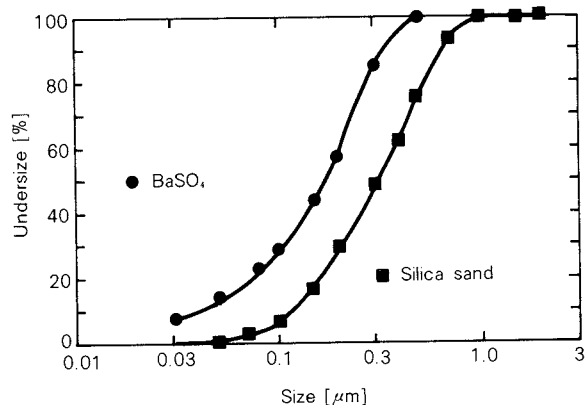
Fig. 9 Examples of the measurement in the submicron range
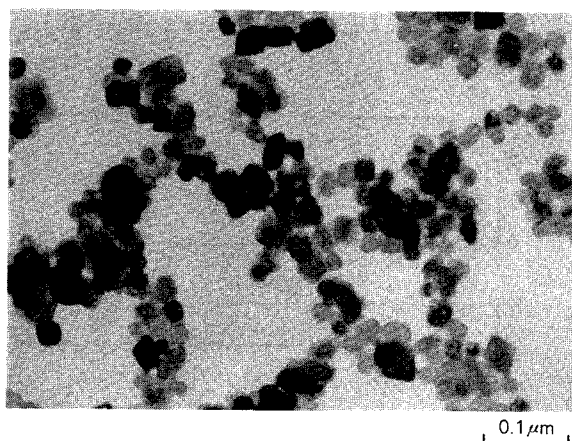
Photo. 2 SEM photograph of BaSO$_4$

5. Conclusion

A new size analyzer based on the unbalance method was constructed on the experimental basis. The apparatus applying the principle of the balancing machines detects the magnitude of unbalance caused by the displacement of the center of gravity owing to the centrifugal sedimentation of the particles which gives the size distribution theoretically.

It was confirmed that this apparatus presented the similar results of the size distribution to other sedimentation methods such as the X-ray extinction, the sedimentation balance and so forth.

The results by this method with the linear acceleration followed by a constant rotation coincides well with those at a constant speed only, taking the experimental errors into consideration.

Additionally, it was found in comparison with the microscopic picture that this analyzer is able to be used for the size analysis less than 0.1 μm down to nearly 0.03 μm.

Nomenclature

$A(r, t)$	:	coefficient of the unbalance	[m]
D_p	:	particle diameter	[m]
K	:	constant for a given measurement condition	[s/m^2]
k	:	spring constant	[N/m]
M	:	weight of the rotating system	[kg]
m	:	weight of the particles in the cell	[kg]
m_i	:	weight of the particles with radius r_i	[kg]
r	:	particle radius	[m]
r_i	:	radius of the particles concerned	[m]
T	:	non-dimensional time	[−]
$U(t)$	:	magnitude of unbalance	[kg·m]
x	:	position in the radial direction	[m]
x_m	:	position of the cell bottom	[m]
x_o	:	position of the surface of suspension at $t = 0$	[m]
α	:	constant for the rotor acceleration	[l/s^2]
$\epsilon, \epsilon_a, \epsilon_b$	:	displacement of the center of gravity	[m]
μ_L	:	viscosity of dispersion liquid	[Pa·s]
ρ_L	:	density of dispersion liquid	[kg/m^3]
ρ_P	:	density of particles	[kg/m^3]
τ	:	non-dimensional time	[−]
χ	:	amplitude of vibration	[m]

References

1) Suito, E., M. Arakawa, T. Masuda, S. Miwa and M. Sase: *Ohyo Butsuri* (J. Applied Physics, Japan), **32**, 823 (1963).
2) Arakawa, M., G. Shimomura, A. Imamura, N. Yazawa, T. Yokoyama and N. Kaya: *Zairyo* (J. Soc. Materials Sci., Japan), **9**, 1141 (1984).
3) Arakawa, M., G. Shimomura, A. Imamura, N. Yazawa, N. Kaya and H. Kitai: KONA **2**, 39 (1984).
4) Arakawa, M., G. Shimomura, A. Imamura, N. Yazawa, N. Kaya and H. Kitai: *Funtai Kogaku Kaishi* (J. Soc. Pow. Tech., Japan), **21**, 768 (1984).
5) Kaye, B.H.: Direct Characterization of Fine Particles, 189, John Willey & Sons (1981).
6) Miwa, S. and G. Shimomura: Kaiten Kikai no Tsuriawase, 6, Corona Publishing (1976).
7) Allen, T.: *Powder Tech.*, **18**, 131 (1977).
8) Brugger, K.: *Powder Tech*, **14**, 187 (1976).

Control of Solid Flow Rate in a Pneumatic Conveyer[†]

Shigeru Matsumoto, Hiromi Harakawa,
Mutsumi Suzuki and Shigemori Ohtani
Department of Chemical Engineering,
Tohoku University *

Abstract

The control characteristics of the solid flow rate are investigated for a pilot scale pneumatic conveyer. The experimental system is a pressure-type vertical conveyer consisting of a 20 mm-I.D. and 5.6 m long transport line. Under a constant air flow rate, the solid flow rate was controlled by manipulating a vibrating feeder based on the feedback of the output signal from the hand-made impact flow-meter which was set downstream of the gas-solid separator. The control system was implemented on a personal computer. Since the output signals of the impact flow-meter contained significant amounts of random noise, the Kalman filter was applied as the observer. The controller was designed based on the discrete I-PD control formula. The formula is a kind of partial model matching method developed by Kitamori. Satisfactory control performance was achieved both as a regulator and as a servo-mechanism for the pilot plant.

1. Introduction

Pneumatic conveyers have been frequently used in many industrial processes which deal with powdery materials, and therefore a number of works have been reported on the design and the operation of this technique. However, there have been very few investigations[1] on the control of pneumatic conveying system. This is mainly attributed to: 1) the lack of reliable on-line measuring technique of controlled variables, 2) the presence of significant amounts of noise in the output signals, which is an inevitable feature in the powder processes, 3) the existence of considerable delay due to the flow system, and 4) the difficulties in modeling of its dynamic behavior due to the very complicated flow mechanism.

The first problem in the design of a control

system is what are the operational objectives that the control system is called upon to achieve. The answer is dependent on the objective of the concerned process system. For instance, if the pneumatic conveyer is used only for the transportation of solids, then it may be required to keep the solids flow rate at a desired value, and/or to alter it to another desired value as fast as possible. On the other hand, if it shall be applied to other objectives such as the pneumatic dryer or the transport reactor, another control objective may be required such as keeping a desired solid inventory or a desired residence time of solids. In such cases it is necessary to monitor directly the in-situ concentration of solids or otherwise to estimate the concentration from other measurable variables by using theoretical or empirical relationships. Since either of them is, however, very difficult to be realized under the present circumstances, this investigation is limited to the situation that the pneumatic conveyer is supposed to provide only a means of transportation of solid, and thus it is concerned with control of the solids flow rate. The foregoing problems [from 1) to 4)] are inevita-

ble in this case also. In the present work, those problems are settled in the following way. For measurement of the solids flow rate, we have developed an impact flow-meter having high sensitivity, and applied the Kalman filter[2] to reduce the effect of noise contained in its output signals. In order to solve the problems 3) and 4), we have adopted the I-PD control scheme which has been developed by Kitamori[3,4]. The effectiveness of the control system implemented is demonstrated by simulated and experimental tests on a pilot scale pneumatic conveyer.

2. Experimental Apparatus and Procedures

2. 1 Apparatus

The schematic diagram of the experimental system is shown in **Fig. 1**, which is a pressure-type vertical conveying system consisting of a transport line of 20 mm-I.D. Pyrex glass tube of 5.6 m length. Air is supplied by a rotary blower and its flow rate is adjusted by an electromotive valve. Solid particles, which are packed in the stand pipe from the hopper to the feeder, are fed by the use of a vibrating feeder. The particles transported up to the top of line are separated in the bag-filter and recycled to the hopper through a sub-hopper in which the impact flow-meter is set. The electromotive valve and the vibrating feeder are supervised by a personal computer (PC8001, NEC). The air flow rate is metered by the use of an orifice-meter. The pressure difference of the orifice-meter and the other static pressures at various locations along the transport line are converted to DC voltages by means of semiconductor pressure transducer and read by the personal computer via a digital voltmeter. The output of the impact flow-meter also is similarly treated. The solid particles used here are spherical glass beads having a Sauter mean diameter of 1.91 mm.

The conveyer system was operated as follows: The solids flow rate was varied by manipulating the vibrating feeder while maintaining a constant air flow rate, seeing that the conventional pressure-type conveying system is operated by adjusting the feeder at a constant air flow rate. Finally, the feedback loop in this work is illustrated by the dot-dash-lines in **Fig. 1**. Details of hardware elements of the con-
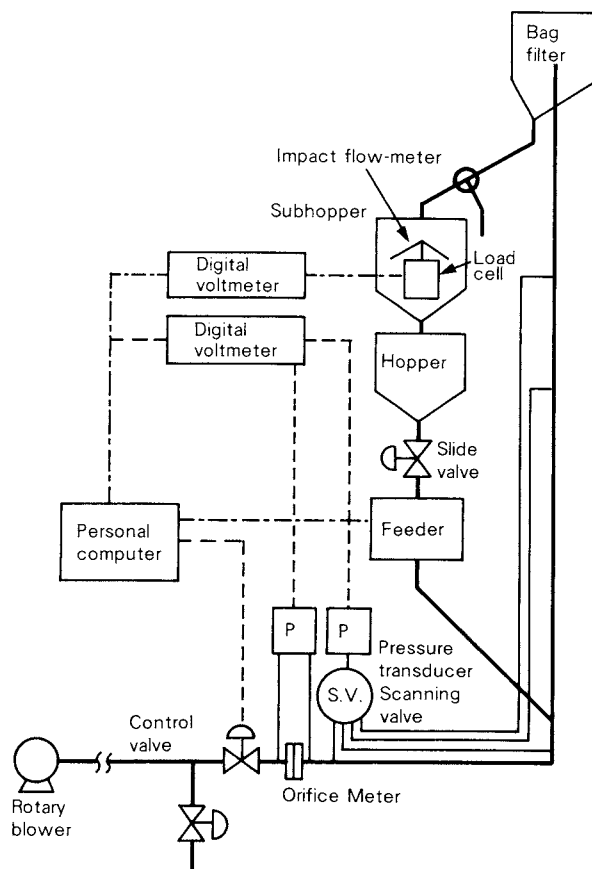
Fig. 1 Schematic diagram of experimental apparatus

trol system are described in the following.

2. 2 Final control element

The feeder used in the work is a closed-type vibrating feeder specially designed for this experiment. Since this is equipped with a continuously variable electronic speed gear, its vibrating frequency is regulated by adjusting the variable resistance, via a small DC servomotor, in the control unit of the speed gear. The angle control of servomotor is achieved by a hand-made motor-driver by means of a rotary encoder. Finally, the manipulated variable becomes the number of pulses to the rotary encoder.

2. 3 Measuring sensor

The solids flow rate is measured by the hand-made impact flow-meter set inside the hopper. The impact flow-meter consists of a high-sensitive load cell at the sensing part of which a small cap made of acrylic resin is fitted. The analog electrical voltages of the load cell are converted to the digital signals by a digital
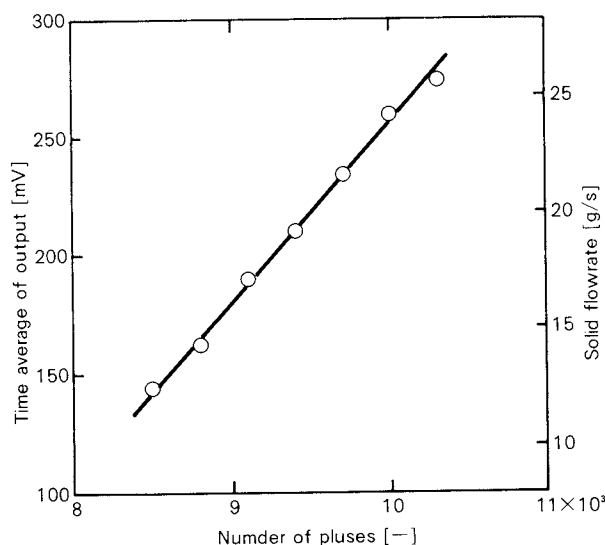
Fig. 2 Relationship between input (pulse number of rotary encoder), and average of system output (output voltage from load-cell) and solids flow rate.

voltmeter. Since the extremely small-sized load cell (200gf in full scale) was used so as to achieve a high sensitivity, the output signals contain significant amounts of random noise. However, the time averaged value of the signals is in proportion to the solids flow rate. If the calibration were made beforehand, the solids flow rate can be evaluated from the output signals. The linear relationship between the flow rate and the output signal equally holded for other particles as well as the glass beads of 1.91 mm used in this work (confirmed for three kinds of glass beads and two kinds of copper beads). From this fact it can be said that the impact flow-meter is useful for the on-line measuring sensor of solids flow rate.

Figure 2 illustrates the relationship between the time averaged output of the sensor (electrical voltage of the load cell) and the manipulated variable (number of pulses to the rotary encoder). In the figure, the relationship with solids flow rate is also illustrated. It can be seen from the figure that the input-output relationship is linear. The gradient of the relation corresponds to the gain constant of transfer function shown later.

3. Process Model

At the beginning of control system design, we have to build an appropriate mathematical model to describe the dynamic behavior of the process to be controlled. For the process system in this work, since the theoretical modeling is virtually impossible due to poor understanding of the behavior, the model was identified by a step-response experiment. In fact, simpler input-output model such as the transfer function representation is enough for the control purpose itself, since the I-PD control scheme will be applied as shown in the following. However, for the Kalman filter to be used as the observer, the model should be expressed in the state space as a stochastic system.

3. 1 Transfer function

Figure 3 shows the output response for a step change of the manipulated variable (300 steps increase) while maintaining a constant opening of the air-flow control valve (at u_a = 18.2 m/s). This situation corresponds to the change of solids flow rate from 22.2 to 24.1 g/s. The output signals are sampled at an interval of 0.237s. It can be seen that the output signals are embedded in significant amounts of noise. This is attributed to the facts that the measuring principle of solids flow rate is based on the impulsive force of particles which is essentially discrete quantity and that the high-sensitive load cell is used as stated above. Thus it does not imply that the actual solids flow rate exhibits such violent fluctuations. Namely, most noises observed are probably the measurement noise, not the process noise. Supposing that the process essentially exhibits the deterministic behavior, it was approximated by the following second order system with dead time,

$$G(s) = \frac{0.0186}{s^2 + 0.25s + 0.25} e^{-2.48s} \qquad (1)$$

where the parameter values were determined by trial and error. Even such a rather rough identification of the model is enough for the control object based on the I-PD formula. The calculated response by Eq. (1) is illustrated in **Fig. 3**.

3. 2 Stochastic system

Since the measurements are very noisy as seen in **Fig. 3**, the output signal itself is not appropriate for a primary feedback signal. Thus some filtering treatment must be necessary to reduce the effect of noise. Among the various
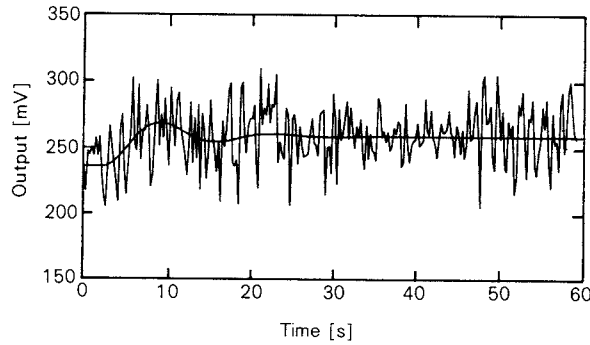
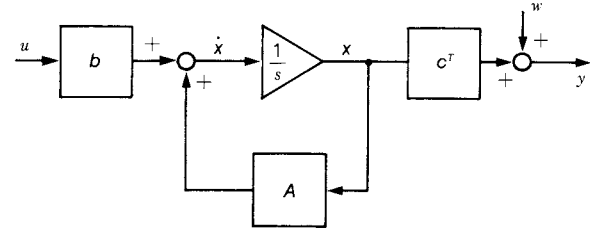Fig. 3 Output signal of step response (the solid line indicates the calculated value by Eq. (1))
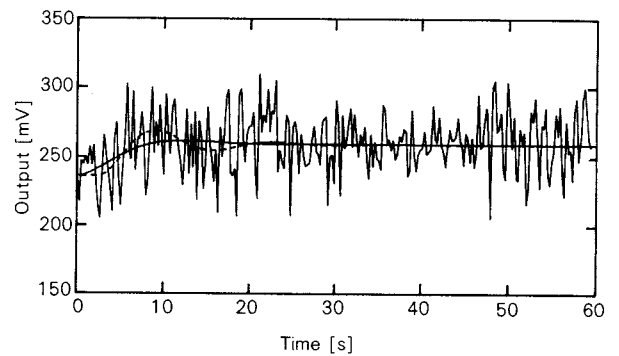

Fig. 4 System model

Fig. 5 Comparison of actual step response with one calculated by model (the solid line indicates the deterministic part of Eq. (8), and the dotted line Eq. (1))

kinds of filtering techniques, we will adopt the Kalman filter to estimate the true process value from the noisy measurements. Namely supposing that the primary output corresponding to the solids flow rate exhibits the deterministic nature and large amounts of noise are added mainly in the measuring process, we express the system by a stochastic state space model. Let the primary output voltage corresponding to the solids flow rate be a state variable. Dividing the state variable vector into two parts; that is, a part drived by process noise (v) in the steady state and one drived by the deterministic input ($\bar{u}$), we have the following state space model,

$$\dot{x}_1 = Ax_1 + dv \qquad (2)$$

$$\dot{x}_2 = Ax_2 + b\bar{u} \qquad (3)$$

$$y = c^T x + w \qquad (4)$$

$$x = x_1 + x_2 \qquad (5)$$

where Eq. (3) is the realization of Eq. (1) and w in Eq. (4) is the observation noise. In order to implement the Kalman filter, it is necessary to know d in Eq. (2). However, statistical information concerning the process noise is not available in practice, we assume $d = b$ for simplicity. Further assuming that both the process and measurement noise are Gaussian, the system model becomes

$$\dot{x} = Ax + bu$$

$$y = c^T x + w \qquad (6)$$

$$u = \bar{u} + v$$

where

$$E\{u(t)\} = \bar{u}(t), \quad E\{v(t)^2\} = Q$$
$$E\{w(t)\} = 0, \qquad E\{w(t)^2\} = R \qquad (7)$$

Consequently, the system (c^T, A, b) can be

obtained as a realization of Eq. (1). Since Eq. (1), however, involves delay, the state space model of the transfer function model becomes infinite-dimensional. To avoid this, we expanded the delay term in the transfer function into the Taylor series and truncated the series after the second order. The resulting realization in an observable canonical form becomes

$$\dot{x} = \begin{pmatrix} 0 & -0.105 \\ 1 & -0.364 \end{pmatrix} x + \begin{pmatrix} 7.80 \times 10^{-3} \\ 0 \end{pmatrix} u$$

$$y = [0, 1] x + w \qquad (8)$$

Figure 4 indicates the block diagram representation of this model. The comparison between the step response with Eqs. (1) and (8) is shown in Fig. 5, where the solid line indicates the deterministic part of Eq. (8) and the dotted line indicates Eq. (1). It can be seen that the oscillatory nature is considerably suppressed while the settling time is similar. This is resulted from the approximation of delay term by the second order system.

4. Design of Control System

4. 1 Kalman filter[2]

The Kalman filter is a kind of observer for stochastic system and then it can be used for

the sequential estimation of the probabilistic behavior of state variable. In order to construct the control system in a time-discrete form, we have to design a stationary discrete Kalman filter. If the system model is discretized at a sampling interval of 0.5s, it can be represented in a discrete form by

$$x_{k+1} = Fx_k + gu_k$$
$$y_k = c^T x_k + w_k \qquad (9)$$

where

$$F = \begin{pmatrix} 0.988 & -0.0477 \\ 0.455 & 0.822 \end{pmatrix}, \quad g = \begin{pmatrix} 3.89 \times 10^{-3} \\ 0.917 \times 10^{-3} \end{pmatrix}$$

$$E\{u_k\} = \bar{u}_k, \quad E\{(u_k - \bar{u}_k)^2\} = Q$$
$$E\{w_k\} = 0, \quad E\{w_k^2\} = R \qquad (10)$$

In the concerned system, y_k represents the output signal of the load cell corresponding to the solids flow rate. Applying the discrete Kalman filter algorithm to the system Eq. (9), the optimal estimate of state variable $\hat{x}_k$ can be obtained by

$$\hat{x}_k = \tilde{x}_k + PcR^{-1}(y_k - c^T \tilde{x}_k)$$
$$\tilde{x}_k = F\hat{x}_{k-1} + g\bar{u}_k \qquad (11)$$

where P is the Kalman filter gain matrix and is determined by the asymptotic solution of the following Riccati equations,

$$P_k = (M_k^{-1} + cR^{-1}c^T)^{-1}$$
$$M_k = FP_{k-1}F^T + gQg^T \qquad (12)$$

Two parameters involved in the Kalman filter, Q (i.e., the variance of process noise) and R (i.e., the variance of observation noise), were evaluated as follows. Considering the variance of Eq. (9), since x_k and w_k are independent each other, we have

$$E\{(y_k')^2\} = c^T E\{x_k'(x_k')^T\} c + E\{w_k^2\}$$
$$y_k' = y_k - E\{y_k\}, \quad x_k' = x_k - E\{x_k\} \qquad (13)$$

Supposing the steady state for Eq. (9), the first term of right-hand side of the above equation becomes

$$c^T E\{x_k'(x_k')^T\} c = c^T h E\{(u_k - \bar{u}_k)^2\} h^T c$$
$$= (h^T c)^2 Q \qquad (14)$$

where

$$h = (I - F)^{-1} g$$

Consequently Eq. (13) becomes

$$E\{(y_k')^2\} = (h^T c)^2 Q + R \qquad (15)$$

Since the observed value, however, is $E\{(y_k')^2\}$ alone, it is impossible to determine both Q and R uniquely. Therefore, in this work, they were assumed in such a way that the $E\{(y_k')^2\}$ agreed with the observed one as well as possible. For this purpose, we examined the standard deviation of the actual output signals as shown in **Fig. 6**. As can be seen from the figure, $E\{(y_k')^2\}$ is dependent on the solids flow rate and hence both Q and R may be dependent on the solids flow rate. In this work, however, R was assumed constant (i.e., $R = 256$) for simplicity, and Q was chosen so as to satisfy the relation of Eq. (15) by trial and error. **Figure 7** indicates the applications of the Kalman filtering to the preceding step response with parameters of Q. With small value of Q (i.e., $Q = 10^4$), since the fluctuations of output signal are mostly regarded as the observation noise, the filter output is almost the same as that by the deterministic model. On the other hand, for the large value of Q(i.e., $Q = 10^5$), the filter output exhibits fast response for the disturbance added to the system due to the overestimation of process noise, though the variations of the output increase. In practice, a trade-off must be made between the degree of smoothing or noise elimination and the responsiveness of the filter to dynamic change in the process.
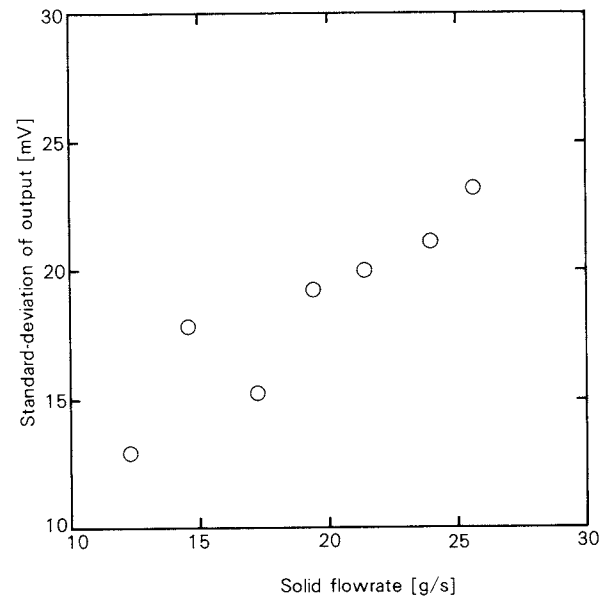
Fig. 6 Relationship between solids flow rate and standard-deviation of output.
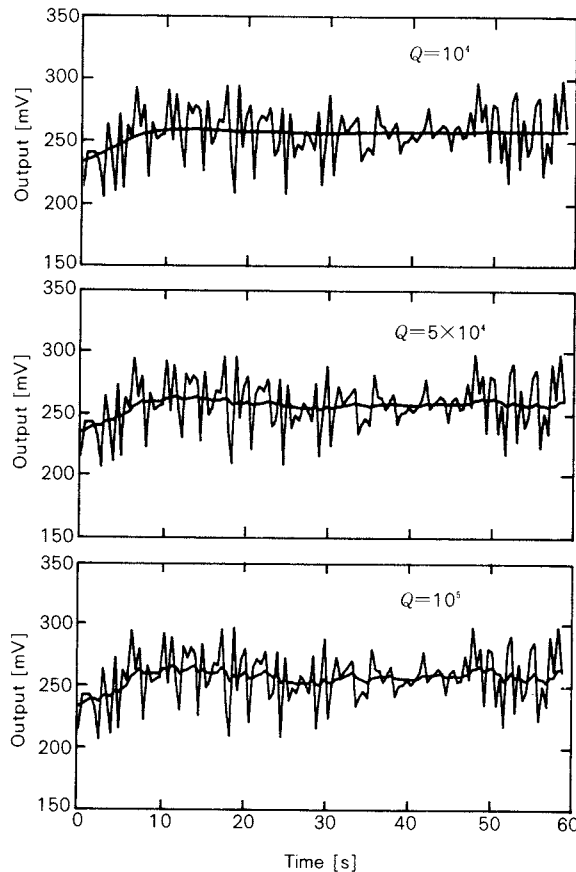
Fig. 7 Effect of parameter Q in Kalman filter.

In this work we assumed $Q=5 \times 10^4$ (in this case, the standard deviation of output based on Eq. (15) becomes 23.2).

4. 2 I-PD control[3,4]

First thing to do in the control system design is to select what kind of control formula should be applied. For instance, if the optimal regulator would be used as a control formula, the process must be represented by the state space model. After the model identification, the parameters of controller are uniquely determined by a weighting matrix for the performance function. In such a case, therefore, the control performance is directly dependent upon the accuracy of the assumed process model. In this work, however, it is very difficult to build an accurate state space model since it is obtained experimentally. Thus it is hardly possible to expect a high control performance by the optimal regulator based on such an uncertain state space model. Particularly, in the present system the presence of significant dead-time also makes the state space

modeling difficult. On the other hand, if the conventional PID controller would be applied, the transfer function model is enough for the representation of the system. However, the presence of dead-time causes trouble in this case too. For instance, if following such approaches, some approximation such as Pade's one may be useful for the dead-time element. However, considerably high-order Pade approximation may be needed to express the significant dead-time, and therefore a large amount of computation time is inevitable.

Thus in this work, I-PD control formula was applied, which was applicable to control system designs in the situation that the dynamic characteristics of the controlled process were not known perfectly. Since this formula is also applicable to the process containing significant dead-time, it is the most appropriate for the concerned system.

Figure 8 indicates the block diagram of the I-PD control. It establishes the improvement of the stability and the speed of response of the controlled object by the feedback compensation in term of $(f_0 + f_1 s)$ and the zero steady-state error by the series compensation of k/s. The object to be controlled is represented by the transfer function written in the power-series denominator form. The dead-time element is also expressed in the following form,

$$G(s) = \frac{1}{a_0' + a_1' s + a_2' s^2 + a_3' s^3 + \cdots}$$

(16)

where the coefficients a_i' for Eq. (1) are

$$\{a_i'\} = \{13.41, 46.67, 128.2, 208.4, \cdots\}$$

The controller parameters k, f_0 and f_1 are chosen in such a way that the coefficients in the power-series denominator representation of the transfer function of the closed-loop system shown in **Fig. 8** coincide with those of the
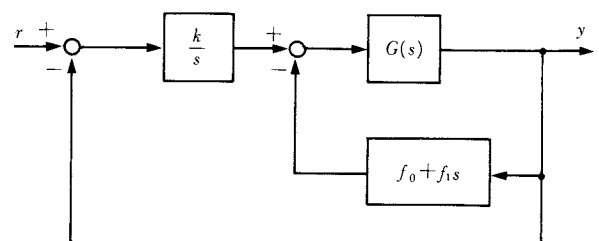
Fig. 8 I-PD control scheme
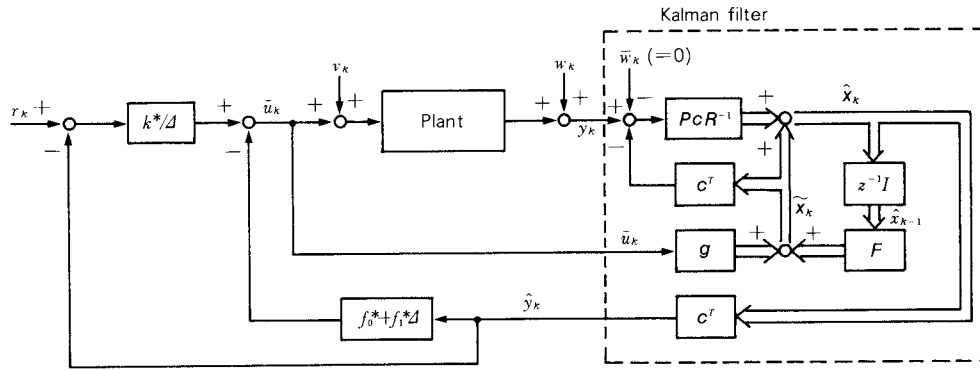
Fig. 9 Scheme of control system ($\Delta = (1 - z^{-1})/T$; difference operator)

following reference model up to as high as possible an order

$$G'(s) = \frac{1}{\alpha_0 + \alpha_1 \sigma s + \alpha_2 \sigma^2 s^2 + \alpha_3 \sigma^3 s^3}$$

(17)

$$\{\alpha_i\} = \{1, 1, 0.5, 0.15, 0.03, \cdots\}$$

In practice, this control formula is implemented in a sampled-data system. Letting T be a sampling time, the rise-time of the closed system, σ, becomes the smallest positive root of the following equation,

$$(a_2' + Ta_1' + T^2 a_0')\alpha_4 \sigma^3 + (-a_3' + \frac{7}{12} T^2 a_1'$$

$$+ \frac{1}{4} T^3 a_0')\alpha_3 \sigma^2 + (-a_3' - \frac{7}{12} Ta_2' +$$

$$+ \frac{1}{18} T^3 a_0') T\alpha_2 \sigma + (-\frac{1}{3} a_3' - \frac{1}{4} Ta_2'$$

$$- \frac{1}{18} T^2 a_1') T^2 = 0$$

(18)

The controller parameters for the sampled-time system, $k^* (=k)$, f_0^* and f_1^*, are

$$k^* = (a_2' + Ta_1' + \frac{1}{3} T^2 a_0')/\{\sigma(\alpha_3 \sigma^2 +$$

$$+ T\alpha_2 \sigma + \frac{1}{3} T^2)\}$$

$$f_0^* = k^*\alpha_1 \sigma - a_0'$$

$$f_1^* = k^*\alpha_2 \sigma^2 - a_1' + \frac{1}{2} Tf_0^*$$

(19)

The sampling time is chosen as $T = 0.5$s from the restriction of computing speed of the personal computer. The resulting values of controller parameters are

$$\sigma = 8.180, \quad k^* = 1.534, \quad f_0^* = -0.861,$$

$$f_1^* = 4.437$$

The final scheme of implemented control system is shown in **Fig. 9**.

5. Simulation and Experimental Results

Prior to the experimental investigations, the control performance was confirmed through the simulation, in which the system was assumed to behave in accordance with Eq. (1). In the simulation, the pseudo-white noises were artificially added into the internal- and observation-process so as to exhibit the similar noisy output. The control system was constructed as stated in the preceding. **Figure 10** indicates the simulation result for influence of rectangular disturbance corresponding to the output deviation of 40 mV added to the system during a period from 10 to 40 seconds. The upper half of the figure indicates the output and the estimate by the Kalman filter, and
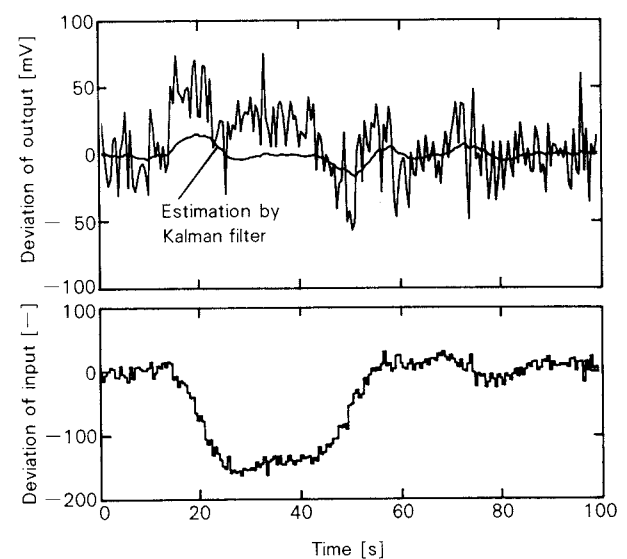
Fig. 10 Influence of rectangular disturbance (simulation)

the lower one the manipulated variable. During the existence of disturbance, small deviations are observed between the output itself and the estimate. This is because relatively smaller variance of process noise is assumed in the Kalman filtering. In the design of the Kalman filter observer, if a large process noise (i.e., large variance Q) is supposed, the filter output is able to follow unmeasurable disturbances to some extent, though it exhibits considerable variations as a result of underestimation of the observation noise (see **Fig. 7**). Consequently, the manipulated variable also varies considerably. It can be concluded that an accurate estimation of the state variables is difficult under the existence of a large stepwise unmeasurable disturbance because of the structural defect of the Kalman filter formula. If paying attention to the output of filter alone in **Fig. 10**, it can be said that the controller works satisfactorily since the disturbance does not influence the output. Seeing that actual disturbances introduced into the process are probably not stepwise but pulsewise, then the present control system is considered to be applicable to the actual process. As for the change of reference signal, the simulation result is shown in **Fig. 11**. In this case, both the Kalman filter estimation and the control performance are satisfactory since the deterministic input is taken into account in the observer.

After the examination through the simulation, the control system was implemented in

Fig. 12 Control performance for the experimental system (for a step change of demand)

the experimental system. **Figure 12** shows an example of control experiment for a step change of reference signal which corresponds to the change of solids flow rate from 15.5 to 20 g/s. It can be seen from the figure that the satisfactory performance is achieved without so much overshoot.

6. Conclusion

Several aspects of a control system design for solids flow rate in a pneumatic conveyer have been discussed through the simulation and the experiments. Although in this case the problem that the output signals contain significant amounts of noise offers the difficulty for implementing the controller, it was solved by the application of the Kalman filter observer. Since the dynamic characteristics of the controlled process were not known perfectly, the control system was designed on the basis of the discrete I-PD control scheme which was a kind of partial model matching method developed by Kitamori. The implementation of the control scheme on the experimental system indicated a satisfactory performance. However, it was found through the simulation that an influence of big stepwise disturbance could not be perfectly excluded from the structural defect of the Kalman filter. Further work shall be necessary on this respect. Although the controlled process in this work is rather simple, it involves some common problems, such as measurement noise and uncertainty in process

Fig. 11 Simulation result for a step change of demand

96

modeling, arising in the design of control system for other powder processes. Thus the results of the present work may provide useful guidelines for future applications of computer control to various powder processes.

Nomenclature

A : coefficient matrix
b : coefficient vector
c^T : coefficient row vector
d : coefficient vector
E : expectation
F : coefficient matrix
f_0, f_1 : parameters of PD-mode compensator
f_0^*, f_1^* : parameters of sampled PD-mode compensator
g : coefficient vector
$G(s)$: transfer function
k, k^* : gain of I-mode
P : gain matrix of Kalman filter
Q : variance of process noise (Eq. (7))
R : variance of observation noise (Eq. (7))
r : reference signal
T : sampling time
u : manipulated variable
u_a : air velocity
v : process noise
w : observation noise
x : state vector
$\hat{x}$: estimate of state vector
y : output
Δ : difference operator
σ : rise time

References

1) Iwamura, T., S. Matsushita, T. Moriyama and S. Fujii: Preprints of The 47th Annual Meeting of The Soc. of Chem. Engrs. Japan, p. 356 (1982).
2) Arimoto, S.: "Kalman Filter", Sangyo Tosho (1977).
3) Kitamori, T.: Trans. Soc. Instrum. & Control Engrs. Japan, 15, 549 (1979).
4) Kitamori, T.: ibid., 15, 695 (1979).

Estimation Method of Powder Yield Locus

Kazutaka Makino and Kohtaro Kuramitsu
*Department of Chemical Engineering for Resources,
Akita University**

1. Introduction

The friction property of powder can be described by powder yield locus. The powder yield locus was first introduced to design a hopper in 1960 by Jenike. This stimulated the conception of the powder process design on the basis of powder property and the powder yield locus became important after Jenike (1960) in powder technology. He also indicated the conception of powder yield locus estimation. In this paper, from this standpoint, several works on powder yield locus are reviewed.

2. Jenike's work[1,2,3]

Jenike has introduced a conception of a yield locus as a powder property necessary to design a hopper for the first time. He noticed elastic, viscous properties of powder as well as a time effect similar to the jelling of Bingham materials and to the upper and lower yield points in mild steel, and characterized powder as a modified rigid-plastic material. The conception of a yield locus was introduced as an engineering powder property necessary to design a hopper. The yield locus is not a straight line in σ - τ plane (σ is normal stress and τ is shear stress) such as in the case of a Coulomb solid and has the following features;

i) For small values of normal stress, the yield locus deviates from the straight line.

ii) A yield locus does not extent infinitely with increasing normal stress, but terminates at an end point.

iii) The position of the yield locus is not fixed, but is a function of the degree of consolidation. Unconsolidated powder has no

strengh at all, and the yield locus reduces to the origin.

The yield locus can describe the powder flow condition in a hopper. The shape of a yield locus depends on the porosity of powder, the packing method into a cell, the pre-consolidation method and so on. Then, Jenike devised a measuring apparatus of a yield locus considering the following points.

i) A consolidated powder flowing in an actual hopper has to be simulated in the measuring apparatus.

ii) The yield locus has to be easily measured by the measuring apparatus.

He developed a test cell as shown in **Fig. 1**, which is called a Jenike's cell. In this test cell, the test plane in powder, on which a specified vertical stress σ_V is applied, is repeatedly sheared by shear stress τ until a steady state is attained. As a result of it, the powder in the test cell is pre-consolidated similarly to the consolidated state in an actual hopper. This preparation is called Jenike's preliminary consolidation. He used the test cell to determine the porosity of powder generated in the cell at the preliminary consolidation, and pointed out that the porosity would be mainly obtainable by the maximum principal stress σ_1 at the preliminary consolidation.

From the above discussions, the yield locus
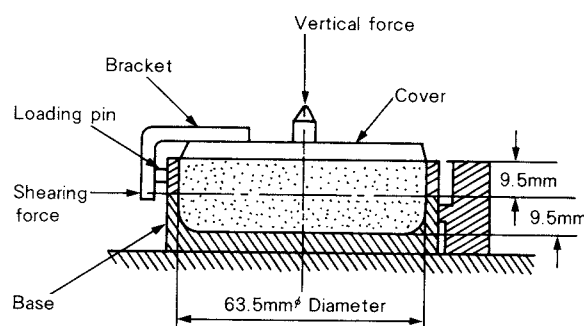
* 1-1, Tegata Gakuen-cho, Akita, 010
TEL. 0188 (33) 5261

Fig. 1 Jenike's shear cell

can be described in the following; The yield locus has to come into contact with the Mohr semi-circle which has the maximum principal stress σ_1 at the preliminary consolidation. When deviating from a straight line in the region of small normal stress σ, it becomes a convex curve on σ-τ plane.

According to the description, the following characteristics of powder flow are evaluated from the yield locus.

i) The mechanical strength of powder is estimated from the value of shear stress τ on the yield locus.

ii) The degree of the dilatation or compression of powder is evaluated from the local shape at a specified point on the yield locus by use of the principal of normality by Drucker[4].

iii) If the Mohr semi-circle at a specified point in powder comes into contact with the yield locus, the shearing failure takes place at the point in powder.

iv) The end point of the left side on the yield locus is described as a point C on the critical Mohr semi-circle as shown in **Fig. 2**.

Jenike also characterized and introduced the following three kinds of powder properties which are necessary to design a hopper. He noticed the fact that powder flow in a hopper during discharge is generally very slow and considered that the continuous flow state could be approximated as static state. Under the continuous flow condition, an element of the flowing powder is continuously reconsolidated under a prevailing pressure. As a result of the characterization, the conception of an instantaneous yield locus (IYL) was introduced for

the analysis of very slow powder flow in a hopper.

When powder flow is stopped, the powder remains under the prevailing static stress for a long time. Powder usually gains strength with the lapse of time. Jenike characterized a mechanical strength of powder in this case by use of the conception of a time yield locus (TYL). Usually a time yield locus (TYL) lies above instantaneous yield locus (IYL) as shown in **Fig. 3**.

The following conception of an effective yield locus (EYL) is introduced from one of the most famous characterizations presented by Jenike. During a continuous flow with shear, a unique critical Mohr semi-circle can be approximately considered to exist corresponding to the stress state at a point in flowing powder. Then, in order to discuss the continuous flow with shear, Jenike introduced the conception of EYL defined as the envelope of the Mohr semi-circles above at possible powder stress states in powder.

The shape of EYL is shown in **Fig. 4**. Fur-
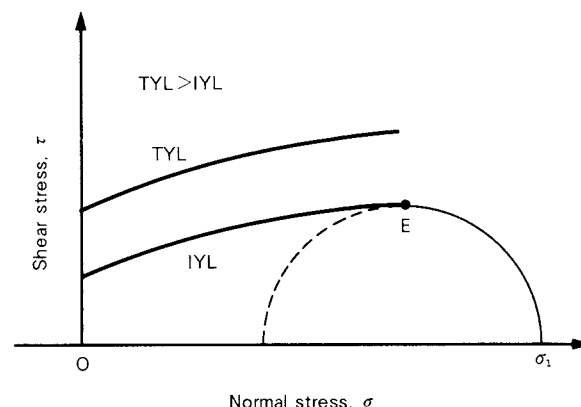
Fig. 3 TYL and IYL (Jenike)

Fig. 4 EYL (Jenike)
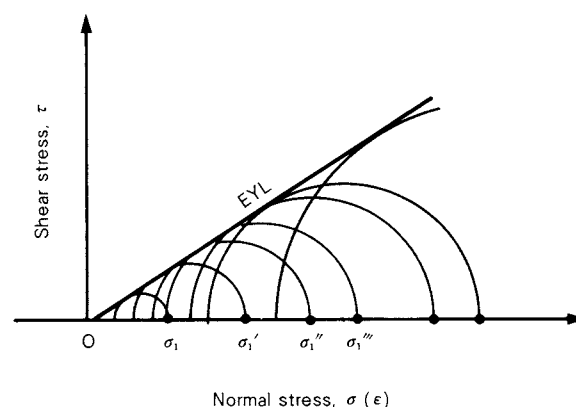
Fig. 2 The end point C of the left side on a yield locus (Jenike)

ther, from experimental investigation, he assumed that the local porosity ϵ in continuous powder flow would be determined by the major principal stress σ_1 at the position. Then,

$$\sigma_1 = \sigma_1(\epsilon) \qquad (1)$$

This means that the σ_1-axis can be interpreted as the axis of the porosity of continuous flow powder with shear in a hopper. Consequently, EYL gives a relation between the stress and the porosity of continuously flowing powder. This is an epochmaking characterization for the powder process design, because the yield locus necessary to the design strongly depends upon the porosity.

Indication of the Estimation Powder Properties

As seen from the above discussions, Jenike characterized the mechanical strength of powder from the standpoint of design. He considered the following points to develop a design method of a hopper.

i) In slow continuous powder flow in a hopper, the dynamical pressure can be negligible. (This introduces the conception of EYL.)

ii) Powder is consolidated accompanying with shear yield. (This introduces the Jenike's preliminary consolidation method, in which the powder in the test cell is continuously twisted or sheared until a steady state is attained.)

iii) From the experimental discussions on the preliminary consolidation method, the porosity of continuously flowing powder is determined by the major normal stress σ_1 at the pre-consolidation. (The conception of EYL can be correlated to the major normal stress σ_1 at a specified point in a hopper, that is, the porosity.)

Considering these points above, he developed a design method which consistes of three factors of stress balance, YL and EYL. We can understand this design method as a new one which is constructed on the basis of powder properties, and find the idea of the estimation method in his approach itself. However, we can not take a look at the necessity of the estimation method in it. Because it is mainly applied to Coulomb powder, of which the yield locus shows a straight line independent of powder porosity and YL equals EYL. Then, in this case, his design method consists of two factors of stress balance and EYL.

In general, EYL is usually a straight line through the origin of the coordinate system and is easily measured. We can obtain the overall data of EYL necessary to design of a hopper only in a laboratory. Certainly, in this case, there is no necessity of the estimation method of powder properties. However, in general, the yield locus is a function of the powder porosity. Therefore, the whole yield loci have to be given for the design of a hopper, that is, the whole yield loci have to be measured or estimated. Here, we can point out that Jenike's approach to the design of a hopper indicates the necessity of the estimation method of yield loci in the hopper process design.

3. Rumpf's work[5,6]

Rumpf played an important role in the estimation method of yield locus. He presented an interesting characterization to estimate tensile strength σ_z of an aggregated particle. The logic of his characterization was constructed by the combination of the material property, which was the adhesion force H on the contacting point between two particles, and an engineering model on the basis of the following assumptions;

i) There are many contact points on the fracture surface of aggregated particles.

ii) Contact points are statistically and isotropically distributed on the surface of a primary particle.

iii) The adhesion forces at every contact point between two particles have narrow distribution around an average value H.

The arrangement of primary particles in an aggregated particle was completely random and the fracture surface could be approximated as an ideal plane though the shape of the actual one was irregular as shown in **Fig. 5**. He elucidated the relation between semi-macro (adhesion force H on the contacting point between two particles) and macro (tensile strength σ_z of an aggregated particle)

$$\sigma_z = \frac{1-\epsilon}{\epsilon} \frac{H}{D_p^2} \qquad (2)$$

where D_p is the diameter of a primary particle.

This equation is one of the most important contributions done by Rumpf in the estimation
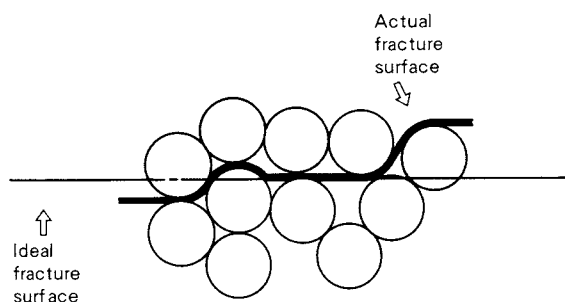
Fig. 5 Actual fracture surface and ideal fracture surface of an aggregated particle (Rumpf)

method of yield locus. We can consider his model as one of statistical models. He showed that the statistical method can connect the conception of a primary particle to that of powder.

4. Ashton-Cheng-Farley-Valentin's work[7]

As already mentioned, Jenike presented the design method of a hopper and indicated the importance of the estimation method of yield loci. On the other hand, Rumpf established a new approach to the estimation method for the tensile strength of aggregated particles. Their approach stimulated the birth of the estimation of yield locus in powder technology.

Ashton-Cheng-Farley-Valentin developed further the Rumpf's approach to yield locus estimation. They also thought that it was convenient for powder process design to discuss the yield criterion of stress condition on a specified plane in powder. The quantity to be estimated is, therefore, not a yield surface in the (p, q, e) system presented by Roscoe et al.[8], defined "at a point", but that in (σ, τ, ϵ) system as shown in **Fig. 6**, defined "at a plane", where p is mean normal stress, q is deviatric stress and e is void ratio. As already explained, the fundamental difference between them is that a point on a surface in (p, q, e) system shows the stress condition or Mohr semi-circle at the corresponding point in powder, and that in (σ, τ, ϵ) system shows the yield criterion of stress conditions on the specified plane. They considered that the latter (σ, τ, ϵ) could be more effective than the former (p, q, e) to explain the mechanism of the slip plane produced in powder and could be used as a convenient powder property for powder process design.

They noticed and discussed fundamentally
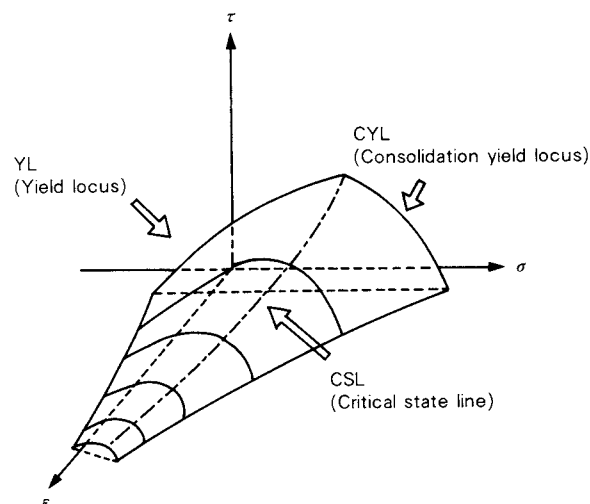
Fig. 6 YL, CYL and CSL in (σ, τ, ϵ) system
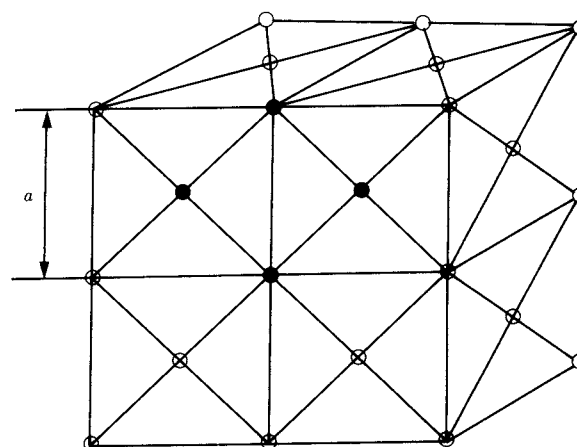
Fig. 7 Regular packing model of face centered cubic lattice by Ashton et al.

the shape of a yield locus in shear side on the basis of the following assumptions;

i) The particle arrangement in powder is assumed to be a regular particle packing of a face centered cubic lattice as shown in **Fig. 7**, and a cell size is "a". (Particle arrangement)

ii) The interaction force between particles in powder changes as shown in **Fig. 8** and gives a maximum value at a distance "r_c". (Interaction function between particles) When the component is subject to a stress below a fixed critical value, it deforms elastically according to the Hooke's law for both tensile and compressive stresses. Under a tensile or compressive stress, the lateral elastic displacement "da" also takes place such that
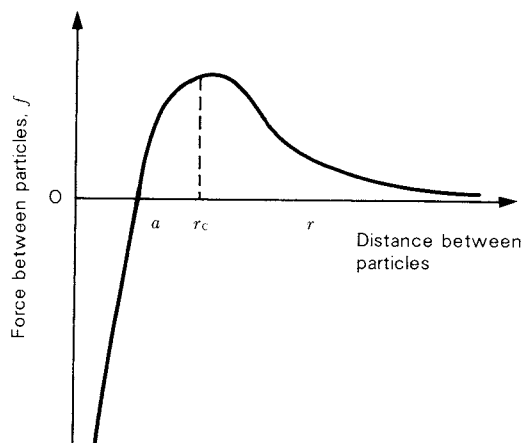
Fig. 8 Interaction function between particles in powder (Ashton et al.)

$$\frac{da'}{a} = \nu \frac{\sigma}{E} \qquad (3)$$

Where E is Young's modulus and ν is Poisson's ratio. The shear strain of powder γ is approximately expressed by the following form.

$$\gamma = \frac{\tau^n}{G} \qquad (4)$$

where G is rigidity modulus. Further, the principal of superposition is assumed, and the deformation under a complex stress system is given by the vector sum of individual deformations caused by independent component stresses.

iii) When the distance between any nearest neighbouring particles becomes to equal to r_c, the powder is in the condition of incipient flow. Further straining leads to yield and flow (Powder yield criterion).

Using these above assumptions, they obtained the following yield locus.

$$(\frac{\tau}{C})^n = \frac{\sigma}{T} + 1 \qquad (5)$$

Where T is the tensile strength of powder, C is the adhesion force and n is the index of the shear.

Eq. (5) shows the shape of a yield locus in the shear side. If the parameters T, C and n at a specified porosity ϵ_0 are measured by an appropriate apparatus or method, the yield locus in the shear side can be estimated only at ϵ_0, but not at other porosities, because the porosity dependency of the parameters is unknown.

Then, their approach does not coincide with Rumpf's one, as Eq. (5) can not describe the dependency of porosity on yield locus. However, we can evaluate their work as an important contribution in the estimation of yield locus. They considered that the estimation model of yield locus had to consist of particle arrangement, interaction between particles and powder yield criterion.

5. Makino-Saiwai-Suzuki-Tamamura-Iinoya's work[9]

According to the above discussions, a fundamental conception can be pointed out to have been established for an estimation method of yield locus in 1960 - 1970. An approach to the conception was presented by Makino et al.[9] in 1978. The model is composed of the following three factors.

i) Particle arrangement

Since actual arrangement of particles is random in general, a statistical superposition method can be applied to the description of particle arrangement. The statistical powder model as shown in **Fig. 9**, in which the n-th layer in the statistical surface of radius $n\bar{r}$ ($n=$ 1, 2, 3 ...), was introduced. It is also assumed that only the first layer has dominant effect on the mechanical behavior of a specified particle. Under these conditions the average distance $\bar{r}$ between two particles is related to the porosity by Eq. (6).

$$\bar{r} = D_p (1 - \epsilon)^{-\frac{1}{3}} \qquad (6)$$
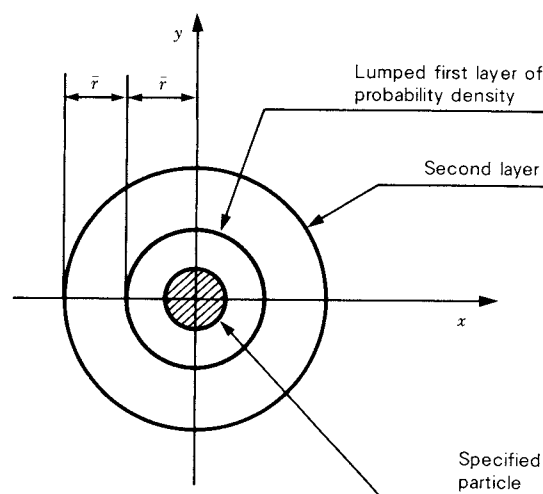
Fig. 9 Particle arrangement described by statistical model (Makino et al.)

The particle arrangement in this model is described by only two factors of a specified particle and the lumped first layer of probability density in **Fig. 9**.

ii) Interaction function between particles

To describe the estimation model of yield locus, an interaction function between a specified particle and a first layer one has to be characterized. In their model, the following interaction function $\phi(r)$ between particles is assumed.

$$\phi(r) = KD_p \frac{1}{(\bar{r}/D_p)^m - (\bar{r}/D_p)^n}$$

$$\times (\frac{1}{m}(\bar{r}/r)^m - \frac{1}{n}(\bar{r}/r)^n) \qquad (7)$$

where, K, m and n are respectively contant determined by the powder and r is the distance between a specified particle and a first layer one. Equation (7) is very similar to Lennard-Jones's interaction function.

iii) Yield criterion of powder

In order to develop powder yield model, an yield criterion of powder has to be assumed. In their model, the powder is assumed to yield when a specified particle shifts from the origin A to the point B of the circle of radius $d/2$ whose center point is at $S(0, s)$ as shown in **Fig. 10**. We call this "yield criterion of particle displacement". The parameters d and s are respectively considered to be powder constant.

From the discussions above, their yield model can be seen to be composed of the lumped particle arrangement, the interaction function similar to Lennard-Jones one and the yield
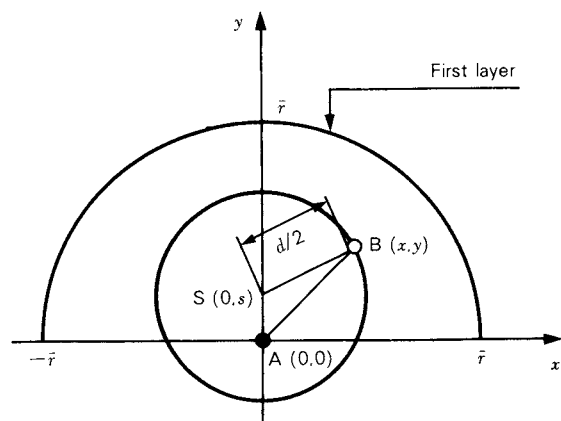
criterion of particle displacement. This model can estimate the whole yield loci from experimental data relating to four parameters (m, n, s and $d/2$). For example, if three data in both tensile and compressive strengths are measured in relation to a powder, it becomes possible to detect optimum values of the four parameters by parameter-fitting to the three data above and to estimate the whole yield loci of powder by use of their model with the four optimum parameters above.

It can be pointed out that this model has a convenient feature, i.e., the values of a few easily measurable input data lead to the whole yield loci. Then, their model can be considered to be an estimation model of yield loci.

Conclusions

In this paper, from the standpoint of the yield locus estimation, four papers of Jenike, Rumpf, Ashton et al. and Makino et al. were reviewed. As a result of it, a new field of the yield loci estimation was pointed out to begin to be opened up. Further fundamental and experimental discussions are expected on the yield loci estimation and the development of the design methods for powder processes on the basis of the yield loci.

References

1) Jenike, A.W., P.J. Elsey and R.H. Wooley: "Flow Properties of Bulk Solids", *Proc. Am. Soc. Test. Mat.*, **60**, 1168 (1960).
2) Jenike, A.W.: "Gravity Flow of Solids", *Trans, Instn. Chem. Engrs.* **40**, 264 (1962).
3) Jenike, A.W.: "Storage and Flow of Solids" *Trans. Soc. Min. Engrs.*, **235**, 267 (1966).
4) Drucker, D.C.: "Some Implications of Work Hardening and Ideal Plasticity", Q. Appl. Math. 7, 411 (1950).
5) Rumpf, H.: "Zur Theorie der Zugfestigkeit von Agglomeraten bei Kraftübertragung an Kontaktpunkten", *Chemie. Ing. Techn.*, **42**, 538 (1970).
6) Rumpf, H.: "Grundlagen und Methoden des Granulierens", *Chemie. Ing. Techn.*, **30**, 144 (1958).
7) Ashton, M.D., D.C.H. Cheng, R. Farley and F.H.H. Valentin: "Some Investigations into the Strength and Flow Properties of Powders", *Rheol. Acta*, **4**, 206 (1965).
8) Roscoe, K.H., A.N. Schofield and C.P. Wroth; "On the Yielding of Soils", *Geotechnique*, **8**, 22 (1958).
9) Makino, K., K. Saiwai, M. Suzuki, T. Tamamura and K. Iinoya; "Analysis of the Static Yield of Powder Layer", *Kagaku Kogaku Ronbun-shu*, **4**, 439 (1978).

Fig. 10 Yield criterion of powder (Makino et al.)

Dry Developer of Toner for Electrophotography

Akira Fushida

*Mita Industrial Co., Ltd.**

1. Introduction

A copier may be one of the most available office automation machines which have been promoting rationalization and efficiency leading to improvement of business works. It is broadly classified into three methods: a direct electrofax (EF), an indirect electrophotography (PPC; Plain Paper Copier), and a diazo method. In 1984, close to 2,280,000 PPC machines were produced, which occupied the share of 97.3 percent in the whole copier markets. It may be considered that a copy quality is affected essentially by a developing method and a toner (developer). The production of the toner for PPC in 1984 is estimated to reach about 30,000 tons in the world.

Various kinds of toner, which have been available together with the expansion of PPC market, are broadly devided into two types; dry and wet type. Today, the two-component dry toner is dominant, which consists of a carrier (iron powder) and a toner (colored powder). With regard to a one-component type, which consists of only toner itself, low-cost copier has been increasing in production to satisfy the needs of miniaturization and simplification. The toner is used for not only these applications but also an electrostatic printer, an electronic plate making machine, and a laser printer where an electrophotographic principle is applied. Based on this consideration, a dry-type toner (developer) will be described in the present paper.

2. Outline of electrophotographic process[1,2]

The electrophotographic process, which was invented basically by C.F. Carlson in 1938, is classified into two methods: an electrofax method (EF) that fixes directly images on a photoconducting material and a xerographic technique (PPC) that transfers images on plain paper. In this section, the xerographic process is outlined (**Fig. 1**).

In general, a xerographic process consists of
(I) Charge: The surface of the photoconductor is charged uniformly in the dark.
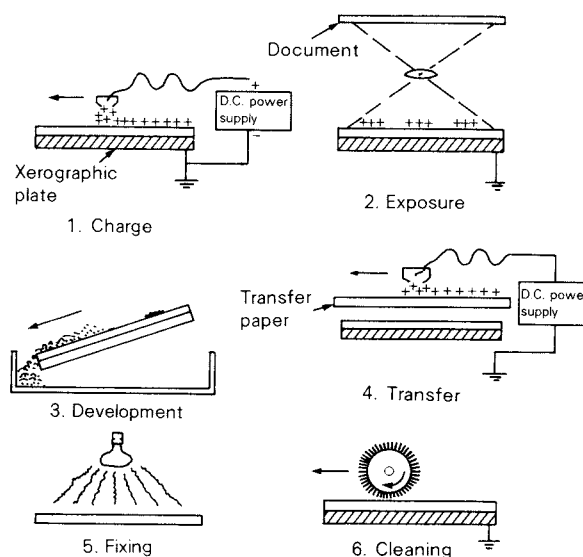
Fig. 1 Basic process of xerography
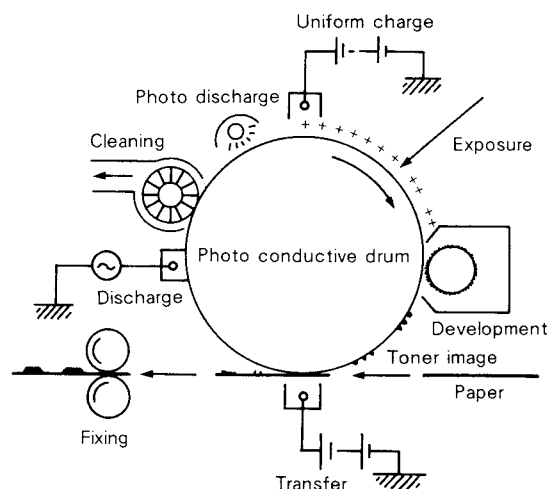
Fig. 2 Process of PPC copier

* 2-28, Tamatsukuri 1-chome, Higashi-ku, Osaka, 540
TEL. 06 (764) 3857

(II) Exposure: Exposure toward the surface of the photoconductor allows the electrostatic latent image to form.

(III) Development: Toner particles with electrical charges opposite in polarity to the latent image are deposited on the photoconductor.

(IV) Transfer: The image formed with toner particles is transferred on the transfer paper by corona discharge from the backside.

(V) Fixing: The toner image is fixed by heating and the final copy is obtained.

(VI) Cleaning: An excessive toner remaining on the photoconductor is cleaned off.

The copies are continuously obtained by repeating the above processes.

The essential point of development is that the toner particles charged with a certain polarity by mixing in a short time are transferred to the process of a latent image forming.

For example, the quality of magnetic brush development depends on:

— the developing condition such as transferred amount of developer, a magnet arrangement, the gap between a photoconductor and a sleeve, and rotation speed ratio, etc.

— the uniformity and stability of toner concentration, charge quantity during mixing of adding toner and developer.

— the control of toner concentration (This is not required for a one-component toner).

— the characteristics of developer such as electromagnetic, flowing, mechanical, and thermal-resistant characteristics.

3. Classification of dry development and dry developer

There are two kinds of dry developer for electrophotography, as listed in **Table 1**. One is a two-component developer which consists of a toner containing colored pigment and thermoplastic regin, and a carrier having a function of adding charge on the toner. Another is a one-component developer which consists of a toner alone. In practice, there are several kinds of inherent characteristics involved in each of them; insulation or conductivity, and magnetism or non-magnetism. These various kinds of developer are employed, according to the developing method. Today, the magnetic brush development, which uses an insulated, non-magnetic toner for two-component developer and an insulated magnetic toner for one-component developer, is dominant. The variety of development methods will be referred to in the later section.

4. Dry developer

In general, an electrophotographic process

| Magnetic toner | Magnetic toner |
| Non-magnetic toner | Non-magnetic toner |
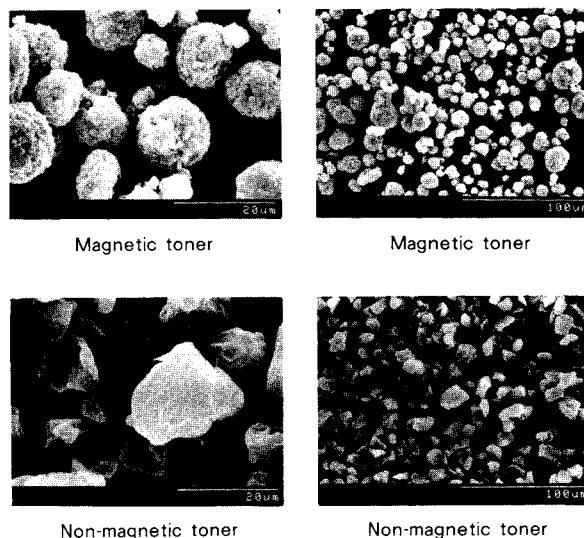
Photo. 1　Electron micrograph of toner

Table 1　Classification of dry developer and development

	Developer (toner/carrier)	Development
Two-component system	Insulated nonmagnetic toner/bead carrier	Cascade
	Insulated nonmagnetic toner/magnetic carrier Insulated magnetic toner/magnetic carrier	Magnetic brush
One-component system	Insulated nonmagnetic toner Conductive nonmagnetic toner	Fur brush Powder cloud Open chamber
	Conductive magnetic toner	Magnedynamic
	Insulated magnetic toner	Jumping

consists of the processes of charge, exposure, development, transfer, fixing, and cleaning. Toner is related directly to the four processes such as development, transfer, fixing, and cleaning as shown in **Table 2**.

The following properties should be taken into consideration for practical application.

(1) Eelectrical property

Toner particles are charged by friction, corona discharge, charge injection by electrostatic induction, etc. The triboelectrical charging is most often used, and in particular, the charge is caused by the fric-

tion with carrier particles. The polarity of charge (positive or negative) follows the triboelectrical series. The charge quantity and its attenuation depend radically on its own electrical resistance, which is controlled at a given resistance, for example, about 10^{13} Ω cm for two-component system.

(2) Particle size

Since a particle size of toner has influence on image quality like resolution, it must be controlled at 10 to 15 μm in an average diameter. This is because when the size is larger, the resolution is reduced in spite of

Table 2　Relationship among electrophotographic process, toner particle property, and picture quality

| Ferrite carrier | Ferrite carrier |

| Iron powder carrier | Iron powder carrier |
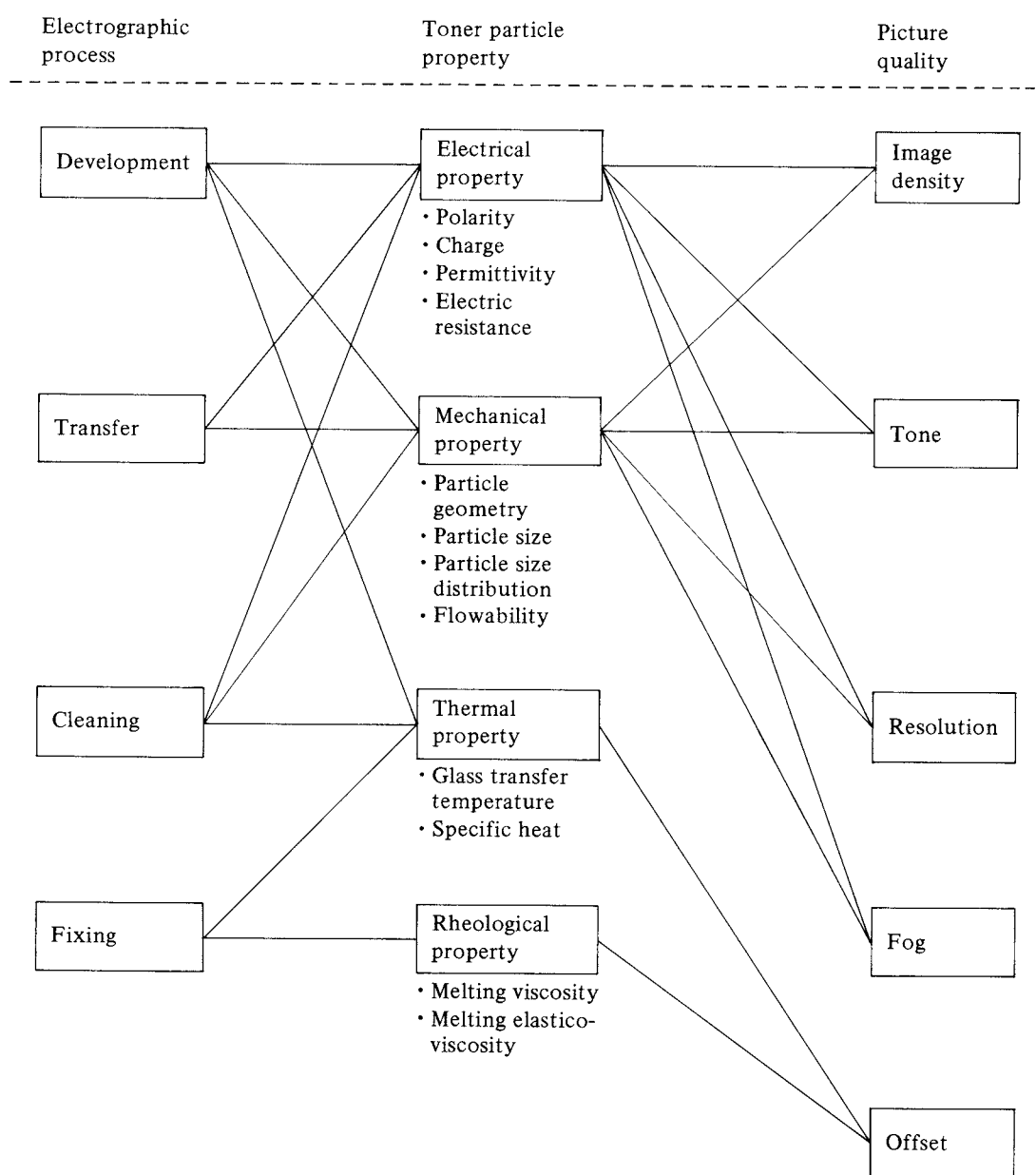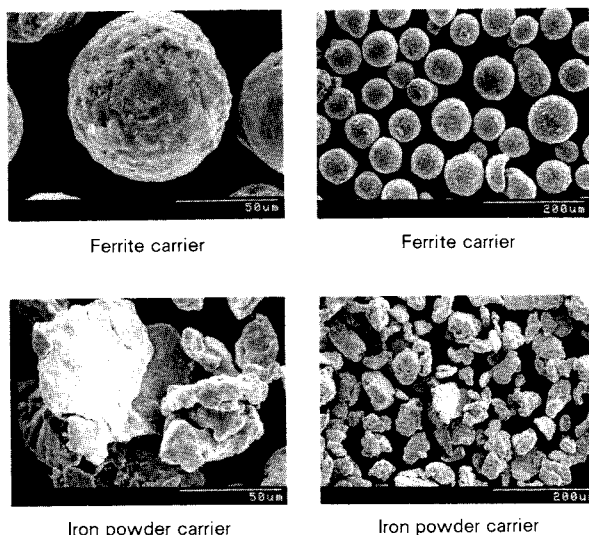
Photo. 2 Electron micrograph of toner

better flowability, and when it is less than 5 μm, fog is apt to take place and productivity is reduced.

(3) Thermal and rheological properties

The thermal and rheological properties are considerably related to the fixing process. When a heat roller is used, in particular, the initial fixing temperature, cold offset, hot offset, winding of transfer paper around the roll, etc. should be taken into consideration. In addition, in consideration of stability of toner keeping and the temperature rise in copier equipment, toner is required not to be blocked under 40 to 50°C. Toner components should be modified carefully because their characteristics have serious influence on two or more electrophotographic processes which result in deciding a final image quality.

The suitable use of one-component developer may demand more careful design, as this developer must play double roles of a toner particle and a carrier particle in a two-component developer.

For a carrier particle in a two-component developer, on the other hand, the performance appropriate to the developing process is required, which is essentially dependent on material, particle size, geometry, electrical and magnetic property, etc. The following materials can be utilized as a carrier:

(i) Glass beads coated with resin
(ii) Iron filings or ferrite powder coated with resin

(iii) Iron filings treated with surface oxygenation
(iv) Resin particles dispersed with magnetic particles

The carrier has a wide range of variety in geometry from irregular to spherical shape, with a diameter of 10 to 500 μm.

5. Composition of dry toner[1]

The toner materials which are available chiefly are a two-component insulated non-magnetic toner and a one-component insulated magnetic toner. The compositions of these toners are listed in **Table 3**. The following materials are often used for these toners.

(i) Thermoplastic resins: polystyrene, styrene-acryl copolymer, polyester, epoxy, polyethylene, and polypropylene
(ii) Dye and pigment: carbon black, nigrosine, and spirit black
(iii) Charge control agent

For positive polarity: electron donor like nigrosine, metal salt of fatty acid, and quaternary ammonium salt

For negative polarity: azo-dye containing metal
(iv) Magnetic material: magnetite and ferrite
(v) Other material (additives): colloidal silica and fatty acid

The significant points for toner design are:

— having well-balanced functions required for electrographic process.
— high quality and long life
— environmental stability
— safety (harmlessness)
— stable preservation
— processing
— low cost

Table 3 Component of toner

Component of toner	Two-component toner	One-component toner
	(wt %)	(wt %)
Thermoplastic region	80 ～ 90	30 ～ 60
Dye or pigment (stain)	5 ～ 15	0 ～ 10
Charge control agent	1 ～ 5	1 ～ 5
Magnetic pigment	0	40 ～ 65
Others(fluidizing material)	0 ～ 5	0 ～ 5

6. Production process of toner

Although there are many ways in production of toner: mechanical size reduction, spray drying, micro-cupsel forming, polymerization, etc., it is almost obtained practically by mechanical size reduction and partly by spray drying for magnetic toner. **Figure 3** shows typical production processes of mechanical size reduction and spray drying.

The following is outlined about the size reduction process.

(i) Mixing of materials

Toner materials such as resin, pigment, dye, charge control agent are mixed to accomplish the subsequent process of heating and kneading in a short time by ribbon blender, V-type mixer, etc.

(ii) Heating and kneading

The mixed materials are melted by heating and kneaded uniformly by using heat roller mill, heating kneader, etc. to prevent fog and scattering of toner particles and promote durability and cleaning treatment.

(iii) Size reduction

After cooled, they are crushed to 1 ~ 3 mm in size by hammer mill or feather mill, and then ground to 10 to 15 μm by jet mill or pin-type mill, etc.

(iv) Classification

The ground toners are classified to satisfy an acceptable size distribution. Air classifiers are often utilized for this purpose.

(v) Surface treatment

The classified toners are mixed with silica powders by V-type mixer and Nauta Mixer to promote its flowability and cleaning treatment.

Since each process above mentioned has great influence on the quality of toner, the selection of equipments and processing conditions should be taken into consideration.

7. Measurement of toner properties

The important points indicated in **Table 2** are explained individually.

(1) Charge quantity

The blow-off method is used in general to measure charge quantity. As illustrated in **Fig. 4**, this method is based on the principle that the toners alone are blown off by high-pressure O_2 or N_2 gas from the developers which are contained in a cylindrical Faraday cage with wire nets at both sides. When toner particles are charged, a capacitor accumulates as much quantity of charge with opposite polarity as the toners taken away out of the cage. Although the value of Q is obtainable by measuring the capacitor voltage from the relation of $Q = CV^{5)}$, this procedure can provide nothing but an average value of the charge quantity.

Another method is that the polarity and relative distribution of the charge on toners are determined when they flow down along the
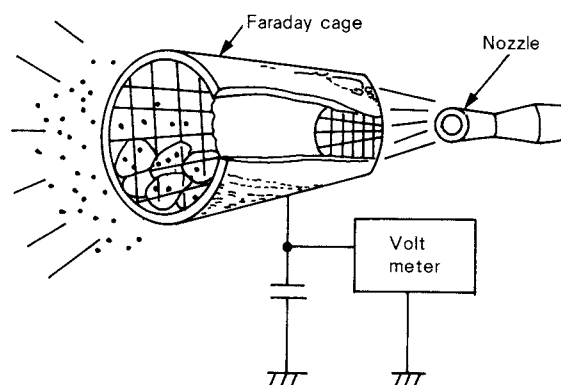
Fig. 4 Blow-off principle
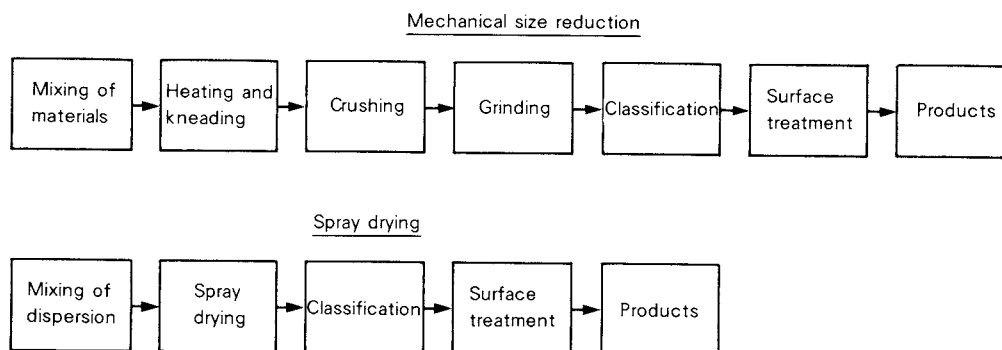
Fig. 3 Production process of dry toners

air stream between two parallel impressed plates, as shown in **Fig. 5**. In addition, it is also reported by R.B. Lewis of Xerox Corp. that the charge distribution is measured by forming the electrical field perpendicularly to the air stream, as shown in **Fig. 6**[3].

(2) Particle size distribution[6]

The particle size distribution of toners is measured in general by Coulter counter. This method is based on the principle that the variation of electrical resistance is transformed to the distribution data. This variation is caused by the toner particles which pass through the aperture of a glass tube (aperture tube) that is placed in an electrolyte of physiological saline called Isoton II. In practice, the toner particles dispersed outside of the aperture tube are sucked toward inside by a vacuum pump.

(3) Other properties

The geometry or the surface condition is observed effectively by an electron microscope. The surface area is measured by BET method. The angle of repose, bulk density, and cohesion are measured by each corresponding tester. We are able to apply directly the measuring equipment of polymer characterization without modification: for example, a differential scanning calorimeter for glass transition temperature and softening point, and a flow tester for melting viscoelasticity.

Fig. 6 Charge spectrograph chamber

Fig. 7 Coulter counter

Fig. 5 Parallel plates equipment
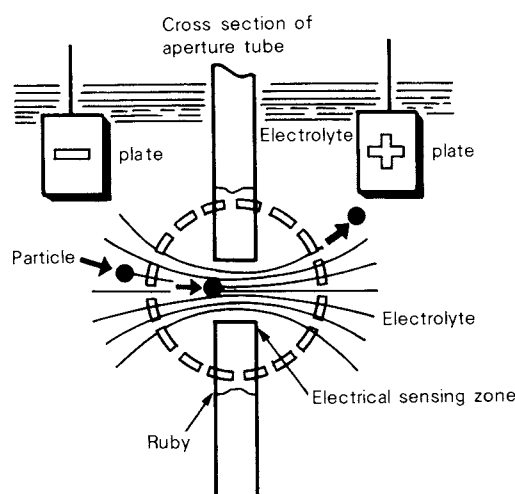
8. Development

Typical developing techniques indicated in **Table 1** are outlined as follows.

(i) Cascade development

The developer material in cascade development consists of a bead or steel material (0.2 to 0.7 mm) coated with resin, called the carrier, and toner particles. Development of the electrostatic image is achieved by cascading the toner-carrier developer over the surface of the photoconductor. Although this developing technique allows line copy images to be sta-
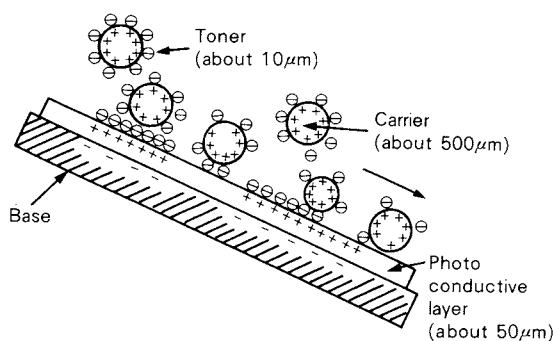
Fig. 8 Cascade development
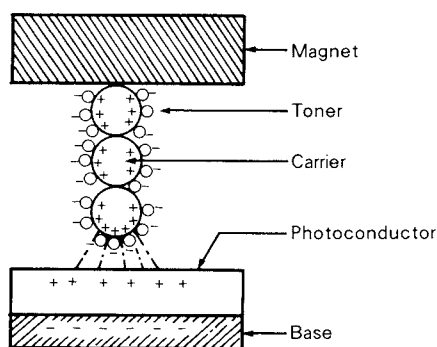
Fig. 9 Magnetic brush development

bilized, the image missing often takes place in the solid black area by the edge effect.

(ii) Magnetic brush development

Magnetic brush development uses a magnetic carrier of iron powder or ferrite of 50 to 200 μm mixed in 3 to 10 weight percent with a insulated toner of 10 to 15 μm. When toner and carrier are mixed, the toner acquires a charge of a certain polarity. Then, development of the electrostatic image is achieved by brushing the ferromagnetic fiber over the surface of the photoconductor. This method provides a high quality in finish copy with a sufficient continuous tone reproduction and less fog because the developer is acted as a developing electrode.

(iii) Fur brush development

Development is accomplished by using a soft fur as a carrier against which toner particles are rubbed to become charged triboelectrically. This development is difficult to control electrically because of the influence of humidity resulting from the use of fur.

(iv) Powder cloud development

The cloud-like toner particles are blown off through a fine metal nozzle, as shown in **Fig. 10**. Development is achieved by means of the toner deposition on the surface of the photoconductor which is spaced closely with an electrostatic latent image.

(v) Magnedynamic development

A toner of magnedynamic development consists of a resin including magnetic iron powder (magnetite) of 50 to 70 weight percent, and is covered with carbon black.

Development is conducted in the way how the magnetic brush formed on the conductive sleeve is brought near to electrostatic latent image to induce opposite-electrical charge by electrostatic induction, as shown in **Fig. 11**. Insulated paper
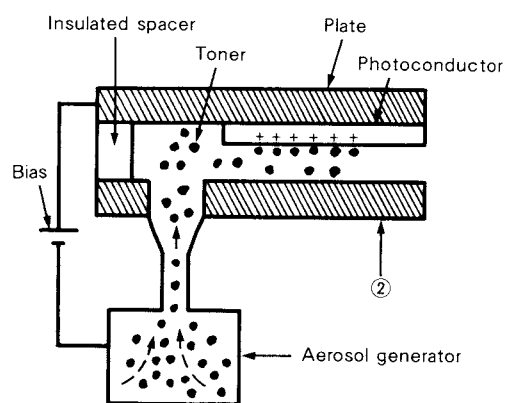
Fig. 10 Powder cloud development
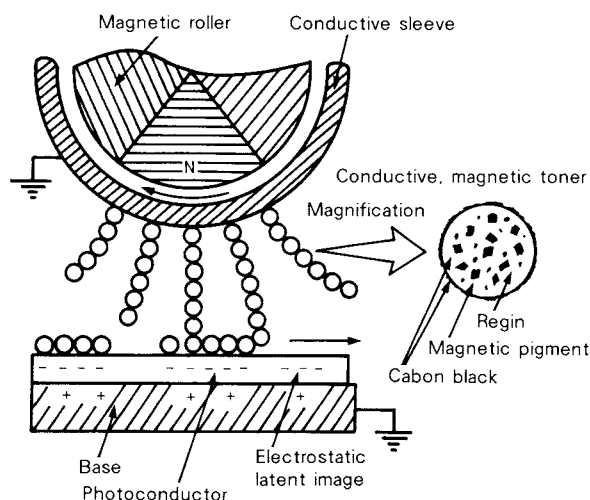
Fig. 11 Magnedynamic development
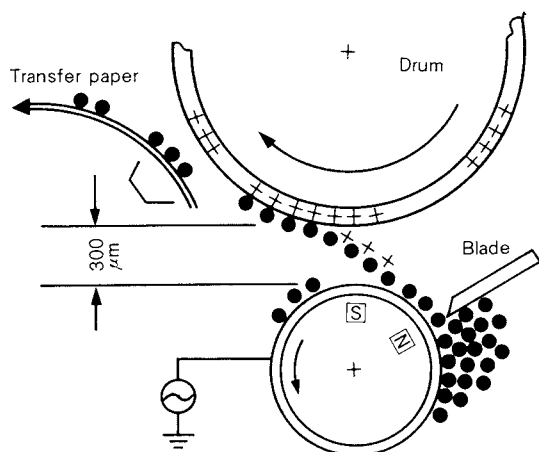
Fig. 12 Jumping development

or EF method is available because of poor transfer ability for plain paper.

(vi) Jumping development

A toner used in jumping development is about 12 μm in diameter and 10^{15} Ωcm in resistance, including magnetite with as much as 35 weight percent. This insulated, magnetic toner material is deposited on the surface of the sleeve by triboelectrification to form the toner layer with a thickness of about 50 μm. Development is achieved by vibrating the toner layer when the gap between the sleeve and the photoconductor is maintained to be 300 μm and the a−c bias of hundred-order Hz is applied.

10. Conclusion

This report has explained the outline of kinds, required properties, production methods, etc. of dry toner developer. It is expected that the coming information society will need a wide-spread use of copier or printer in domestic work as well as in office business and that cost reduction may become the most important interest. For cost reduction, it should be taken into consideration to find out a more efficient process of toner production, in particular size reduction, classification, etc., and a new process such as spray and polymerization.

In recent years, the variety of developing techniques and developers has improved and stabilized the copy quality. However, there is a strong demand for higher quality, longer life, and less maintenance.

The author believes that better toner evolution requires not only matching to each process but also cost reduction, less polution, easier processing, environmental stability, etc.

References

1) Inoue, E.: "Denshi Shashin Gijutsu (Electrophotography technique)" Kyoritsu Shuppan (1982).
2) Kinoshita, A. and H. Machida: "Kiroku Zairyo to Kankousei Jushi (Recording material and photoconductive resin)" Nippon Gakujutsu Shinkohkai (1979).
3) Lewis, R.B., et al.: *J. Soc. Electrophotography, Japan,* 22, 81 (1983).
4) Takahashi, K.: "Shashin Kougaku no Kiso (Fundamental knowledge of Electrophotography)" The Society of Photography, Japan (1982).
5) Blow-off catalogue (Toshiba Chemical Co., Ltd., 1977).
6) Coulter Counter catalogue (1983).

New R&D Center Starts Operations at Hosokawa Micron Corp.

Hosokawa Micron Corp. which is a financial supporter of *KONA* built, as one of the commemorative events for its 70th anniversary, a new R&D Center (See Photo. 1) in a neighboring area of its Hirakata factory early in April, 1986. On April 18, the celebration party for the 70th anniversary of Hosokawa Micron Corp. combined with the announcement of completion of this new building was held with much enthusiasm at its Hirakata factory. About one thousand people in official, academic, and business fields, including Mr. Yasushi Oshima, *the Mayor of Osaka City* and Mr. Keizo Saji, *the President of Osaka Chamber of Commerce and Industry* were invited to this party.

Object of foundation

This R&D Center was founded to function as the kernel of R&D activities of Hosokawa Micron group units which are scattered all over the world. Its facilities for test or research works appear to have the first-rate scale and level through the world. It is said to be able to carry out tests of combined process system as well as individual equipments so as to fulfill a veriety of needs of customers.

Outline of facilities

This Center consists of two sections: administrative and test section.

The administrative section (four stories) includes a variety of rooms such as clean room, equipments exhibition room, measuring room as well as clerks' office, conference room and reception room. In the test section (two stories), on the other hand, Hosokawa products are set in each enclosed space with full utility. It is also equipped with special test facilities for cryogenic grinding, pulse combustion drying with sound proof construction and powder painting, etc. (See Photo. 2).
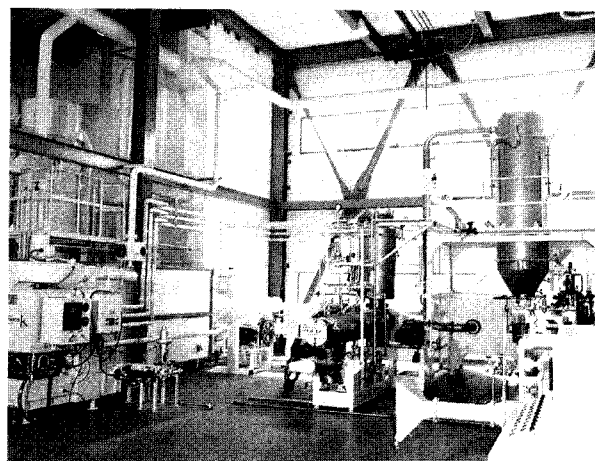
▲
Photo. 2
Interior of R&D Center
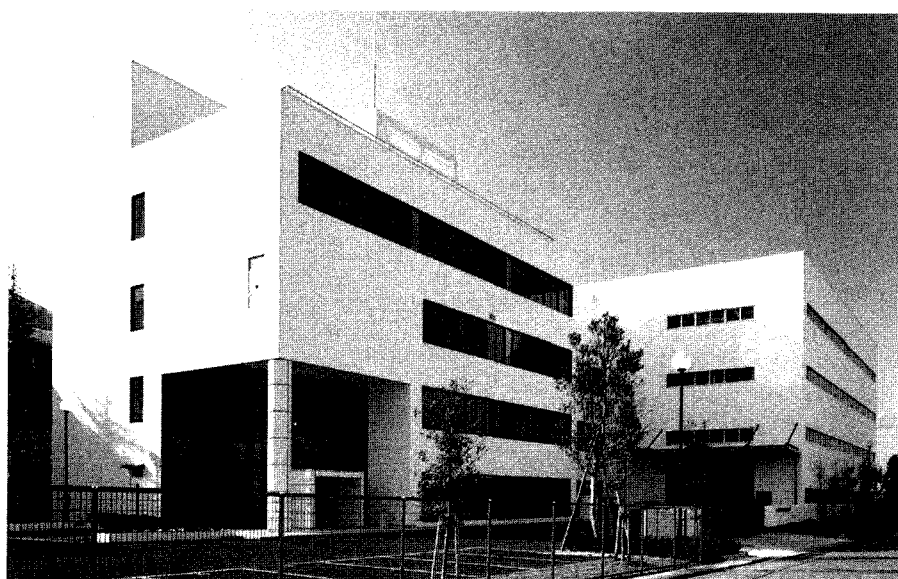
◀ Photo. 1
Exterior of R&D Center

Exhibition of new products and technical lecture meeting

About two hundred people (researchers and customers) were invited to this center on April 23 to observe new products and listen to a technical lecture meeting.

New products displayed:

HOSOKAWA MICRON	Angmill AM-35 and AM-60	(Size reduction system to produce submicron particles)
HOSOKAWA MICRON	Aquamizer	(Stirred ball mill)
HOSOKAWA MICRON	Fine Sharp Separator FSS-0 and FSS-SR	(Air classifier for fine particles)
HOSOKAWA MICRON	Particle Charge Spectrometer	(Particle size and charge analyzer)
HOSOKAWA/AKASHI	Sedimenputer SPT-C	(Particle size analyzer based on centrifugal unbalance)
HOSOKAWA MICRON	Penetration analyzer	(Measuring instrument for liquid penetration rate)
HOSOKAWA MICRON	Mini-table Feeder MTF-1	(Laboratory-scale table feeder)
HOSOKAWA MICRON	Labomixer	(Laboratory-scale Nauta Mixer − Reactor)
HOSOKAWA/GERICKE	Nibbler	(Crusher for agglomerate materials)
HOSOKAWA/GERICKE	Microfeeder GMD60	(Laboratory-scale feeder)
HOSOKAWA/MIKRO	Mikro PSA	(Dry sieve analyzer)

Technical lecture meeting (See Photo 3):

Speaker	Title
Shigeo Miwa (Professor of Doshisha Univ.)	History of fine grinding and advanced technology
Yuichi Yamamura (Professor emeritus of Osaka Univ.)	Attacking mechanism of cancer and prevention against it

Photo. 3 *Technical lecture meeting*

The Party of Powder Technology (Japan) held the 19th symposium at Sunshine Prince Hotel in Tokyo on August 28th, 1985. The present symposium focused on the two sessions of interesting physical properties of particulate materials described below.

Session 1   Electrostatic behaviors of particulate materials

Chairmanship: Yasuo Kousaka (Univ. of Osaka Prefecture)

- Electric behaviors of particulate materials

  Senichi Masuda
  (Univ. of Tokyo)

- Electric charge on submicron particles and electrostatic air filters

  Hitoshi Emi
  (Kanazawa Univ.)

- Cohesive force of powder layer in electric field

  Fumikazu Igasaki
  (National Chemical Lab. for Industry)

- Measurement of electric charge on particulate materials

  Toyokazu Yokoyama
  (Hosokawa Micromeritics Lab.)

Session 2   Cohesion and dispersion of particulate materials

Chairmanship: Naoya Yoshioka (Professor Emeritus of Kyoto Univ.)

- Cohesion and dispersion of particulate materials

  Genji Jimbo
  (Nagoya Univ.)

- Recent interesting reports on cohesion of particulate materials

  Ryuichi Aoki
  (Tokyo Univ. of Fisheries)

- Dispersion of particulate materials due to high-speed air stream

  Akira Suganuma
  (Univ. of Tokyo)

- Estimation on kneading and dispersion of magnetic particles

  Kei Miyanami
  (Univ. of Osaka Prefecture)
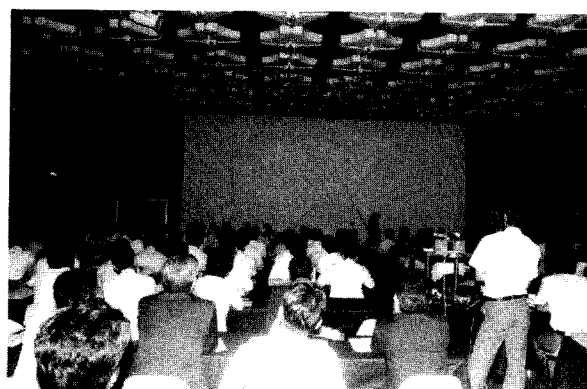
Photos: *The 19th symposium on powder technology in 1985*

Public meeting concerning powder technology recently held in Japan

21st Technical meeting

promoted by the Society of Powder Technology, Japan
held at Tokyo on June 24–25, 1986

Recently developed techniques and analyzers were reported for characterizing a variety of powder properties such as particle size (distribution), concentration, electrical charge, and mechanical properties. In this meeting, 20 lectures are given with actual exhibition of several apparatuses. The main lectures were:

- Characteristics and particle size of powder materials (Masafumi Arakawa, Kyoto Institute of Technology)

- Cohesion, shear, and flowability of powder materials (Noriyoshi Kaya, Hosokawa Micromeritics Lab.)
- Measurement on the degree of mixing and kneading, and water concentration (Munetake Sato, Univ. of Osaka Prefecture)
- Measuring instruments for industrial powder materials (Hiroaki Masuda, Hiroshima University)
- Particle charge analyzer (Toyokazu Yokoyama, Hosokawa Micromeritics Lab.)

22nd Summer seminar

promoted by the Society of Powder Technology, Japan
held at Kobe on July 15–17, 1986

This seminar focused on the characteristics and construction of powder materials including 19 lectures. The main lectures were:

- Construction and characteristics of randomly packed particles (Keishi Goto, Toyohashi Institute of Technology and Science)
- Powder processing and particle agglomerate construction (Masafumi Arakawa, Kyoto Institute of Technology)

2nd meeting on particle processing technology

promoted by the Society of Powder Technology, Japan (Particle Preparations and Design Dept.)
and
the Association of Powder Process Industry & Engineering (Division Meeting on Particulate Modification Technology)
held at Kao Corp., Wakayama Factory on July 18, 1986 (The number of attendants was 90.)

The present meeting was held to observe the particle processing activities in chemical industries after inspection of Kao Corp., Wakayama Factory.
The lectures given were:

- Surface improving technique for powders by using organic polymer materials (Hisao Mitsui, Kao Corp.)
- Recent works on production of medicine by spray drying (Hirofumi Takeuchi, Gifu Pharmaceutical University)
- Production of amorphous inorganic medicine by sol-gel method (Noboru Toge, Univ. of Osaka Prefecture)
- Bio-technology in Hayashibara Corp. (Yoshio Tsujisaka, Hayashibara Corp.)

Academic publication concerning powder technology in Japan (printed in 1985)

Journal of the Society of Powder Technology, Japan Vol.22 (1985)

Title	Author(s)	Page
• The Control of Solid Flow Rate in Pneumatic Conveyer	S. Matsumoto, H. Harakawa, M. Suzuki and S. Ohtani	3—10
• Experimental Study on the Compaction of Fine Powder with Vibration	F. Takeuchi, S. Fukuda, K. Yamanaka and T. Kano	73—78
• The Surface Active Site Distribution of Ceramic of Ceramic Powders Produced by the Ultra-fine Grinding — SiC, Si_3N_4, SiO_2 —	Y. Kanno	139—143
• The Effect of the Pre-shear on the Shear Test of a Powder Bed	H. Hirota, T. Kobayashi, H. Tajiri, H. Murata, M. Wakabayashi and T. Oshima	144—149
• The Utilization of Wasted Fine Clayey Particles as Carriers in Solid Formulations		
• The Particulate Fouling Mechanism on Heat Transfer Tudes in Turbuent Gas Flow	S. Toyama, H. Mori and A. Yamaguchi	199—206
• An Experiment of the Breaking Hardness Distribution for Several Kinds of Granular Foods	M. Yamashiro and Y. Yuasa	207—214
• Measurements of Yield Loci of Powder Bed in the Normal Stress Ranging from Positive to Negative	M. Hirota, T. Kobayashi and T. Oshima	271—277
• Coating of Seed Particles in Tumbling Fluidized Bed by Atomizing the Suspensions of Clayey Particles	E. Abe, H. Hirosue, and H. Kikuchi	278—287
• An Analysis of the Grinding Process of Vibration Milling	H. Yamamoto, Y. Kuwahara and S. Yashima	335—341
• Fine Grinding by a Vibration Mill — The Effects of Vibration Amplitude and Frequency —	N. Sasaki and K. Murakami	342—345
• Grindability of Iron Ore, Pellet, and Coal in the Ore Treatment Process	N. Imanishi	346—353
• Fundamental Research on the Mechanisms of Dry and Wet Type Friction Grinding by a Packed Granule Shearing Tester	S. Okuda and T. Fukuoka	354—361
• Analysis of Production Process of Fine Size Fraction of Silicate Sand by Ball Mill Grinding	G. Jimbo and T. Shibata	362—371
• Discontinuous Flow and the Frictional Property of Granular Materials	J. Hidaka, Y. Kirimoto, S. Miwa and K. Makino	427—435
• Experimental Research on the Critical Bridging Span for a Silo —Part 1: The Flow Characteristics of Coarse Grain Materials—	T. Tamura, H. Haze, M. Kato and T. Yamada	511—521
• Discussions on the Variation of Mechanical Powder Strength	K. Makino, A. Higashiyama, M. Yamada and K. Kuramitsu	522—525
• A New Measuring System of the Porosity Distribution Generated in Powder Bed	K. Makino, A. Higashiyama, M. Yamada and K. Kuramitsu	526—529
• Development of a Vibration Type Powder Tester	M. Satoh, S. Komura and K. Miyanami	530—534
• Flow Visualization on a Sphere in a Packed Bed	Y. Tsuji, Y. Morikawa, M. Nakao and N. Nakatsukasa	599—605
• Modulus of Compressibility of Powders in Tapping Compaction	H. Igarashi	606—611
• The Estimation of the Void Fraction in a Cohesive Sphere Bed with Size Distribution	M. Suzuki and T. Oshima	612—617

Title	Author(s)	Page
• The Effect of Various Histories on the Tensile Strength of Powder Bed and the Creeping Failure Phenomenon	H. Kamiya, S. Furukawa, J. Tsubaki and G. Jimbo	618—625
• Continuous Separation of Spherical and Non-spherical Particles by a Rotating Conical Disk with a Spiral Scraper —Effect of Some Factors on Separation Performance—	K. Yamamoto and M. Sugimoto	626—633
• Effects of Tensile Strength and Tensile Breakup Energy on the Yield of Wet Granular Structures	K. Terashita, K. Nishimura, N. Shinke and K. Miyanami	634—640
• Some Findings Necessary for the Analyses of a Solid-Solid Reaction	M. Shirai and T. Tanaka	683—687
• Calculating the Conversion of a Diffusion Controlled Solid-Solid Reaction	M. Shirai and T. Tanaka	688—692
• The Interaction between the Pressure Loss of Gas and the Flow of a Medium in a Moving Granular Bed Filter	S. Mizukami, M. Wakabayashi and H. Murata	753—759
• The Solid-Solid Reaction Theory Compared with Previous Experiments	M. Shirai and T. Tanaka	760—764
• Separation Characteristics of Particles According to the Shape on a Rotating Conical Disk with a Spiral Scraper	K. Yamamoto and M. Sugimoto	813—819
• Particle Size Distribution Measurement of Coagulated Powders Using an Image Analyzer	A. Kimura, K. Tanabe, R. Yamamoto and T. Arai	820—826
• Two-Dimensional Packed Structures of Long Cylinder	S. Toyama, M. Nakamura, H. Mori and M. Kishi	827—832

Funsai (The Micromeritics) No.30 (1986)

Title	Author(s)	Page
• Characteristics of Various Si_3N_4 Powders Modified by Comminution Grinding	Y. Kanno	4—9
• The Use of Gas Pressure Gradients to Control Powder Packing Density	A. G. McLean, S. Suganuma, K. Matsumoto and R. Aoki	10—14
• Characteristics of Hosokawa Micron Mini-table Feeder (MTF-1)	K. Mizui	15—20

Kagaku Kogaku Ronbunshu Vol.11 (1985)

Title	Authors	Page
• Effect of the Flowability of Dust on Characteristics of Dust Collection by a Filter Cloth	M. Hirota, A Fudoh, Y. Mizuno and T. Oshima	7—12
• An Experiment of Impact Grinding for Investigating the Characteristics of a Screen Mill	Y. Kuga, J. Koga, K. Yamaguchi and I. Inoue	13—19
• Backwashing of Spongy Metal Magnetic Filtration	S. Endoh, K. Yamaguchi and S. Okamoto	20—26
• Particle Reentrainment from Powder Bed of Fine Particles in a Rectangular Air-Flow Channel	H. Masuda, S. Matsusaka and S. Ikumi	48—54
• Collection Efficiency of Granular Bed Filters due to Diffusion, Interception and Sedimentation	H. Mori, N. Kimura, T. Aragaki, S. Toyama and M. Shirato	134—139

Title	Authors	Page
● Statistical Analysis of the Fatigue Failure Phenomenon of Powder Bed by Loading with Dynamic Repeated Tensile Stress	H. Kamiya, J. Tsubaki and G. Jimbo	186—192
● Increasing Process of Displacement in Fatigue Failure Phenomenon of Powder Bed by Repeating Dynamic Tensile Stress	H. Kamiya, J. Tsubaki and G. Jimbo	210—216
● Grinding Rate of a Ball Mill Operated under Centrifugal Force	T. Honma, M. Kuriyama M. Hasegawa and Y. Kanda	311—316
● TiO$_2$ Particles by Chemical Vapor Deposition —Particle Formation Mechanism and Chemical Kinetics—	T. Kanai, H. Komiyama and H. Inoue	317—323
● Void Fraction of Multi-Component Randomly Packed Beds with Size Distribution	M. Suzuki, H. Ichiba, I. Hasegawa and T. Oshima	438—443
● Temperature Rise in Brittle Materials by a Rotating Friction Mill	S. Morohashi, N. Ooi, I. Matsubara and S. Yashima	687—695

Journal of Chemical Engineering of Japan Vol. 18 (1985)

Title	Authors	Page
● An Investigation of the Comminution Process of a Screen Mill Based on Data of Impact Crushing	Y. Kuga, J. Koga, K. Yamaguchi and I. Inoue	270—273
● Laboratory Liquid-Solid Reactor in Heterogeneous Catalysis	T. Maruyama, Z. Yoshida and S. Miki	502—509

Journal of the Society of Materials Science, Japan Vol. 34 (1985)

Title	Author(s)	Page
● Mechanochemical Behavior of Basic Magnesium Carbonate by Grinding	T. Sakai, N. Ohi and M. Sugimoto	1239—1244
● Fundamental Studies on Compacting Fabrication of Fine Powder	M. Arakawa	1245—1248
● Tensile Strength and Internal Friction Factor of Wet Fine Coal	K. Terashita, K. Furubayashi T. Konishi and K. Miyanami	1249—1254
● Simulation of Mixing of Two Groups of Particles with Different Electric Resistance	T. Yoshioka, T. Kaneko Y. Fujihara and Y. Yoshimura	1255—1259

Journal of the Japan Society of Powder and Powder Metallurgy Vol. 32 (1985)

Title	Authors	Page
● The Estimation of Distance between Loose Powder Bulk Density Zones Formed in Powder from Its Acoustic Emission — In Case of Plunger Penetration—	K. Makino, M. Yamada, T. Tuda, K. Kramitsu and J. Hidaka	8-13
● The Surface-treatment of Silicon Nitride with Organo-silyl Chlorides and Their Surface Properties	H. Utsugi, A. Endo, N. Suzuki and K. Ono	43—47

Hosokawa Micron Corp. developed recently many new products for powder handling. Some of them are introduced below.

HOSOKAWA MICRON AQUAMIZER
(Wet-type stirred ball mill)

Power required : 0.4 − 37 kW
Capacity : 7.9 − 1100 ℓ

Features:
- High production capacity
- Less contamination due to wear abrasion
- Less maintenance requirement
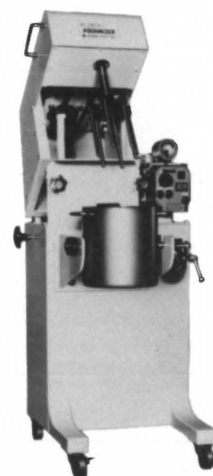
HOSOKAWA MICRON LABOMIXER
(Laboratory-scale Nauta Mixer − Reactor)

Power required : 50 W
Capacity : 2.5 ℓ

Features:
- Fastest mixing with highest accuracy
- Homogenious dispersion of materials
- Easy operation and maintenance
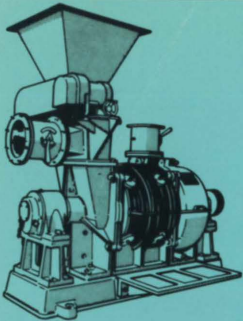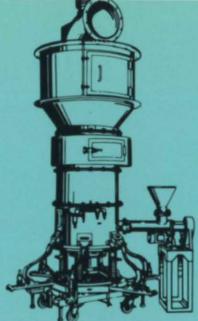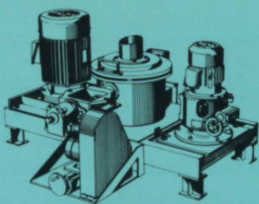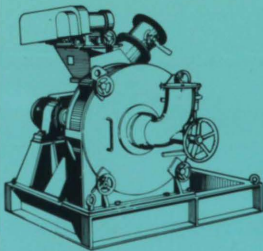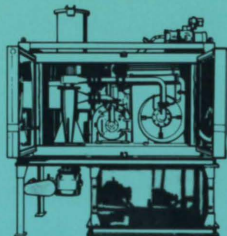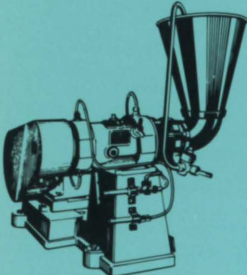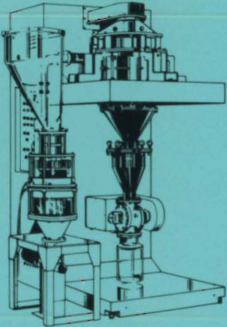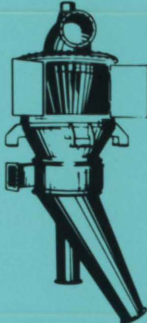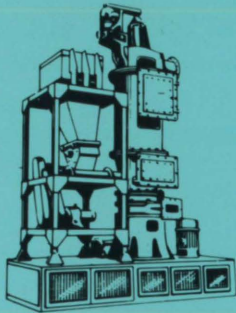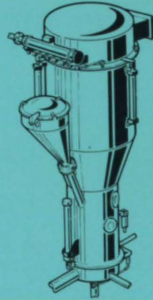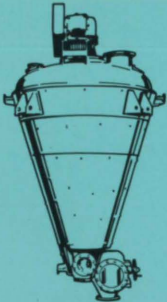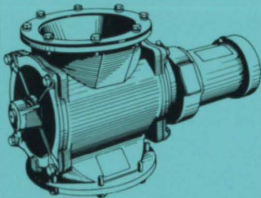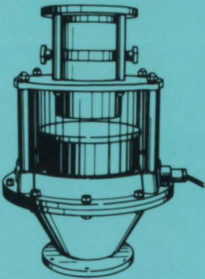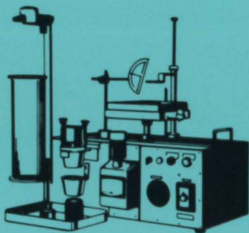
HOSOKAWA MICRON MINI-TABLE FEEDER
(Laboratory-scale table feeder)

Power required : 40 W
Feeding rate : 1 − 15 ℓ/Hr

Features:
- Suited for cohesive fine powders
- Wider application range
- Simple construction − easy to operate and clean